ANNUAL REPORT

University Research Initiative

Contract No.: N00014-92-J-1808

March 1993 - April 1994

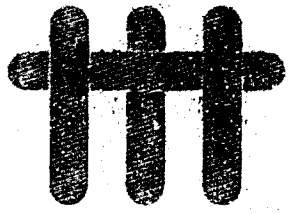

The Processing and Mechanical Properties of High Temperature/ High Performance Composites

by

A.G. Evans & F. Leckie
University of California,
Santa Barbara

University of Pennsylvania
Harvard University
Washington State University
Carnegie Mellon University
University of Virginia

Book Vol. 2

Interface Effects

SUMMARY

OF

TABLE OF CONTENTS

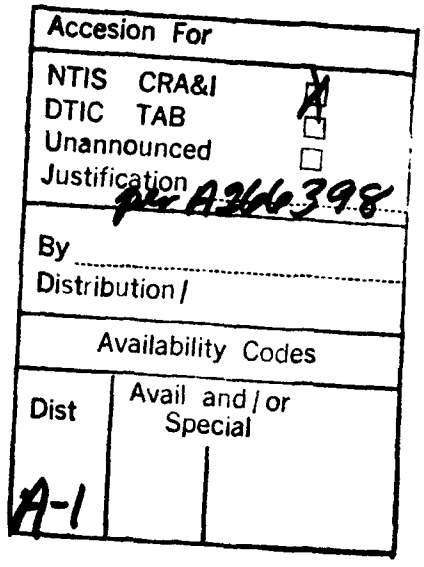

KJS 4/27/94

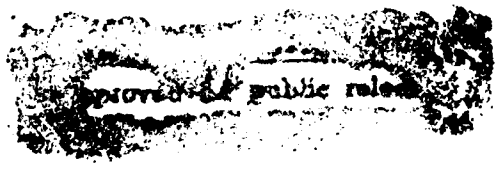

BOOK 5

INTERFACE EFFECTS

70.	A Theory for Cleavage Cracking in the Presence of Plastic Flow	Z. Suo C. F. Shih A. G. Varias
71.	Dislocation Nucleation from a Crack Tip: A Formulation Based on Anisotropic Elasticity	Y. Sun G. E. Beltz

KJS 4/27/94

EXECUTIVE SUMMARY

The general emphasis for 1994 would be on increased software development, testing of subelements and design calculations. For these purposes, the constitutive law coding and development would be coordinated by Nick Aravas, and implemented in ABAQUS. The initial implementation would be the elastic/plastic model for MMCs with interface debonding developed in 1993 (Leckie). This would be extended in 1994 to include creep and some aspects of thermomechanical cycling. The code would be used for design calculations concerned with MMC rotors, actuators and vanes (Leckie). A plan is being formulated to collaborate with Pratt and Whitney to acquire MMC sub-elements representative of these components during 1994. Experimental tests on these subelements would be capable of providing a direct validation of the code capabilities.

Constitutive law and fatigue lifing software would be created for CMCs using continuum damage mechanics (CDM) approaches (Leckie, McMeeking). The approach has been motivated by micromechanics models developed in 1993 (Hutchinson, Zok, Evans). These codes would be used to calculate stress redistribution effects and fatigue life on simple sub-elements, such as center notched and pin-loaded plates. Comparison with experimental measurements needed to test the fidelity of the models will be based on moiré interferometry and thermoelastic emission. This effort is coordinated with the NASA EPM program through both General Electric and Pratt and Whitney. A plan for acquiring sub-elements from DuPont Lanxide is being formulated.

A new emphasis for 1994 would be on the transverse properties of CMCs. The measurements and calculations performed in 1993 have indicated a strategy for curved sections and junctions that would establish a consistent design approach. The basic approach for resisting failures from combinations of interlaminar shear and transverse tension involves the use of stitching and angle ply weaving patterns that inhibit major reductions in stiffness when matrix cracks are induced by transverse loads and bending moments. For this purpose, calculations would be performed that combine

the mechanics of delamination cracks with models of bridging by inclined fiber bundles (Hutchinson, Ashby, Evans, McMeeking). The insight gained from these calculations would be used to design and acquire sub-elements, such as C sections and T junctions.

Additional software development will be for creep and creep rupture (McMeeking). The models devised in 1993 and test data relevant to MMCs will be combined into a code that predicts the creep and rupture of unidirectional MMCs subject to multiaxial loads. Some aspects of this code will also be applicable to CMCs.

Two new activities will be introduced in 1994: thermal properties and damping. The thermal properties will be studied on both CMCs and MMCs (Ashby, Hutchinson). Measurements of thermal diffusivity will be made by the laser flash method and related to the properties of the interface and the density of matrix damage in the material. Thermal expansion measurements will also be performed with emphasis on determining hysteresis effects, which can be related to the temperature dependence of the interfaces properties, through cell models. The latter might evolve into a diagnostic for establishing relationships between the interface properties and thermomechanical fatigue.

The processing activities in the program will have newly established goals in 1994. The principal emphasis will be on concepts for affordable manufacturing. The issues selected for investigation will be consistent with manufacturing processes that allow near-net shape consolidation while still yielding reasonable combinations of longitudinal and transverse properties. Performance models developed in the program would be used as an initial test of concept viability.

Beyond these general trends, specific activities are planned for 1994. These are elaborated below. The status of understanding and development in each of these areas is summarized in Table I. Increasing magnitudes between 0 and 1 designate a knowledge range from limited to comprehensive.

TABLE 1A

Status of Design Knowledge for MMCs

	$[0°]_n$ MMC				$[0°/90°]_n$	
	LONG.		TRANS.			
	P	S	P	S	P	S
Tensile Strength	3/4	1	1	1/2	1/4	~0
Creep and Creep Rupture	3/4	0	1	0	0	0
Cyclic Flow (Isothermal, TMF)	1/4	0	1	1/2	0	0
Crack Growth (Isothermal Fatigue)	1	1	0	1/2	0	0
Crack Growth (TMF)	1/2	1/2	0	0	0	0
Compressive Strength	3/4	0	0	0	0	0

TABLE 1B

Status of Design Knowledge for CMCs

	[0/90]		[45/45]	
	P	S	P	S
Stress/Strain	3/4	1/4	1/2	0
Fatigue	3/4	0	0	0
TMF	1/4	0	0	0
Creep and Rupture	1/2	0	0	0
Compression Strength	3/4	1/4	0	0
Transverse Properties	3/4	1/2	—	—
Thermal Properties	1/4	0	—	—

P Primary Structure

S Secondary Structure

2. CONSTITUTIVE LAWS

Two approaches will be used to create a formulation capable of representing the in-plane properties of CMCs. One would be based on Continuum Damage Mechanics (CDM) (Leckie). The other would use concepts analogous to those used in plasticity theory (Hutchinson). The CDM approach uses damage parameters that relate explicitly to micromechanics models. A potential function has already been identified as the state variable which separately represents the strain from the elastic compliance change caused by the matrix cracks and the inelastic strains associated with the debonding and sliding interfaces. Derivatives of the potential with regard to strain and damage give the relationships between variables, such as stress, interface sliding resistance, matrix crack density, etc.

The first version of the CDM model would use the minimum number of damage variables potentially capable of representing the behavior of laminated or woven composites. Cross terms between the damage variables would not be considered at this stage. Moreover, matrix cracks would be introduced normal to the maximum principal tensile stress, consistent with the experimental observations.

The plasticity theory approach would seek a formulation based on matrix cracks occurring normal to the maximum principal tension. It would introduce parameters that reflect the inelastic strain caused by interface sliding upon off-axis loading which would be calibrated from tests performed in tension in 0/90 and 45/45 orientations.

The insight needed to characterize off-axis loading effects will be gained from cell models (Hutchinson) in a manner analogous to that previously used for axial loads. The principal objective will be to understand trends in matrix crack opening and interface debonding/sliding with applied loads. The stress on the fibers will be calculated with the intent of predicting effects of loading orientation on fiber failure. The models will be compared with measurements made in 45/45 tension, using various CMCs (Evans).

Calibration of the damage parameters for each material would be made from hysteresis loop measurements in accordance with procedures developed in 1993. Experimental results obtained in 0/90 tension, 45/45

tension and in-plane shear will be used. In future work, it is hoped that shear tests will not be necessary.

The validation of the constitutive laws will be achieved by comparing calculations with measurements made on sub-elements, especially pin-loaded holes (Evans). The experimental results include residual strains obtained by Moiré interferometry (Fig. 2.1), ultimate loads for either tensile or shear failure and principal strain trajectories delineated by matrix cracking patterns. Acoustic methods will also be developed to probe the local values of the elastic modulus (Clarke, Wadley) which could be compared directly with the CDM predictions.

3. FATIGUE LIFING

3.1 CMCs

A software program for isothermal low cycle fatigue (LCF) of CMCs, developed in 1993 (Fig. 3.1) will be extended in 1994. The present program asserts that fatigue is associated with cyclic degradation of the interface sliding resistance, τ, which can be characterized by analyzing hysteresis loops measured periodically during a fatigue test. With this methodology, S-N curves have been predicted for both unidirectional and woven 0/90 composites tested in cyclic tension as well as changes in compliance and permanent strain. Some additional effort is required to analyze data on 0/90 laminates in order to validate the model predictions. The extensions envisaged for 1994 include thermomechanical fatigue (TMF), strain controlled LCF and off-axis fatigue (Zok, Evans). Experiments are planned which would assess the effects of temperature cycling and of inclined fibers on τ degradation, measured from hysteresis loops. Various cell model calculations (Hutchinson) will be used to interpret the experiments. The results will be used to establish general *rules* for interface degradation in CMCs.

The off-axis experiments will also give insight into the fiber failure criterion that replaces the global load sharing (GLS) results successfully used for 0/90 loadings. This study will coordinate with the cell calculations described above, and the 45/45 tensile experiments.

Notch fatigue studies will be initiated. These will examine cyclic stress redistribution and notch sensitivity (Evans).

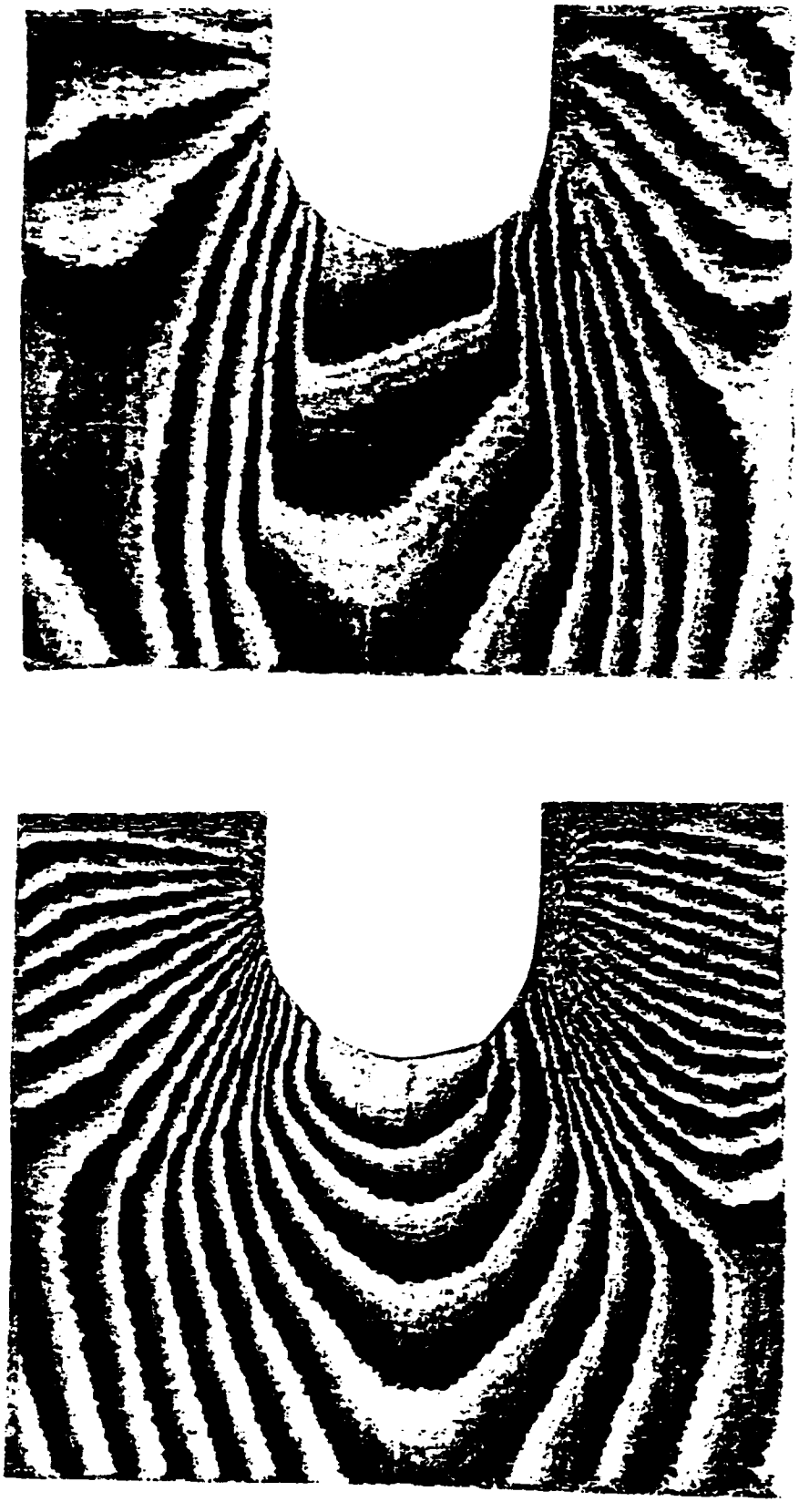

Figure 2.1

Fatigue Methodology

CMC Life Program

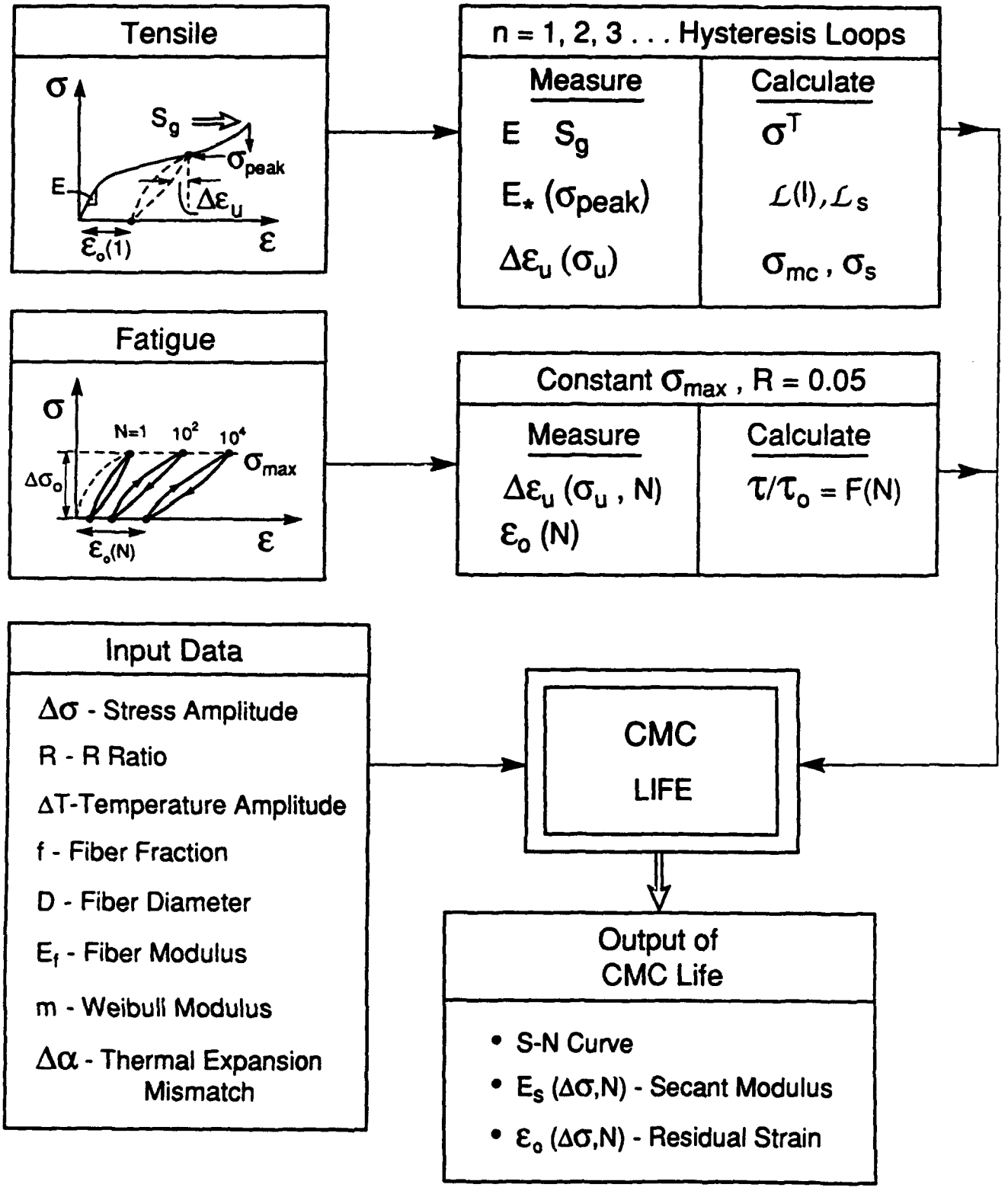

Figure 3.1

3.2 MMCs

Fatigue crack growth and notch strength studies in MMCs will be extended to 0/90 laminates (Zok, Suo). The experiments concerned with crack growth will be interpreted using crack bridging models. The utility of such models has been validated in previous years through studies on unidirectional MMCs. It is envisaged that the fatigue crack growth characteristics of the unidirectional and 0/90 configurations will be related through the volume fraction of fibers aligned with the loading direction. The notch strength behavior will also be interpreted using crack bridging models. Such models have been developed in 1993 and found to be useful in rationalizing the behavior of unidirectional materials (Zok, Suo). In all cases, the mechanical measurements will be augmented by *in-situ* observations to identify changes in damage mechanisms with temperature, fiber architecture, etc. Plans to study the influence of panel thickness on fatigue and fracture resistance are also being developed, as well as tests to understand the potential for crack growth in mixed mode loadings (Hirth, Zok).

Studies of the TMF response of MMCs loaded parallel to the fiber axis will be initiated (Zok, Leckie). Experiments will evaluate both in-phase and out-of-phase loadings. Models of load shedding (matrix-fibers) will be used to interpret the hysteresis loops and to develop fatigue life models applicable to low cycle, high strain TMF.

4. CREEP AND RUPTURE

4.1 MMCs

The considerable progress made in 1993 towards identifying and understanding the mechanisms of creep and rupture in unidirectional MMCs containing non-creeping fibers (McMeeking, Zok) will be used to develop creep rupture software. The longitudinal creep model to be used incorporates stochastic fiber fracture and interface sliding in a format amenable to the prediction of primary and tertiary creep in terms of matrix creep strength, interface sliding resistance, fiber strength, Weibull modulus, etc. The concepts would be visualized in a rupture mechanisms map

(Fig. 4.1). The transverse creep behavior would include interface debonding, which greatly accelerates the creep, leading to marked anisotropy. A constitutive law for creep that includes these effects will be developed (Aravas, McMeeking).

Additional experiments and calculations will be conducted to assess the effects of notches and holes on creep rupture (Zok, Suo). Experience with MMCs at ambient temperature indicates that the notch sensitivity is largely dictated by matrix properties (i.e., strength and ductility). The reduction in matrix properties at elevated temperatures may lead to a substantial elevation in notch sensitivity. However, this behavior may be complicated by the development of alternate damage processes, such as shear bands.

4.2 CMCs

Studies of the creep and rupture of CMCs will continue with emphasis on materials containing creeping fibers. A particular emphasis will be on matrix cracking that arises as fiber creep relaxes fiber bridging tractions (McMeeking, Evans). The experimental studies will be performed on SiC/SiC composites. Hysteresis loop measurements will be used to monitor matrix damage during composite creep, using procedures devised in 1993. Models will be developed based on time dependent fiber bridging concepts (McMeeking, Cox).

It is envisioned that the lifetime of some CMCs will be dictated by time-dependent rupture of the fibers. A lifetime prediction tool for such a composite *must* incorporate the knowledge of fiber strength degradation over time. A new activity will be initiated to address this problem (Suo, Evans). The initial work will involve a survey of data in the existing literature, and a comparison with available models. A new model is being developed for single crystal fibers. This model involves a residual pore inside a fiber which changes shape, under stress, via surface diffusion, to become a crack. These issues will be viewed in the broad context of fiber and composite manufacture.

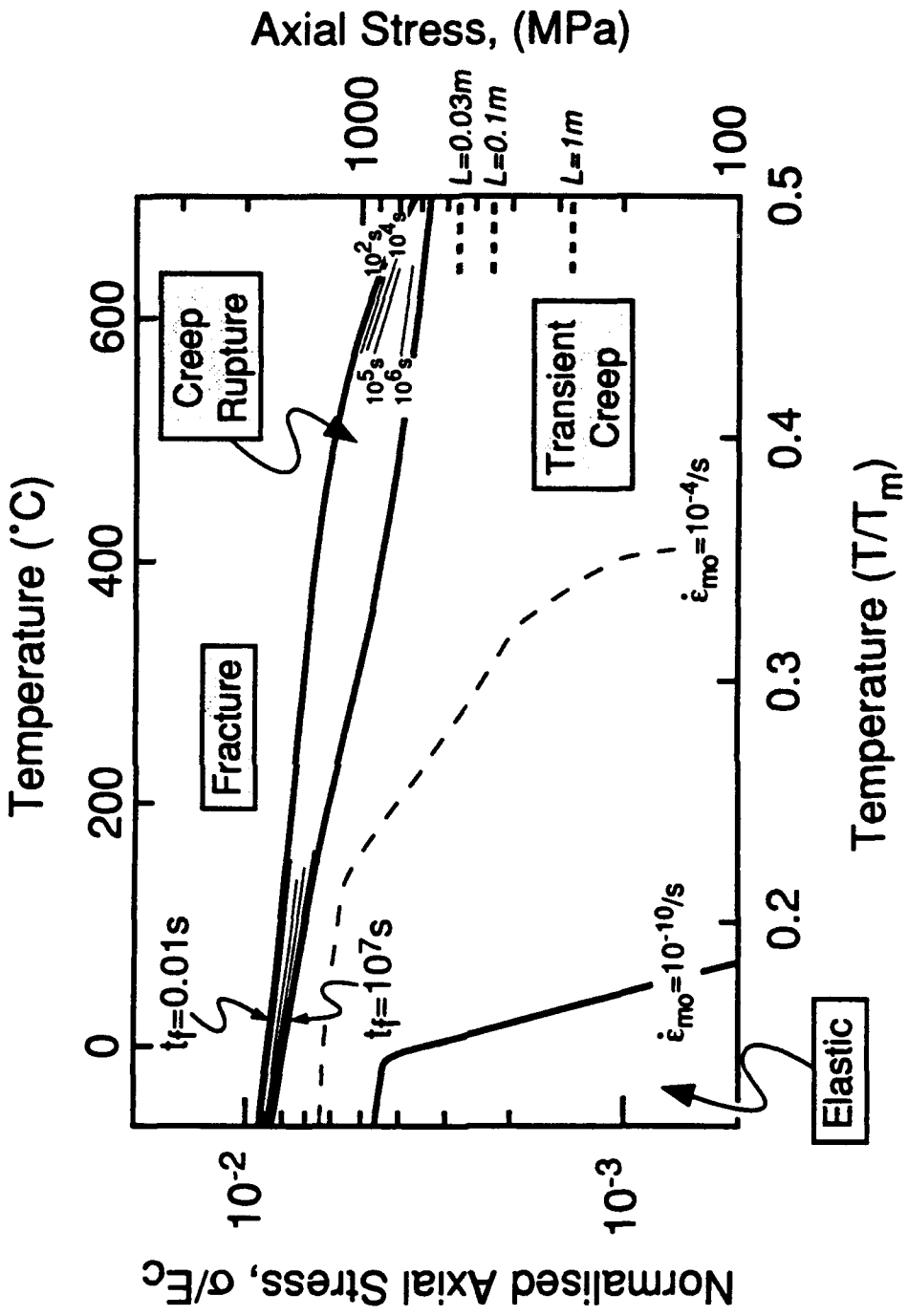
Axial Stress, (MPa)
1000
100
L=0.03m
L=0.1m
L=1m
0.5
0.4
0.3
0.2
Temperature (T/T_m)
600
400
200
0
Temperature (°C)
Creep Rupture
Fracture
Transient Creep
Elastic
10^2s
10^4s
10^5s
10^6s
t_f=0.01s
t_f=10^7s
ε̇_mo=10^-4/s
ε̇_mo=10^-10/s
10^-2
10^-3
Normalised Axial Stress, σ/E_C

Figure 4.1

5. TRANSVERSE PERFORMANCE OF CMCs

Analyses and tests performed in 1993 (Ashby, Hutchinson, Bao) have highlighted the essential issues related to components that experience combinations of transverse tension and interlaminar shear. In both loadings, matrix cracks form at manufacturing flaws at low stresses, of order 10-100 MPa. These cracks extend across the plies and interact minimally with the fibers. Although the crack configurations differ for transverse tension and interlaminar shear loadings, multiple cracks always form. This multiplicity of cracking causes a major reduction in stiffness, which can cause unacceptably large displacements and also redistribute stress into other areas. The formation of the matrix cracks is probabilistic in nature and governed by the size distribution of manufacturing flaws. Design based on the prevention of such transverse cracks must rely on weakest link statistics, usually with a low Weibull modulus. Alternatively, it may be assumed that cracks *inevitably* form and, instead, reliance is placed on *controlling* the diminished modulus of the material, after matrix cracking has occurred. This approach relies on having 3-D architectures, with transverse fibers introduced locally either by stitching or by using angle plies. To explore this possibility, calculations will be performed (Hutchinson, Evans) to examine fiber architectures that lead to minimum stiffness loss, subject to acceptable in-plane properties. Based on these calculations, sub-elements will be designed that test out the concepts.

6. COMPRESSIVE BEHAVIOR

The studies completed in 1993 on the compressive failure of polymer matrix composites by the growth of kink bands (Budiansky, Fleck) will be extended to metal matrix composites, through a coordination with 3M. Compressive failure of Al and Ti MMCs with small diameter fibers has been observed by 3M to occur in accordance with the same kink band mechanism known to operate in PMCs and in C/C composites. The theory should thus extend to the MMCs, with the fiber misalignment, the shear yield strength of the matrix and its work hardening coefficient as the principal variables. A comparison between the theory and experimental

results would provide the basis for specifying the compressive properties of MMCs.

Compression failure of CMCs occurs by different mechanisms (Ashby). The dominant failure modes are similar to those that operate in porous brittle solids such as monolithic ceramics, concrete and rocks. The theory is well established and validated for these materials. Applications of the theory to various CMCs will be made and applied to the understanding of a behavior of pin-loaded holes (Evans, Ashby).

7. THERMAL PROPERTIES

A new focus on the thermal properties of CMCs and MMCs will be initiated in 1994. Calculations of the effects of matrix cracks in the thermal expansion of CMCs will be made (Hutchinson). These will be compared with data obtained from TMF testing (Zok). The effects of such cracks on the in-plane thermal conductivity will also be calculated (Hutchinson). Measurements will be performed using the laser flash method (Ashby).

Thermal conductivity measurements will be initiated on Ti MMCs (Ashby). These will be used to understand the effects of the fiber/matrix interphases and of matrix damage on the transverse and in-plane thermal conduction.

8. MATERIALS SELECTION

The Cambridge Materials Selector software will be expanded in 1994 to include high temperature creep design with the corresponding data base (Ashby). This expanded version will permit estimates to be made of temperature limits for MMCs based on creep controlled TMF and on the transverse creep of components with unidirectional reinforcements.

9. DESIGN CALCULATIONS AND SUB-ELEMENT TESTS

A larger fraction of the effort in 1994 will be on design and sub-element testing, particularly for MMCs. Discussions are now in progress with Pratt and Whitney, Textron and 3M to perform design calculations using the

constitutive equations developed at UCSB and to produce sub-elements for testing.

The design emphasis for MMCs will be on various diffusion bonded joints with Ti matrices and monolithic Ti attachments. Two specific subelements are envisaged. The first involves unidirectionally reinforced rods (or plates), clad with monolithic metal. The purpose of the cladding is to prevent exposure of the fibers to the environment and to mechanical abrasion. The design of clad MMC structures requires consideration of (i) the residual stresses resulting from thermal mismatch between the cladding and the composites section, (ii) the potential for fatigue cracks to initiate and grow through the monolithic material, and (iii) the interaction of such cracks with the composite section and their influence on the strength and life of the structure. The design and testing of such subelements (Zok, Leckie) will be augmented by calculations of crack growth and fracture, incorporating the effects of thermal and elastic mismatch between the cladding and the composite (McMeeking). The clad structures will also be used to initiate studies on the reinforcement of holes in composite sections with monolithic metal patches, as drawn in Fig. 9.1 (Zok, Suo). The second subelement involves the attachment of a MMC actuator rod to a pin-loaded monolithic section (Fig. 9.2). The critical design issues relate to the strength and fatigue resistance of the interfaces between the composite and monolithic matrices. Design studies shall also be completed on rotor rings with special efforts made to produce rule-based design procedures which would be used by industry at the conceptual level of design to determine sizes and the efficient disposition of material.

For CMCs, the sub-element studies would be based on the calculations described above in Section 5. These would include C sections and T junctions (Fig. 9.3) Negotiations for manufacturing these sub-elements will be initiated and tests performed at UCSB.

10. AFFORDABLE MANUFACTURING

As our understanding of composite mechanics and its interplay with design and performance has evolved, it has become increasingly evident that *cost* and *reproducibility*, are major constraints. Even as processing

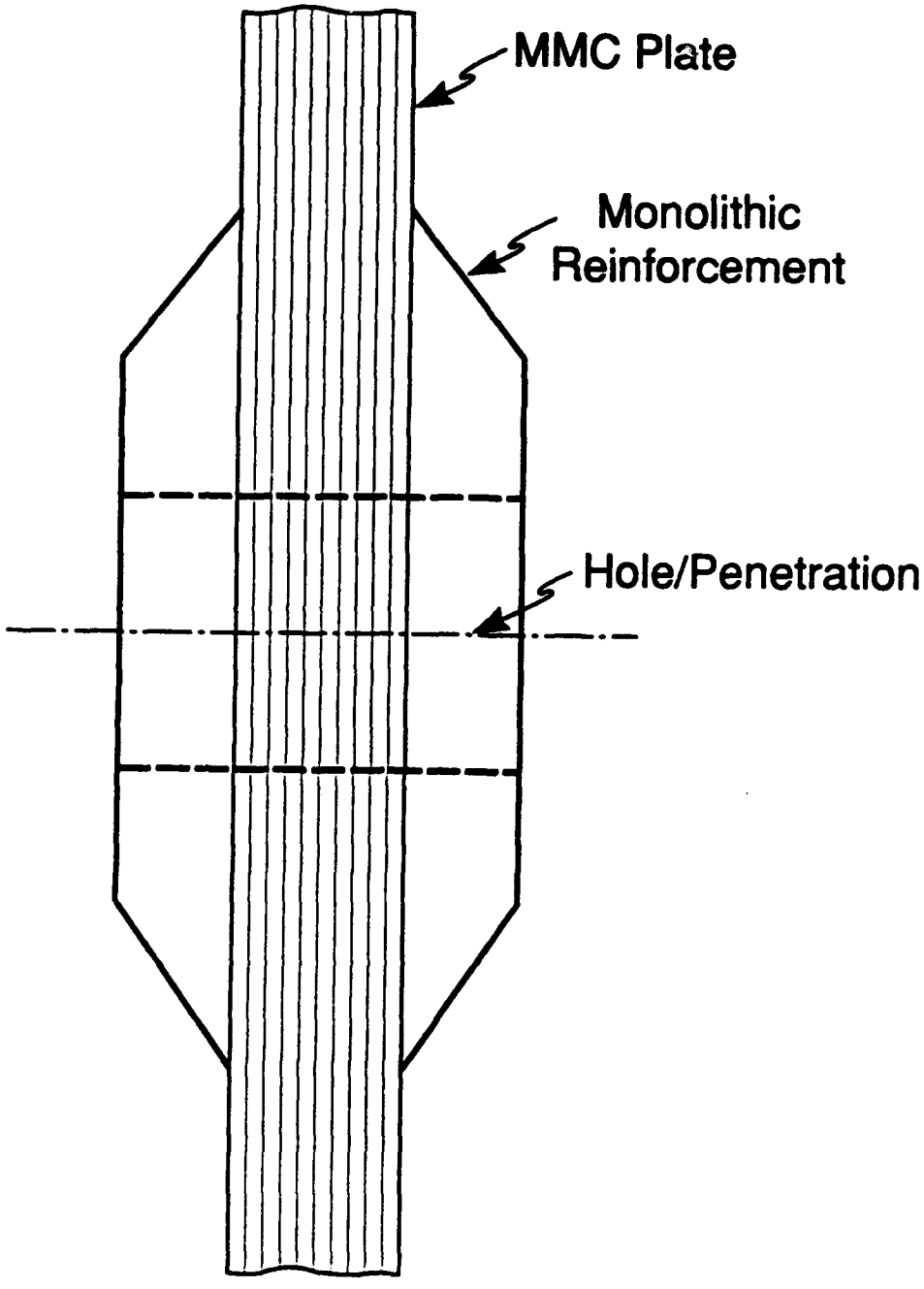

Figure 9.1

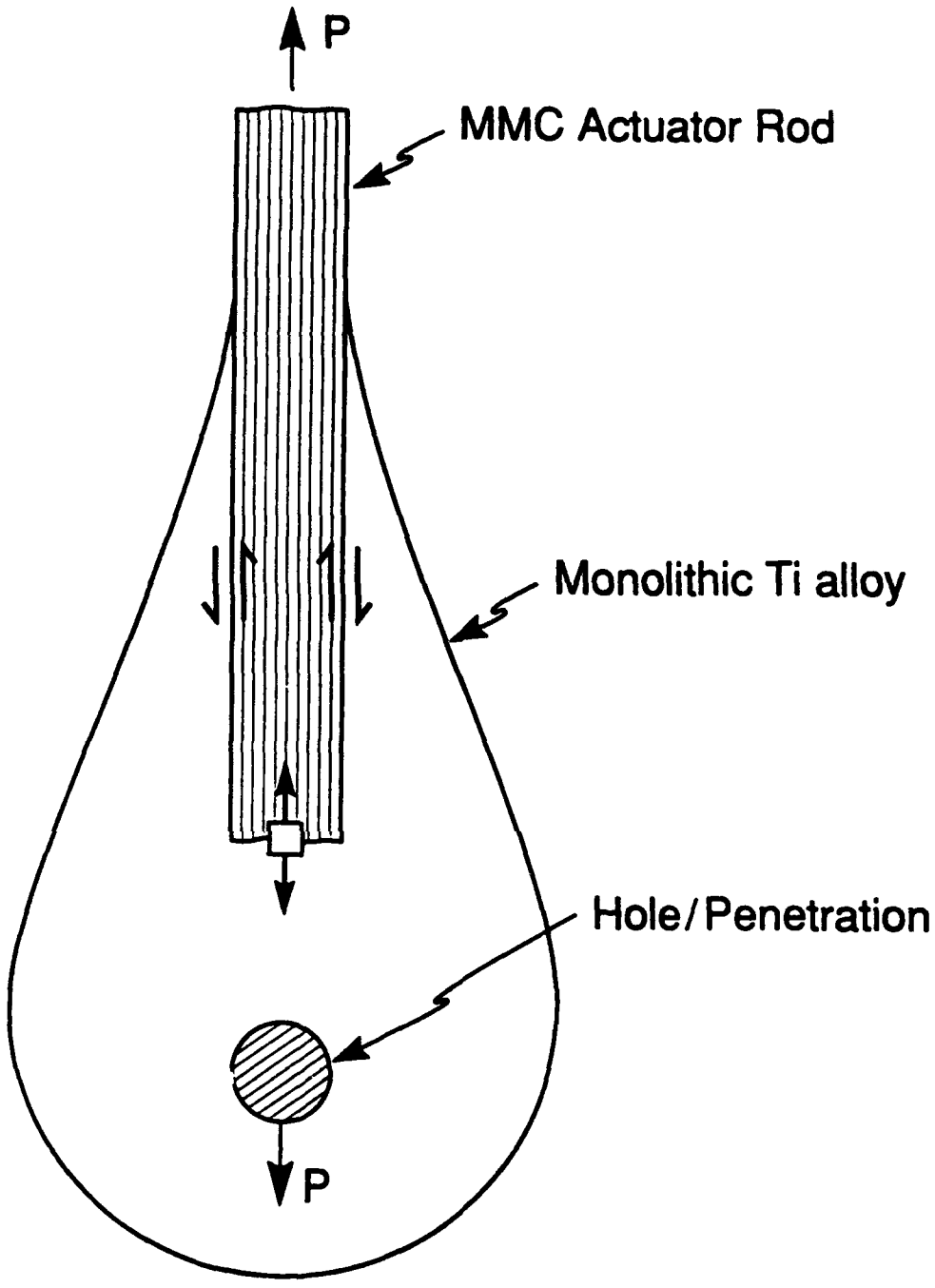

Figure 9.2

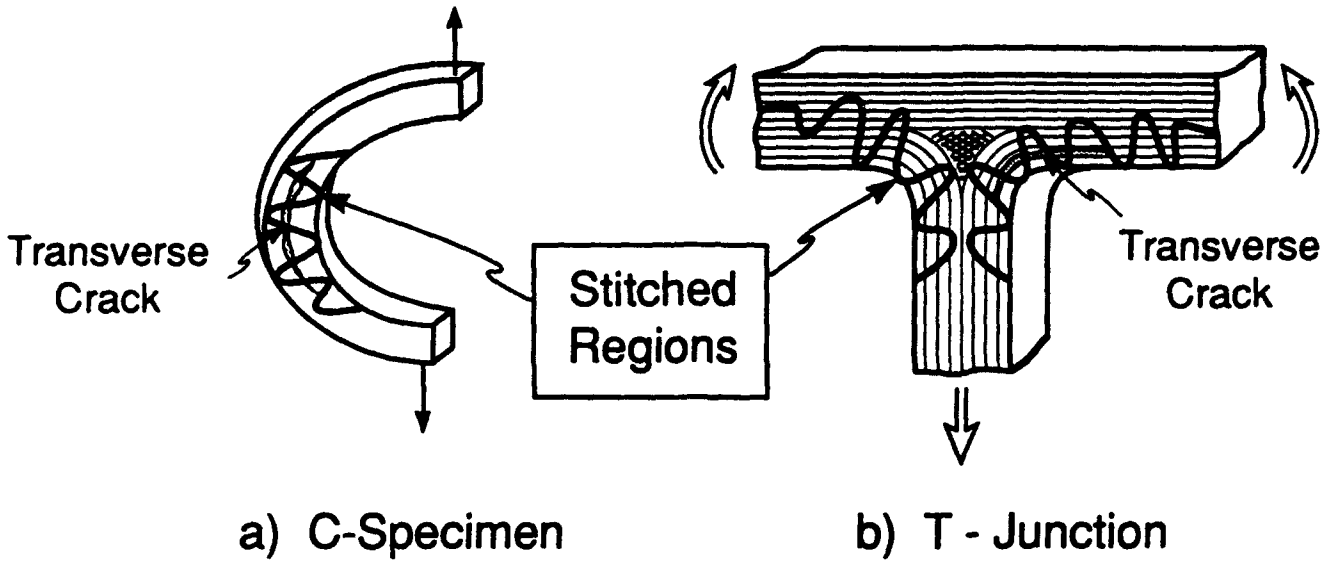
Transverse
Crack
Stitched
Regions
Transverse
Crack
a) C-Specimen
b) T - Junction

Figure 9.3

developments make the prospect of affordable high temperature fibers more realistic, evolving knowledge on the mechanical and thermochemical functions of interfaces have led to design concepts involving carefully tailored interphase layers, with unfavorable impact on cost. Moreover, if affordable coated fibers were available today, fabrication costs associated with consolidation and pressure densification would often remain prohibitive. Future processing and manufacturing activities are predicated on these issues, especially the need for new ideas, and the related knowledge base.

10.1 MMCs

Melt processing methods provide the more affordable options in composite synthesis with the added benefit of near-net shape capability. For continuous fiber composites melt infiltration also enables full density while minimizing the consolidation stresses that typically cause premature reinforcement failure in solid state processes. However, melt processing requires a high degree of thermochemical compatibility between matrix and reinforcement since deleterious diffusional interactions would be accelerated by the liquid phase. Conventional melt processing also exhibits limited ability to control the volume fraction and spatial uniformity of the reinforcements.

Among metal matrices, Ti alloys epitomize unsuitability for direct melt infiltration owing to aggressive reactivity. Fiber clustering is also a concern, even in solid state processes based on powder or foil matrices. Composite consolidation by vapor deposition (PVD) of the matrix on the fibers provides an avenue for improving *homogeneity of fiber spacing*. However, present schemes require expensive pressure densification with its many problems. A potential solution involves a hybrid manufacturing route wherein part of the matrix is first applied to the fibers by PVD. The pre-metallized fibers are then assembled into a preform having the desired shape and then infiltrated with the remaining matrix in liquid form.

Direct infiltration with Ti alloys could be feasible owing to the protection of the fiber by the PVD layer, but the high temperatures involved would exacerbate the diffusional interactions at the fiber-matrix interface. An alternate approach involves depositing the more refractory constituents of

the matrix (e.g., Ti, Nb, Mo, etc.) by PVD and then infiltrating with the lower melting point constituents (e.g. Al). Based on stoichiometric considerations, the latter approach would be suitable for matrices with $\gtrsim$ 25 at.% Al, notably the orthorhombic and α_2 alloys. The obvious problem with this approach is the homogenization of the matrix after consolidation, which may require lengthy high temperature treatments in the solid state. However, a significant part of the matrix synthesis reaction could be effected in the presence of molten Al, followed by a final heat treatment in the solid state. While this lower temperature infiltration approach is evidently desirable from a manufacturing viewpoint, it is not clear that matrix homogenization can be achieved.

A program involving modeling and experimental work will be initiated in 1994 to generate the knowledge base appropriate to hybrid approaches for Ti matrix composites (Levi, Evans). Cell models (single fiber environment) would be developed to study diffusional interactions and remelting/solidification phenomena as a function of processing cycle (temperature-time history). Experiments would be performed to elucidate the relevant aspects of microstructural evolution and provide the reaction and interdiffusion kinetics needed to calibrate the models. Initial experiments would be performed by infiltrating pure Ti-wire preforms with molten Al and subjecting the "composite" to different treatments in the semi-solid state. Subsequent experiments would focus on developing a metallization route for Ti-Nb alloys on SiC fibers and on the relevant interactions with infiltrated Al. Larger scale modeling issues would be tackled in 1995 if the proposed approach appears promising.

Ongoing activities on the understanding of microstructure evolution and its relationship to properties in *in-situ* TMC systems based on TiB reinforcements would be continued (Levi). These are by nature affordable composites which exhibit inherent thermochemical stability and may be cast into shapes using conventional Ti processing techniques. A potential application of these materials would be in joints with unidirectionally reinforced composites, wherein their higher modulus and creep resistance combined with acceptable toughness and isotropic properties could be advantageous. It is also anticipated that these materials could be used for cladding in PVD or plasma-sprayed form, thereby reducing the potential for fatigue crack initiation in the cladding. Since TiB is thermochemically stable

with practically all Ti matrices of interest in fiber composites, such strengthening concepts may be readily implemented.

10.2 CMCs

Measurements and observations in 1993 have shown that strong, high strain to failure CMCs can be fabricated using an inexpensive method that involves a) packing a powder around fibers within a fiber preform using pressure filtration and b) making the powder matrix strong by heat treatment followed by infiltration with a liquid precursor that decomposes to an inorganic material. A composite made this way, with polycrystalline alumina fibers in a silicon nitride matrix, demonstrated that the *matrix* deflects the crack. This observation is significant since it suggest that a class of CMCs can be processed without needing weak fiber/matrix interfaces. The potential of this observation will be explored (Lange, Evans), by processing a composite with strong, polycrystalline alumina fibers in a mullite matrix because the thermomechanical properties of mullite minimize thermal stresses and resist creep. In addition, the thermal expansion mismatch is relatively small. Mixed Al, Si metal alkoxide precursors which can be gelled *in-situ*, prior to decomposition, will be used to strengthen the matrix.

Manufacturing studies would initiate with understanding the precursor infiltration into mullite power compacts. The densification of the matrix would be determined as a function of the cyclic infiltration. Microstructure changes would be controlled to avoid flaw populations during densification. The fracture toughness and the strength of the matrix would be determined as a function of the number of precursor infiltration cycles. Composite processing would initiate with precursor infiltration into alumina fiber preforms by pressure filtration, with emphasis on the colloidal aspects of this processing step. The goal would be to determine the processing conditions needed to produce a matrix that optimizes the ability to deflect cracks without degrading fiber strength. To optimize composite processing, panels for testing under conditions of both strain and stress control would be manufactured.

11. STRESS AND DAMAGE SENSORS

The extensive exploitation of the optical fluorescence method of measuring stresses in sapphire fiber and alumina-containing ceramic composites begun in 1993 will be continued in 1994 (Clarke, Wadley). The emphasis is on using the method to understand basic, unresolved issues in stress redistribution in composites by the direct measurement, with high spatial resolution, of the stresses themselves. Particular attention will be paid to determining the stress distribution associated with interfacial sliding. One of the problems to be addressed relates to new concepts for oxidation resistant interfaces within MMCs and CMCs, particularly the concomitant roles of fiber roughness and sintering on interface sliding and debonding, after exposure to high temperatures and cyclic loadings. For this purpose, fibers with fugitive, low modulus coatings will be explored and fluorescence measurements used to understand stress evolution and its connection with fiber durability within the composite. A second problem relates to the distinction between the line spring and large scale sliding models for fiber bridging (Budiansky, Hutchinson), so as to determine the range of applicability of the two models. The two competing models predict different distributions of stresses in the fibers within the bridging zone and hence are amenable to validation on the basis of the measured stress distribution.

Two approaches to measuring local damage are under development and will be the focus of the sensor activities. One is the use of acoustic methods (Wadley) to probe local variations in the elastic modulus of CMCs as a function of load. This should provide a means of mapping the distribution of damage which can be compared directly with the predictions of continuum damage mechanics models. The second approach (Clarke) is to detect the third harmonic signal generated by the presence of local damage. Preliminary experimental results obtained in 1993 concerned with the detection of crack-like voids in thin metal lines, together with computer simulation studies, have demonstrated the viability of the technique. This work will be extended in order to detect damage accumulation in CMCs and MMCs.

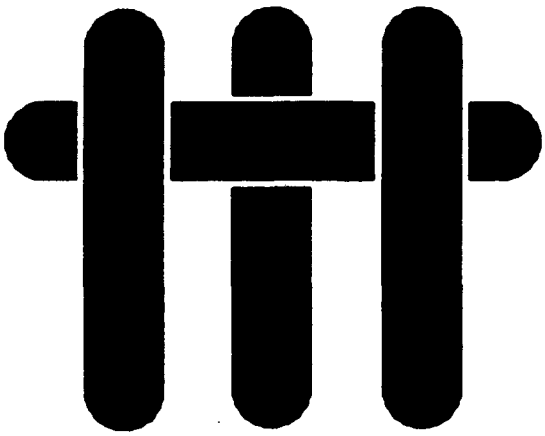

MECHANICS OF THE PUSH-OUT PROCESS FROM *IN SITU* MEASUREMENT OF THE STRESS DISTRIBUTION ALONG EMBEDDED SAPPHIRE FIBERS

Qing Ma*, Lei Carol Liang**, David R. Clarke* and John W. Hutchinson**

*Materials Department, University of California, Santa Barbara, California 93106
**Division of Applied Sciences, Harvard University, Cambridge, MA 02138

ABSTRACT

The basic mechanics of the fiber push-out process are studied by measuring the stress distributions along *c*-axis sapphire fibers in γ–TiAl matrices. The stress measurements were made *in situ* during fiber push-out tests using a piezo-spectroscopy method. By focussing an optical microprobe into a sapphire fiber, the frequency shift distribution of the characteristics R lines of Cr^{3+}, and hence the stress distribution along the fiber were determined at each increment of applied load. By comparing the measured stress distributions with ones calculated using finite element method, key mechanical parameters including residual stress before composite slicing, debond length at each load, debond energy and the frictional stress along the interface in both debonding and sliding phases were determined. Two coating systems (Mo/Al_2O_3 and CVD-C/Al_2O_3) were studied. The results also show that while the debond energies differ by an order of magnitude, the frictional stresses are very similar in magnitude, suggesting that the interface morphology is of greater importance than the nature of the coating.

1 Introduction

The fiber push-out test [1,2] has become an invaluable method of evaluating the mechanical response of fibers in a matrix. Its attraction stems from both its relative simplicity as a test method and from the fact that actual embedded fibers in a composite can be probed. One draw back however is that very little data about each fiber is actually obtained from the test. Normally the push-out load is recorded as a function of fiber displacement. From this only the average effective frictional stress along the debonded interface can be obtained with reasonable accuracy during the fiber sliding process (the sliding phase) after the whole interface debonds, and when large displacement occurs. Attempts to deduce information about the interface debonding process (the debonding phase), prior to the sliding phase, from the load-displacement curve have been made. For example, the load drop at the transition between the debonding phase and the sliding phase has been used to estimate the interface debond energy Γ. Unfortunately, any connection between the load drop and Γ is obscured by two problems. First, the steady state debonding process necessarily assumed in deriving any relationship between load drop and Γ has not been confirmed rigorously by experiments. In fact, recent calculations [3] indicate that the debonding can be unstable, at least under certain conditions. Secondly, it has been demonstrated that due to the asperity roughness of the interface, there is an "unseating" effect at the transition, which may increase the apparent load drop [4]. Any such surface morphology also affects the interpretation of the frictional resistance, τ, obtained during the sliding phase, where large sliding distances averaging the asperity effect along the fiber occurs. The measured frictional resistance may therefore not be relevant for the debonding and sliding process experienced in brittle matrix composites where only a small amount of sliding may occur before the fiber fractures.

In this contribution, we show that considerably more data is obtainable from the push-out test when the stress distribution along the fibers *during* the push-out process is determined. Such stress distribution measurements were made using techniques similar to that used in an earlier work [5], where residual stresses in embedded fibers were measured. This measurement technique is based on the piezo-spectroscopic properties of Cr^{+3} ions in sapphire, in which the characteristic fluorescence R lines shift linearly with hydrostatic stress components. For the axisymmetric problems of a *c*-axis fiber embedded perpendicular to the composite surface, the shift $\Delta\nu$ depend on the radial stress σ_r and axial stress σ_z according to the following relationship:

$$\Delta\nu = 2\Pi_a\sigma_r + \Pi_c\sigma_z \tag{1}$$

where Π_a and Π_c are the piezo-spectroscopic coefficients for the *a* and *c* directions. They have been measured to have value of 2.70 and 2.15 $cm^{-1}GPa^{-1}$, respectively [6]. A positive shift implies tension and a negative shift implies compression. The frequency measurements were implemented using an optical microscope having a small depth of field to both excite and collect the fluorescence signals around its focal point. The depth profile of the frequency shift is measured as a function of depth z through an exposed fiber end as the point of focus was moved successively deeper. The detailed methodology will be described in section 2.

In our experiments, a load is applied at one end of the fiber, and is increased in several discrete steps until total interface debond occurs. At each load, the fluorescence shift distribution along the entire sapphire fiber is measured through the other end of the fiber. Several fibers with two different coatings (molybdenum and CVD-graphite) were measured whilst under load in the pushed-out test. In preliminary experiments, it was observed that the fibers with the same coating behave in a similar manner. In section 3, the measured

shift distributions in both debonding phase and sliding phase will be presented for two fibers with the two different coatings.

In section 4, finite element calculations are used to generate stress distribution functions along a fiber with a number of different debond lengths. These stress functions are linear summations of independent components resulting from the external load, residual stress and interfacial frictions. Fitting these functions to the measured frequency shift distributions in the debonding phase provides details of the axial and radial stress distributions at different stages of the push-out tests, along with the debond lengths, the debond energies and the friction in the debonding phase. The friction in the sliding phase is obtained by using a shear lag model combined with the Lamé solutions for a concentric fiber and matrix.

2 Experimental Method

2.1 The Through-Focus Depth Profiling Method

As illustrated in figure 1, the fluorescence from depth z below the top surface is measured by focussing a laser beam through the fiber top surface using a microscope objective lens. By focussing to successively greater depths and measuring the frequency shift, a profile along the length of the fiber is obtained. Because of the small depth of field of the lens, the fluorescence excited will be collected from only a small volume on either side of the focal plane. The measured frequency shift $\overline{\Delta\nu(z)}$ is hence a weighted average of that within the effective excitation volume. Therefore, the actual depth profile of the frequency shift has to be deconvoluted from that measured by using the depth of field function of the microscope. As described in reference [5], the depth of field function near the top surface can be measured by systematically moving the plane of focus from a position above the top

surface to a position below the surface while recording the fluorescence intensity $I(z)$. The depth of field function near the top surface is then:

$$g(z,0) = \frac{dI(z)}{dz} \tag{2}$$

Here the second variable in g equals zero indicating that the depth of field function is measured at the top surface. As the distance below the top surface increases, the depth resolution deteriorates, primarily as a result of the decrease of the effective numerical aperture resulted from the ray blocking by the matrix on the sides of the fiber. It is necessary, therefore, to obtain the depth of field function as a function of depth in order to correctly deconvolute the measured shifts at depths larger than several fiber diameters. For this purpose, the depth of field functions near the bottom surface of samples of different thicknesses were measured using the same method as described above. The depth of field function at an arbitrary depth can then be obtained by interpolation. For illustration, the depth of field function at the top surface and at 600μm depth are plotted in figure 2 for our optical microscope using a 40/.55 water immersion lens and a 50μm collection aperture. Due to limited number of sample thickness used, some error is expected in the resulting depth of field function. However, it was confirmed that for any practical purposes, any reasonable error involved in the depth of field function can only affect the deconvoluted curves within one fiber radius from the fiber bottom end, because the measured frequency shift distributions are smooth functions of depth z.

Having established the depth of field function, the measured shifts can then be related to

the true shift profile $\Delta\nu(z)$ by:

$$\overline{\Delta\nu(z)} = \frac{\int_{-z}^{t-z} \Delta\nu(z+u)g(u,z)du}{\int_{-z}^{t-z} g(u,z)du} \tag{3}$$

In order to evaluate the deconvolution it was assumed that the true shift $\Delta\nu(z)$ is a polynomial function of z but with unknown coefficients. By fitting the polynomial function convoluted with the depth of field function using equation 3 to the measured distribution, the values of the coefficients were obtained. The initially assumed function, with the coefficients obtained by fitting, is then regarded as the deconvoluted shift $\Delta\nu(z)$. The accuracy of this method has been previously demonstrated [5] and can be judged later in this paper by viewing figure 12, where the dashed curves are the true shift $\Delta\nu$ (the solid curves) convoluted by the depth of field function. They have excellent fit with the measured data.

2.2 Push-Out Method

In order to simultaneously measure both the load and the frequency shifts *in situ* during push-out tests, a special mechanical loading fixture was made to fit under the optical microscope of the microprobe. The fixture is illustrated in figure 3. A fiber selected for the push-out experiment was aligned with the conical opening on the top plate. The cone shape facilitates a large collection angle. The load is applied to the bottom end of the sapphire fiber by using a short push rod made of a Nicalon SiC fiber. The load is applied using a micrometer, through a lever and is measured by a load cell in series. This lever arrangement is simply for the purpose of reducing the vertical dimension of the fixture, so that it could fit under our optical microscope for the fluorescence measurements. During the push-out experiments, the load was increased incrementally. At each load step, the frequency shift profile was measured along the entire fiber by the through-focus technique described in the

previous section. When the load was increased to a certain critical value, the whole fiber-matrix interface debonded and the fiber slid. The pushed-out distance was typically of order of 10μm. The fiber was then pushed further using the micrometer so it slid for another 10μm or so to reach a stable sliding mode. The frequency shift profile is measured again with the load applied. This profile gives information about the frictional resistance in the sliding phase.

2.3 Specimen Preparation and Fiber Selection

Thin slices ($\sim$ 0.5 mm) of the composites, cut perpendicular to the sapphire fibers, were polished so as to obtain an optical finish at both fiber ends. The polishing facilitates the observation and the optical measurements, as well as insuring the mechanical integrity of the fiber. Because of the large statistical variations often observed in conventional push-out tests, procedures were established to select fibers for the detailed push-out studies in this work. First, visual inspections using optical microscopy were used to select fibers that were actually perpendicular to the surfaces of the composite slice. This was assessed by using the transmitted light of the microscope and comparing the relative lateral displacement between the two fiber ends. From these fibers, ones having both a circular cross section with diameters $\sim 120-130\mu$m, and a uniform coating were selected for the actual measurements. The depth profiling method described above was then used to measure the distribution of shifts due to residual stresses. A large fraction of the fibers measured showed irregular shift distributions, indicating inhomogeneities in the coating layers. Fibers with smooth symmetric profiles (see figure 4 and 6) were finally selected for push-out studies.

3 Frequency Shift Distributions

Sapphire fiber (*c*-axis) reinforced γ-TiAl matrix composites with two different interfaces were fabricated by HIPPING at UCSB for this work. One had a double coating of Mo/Al_2O_3 and the other CVD-C/Al_2O_3. The material processing methods were described elsewhere [4]. In the following, the measured shift profiles in both the debonding phase and the sliding phase are presented.

Plotted in figure 4 are the measured frequency shifts $\Delta\nu$ as a function of depth z for a fiber with Mo/Al_2O_3 coatings in the debonding phase. The top surface is at $z = 0$ and the bottom surface, where the pushing load is applied, is at $z = 516mum$. Six frequency shift depth profiles were obtained at successively higher applied load. The top curve was measured without any load, thus corresponding to the residual stress state in the fiber. The negative shift in the interior is consistent with there being a compressive residual stress in both the axial and radial directions developed due to thermal mismatch between the sapphire fiber and the γ-TiAl matrix (Table I). The magnitude of the shift decreases near the top and bottom surfaces because of stress release occurring due to sample preparation. The noticeable asymmetry of the curve about the sample mid-plane is partially due to the decreasing depth resolution with increase of depth as mentioned in the last section and can be effectively corrected by deconvolution. When an increasing load, P, is applied, the magnitude of the negative shift correspondingly increases in the lower part of the fiber, but remains essentially constant near the top end.

When the load was increased above $P = 4.01$ GPa, the whole interface debonded, and the fiber suddenly slid out by a distance of about 10μm. To reach a stable sliding mode, the fiber was pushed further so as to slide another few microns. The frequency shift profile was

then measured again with the fiber under load. This profile is plotted in figure 5 along with two other profiles, one obtained after release the load and the other after the fiber had been pushed back into its initial seated position. The flat profile for the seated case indicates that the axial stress is mostly released by a slight displacement.

The behavior of the CVD-C/Al_2O_3 coated fibers is very similar to that of the Mo/Al_2O_3 coated fiber as shown in figure 6. However, the maximum load needed to push-out the fiber was only slightly above 2 GPa, considerably smaller than that for the Mo/Al_2O_3 coated fiber. This indicates that the CVD-C/Al_2O_3 coating has lower debond energy or has lower friction in the debonding phase. The shift profile in the sliding phase was also measured for the CVD-C/Al_2O_3 coating and is analyzed in the next section.

4 Data Analysis

To obtain the maximum information, such as the debond energy and interfacial friction as well as the interfacial debond length from the measured shift profiles, it is necessary to use elasticity models relating the stress distribution in the fiber to these interfacial parameters.

4.1 The Debonding Phase

The stress distributions in the fiber debonding phase, with the complexity introduced by the debond interface crack, cannot be accurately obtained by analytical means. We therefore employed FEM to calculate the stress distributions. The model used in the calculation is illustrated in figure 7. The details involved in the modeling were described in an earlier work [3]. Briefly, the axial stress σ_z and the radial stress σ_r along the core of the fiber are

calculated as superpositions of several independent terms:

$$\sigma_z = P\, f^{(1)}(\frac{z}{R_f}, \frac{l}{R_f}) + P_R\, f^{(2)}(\frac{z}{R_f}, \frac{l}{R_f}) + \tau_0\, f^{(3)}(\frac{z}{R_f}, \frac{l}{R_f}) \tag{4}$$

$$\sigma_r = -N_R + P\, g^{(1)}(\frac{z}{R_f}, \frac{l}{R_f}) + P_R\, g^{(2)}(\frac{z}{R_f}, \frac{l}{R_f}) + \tau_0\, g^{(3)}(\frac{z}{R_f}, \frac{l}{R_f}) \tag{5}$$

where P is the applied load, P_R and N_R are the axial and radial residual stresses in the fiber before the composite is sliced, τ_0 is the assumed constant friction in the debonded interface region, l is the length of the interface crack, and R_f is the fiber radius. To compare with our experiments, the stress functions f and g were calculated for a number of different debond lengths, l, and for the aspect ratios t/R_f corresponding to the samples used. The model used in this calculation was modified from the previous one [3] in order to incorporate the relatively thick ($\sim 10\mu$m) Al_2O_3 coating on the fiber. Actual mechanical properties of the fiber, matrix and coating (listed in Table I) were used in the finite element calculations.

In the analysis following, we first compare the measured shift profile for the residual stress with that computed so as to obtain the residual stresses P_R and N_R in the fiber before slicing. In doing so, we first assume the whole interface is completely bonded. Figure 8a shows the comparison between the measured shift profile (after deconvolution) and that calculated (the dashed line). The slower variations at the two ends in the measured profile suggest that in reality the interface is debonded to some extent at the two ends as a result of the sample slicing. FEM calculations of the interface shear stress, assuming no debonding, gives values near the two ends considerably higher than the interface shear strength for weak interface systems [5]. However, as illustrated in figure 8b, by allowing the interface to debond about $1.5R_f$ from the two surfaces, the fitting between the computation and the data becomes excellent. This fitting also provides values for the axial and radial residual stress in an

infinite body, P_R and N_R, respectively (figure 8b). The ratio P_R/N_R compares favorably to the analytical result for a fiber embedded in an infinite body. Also, to obtain a good correspondence, an appropriate friction stress has to be applied along the debonded section of the interface. The negative sign indicates that the friction is preventing the fiber from moving outwards as expected. From the above fitting the detailed axial and radial residual stress distributions in the fiber in the slice are obtained as shown in figure 9.

Having obtained the residual stresses P_R and N_R, comparisons are made for the other profiles obtained at various loadings as illustrated in figure 10. The fitting is obtained by varying both the debond length and the interfacial friction in equation 4 and 5 until the best fit to the frequency shift profile is achieved. Since in the finite element calculations, the debond was only allowed to propagate up from point of loading, i.e., in the bottom part of the fiber, the lack of fitting near the top end is of little significance. Also, because the experimental data has large error within a distance R_f from the bottom surface due to optical effects, fitting in that region is only lightly weighted.

For a load $P = 0.76$ GPa, the applied stress is still less than the axial residual stress P_R, so the monotonic loading condition assumed in the calculation is not strictly valid. As a result, the parameters from the fitting are considered less reliable. When $P = 1.45$ GPa, which exceeds P_R, it is expected that the direction of friction in the interface has been fully reversed. However, because the load is mostly balanced by P_R, relatively small amount of friction is required to establish the equilibrium. Further, the effective load exerted on the debond crack tip is also small, so that the debond length remains unchanged from the residual stress case. When the applied load is further increased, the effective load on the debond front also increases, which induces debond crack growth as the fitting demonstrates. The friction also increases with load for reasons which will be discussed later in section 5.

The parameters obtained by matching the finite element calculation to the measured frequency shift are listed in Table II for the Mo/Al_2O_3 coating. The shift profiles measured for the $CVD\text{-}C/Al_2O_3$ coated fiber were analyzed similarly. The comparison between measured and calculated profiles are plotted in figure 11 and fitted parameters are listed in Table III.

The debond energy can also be obtained from the data. Recognizing that the effective load applied on the debond crack, P_{eff}, is the externally applied load P balanced by the residual axial stress P_R and the frictional stress τ_0 applied through the interface shear lag:

$$P_{eff} = P - P_R - \frac{2l}{R_f}\tau_0 \tag{6}$$

Dimensional analysis indicates that the elastic energy involved can be expressed in terms of the effective applied load and the debond length, l, as

$$U = \beta \frac{P_{eff}^2}{2E} \pi R_f^2 l \tag{7}$$

The strain energy release rate, G, is therefore

$$G = \frac{\partial U}{\partial A} = \frac{\partial U}{\partial (2\pi R_f l)} = \beta \frac{R_f}{4E_f} P_{eff}^2 \tag{8}$$

The debond energy, Γ, can then be obtained by equating to the strain energy release rate, namely,

$$\Gamma = G = \frac{\beta R_f}{4E_f}(P - P_R - \frac{2l}{R_f}\tau_0)^2 \tag{9}$$

Using Lamé solution [3,7], it can be shown that β is a function of the elastic properties of the fiber and the matrix and is always very close to unity. Using the average values for the effective load P_{eff}, from the data in Tables II and III, values for the debond energy for the

two coating systems are obtained:

$$\Gamma_{Mo} = 0.57 \text{ J/m}^2$$

$$\Gamma_C = 0.03 \text{ J/m}^2$$

Note that data obtained at relative small loads were not used for the energy calculations, because they do not correspond to the critical loading conditions.

4.2 The Sliding Phase

The frequency shift profiles in the sliding phase for the molybdenum and graphite coated fibers are plotted in figure 12. The solid dots are the measured shifts at the depths indicated, and the solid curve is the deconvoluted shift profile, obtained using the depth of field function, representing the true frequency shift profile. For comparison, the dashed curve is the true shift convoluted with the depth of field function, which fits the measured data, demonstrating the accuracy of the deconvolution procedure. For both fibers, the profiles are essentially linear in the center section, and show rather complicated end effects within the distance about one fiber diameter from the two surfaces. To avoid the end effects, only the center section of the curves is used to determine the value of the friction during sliding. This can be easily accomplished using the standard shear lag relationship:

$$\frac{d\sigma_z}{dz} = -\frac{2}{R_f}\tau \tag{10}$$

together with the Lamé solution [3]:

$$\sigma_r + N_R = B\,(\sigma_z + P_R) \tag{11}$$

where B describes the effective Poisson's effect,

$$B = \frac{\nu_f E}{(1-\nu_f)E + (1+\nu)E_f} \tag{12}$$

and E and ν are the Young's modulus and Poisson's ratio of the matrix.

Combining equations 1 and 11, we obtain an explicit relationship between the frequency shift and the axial stress in the sliding phase

$$\sigma_z = \frac{\Delta\nu + 2\Pi_a(N_R - B\,P_R)}{2\Pi_a B - \Pi_c} \tag{13}$$

As in a typical push-out test, it is difficult to obtain the variation of friction along the fiber due to the variation of normal stress across the interfaces. This is because the Poisson's effect is not large enough to produce a clear curvature. Therefore the solution for the stress distribution reduces to one with an effective constant friction τ_0 [3]. Using equation 13 to fit the center section of the curves in figure 12, the sliding frictional stress for the two different coatings are found to be

$$\tau_{0\,Mo} = 180 \text{ MPa}$$

$$\tau_{0\,C} = 140 \text{ MPa}$$

5 Discussion

By comparing the measured frequency shift profiles with those calculated using a finite element model, we have obtained values for the debond energies, the frictional stresses, and the debond length at different applied loads. In this section, we discuss their accuracies and implications.

From Tables II and III, it is evident that the debond length increases as the push load increases once the load exceeds the residual axial stress P_R. This provides direct evidence that the debond growth process is a steady state, crack growth process when the debond length is smaller than, or comparable to, half the fiber length. The whole interface debonds suddenly when the load is further increased. This suggests that there might be a unstable crack growth process near the top end of the fiber. Both of these observations are consistent with the theoretical predictions using FEM [3]. The debond lengths in Tables II and III appear to be multiples of the fiber radius. However, this is a consequence of the stress functions being calculated for only a limited number of debond lengths. Therefore, the actual debond length at a certain load could be either slightly larger or smaller than that obtained from the fitting. This can be determined by examining the effective load P_{eff} at each applied load. When the applied load is larger than P_R, the effective load has to be positive, and according to equation 9, they should have the same value during steady state debond growth, for that the debond energy is always the same for a certain system. However, from Tables II and III, we have both positive and negative values for the effective load, indicating that the debond lengths are indeed deviated from the true values. Since excellent fittings were obtained in the last section, it is reasonable to assume that the deviations are relatively small, and therefore the average value for the effective loading for the two coatings are relatively accurate. Consequently, the debond energies we obtained are considered relatively accurate. We can then compare the effective load at each applied load with the average effective load $\overline{P_{eff}}$ to determine whether the listed debond length is too large or too small. For example, for the Mo coating, $P_{eff} < \overline{P_{eff}}$ at $P = 1.45$ GPa, indicating that the real debond length is slightly smaller than $1.5R_f$. At $P = 2.26$ GPa, $P_{eff} > \overline{P_{eff}}$, indicating that the real debond length is slightly larger than $3.3R_f$, and so on. Using this procedure, we can qualitatively

correct the uncertainty in the debond length. This data is shown superimposed with the frequency shift data in figure 13 illustrating the debond growth in the two systems.

One of the principal results of this work is determining frictional stress values in the debonding phase and its dependence on the type of coating. In figure 14 are plotted the friction-load dependence for the two coating systems. Two characteristics are evident. First, the friction increases with load. Although the friction in the calculation is assumed, for simplicity, to be constant along the interface, the load dependence clearly suggest that the friction depends on the normal stress across the interface, and may therefore be partially Coulombic. To obtain the friction law, the normal stress averaged across the length of the debonded interface was calculated for each applied load. The frictional stress as a function of such normal stress is then plotted in figure 15 for the two coating systems. Instead of obeying a linear, Coulombic dependence, the relationship appears to be parabolic, suggesting that the friction may depend on small displacements of the fiber from its seated position. Such asperity effects have been reported previously [4,8] and are addressed elsewhere [9,10]. The second characteristic feature is that the frictional stress for the two different coating systems is quite similar. This strongly suggest that the friction in the debonding phase depends primarily on the interface morphology, which in turn is determined by the sapphire fiber surface morphology, rather than on the coating material *per se*. Therefore, in order to reduce the friction in the debonding phase, it is important to improve the fiber surface smoothness. Further, the large difference in the maximum load needed to push-out the fibers and in the debond energy suggests that the debond energy determines the push-out load, and therefore plays an important role in determining the composite property.

Finally, we have also been able to determine the friction in the sliding phase for the two systems. The values obtained here and in other studies using conventional push-out

techniques agree rather well [4], with the friction for the CVD-graphite coating usually exhibiting a smaller values than that of the Mo coating. We can therefore conclude that in the sliding phase, the properties of the coating material are also important for frictional sliding.

6 Conclusion

By measuring *in situ* the stress distributions along sapphire fibers at different stages of the push-out test, and comparing them with those calculated using a finite element model, the key mechanical parameters controlling the push-out process have been determined, and their implications discussed.

The measurements of the residual stress distributions along the fibers before loading and comparison to the computations provide the values of the residual stresses in the composite prior to slicing a thin section for the push-out test. They also give the extent of interface debonding caused by the slicing.

It is observed that the debond length increases stably with increasing applied load when the debond is not significantly greater than half of the fiber length. This provides clear evidence that the debonding process in this region is a steady state crack growth process. The sudden debond of the interface afterwards suggests that there is also a unstable crack propagation process near the end. These observations agree with the predictions made using earlier FEM calculations [3].

The interfacial friction in the debonding phase is shown to increase with the applied load. Further, the dependence of the friction on the average normal stress across the debonded interface is nearly parabolic. These observations suggest that the friction is partially Coulombic and is strongly influenced by the asperities along the interface. In the debonding phase,

the displacement is very small, so that the fiber is in a unseating process, and hence the effective friction may depend on the displacement, in addition to the normal stress. Another significant feature of the friction in the debonding phase is that it is very similar for the two coating systems. This further suggests that the interface morphology largely determines the interface friction, while the coating material plays a less important role. However, the friction in the sliding phase obtained for the two coating systems are different in value and are very similar to those obtained by conventional push-out tests [4].

The debond energies were also obtained for the two interfaces. For the CVD-C coated fiber, the energy is about one order of magnitude smaller than that for the Mo coated fiber, which explains why the load required to push-out a CVD-C coated fiber is only half of that for the Mo coated one. The implication of this is that the debond energy will also significantly influence the fracture properties of composites

ACKNOWLEDGMENT

This work was supported by the Office of Naval Research under grant N00014-91-J-1875 (QM) and the DARPA URI program at UCSB and Harvard under contract N00014-92-J-1808 (DRC, LCL, JWH). The authors are grateful to Dr. T.J. Mackin, J. Yang and R. Hanson, UCSB, for providing the composite samples used in this w rk.

References

1. D.B. Marshall, J. Am. Ceram. Soc. 67, C259 (1984).

2. P.D. Warren, T.J. Mackin and A.G. Evans, Acta Metall. Mater. 40, 1243 (1992).

3. L.C. Liang and J.W. Hutchinson, Mechanics of Materials, 14, 207 (1993).

4. T.J. Mackin, J.Y. Yang, C.G. Levi and A.G. Evens, Mat. Sci. Eng., A161, 285 (1993).

5. Q. Ma and D.R. Clarke, Acta Metall. Mater., 41, 1817 (1993).

6. R.G. Munro, G.J. Piermarini, S. Block and W.B. Holzapfel, Journal of Applied Physics, 57, 165 (1985).

7. J.W. Hutchinson and H.M. Jensen, Mech. Materials, 9, 139 (1990).

8. T.J. Mackin, P.D. Warren and A.G. Evans, Acta Metall. Mater., 40, 1251 (1992).

9. W.C. Carter, E.P. Butler and E.R. Fuller, Jr., Scripta Metall. Mater., 25, 579 (1991).

10. L.C. Liang and J.W. Hutchinson, in preparation.

TABLE I

Properties of Fiber, Matrix and Coating

PROPERTY	Sapphire	γ-TiAl	Al_2O_3 Coating
E (GPa)	420	173	420
ν	0.27	0.33	0.27
α (10^{-6}/°C)	8.3 (a), 9.0 (c)	11 $\sim$ 13	8.6

TABLE II

Fitting Parameters Obtained for the Mo/Al_2O_3 Coated Fiber

APPLIED LOAD P (GPa)	FRICTIONAL STRESS τ_0 (GPa)	DEBOND LENGTH l/R_f	EFFECTIVE LOAD P_{eff} (GPa)
0.00	-0.15	1.5	
0.76	0.04	1.5	
1.45	0.095	1.5	-0.035
2.26	0.14	3.0	0.22
3.15	0.22	4.5	-0.03
4.01	0.27	4.5	0.38

TABLE III

Fitting Parameters Obtained for the CVD-C/Al_2O_3 Coated Fiber

APPLIED LOAD P (GPa)	FRICTION STRESS τ_0 (GPa)	DEBOND LENGTH l/R_f	EFFECTIVE LOAD P_{eff} (GPa)
0.00	-0.12	1.5	
0.68	-0.03	1.5	
0.98	0.05	1.5	
1.25	0.09	1.5	0.03
1.55	0.10	3.0	-0.01
1.85	0.13	3.0	0.12
2.14	0.15	4.0	-0.01

Figure Captions

Figure 1. Schematic diagram of the optical arrangement used to collect fluorescence from a region in an embedded sapphire fiber under push-out load. When the laser excitation is focused at a distance z below the top surface, only the signal generated in a small volume above and below the focal plane is effectively collected by the lens.

Figure 2. The depth of field functions, measured at the top and the bottom surfaces of a sapphire fiber. The degrading of the depth resolution is caused by the ray blocking effect of the matrix, which decreases the effective numerical aperture of the system.

Figure 3. The mechanical loading fixture used for the push-out test. It is designed to fit under a optical microscope for *in situ* fluorescence measurement. The dimensions are not drawn in scale The push rod made of a Nicalon SiC fiber, for example, is only 100μm in diameter, and the sample thickness is $\sim$ 0.5 mm.

Figure 4. Measured frequency shifts $\Delta\nu$ as a function of depth z for a fiber with Mo/Al_2O_3 coatings in the debonding phase. The top surface is at $z = 0$ and the bottom surface, where the pushing load is applied, is at $z = 516\mu$m. Six shift depth profiles were obtained at different loads sequentially. The top curve was measured without any load, thus corresponding to the residual stresses in the fiber.

Figure 5. The shift profiles for a fiber with Mo/Al_2O_3 coatings, measured after the whole interface debonds. Three profiles correspond to cases of fiber with load applied (bullet), with load released (square) and pushed back to its seated position (diamond), respectively.

Figure 6. Measured frequency shifts $\Delta\nu$ as a function of depth z in the debonding phase for a fiber with CVD-C/Al_2O_3 coatings.

Figure 7. Schematic diagram of the push-out configuration of the finite element model.

Figure 8. Comparison between the measured shift profile (deconvoluted) and that calculated. (a) Assuming no debond near the fiber ends; (b) Assuming appropriate debond and friction near the fiber ends to match the data.

Figure 9. Axial and radial residual stress distributions in the Mo-coated fiber after slicing.

Figure 10. Comparison of the shift profiles obtained at various loadings for the Mo/Al_2O_3 coated fiber, together with the parameters used to obtain the best fit. Since in the FEM calculations, the debond was only allowed at the bottom of the slice, the fitting near the top end carries little significance.

Figure 11. Comparison of the shift profiles obtained at various loadings for the CVD-C/Al_2O_3 coated fiber.

Figure 12. Shift profiles obtained in the sliding phase for the Mo/Al_2O_3 and CVD-C/Al_2O_3 coated fiber, respectively. The solid dots are the measured shifts and the solid curve is the deconvoluted shift profile obtained using the depth of field function and therefore representing the true shift profile. The dashed curve is the true shift convoluted with the depth of field function.

Figure 13. Estimated positions of the tip of the debond crack as the applied load increases for the Mo/Al_2O_3 coating and CVD-C/Al_2O_3 coating, respectively.

Figure 14. The dependence of frictional stress on the applied load for the two coating systems.

Figure 15. The dependence of frictional stress on the average normal stress across the debonded interface for the two coating systems. The curves show parabolic fittings.

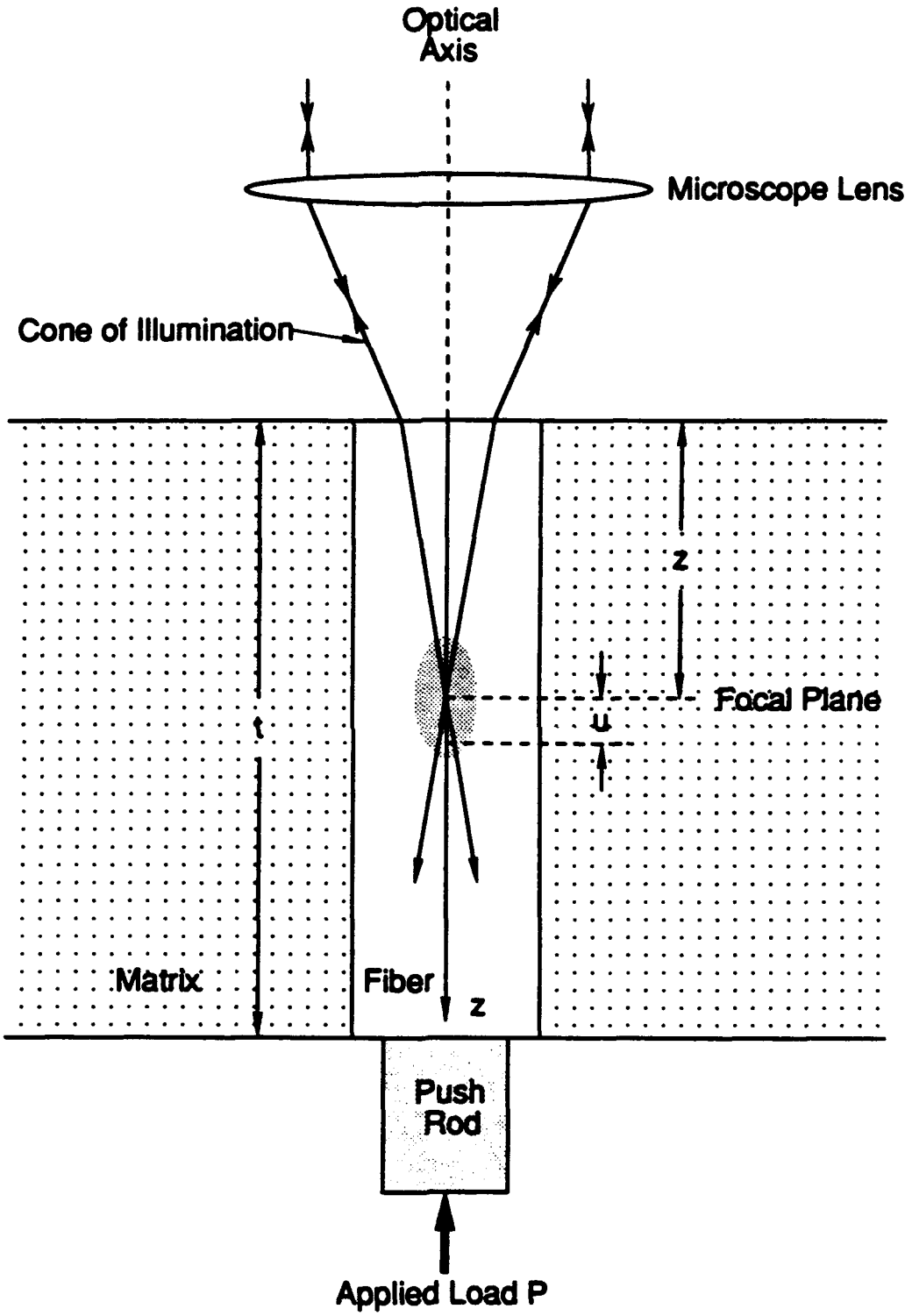
Optical Axis
Microscope Lens
Cone of Illumination
z
Focal Plane
u
t
Matrix
Fiber
z
Push Rod
Applied Load P

Fig. 1

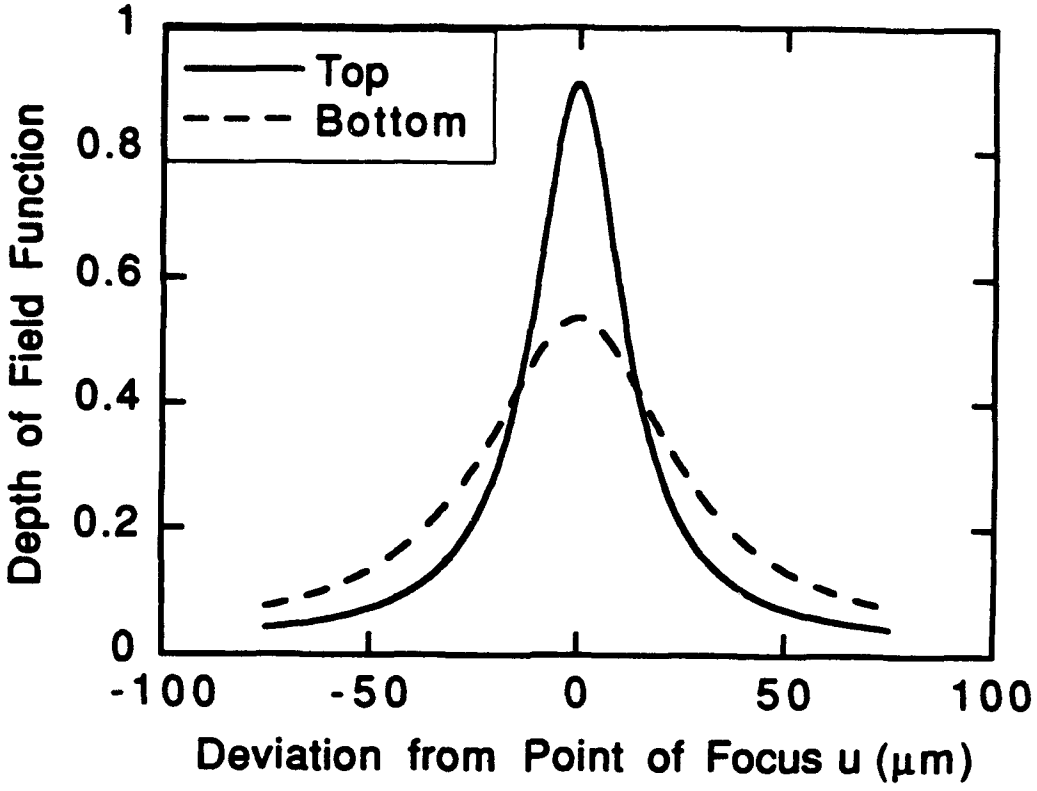
Top
Bottom
Depth of Field Function
1
0.8
0.6
0.4
0.2
0
-100
-50
0
50
100
Deviation from Point of Focus u (μm)

Fig. 2

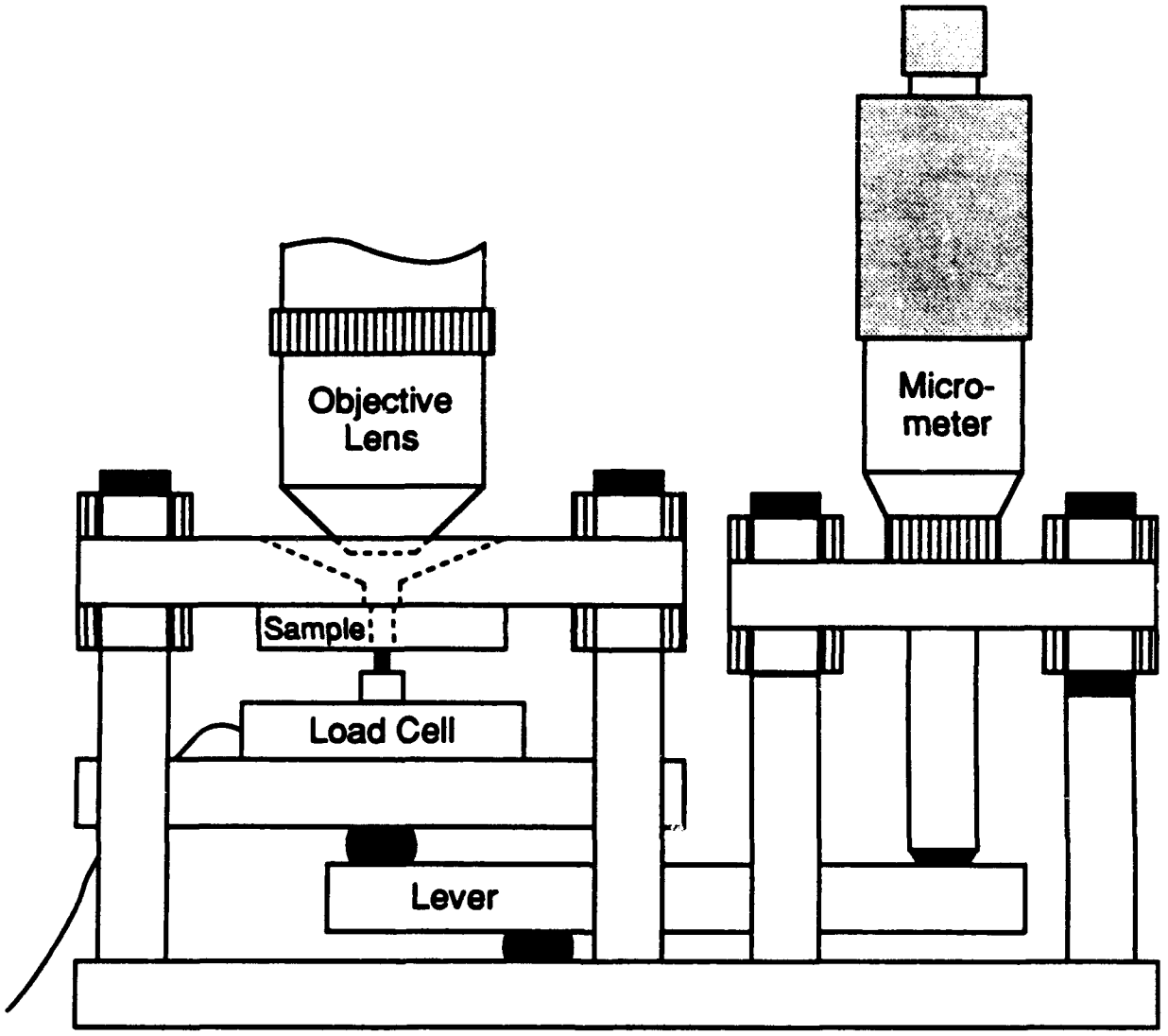

Fig. 3

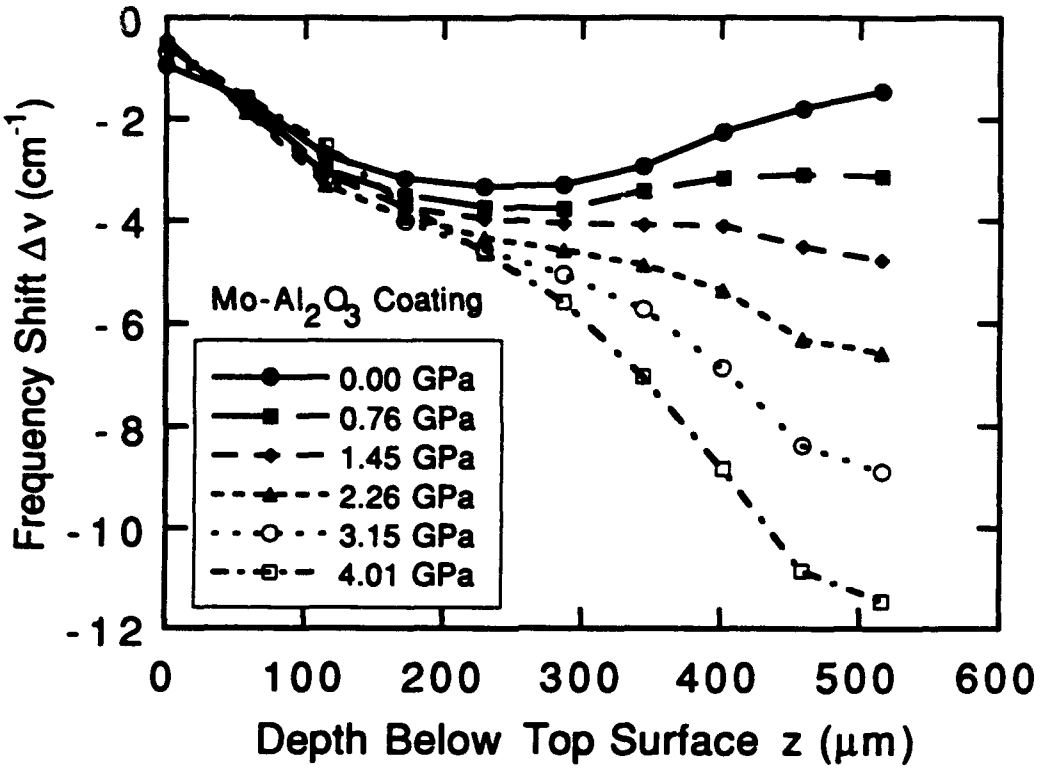
Frequency Shift Δν (cm⁻¹)
0
-2
-4
-6
-8
-10
-12
Mo-Al2O3 Coating
0.00 GPa
0.76 GPa
1.45 GPa
2.26 GPa
3.15 GPa
4.01 GPa
0
100
200
300
400
500
600
Depth Below Top Surface z (μm)

Fig. 4

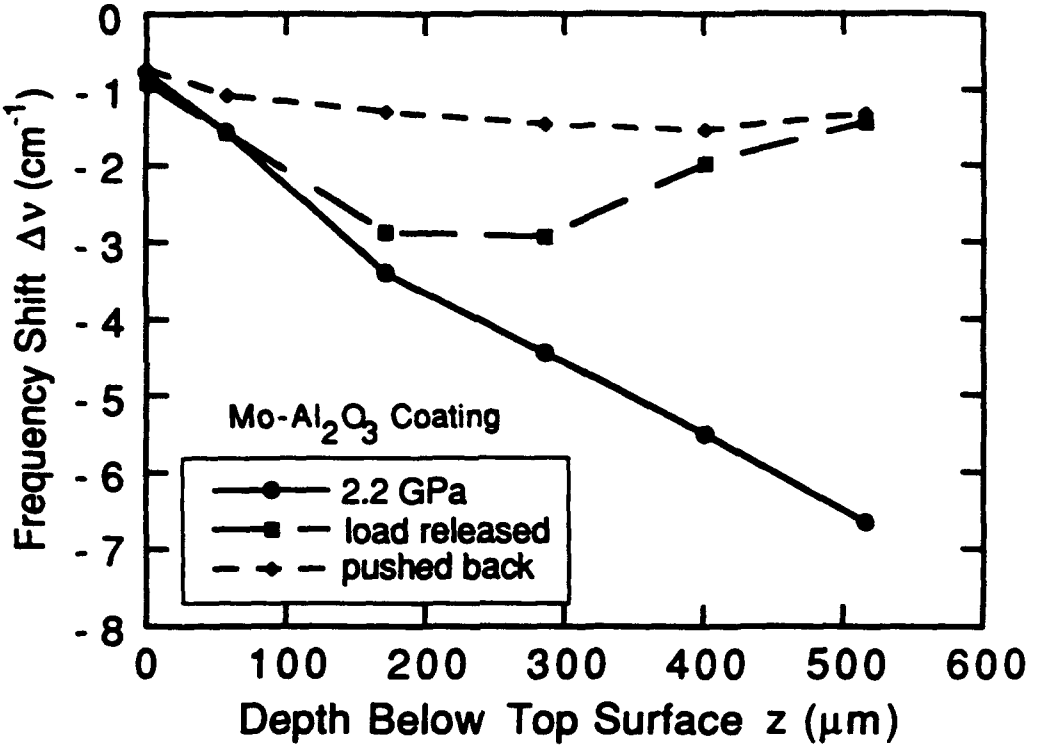
0
- 1
- 2
- 3
- 4
- 5
- 6
- 7
- 8
Frequency Shift Δν (cm-1)
Mo-Al2O3 Coating
2.2 GPa
load released
pushed back
0
100
200
300
400
500
600
Depth Below Top Surface z (μm)

Fig. 5

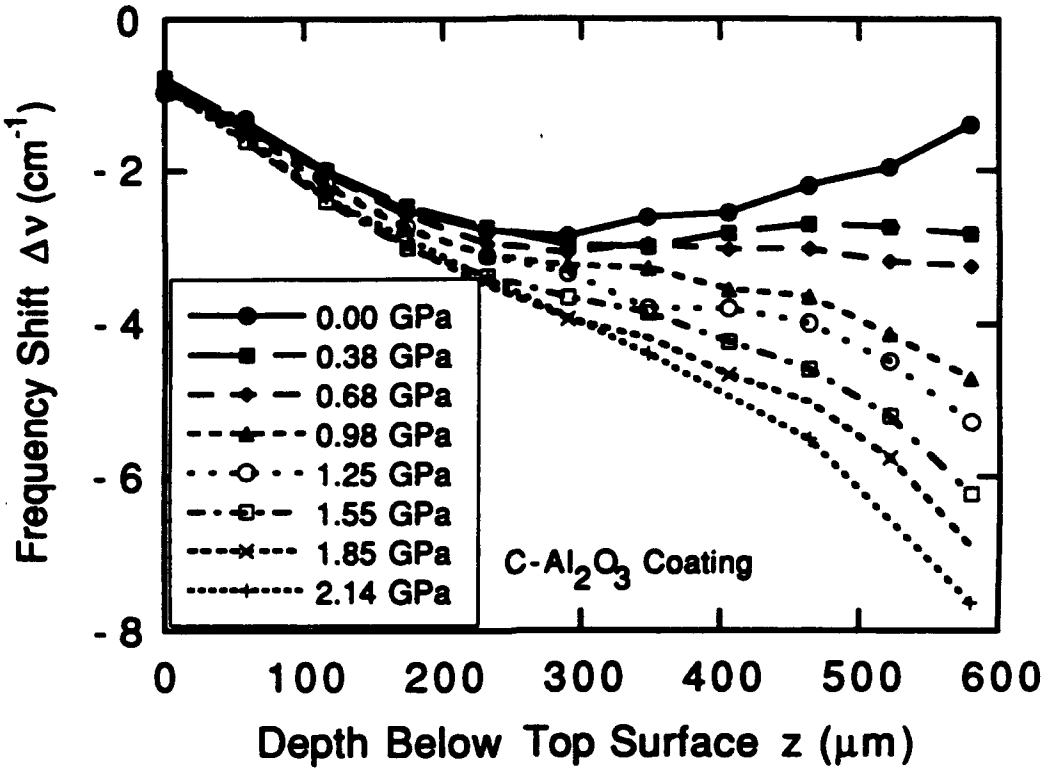
0
- 2
- 4
- 6
- 8
Frequency Shift Δν (cm⁻¹)
0.00 GPa
0.38 GPa
0.68 GPa
0.98 GPa
1.25 GPa
1.55 GPa
1.85 GPa
2.14 GPa
C-Al2O3 Coating
0
100
200
300
400
500
600
Depth Below Top Surface z (μm)

Fig. 6

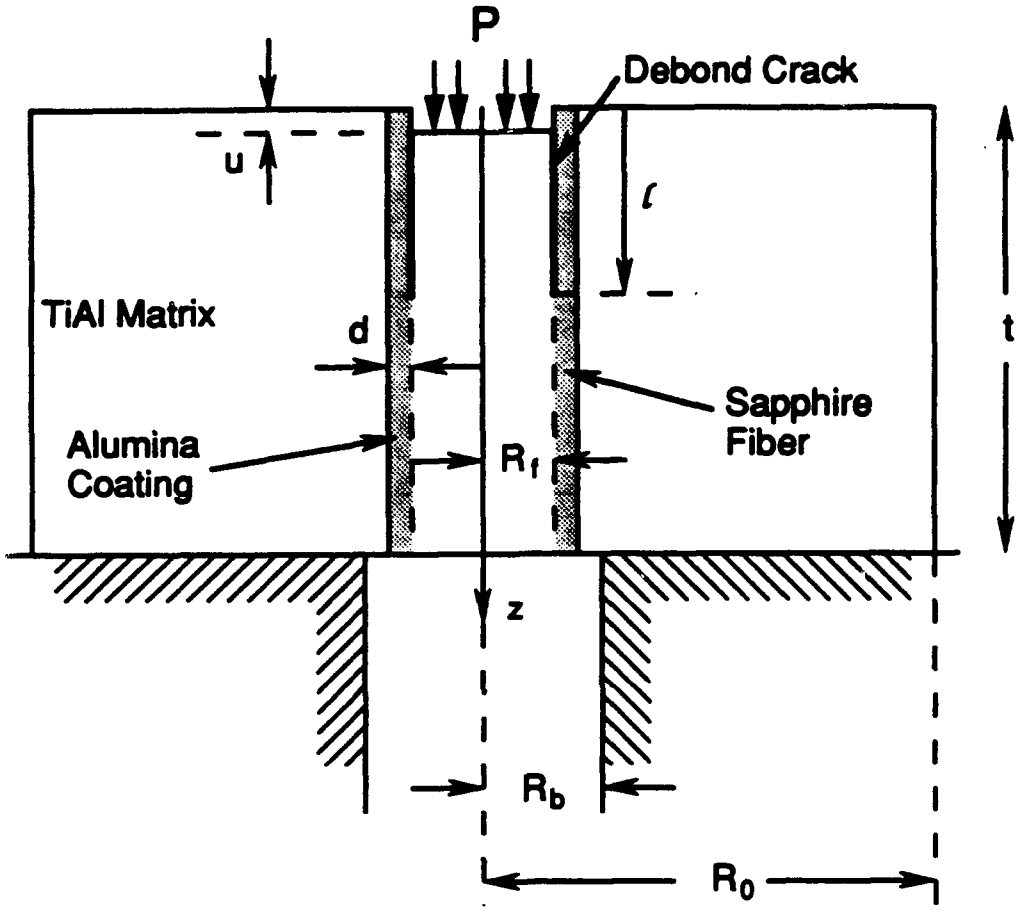
P
Debond Crack
u
ℓ
TiAl Matrix
d
t
Sapphire
Fiber
Alumina
Coating
R_f
z
R_b
R_0

Fig. 7

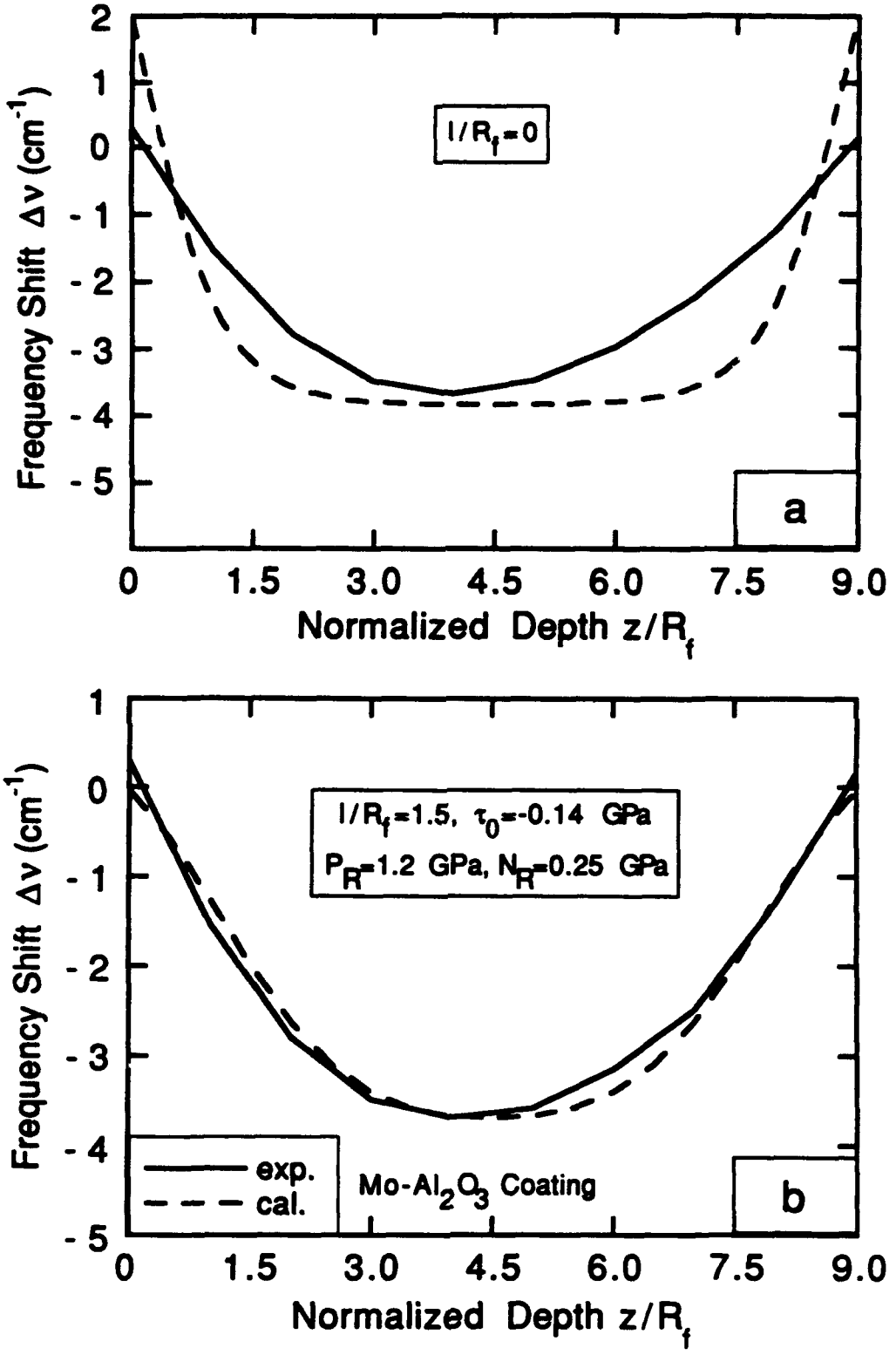
Frequency Shift Δν (cm⁻¹)
2
1
0
- 1
- 2
- 3
- 4
- 5
1/R_f=0
a
0
1.5
3.0
4.5
6.0
7.5
9.0
Normalized Depth z/R_f
Frequency Shift Δν (cm⁻¹)
1
0
- 1
- 2
- 3
- 4
- 5
1/R_f=1.5, τ_0=-0.14 GPa
P_R=1.2 GPa, N_R=0.25 GPa
exp.
cal.
Mo-Al2O3 Coating
b
0
1.5
3.0
4.5
6.0
7.5
9.0
Normalized Depth z/R_f

Fig. 8

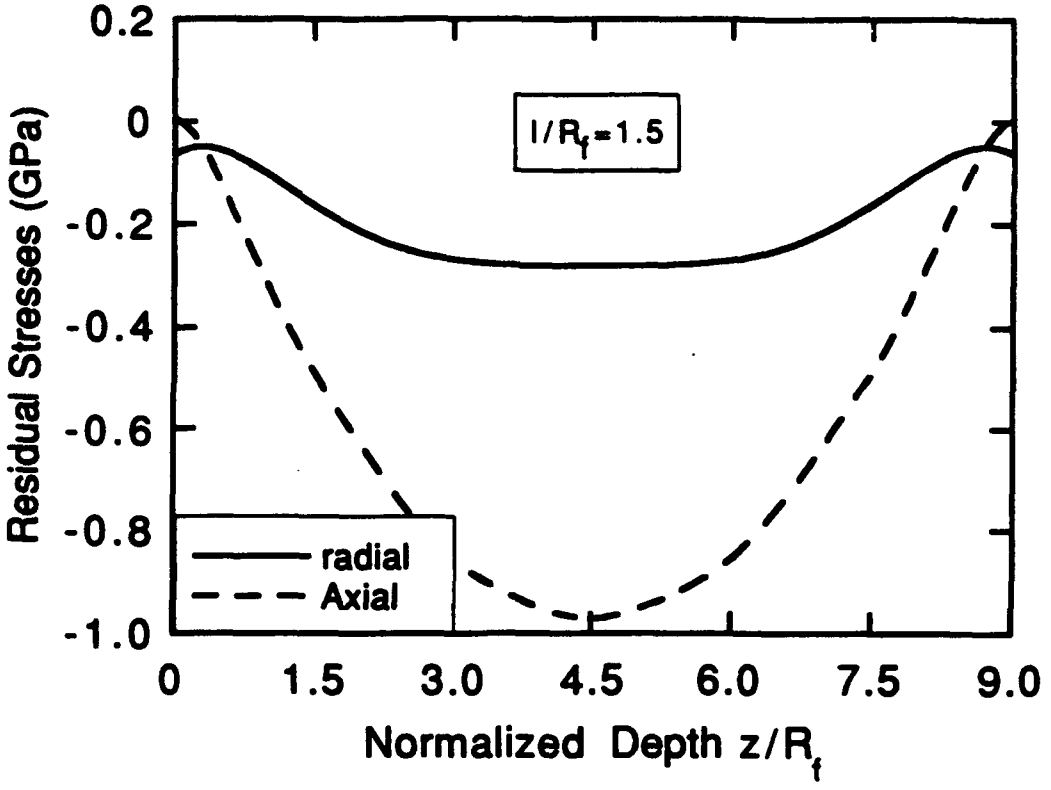
0.2
0
-0.2
-0.4
-0.6
-0.8
-1.0
Residual Stresses (GPa)
l/R_f=1.5
radial
Axial
0
1.5
3.0
4.5
6.0
7.5
9.0
Normalized Depth z/R_f

Fig. 9

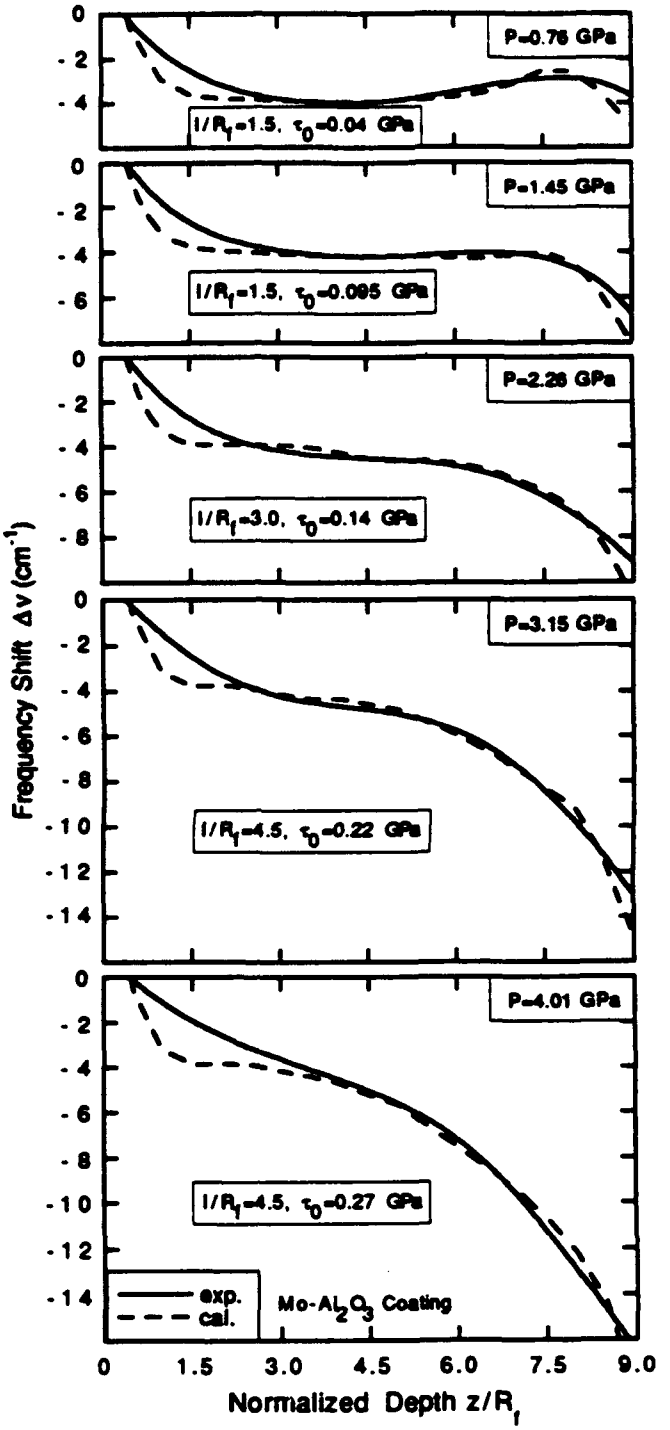
P=0.76 GPa
l/R_f=1.5, τ_0=0.04 GPa
P=1.45 GPa
l/R_f=1.5, τ_0=0.095 GPa
P=2.28 GPa
l/R_f=3.0, τ_0=0.14 GPa
P=3.15 GPa
l/R_f=4.5, τ_0=0.22 GPa
P=4.01 GPa
l/R_f=4.5, τ_0=0.27 GPa
exp.
cal.
Mo-Al2O3 Coating
Frequency Shift Δν (cm⁻¹)
Normalized Depth z/R_f
0
1.5
3.0
4.5
6.0
7.5
9.0

Fig. 10

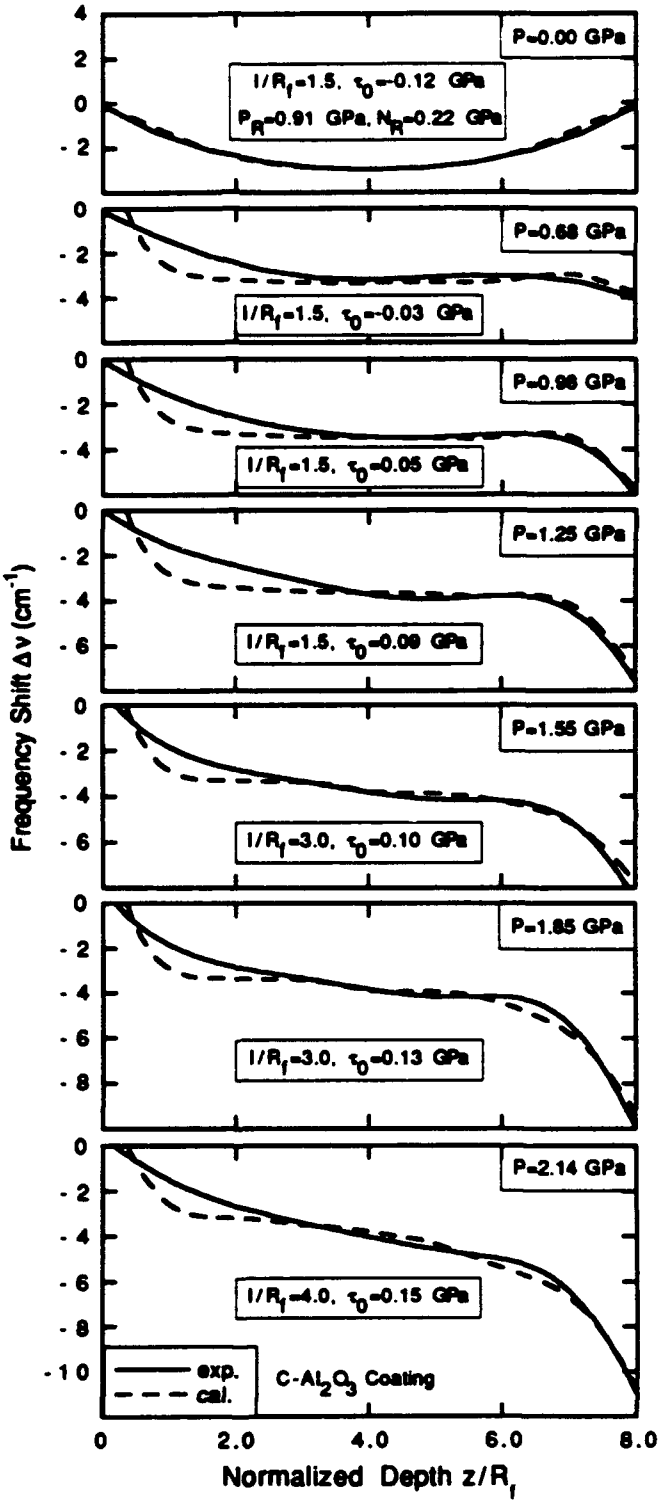
P=0.00 GPa
l/R_f=1.5, τ_0=-0.12 GPa
P_R=0.91 GPa, N_R=0.22 GPa
P=0.68 GPa
l/R_f=1.5, τ_0=-0.03 GPa
P=0.98 GPa
l/R_f=1.5, τ_0=0.05 GPa
P=1.25 GPa
l/R_f=1.5, τ_0=0.09 GPa
P=1.55 GPa
l/R_f=3.0, τ_0=0.10 GPa
P=1.85 GPa
l/R_f=3.0, τ_0=0.13 GPa
P=2.14 GPa
l/R_f=4.0, τ_0=0.15 GPa
exp.
cal.
C-Al2O3 Coating
Frequency Shift Δν (cm-1)
Normalized Depth z/R_f

Fig. 11

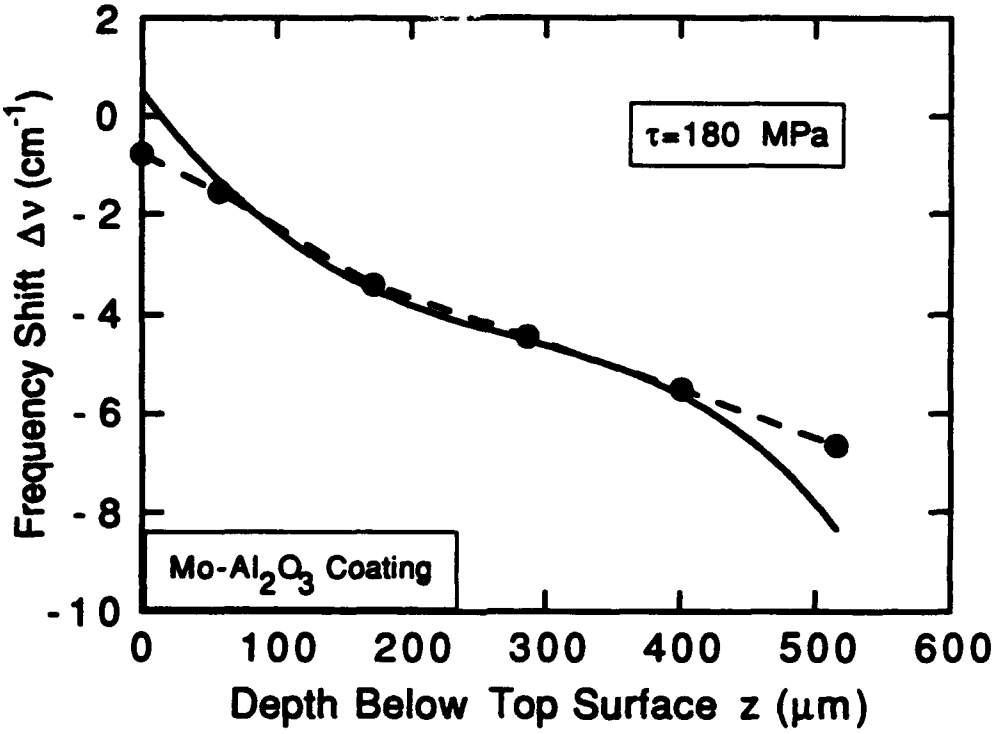
τ=180 MPa
Mo-Al2O3 Coating
Frequency Shift Δν (cm-1)
Depth Below Top Surface z (μm)
2
0
-2
-4
-6
-8
-10
0
100
200
300
400
500
600

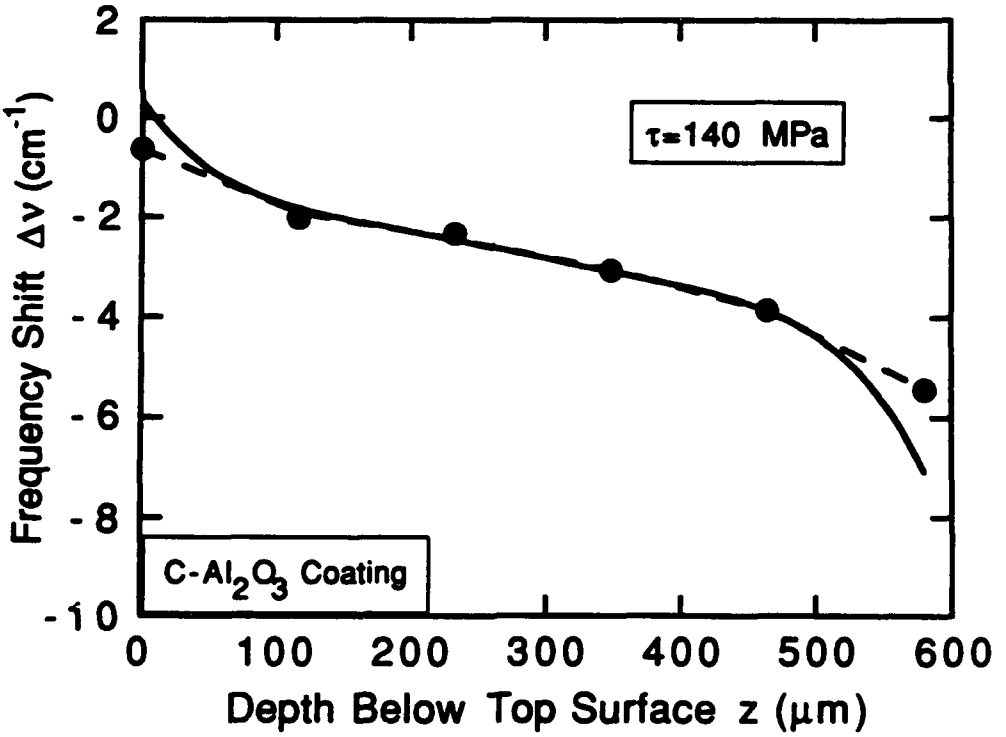
τ=140 MPa
C-Al2O3 Coating
Frequency Shift Δν (cm-1)
Depth Below Top Surface z (μm)
2
0
-2
-4
-6
-8
-10
0
100
200
300
400
500
600

Fig. 12

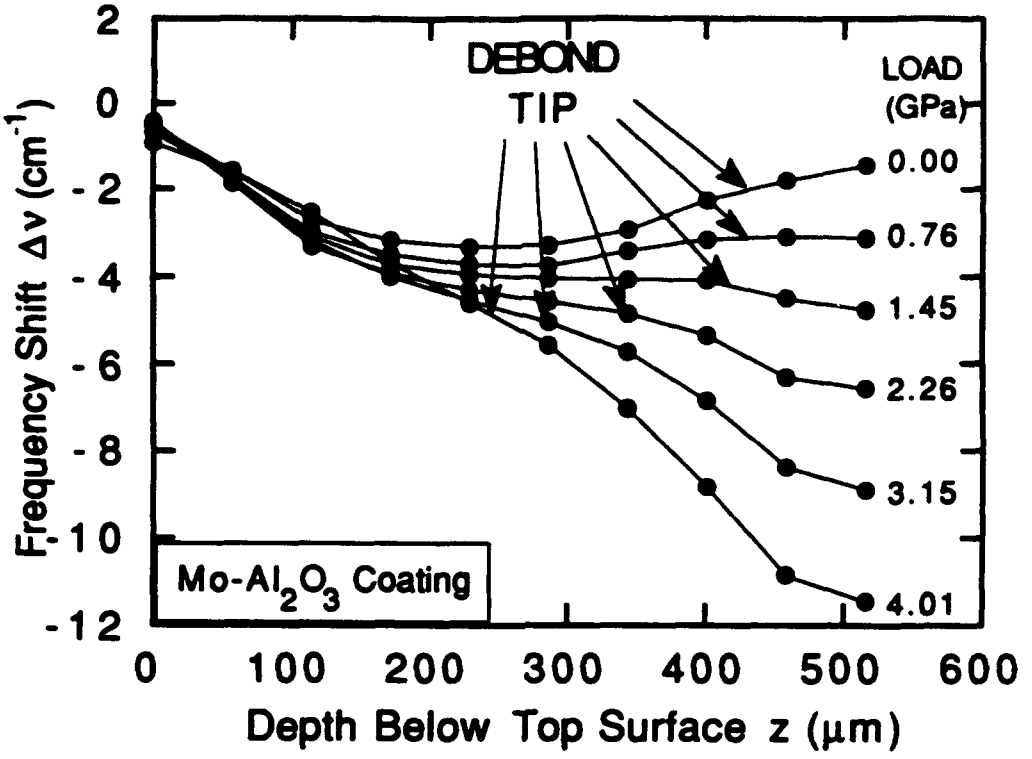
DEBOND
TIP
LOAD
(GPa)
0.00
0.76
1.45
2.26
3.15
4.01
Mo-Al2O3 Coating
Frequency Shift Δν (cm-1)
2
0
-2
-4
-6
-8
-10
-12
0
100
200
300
400
500
600
Depth Below Top Surface z (μm)

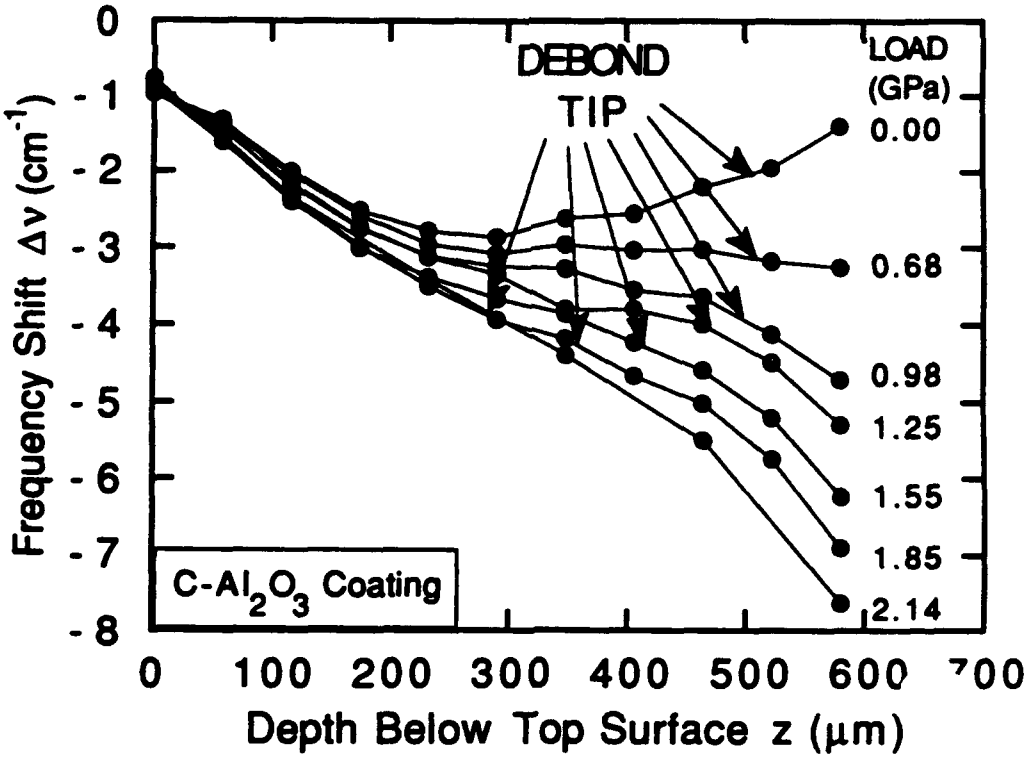
DEBOND
TIP
LOAD
(GPa)
0.00
0.68
0.98
1.25
1.55
1.85
2.14
C-Al2O3 Coating
Frequency Shift Δν (cm-1)
0
-1
-2
-3
-4
-5
-6
-7
-8
0
100
200
300
400
500
600
700
Depth Below Top Surface z (μm)

Fig. 13

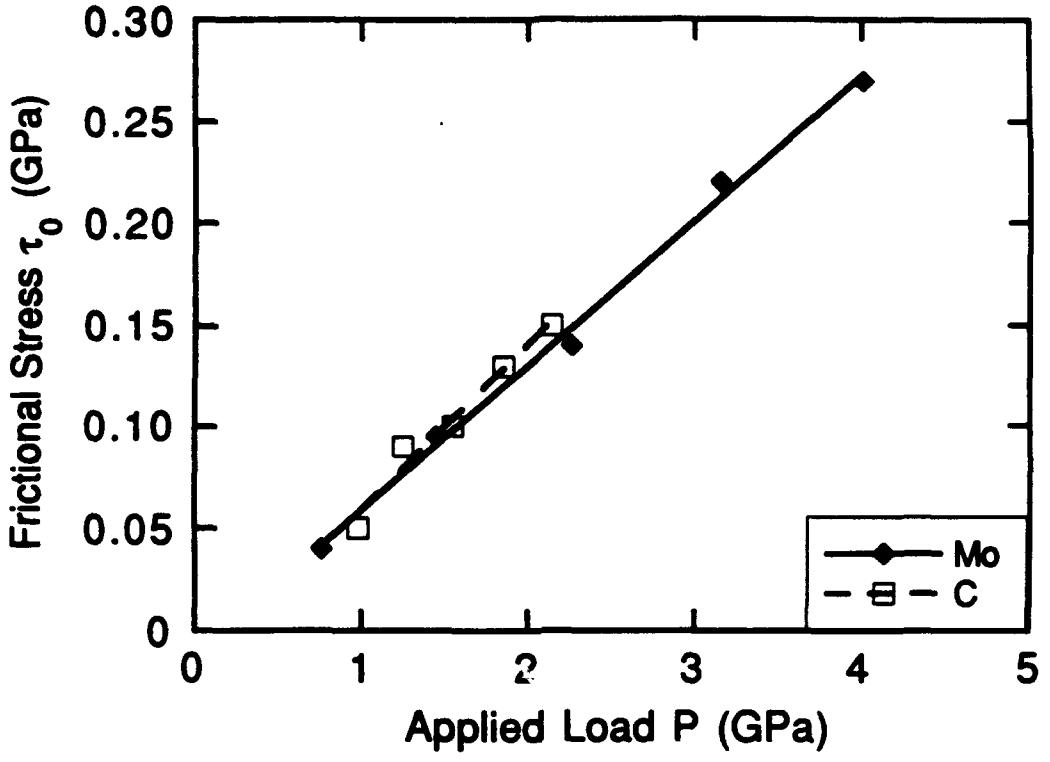
0.30
0.25
0.20
0.15
0.10
0.05
0
Frictional Stress τ_0 (GPa)
0
1
2
3
4
5
Applied Load P (GPa)
Mo
C

Fig. 14

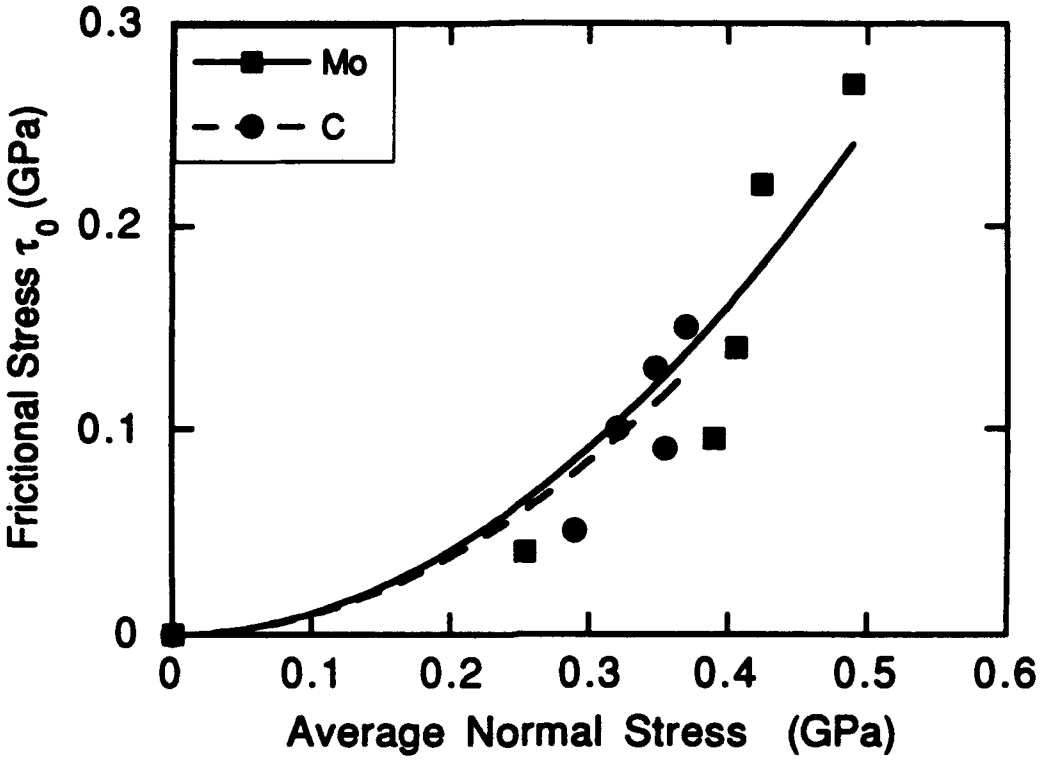
0.3
0.2
0.1
0
Mo
C
Frictional Stress τ_0 (GPa)
0
0.1
0.2
0.3
0.4
0.5
0.6
Average Normal Stress (GPa)

Fig. 15

MATERIALS

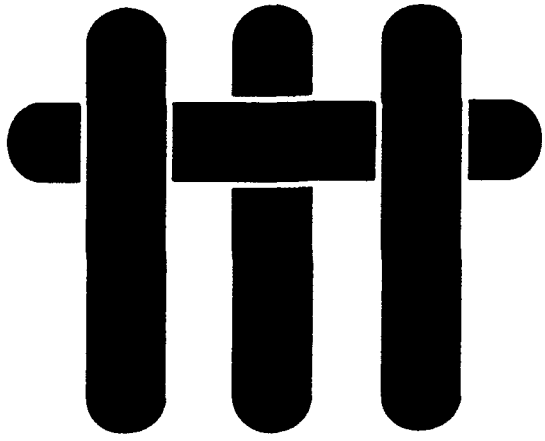

RELATIONSHIPS BETWEEN HYSTERESIS MEASUREMENTS AND THE CONSTITUENT PROPERTIES OF CERAMIC MATRIX COMPOSITES

I: THEORY

by

E. Vagaggini, J.-M. Domergue and A.G. Evans
Materials Department
College of Engineering
University of California, Santa Barbara
Santa Barbara, California 93106–5050

KJS-Evans-36-TA-Mthd C/M | 93/12/21-10:10 AM-2/8/94

NOMENCLATURE

a_i	composite coefficients defined by Hutchinson and Jensen[22]
b_i	composite coefficients defined by Hutchinson and Jensen[22]
c_i	composite coefficients defined by Hutchinson and Jensen[22]
f	fiber volume fraction
$\bar{d}$	mean matrix crack spacing
$\bar{d}_s$	mean crack spacing at saturation
ℓ_i	mean debonding length
ℓ_u	sliding length upon unloading
ℓ_r	sliding length upon reloading
p	residual pressure at the interface
q_f	axial residual stress in fiber
q_m	axial residual stress in matrix
u	crack opening displacement
E	Young's modulus of composite
E_f	Young's modulus of fiber
E_m	Young's modulus of matrix
E_s	secant modulus of composite
E^*	Young's modulus of material with matrix cracks
E_p	tangent modulus minimum (Fig. 6)
$\bar{E}$	hysteresis modulus of the composite
R	fiber radius
ε	strain
ε_0	permanent strain
ε_p	peak strain
ε^e	elastic strain
ε^s	sliding strain

ε^T misfit strain

ε^* misfit relief strain caused by matrix cracks

$\delta\varepsilon$ hysteresis loop width

$\delta\varepsilon_{1/2}$ hysteresis loop width at $\bar{\sigma}_p/2$

$\Delta\varepsilon_o$ inelastic strain difference (Fig. 6)

$\Delta\varepsilon_p$ inelastic strain difference (Fig. 6)

ν Poisson's ratio (assumed to be the same for fiber and matrix)

$\bar{\sigma}$ stress applied on the composite[¥]

$\bar{\sigma}_o$ stress acting on 0° plies in a 2-D material

$\bar{\sigma}_D$ 'debond' stress at zero misfit stress

$\bar{\sigma}_i$ 'debond' stress

$\bar{\sigma}^0_{mc}$ matrix cracking stress with zero debond energy[31]

$\bar{\sigma}_{mc}$ matrix cracking stress

$\bar{\sigma}_p$ peak stress

$\bar{\sigma}_s$ stress at crack saturation

$\bar{\sigma}^T$ misfit stress

τ interface sliding resistance

τ_0 constant interface sliding resistance

Γ_i interface debond energy

Γ_m matrix fracture energy

Σ non-dimensional stress, $\bar{\sigma}/\bar{\sigma}_p$

$\Sigma_i \rightarrow \bar{\sigma}_i/\bar{\sigma}_p$

$\Sigma^T \rightarrow \bar{\sigma}^T/\bar{\sigma}_p$

$\Sigma_D \rightarrow \bar{\sigma}_D/\bar{\sigma}_p$

$\Sigma_u \rightarrow \bar{\sigma}_u/\bar{\sigma}_p$

$\Sigma_r \rightarrow \bar{\sigma}_r/\bar{\sigma}_p$

[¥] The bar superscript is used to be consistent with Hutchinson and Jensen[22] analysis which denotes a stress applied on the composite.

ABSTRACT

A methodology for assessing constituent properties of ceramic matrix composites (CMCs) from stress/strain curves is developed. The procedures demonstrate how the properties of the interface and the misfit strain can be related to the unload/reload hysteresis and the permanent strain. The approach is illustrated in companion papers by obtaining experimental measurements on two CMCs. The results demonstrate why differences in the sliding stress and the debond energy of the interfaces result in substantial changes in the shape of the stress/strain curve.

1. INTRODUCTION

The non-linear behavior of ceramic matrix composites (CMC) caused by matrix cracking and fiber pull-out has a critical influence on the sensitivity of the material to stress concentrations caused by notches, holes, etc.[1-6] An experimental methodology for characterizing the inelastic strain is needed. In particular, since CMCs are subject to constituents that can be influenced by processing, it is desirable to develop a methodology that relates the macroscopic behavior to constituent properties (fibers, matrix, interface). Then, the influence of changes in the constituents and of processing conditions on the macroscopic behavior can be predicted. A set of constituent properties that influence the inelastic strain, as well as methods of measurement, is summarized in Table I. A recently proposed methodology[7] is developed in this article. The procedure is illustrated and applied in two companion papers[8,9] with examples given for two CMCs (SiC/SiC and SiC/CAS), both 1-D and 2-D. Measurements[10,11] and analysis[12] have established that the inelastic strains are primarily attributed to the displacements caused by multiple matrix cracks. These strains, which relate explicitly to constituent properties,[12] are emphasized.

Tensile stress/strain, $\bar{\sigma}(\varepsilon)$, curves for three CMCs (Fig. 1a, b) indicate the non-linearity. For the C matrix material, the matrix does not exhibit multiple cracking and the inelastic strain derives solely from stochastic fiber failure.[13] Such materials are not addressed. Conversely, in CAS and SiC matrix materials, the inelastic strain derives principally from multiple matrix cracking.[12,14] The emphasis is on materials of this type. Schematics of the stress/strain curves for unidirectional and cross-ply CMCs (Fig. 1c) illustrate some essential features. For unidirectional CMCs, matrix cracks commence at a characteristic stress, designated $\bar{\sigma}_{mc}$.[15,16] The crack density increases as the stress increases above $\bar{\sigma}_{mc}$.[17] Moreover, the interfaces debond and slip within a zone of length ℓ_i, adjacent to the cracks.[15-18] Subsequently, the interface slip zone emanating

from neighboring cracks overlaps.[17] At this stage, crack saturation occurs, at another characteristics stress, designated $\bar{\sigma}_s$.[12,17] Typically, $\bar{\sigma}_s/\bar{\sigma}_{mc}$ is in the range, 1.5 to 3.[10-12,14] In some cases, composite failure occurs before $\bar{\sigma}_s$ is reached (Fig. 1a).[14] The methodology developed in this article demonstrates that it is only necessary to conduct experiments in the stress range, $\bar{\sigma}_{mc} < \bar{\sigma} < \bar{\sigma}_s$, where slip overlap is not an issue, in order to evaluate constituent properties.

The behavior of cross-ply CMCs is more complex (Fig. 1b, c). It involves initial cracking in the 90° plies.[19] Subsequently, these cracks begin to penetrate the 0° plies, at stress $\bar{\sigma}^*_{mc}$ and extend stably, subject to increased loads.[11,20] In some materials, additional matrix cracks form in the 0° plies, as the load continues to increase.[14] Eventually, the slip zones associated with the cracks in the 0° plies overlap and saturation occurs, at stress, $\bar{\sigma}^*_s$. In some cases, such as SiC/SiC, composite failure interferes before $\bar{\sigma}^*_s$ is reached.[14]In the stress range, $\bar{\sigma}^*_{mc} < \bar{\sigma}_0 < \bar{\sigma}^*_s$, the inelastic strains evolve in a manner similar to those occurring in unidirectional material. Again, this is the stress range emphasized in this article, as indicated on Fig. 1b.

After the onset of matrix cracking, and upon unloading/reloading, there is a reduction in elastic modulus (Fig. 2), hysteresis usually occurs, and there is a permanent strain. Each of these features contains important information about the constituent properties, particularly the interface debonding/sliding behavior expressed by the debond energy Γ_i and the sliding stress τ, as well as the fiber/matrix thermal expansion mismatch, represented by the misfit stress, $\bar{\sigma}^T$. Complementary information about constituent properties can be obtained from fiber pull-out and from fracture mirror measurements, conducted on the composite after testing to failure.[4,21] The spacing of the matrix cracks in the 0° bundles also relates to constituent properties.[17,22]

The interface properties, Γ_i and τ, have been obtained on CMCs by a variety of test methods. These include fiber push-in[23,24] and push-through tests,[25,26] as well as tensile microcomposite tests.[27] These methods have several disadvantages for the

routine evaluation of constituent properties suitable for stress/strain curve simulation and design purposes. The principal disadvantage is that the test methods and their interpretation are intricate, especially for the small diameter fibers used in CMCs. Moreover, they are even more difficult to apply at elevated temperatures, as well as for evaluation of interface degradation ('wear') effects that occur either upon cyclic loading or during creep. A further limitation is that these methods are applied to individual fibers, whereas average values are needed to allow for fiber-to-fiber variations in τ and Γ_i, as well as fiber misalignment, waviness, etc.

The preferred methodology would provide *averages* measured on CMCs with typical fiber variability and misalignment. It should also be applicable at elevated temperatures and after cyclic loading. Moreover, it should be straightforward experimentally and involve procedures that give τ, Γ_i and $\bar{\sigma}^T$ in an explicit, reproducible manner. The use of hysteresis measurements made at stresses above that needed to induce matrix crack, but below the saturation stress, is explored here as a methodology having this potential. For this purpose, the *basic formulae* that relate the stress/strain cycle to constituent properties are developed for stresses below $\bar{\sigma}_s$. The behavior at larger stresses has been analyzed separately.[12]

The present analysis is restricted to the case wherein the sliding resistance behind the debond is spatially uniform, as found for composites in which sliding is controlled by fiber roughness.[23,25,26] This premise represents the simplest level at which the interface properties can be characterized and used to simulate inelastic strains. However, the possible degradation of τ, caused by wear mechanism, upon cyclic loading, etc.,[28] is addressed by the methodology. Indeed, it will be shown[8,9] that the hysteresis approach allows such changes in τ to be measured. When appreciable spatial variations in τ occur along the slip length, such variations are evident from the hysteresis loops[8] . The interpretation would then have to be modified in a manner similar to that used for Coulomb friction.[18] This level of complexity would only be used

when the uniform τ approach gives unacceptable discrepancies. A straightforward methodology for experimental implementation is presented in two companion papers.[8,9]

Once the above methodology has been developed and validated, the constitutive law can be used to *simulate* stress/strain curves, in terms of constituent properties. Examples of simulated curves will be given which highlight the relative influences of the constituents.

2. PHILOSOPHY

The basic concept requires that the composite be loaded in tension, to a stress in excess of the matrix cracking stress, but below the crack saturation stress. An unload/reload cycle is then performed and the strain monitored.[29] Each hysteresis loop is analyzed to evaluate the constituent properties. If these properties change with stress, there would be associated differences in the hysteresis loop shape and width. Moreover, changes in constituent properties upon cyclic loading[28] would be evident for loop measurements made periodically during a fatigue test.

The strains that occur upon unloading and reloading measured using conventional mechanical testing machines, are typically recorded at very small stress intervals (of order 0.5 MPa) and stored on disc. The strains can be comprehensively analyzed by a number of alternative procedures, discussed in the companion papers,[8,9] to ensure that the information has high fidelity. Deviations from the formulae described below are readily discerned and may be used to test the utility of the analysis. As a further assessment, the constituent properties obtained from the hysteresis loops may be used to simulate the stress/strain curves using formulae given by He *et al.*[12] . Comparison with experimental measurements provides the ultimate test of the fidelity of the constituent properties.

The hysteresis formulae are derived by applying the same cell model previously used to predict the stress/strain curves associated with matrix cracking,[12,18] (Fig. 3) as well as for analyzing push-in[23] and microcomposite tests.[27] The variables are the crack spacing, the stress applied on the composite, the interface properties, τ and Γ_i, the misfit stress, $\bar{\sigma}^T$, and the elastic properties of the fibers, E_f, ν_f and matrix, E_m, ν_m.

One requirement for full use of the methodology is that independent information be available about the matrix crack spacing in the 0° plies. However, this information is required *only at one stress level above the matrix cracking stress.* Procedures for measuring the crack spacing are now well established for many CMCs. These procedures are based either on acetate replicas, or direct optical microscopy or upon etching followed by microscopy.[10,11,14] Such procedures are straightforward and are used in the companion papers.[8,9]

3. THE MATRIX CRACKING MODEL

Analyses by Hutchinson and Jensen (H J),[18] and by Marshall[23] provide the basic formulae. These solutions relate the material displacements to the applied stress in the presence of matrix cracks, with debonding and sliding interfaces, for various loading and unloading situations (Fig. 4). These displacements are related directly to the inelastic strains, subject to independent information about the spacing between matrix cracks. The basic situation is depicted on Figs. 3 and 4 and amplified in Appendix I. During loading, upon matrix cracking, interface debonding followed by frictional sliding are considered to occur. The debond length, ℓ_i, depends on the debond energy, Γ_i, the sliding stress, τ, and the misfit stress, $\bar{\sigma}^T$. Upon unloading, reverse sliding initiates at the crack surface, without further debonding. The reverse slip length, ℓ_u,[30] increases as the load is reduced. Upon subsequent reloading, sliding without debonding again occurs with a sliding length, ℓ_r, that increases until the original stress is regained.

The non-linear phenomena associated with matrix cracking are schematically depicted in Fig. 2. The *inelastic* strain upon loading has one term, ε^s, that arises from the matrix crack opening caused by interface debonding/sliding, and a second ε^* caused by relief of the misfit strain. The *elastic* strain, ε^e, depends upon the elastic stiffness, E^*, of the material containing matrix cracks.[12] The total strain ε at stress $\bar{\sigma}$ is thus,

$$\varepsilon = \varepsilon^* + \varepsilon^e + \varepsilon^s \tag{1}$$

where $\varepsilon^e = \bar{\sigma}/E^*$. The permanent strain at zero load, ε_0, also includes contributions from misfit relief, ε^*, and sliding , ε_0^s (Fig. 2),

$$\varepsilon_0 = \varepsilon_0^s + \varepsilon^* \tag{2}$$

The behavior during an unload/reload cycle is illustrated in Fig. 2. A small elastic deformation occurs upon initial unloading (Fig. 2). The slope E^* reflects the elastic stiffness of the composite containing matrix cracks. Additional displacements arise when reverse sliding initiates at the crack plane. This process commences when the interface shear stress, induced upon unloading, exceeds τ. The zone of reverse slip is confined within the debond zone (created upon loading), provided that the debond energy Γ_i is relatively small.[18,23] When this condition exists, the non-linear unloading displacements are shown to be quadratic, down to zero stress. Otherwise, the reverse slip zone stops at the debond tip and a change in slope occurs, with the final unloading phase being linear. One important consideration, addressed below, concerns the criterion governing this change in behavior.

The analysis of the non-linear strain is presented at two levels, for clarity. The first considers small Γ_i, such that the reverse slip process is not impeded at the end of the debond. This condition is referred to as small debond energy (SDE). The second

examines the interaction between the debond and reverse slip, at large Γ_i, designated large debond energy (LDE). A parameter that specifies whether the debond energy is large or small with regard to its effects on the unload/reload behavior has been identified as:[18,23]

$$\Sigma_i \equiv \bar{\sigma}_i/\bar{\sigma}_p = (1/c_1)\sqrt{E_m\Gamma_i/R\bar{\sigma}_p^2} - \bar{\sigma}^T/\bar{\sigma}_p \quad (3)$$

where R is the fiber radius, E_m is Young's modulus for the matrix, $\bar{\sigma}_p$ is the peak stress reached before unloading and c_i are coefficients defined by H J[18] (Table II).‡ The stress $\bar{\sigma}_i$ is the 'debond' stress, which corresponds with the applied stress at which a debond can be initiated. Note that the misfit stress $\bar{\sigma}^T$ is related to the misfit strain, ε^T, by,

$$\bar{\sigma}^T = (c_2/c_1)E_m\varepsilon^T \quad (4)$$

This stress is also related to the residual stresses, by means of the formulae summarized in Table III. The debond stress, $\bar{\sigma}_i$, can be expressed in terms of the misfit stress by

$$\bar{\sigma}_i = \bar{\sigma}_D - \bar{\sigma}^T \quad (5)$$

where σ_D now refers to the debond stress at zero misfit stress

$$\bar{\sigma}_D = (1/c_1)\sqrt{E_m\Gamma_i/R}$$

Consequently, Eqn. (3) has the useful non-dimensional form,

‡ Note that, in HJ terminology, type II boundary conditions apply.[18]

$$\Sigma_i = \Sigma_D - \Sigma^T \tag{6}$$

It has been demonstrated[23] that reverse slip upon unloading does not reach the debond tip whenever $\Sigma_i \leq 1/2$, or when

$$\Gamma_i \leq \frac{c_1^2 R \bar{\sigma}_p^2}{2E_m}\left[1+2\Sigma^T\right] \tag{7}$$

This condition specifies SDE. Otherwise, LDE obtains and reverse slip arrests at the debond tip, when the stress upon unloading reaches a transition value σ_{tu} given by

$$\bar{\sigma}_{tu} = 2\bar{\sigma}_i - \bar{\sigma}_p \tag{8a}$$

Symmetrically, upon reloading, sliding again stops at the debond, at a stress

$$\bar{\sigma}_{tr} = 2\left(\bar{\sigma}_p - \bar{\sigma}_i\right) \tag{8b}$$

Based on Σ_i as a parameter, these sliding behaviors can be represented by a mechanism map (Fig. 5). At stresses below $\bar{\sigma}_{mc}$, the material is elastic. The relationship between $\bar{\sigma}_i$ and $\bar{\sigma}_{mc}$, analyzed elsewhere,[31] thus represents a lower bound for the onset of inelastic deformation. At higher stresses, inelastic strains develop, because of debonding and sliding. In this range, the hysteresis and the permanent strain are dependent on Σ_i. SDE and LDE are separated by $\Sigma_i = 1/2$. The consequence of reverse slip interacting with the debond, in LDE materials, is evident in the hysteresis loop (Fig. 6), as described below.

In the following analysis the *inelastic* strains caused by interface debonding and sliding that result in *hysteresis* and a *permanent* strain are considered. SDE and LDE are

analyzed separately. Then, the additional contributions to the strain caused by the increase in compliance and by misfit relief are addressed. Finally, some special issues concerned with the crack density are examined.

4. SMALL DEBOND ENERGY (SDE)

4.1 Crack Opening Displacements

The previous analyses of interface inelastic deformation have emphasized crack opening displacements.[18,23] To make connections with this literature, the present analysis also commences with these basic results. The opening displacement of a crack upon *unloading*, u_u, at small Γ_i is given by[23]

$$u_u = u_p - \left[\frac{(b_2+b_3)(1-a_1 f)^2 R}{4\tau_o E_m f^2}\right]\left(\bar{\sigma}_p - \bar{\sigma}_u\right)^2 \tag{9a}$$

with[10,23]

$$u_p = \left[\frac{(b_2+b_3)(1-a_1 f)^2 R}{2\tau_o E_m f^2}\right]\left[\left(\bar{\sigma}_p + \sigma^T\right)^2 - \sigma_D{}^2\right] \tag{9b}$$

where f is the fiber volume fraction. Convenient non-dimensional forms of Eqn. (9) are

$$U_u \equiv u_u/R = U_p - \mathcal{U}\left[1-\Sigma_u\right] \tag{10a}$$

and

$$U_p \equiv u_p/R = 2\mathcal{U}(1-\Sigma_i)\left[2\Sigma^T + 1 + \Sigma_i\right] \tag{10b}$$

where $\mathcal{U}$ is a non-dimensional parameter, referred to as the 'Crack Opening Index,'

$$\mathcal{U} = \left[\frac{(b_2+b_3)(1-a_1 f)^2\,\bar{\sigma}_p^2}{4\tau_o E_m f^2}\right]$$

$$\equiv \frac{c_1^2}{\tau_o E_m}\bar{\sigma}_p^2$$

such that,

$$U_u = \mathcal{U}\left[4(1-\Sigma_i)\Sigma^T + 1 - 2\Sigma_i^2 + 2\Sigma_u - \Sigma_u^2\right] \tag{10c}$$

The corresponding result for reloading (the subscript r refering to the current value during the reloading phase) is,

$$U_r \equiv u_r/R = u_o + \mathcal{U}\Sigma_r^2 \tag{11a}$$

with

$$U_0 \equiv u_0/R = \mathcal{U}\left[4(1-\Sigma_i)\Sigma^T + 1 - 2\Sigma_i^2\right] \tag{11b}$$

such that

$$U_r = \mathcal{U}\left[4(1-\Sigma_i)\Sigma^T + 1 - 2\Sigma_i^2 + \Sigma_r^2\right] \tag{11c}$$

Here, u_o is the residual crack opening at zero load. Hysteresis loops simulated using these relationships are presented on Fig. 4.

The preceding results can be re-expressed in terms of alternative displacement quantities. When the tensile displacement, Δ, along a gauge section, length L_o, is measured and only one matrix crack exists in that section, the displacement consists of three terms,

$$\Delta = \Delta^s + \Delta^e + \Delta^* \tag{12}$$

The term, Δ^S, represents the *extra displacement* caused by the existence of the crack, which has induced debonding and sliding. The other terms, Δ^e and Δ^* are associated with the elastic stretching of the fiber and matrix. The extra displacement Δ^S is related to the crack opening displacement, u^s by,

$$\Delta^s = \left[\frac{b_2}{b_2 + b_3}\right] u^s \tag{13}$$

When the gauge section contains *multiple cracks*, the displacement Δ^S is related to the non-linear strain ε^s, provided that the peak stress $\bar{\sigma}_p$ is below the saturation value, $\bar{\sigma}_s$. Then,

$$\Delta^s = \varepsilon^s . \bar{d} \tag{14}$$

where $\bar{d}$ is the mean crack spacing.

4.2 The Strains

Important relationships exist between the total strains and the constituent properties. These are obtained using Eqns. (1), (10), (11), (13) and (14). Upon unloading and reloading the strains are described by quadratic, symmetric curves (Fig. 6a) such that

$$\begin{aligned} \varepsilon_u &= \varepsilon_u^s + \varepsilon_u^e + \varepsilon^* \\ &\equiv \mathcal{H}\left[4(1-\Sigma_i)\Sigma^T + 1 - 2\Sigma_i^2 + 2\Sigma_u - \Sigma_u^2\right] + \sigma_u/E^* + \varepsilon^* \end{aligned} \tag{15a}$$

and

$$\begin{aligned} \varepsilon_r &= \varepsilon_r^s + \varepsilon_r^e + \varepsilon^* \\ &\equiv \mathcal{H}\left[4(1-\Sigma_i)\Sigma^T + 1 - 2\Sigma_i^2 + \Sigma_r^2\right] + \sigma_r/E^* + \varepsilon^* \end{aligned} \tag{15b}$$

where $\mathcal{H}$ is a non-dimensional parameter for the material, designated the 'Inelastic Strain Index,'

$$\mathcal{H} = b_2(1-a_1 f)^2 R\bar{\sigma}_p^2/4\bar{d}\tau_o E_m f^2 \tag{16a}$$

such that

$$R/\bar{d} = \tau_o\left[\mathcal{H} E_m/\bar{\sigma}_p^2\right]\chi \tag{16b}$$

where

$$\chi = (4/b_2)\left(f/(1-a_1 f)\right)^2 \tag{16c}$$

It will be shown that $\mathcal{H}$ is the key index governing the contribution to the inelastic strain from interface sliding. However, since $\mathcal{H}$ depends explicitly on the applied stress, it is sometimes more insightful to define an alternative 'Inelastic Strain Parameter,' $\mathcal{L}$ that depends only on material properties, where

$$\mathcal{L} = \mathcal{H}/\bar{\sigma}_p^2 \tag{16d}$$

Clearly, $\mathcal{L}$ has dimensions (stress)$^{-2}$.

The first two terms in Eqn. (15), ε_u^s and ε_r^s, are the sliding and debonding contributions to the total strain. Complete analysis of the hysteresis loops can be conducted from these formulae. Both unloading and reloading commence with the same slope, E^*. Moreover, both have a minimum slope, E_p (Fig. 6a), given by

$$1/E_p = 1/E^* + 2\mathcal{H}/\bar{\sigma}_p \tag{17}$$

The permanent strain is now obtained, using Eqn. (15a), as $\bar{\sigma}_u \to 0$, giving

$$\begin{aligned} \varepsilon_0 &= \varepsilon_0^s + \varepsilon^* \\ &\equiv \mathcal{H}\left[4(1-\Sigma_i)\Sigma^T + 1 - 2\Sigma_i^2\right] + \varepsilon^* \end{aligned} \tag{18}$$

with ε_0^s being the debonding and slid g contribution. The corresponding peak strain is‡

‡ These results also apply for LDE.

$$\varepsilon_p = \varepsilon_p^s + \varepsilon_p^e + \varepsilon^* \equiv 2\mathcal{H}(1-\Sigma_i)\left[1+\Sigma_i+2\Sigma^T\right] + \bar{\sigma}_p/E^* + \varepsilon^* \tag{19}$$

Note that the secant modulus, E_s, is related to these strains by

$$1/E_s = \varepsilon_p / \bar{\sigma}_p \equiv 1/E^* + \left(\varepsilon^s + \varepsilon^*\right)/\bar{\sigma}_p \tag{20}$$

Another modulus is, in some cases, more convenient for data analysis, designated the *hysteresis modulus*, $\bar{E}$. This modulus is the slope between the bottom and the top of the hysteresis loop (Fig. 2). It can be expressed as a function of the difference between the permanent strain and the peak strain

$$\bar{E} = \bar{\sigma}_p/\left(\varepsilon_p - \varepsilon_o\right) \tag{21a}$$

Then, with Eqns. (18), (19) and (21a)

$$1/\bar{E} \equiv 1/E^* + \mathcal{H}/\bar{\sigma}_p \tag{21b}$$

These SDE results reduce to the approximate results, derived previously,[32] when various contributions to the strain are *neglected*: the Poisson effect, the misfit relief effect and the compliance effect. Generally, these effects are important and must be included in order to either use inelastic strain information to evaluate constituent properties or to simulate stress/strain curves.

Two strain differences, $\Delta\varepsilon_o$ and $\Delta\varepsilon_p$, defined on Fig. 6a, are also convenient for data analysis. These are given by,

$$\Delta\varepsilon_o = \varepsilon_o - \left(\varepsilon_p - \bar{\sigma}_p / E_p\right) \tag{22a}$$

and

$$\Delta\varepsilon_p = \left(\varepsilon_p - \bar{\sigma}_p / E^*\right) - \varepsilon_o \tag{22b}$$

Then, upon introducing the preceding expressions for the strains, it is found that (for SDE) both strain differences have the same magnitude,

$$\Delta\varepsilon_o = \Delta\varepsilon_p \equiv \mathcal{H} \tag{22c}$$

This equivalence contrasts with LDE, elaborated below.

5. LARGE DEBOND ENERGY (LDE)

When the debond energy is large, interaction of the reverse slip zone with the end of the debond results in a hysteresis curve with two unload/reload regimes (Fig. 6b). Initial sliding upon unloading occurs subject to a continuously increasing reverse slip length (as for SDE, Eqn. 15a), such that

$$\begin{aligned} \varepsilon_u &= \varepsilon_u^s + \varepsilon_u^e + \varepsilon^* \\ &\equiv \mathcal{H}\left[4\left(1-\Sigma_i\right)\Sigma^T + 1 - 2\Sigma_i^2 + 2\Sigma_u - \Sigma_u^2\right] + \sigma_u / E^* + \varepsilon^* \end{aligned} \tag{23}$$

This behavior continues until the reverse slip zone reaches the end of the debond zone. This event occurs at a transition stress,

$$\Sigma_{tu} = 2\Sigma_i - 1 \tag{24}$$

At smaller unloading stresses, the unloading occurs at *fixed slip length* and is thus linear, as given by:

$$\begin{aligned} \varepsilon_u &= \varepsilon_u^s + \varepsilon_u^e + \varepsilon^* \\ &\equiv 2\mathcal{H}(1-\Sigma_i)\left[2\Sigma^T + (1-\Sigma_i) + 2\Sigma_u\right] + \sigma_u/E^* + \varepsilon^* \end{aligned} \tag{25}$$

The behavior on reloading mirrors that on unloading (Fig. 6b). The initial segment is non-linear

$$\begin{aligned} \varepsilon_r &= \varepsilon_r^s + \varepsilon_r^e + \varepsilon^* \\ &\equiv \mathcal{H}\left[4(1-\Sigma_i)\Sigma^T + 2(1-\Sigma_i)^2 + \Sigma_r^2\right] + \sigma_r/E^* + \varepsilon^* \end{aligned} \tag{26}$$

The non-linear behavior obtains at stresses up to

$$\Sigma_{tr} = 2(1-\Sigma_i) \tag{27}$$

At larger stresses, linearity resumes, such that

$$\begin{aligned} \varepsilon_r &= \varepsilon_r^s + \varepsilon_r^e + \varepsilon^* \\ &\equiv 2\mathcal{H}(1-\Sigma_i)\left[2\Sigma^T - (1-\Sigma_i) + 2\Sigma_r\right] + \sigma_r/E^* + \varepsilon^* \end{aligned} \tag{28}$$

The tangent modulus when unloading and reloading begin is again E^* (as for SDE). However the minimum slope, E_p, is now

$$1/E_p = 1/E^* + 4\mathcal{H}(1-\Sigma_i)/\bar{\sigma}_p \tag{29}$$

The corresponding relationship for the permanent strain is

$$\begin{aligned} \varepsilon_0 &= \varepsilon_0' + \varepsilon^* \\ &\equiv 2\mathcal{H}(1-\Sigma_i)\left[2\Sigma^T + 1 - \Sigma_i\right] + \varepsilon^* \end{aligned} \tag{30}$$

The peak strain is necessarily the same as that for SDE (Eqn. 19). Consequently, the secant modulus is also the same (Eqn. 20).

However, the hysteresis modulus now involves the debond energy and is given by

$$1/\bar{E} = 1/E^* + 4\mathcal{H}\Sigma_i(1-\Sigma_i)/\bar{\sigma}_p \tag{31}$$

The strain differences $\Delta\varepsilon_0$ and $\Delta\varepsilon_p$ (Fig. 6b) are given by

$$\Delta\varepsilon_0 = 4\mathcal{H}(1-\Sigma_i)^2 \tag{32}$$

and

$$\Delta\varepsilon_p = 4\mathcal{H}\Sigma_i(1-\Sigma_i) \tag{33}$$

The relationships between these strain differences are presented on Fig. 7.

6. THE HYSTERESIS LOOP

Analysis of the hysteresis loop based on the total strain formulae indicates the existence of three regimes. For SDE, Eqn. (15) gives the loop width $\delta\varepsilon$ at fixed strain ($\bar{\sigma} = \bar{\sigma}_u = \bar{\sigma}_r$) as

$$\delta\varepsilon/\mathcal{H} = 2\Sigma(1-\Sigma) \tag{34}$$

The maximum loop width occurs at $\Sigma = 1/2$, with

$$\delta\varepsilon_{max} = \mathcal{H}/2 \tag{35}$$

For LDE, the loop width is *reduced*. In the range, $1/2 \le \Sigma_i < 3/4$.

$$\delta\varepsilon/\mathcal{H} = \begin{cases} 4(1-\Sigma_i)\Sigma - \Sigma^2 & [0 \le \Sigma \le 2\Sigma_i - 1] \\ -(1-2\Sigma_i)^2 + 2\Sigma - 2\Sigma^2 & [(2\Sigma_i - 1) \le \Sigma \le 2(1-\Sigma_i)] \\ 3 - 4\Sigma_i + 2(2\Sigma_i - 1)\Sigma - \Sigma^2 & [2(1-\Sigma_i) \le \Sigma \le 1] \end{cases} \tag{36}$$

such that the maximum loop width still occurs at $\Sigma = 1/2$, with

$$\delta\varepsilon_{½} = \mathcal{H}\left[1/2 - (1-2\Sigma_i)^2\right] \tag{37}$$

When $3/4 \le \Sigma_i \le 1$,

$$\delta\varepsilon/\mathcal{H} = \begin{cases} 4(1-\Sigma_i)\Sigma - \Sigma^2 & [0 \le \Sigma \le 2(1-\Sigma_i)] \\ 4(1-\Sigma_i)^2 & [2(1-\Sigma_i) \le \Sigma \le 2\Sigma_i - 1] \\ 3 - 4\Sigma_i + 2(2\Sigma_i - 1)\Sigma + \Sigma^2 & [2\Sigma_i - 1 \le \Sigma \le 1] \end{cases} \tag{38}$$

In this case, the loop has uniform width over a range in stress, $2(1-\Sigma_i) \le \Sigma \le (2\Sigma_i - 1)$. The width in this range is

$$\delta\varepsilon_{max}/\mathcal{H} = 4(1-\Sigma_i)^2 \tag{39}$$

The overall trends in $\delta\varepsilon$ and in the maximum loop width are presented in Fig. 7.

7. ELASTIC AND MISFIT STRAINS

Two important effects arise without interface sliding, reflected in the magnitudes of E^* and ε^*. These two quantities are connected by the relationship,[18]

$$\varepsilon^* = \varepsilon^T E_m(E/E^* - 1) f a_2/E(1 - a_1 f) \tag{40}$$

The elastic modulus, E^*, has a dependence on crack spacing, given by[12]

$$E/E^* - 1 = (R/d)\mathcal{B} \tag{41}$$

where the function $\mathcal{B}$ depends on f and E_f/E_m. Calculated values are plotted on Fig. 8. Moreover, the misfit relaxation strain, ε^*, is related to E^* and σ^T, as shown by the construction in Fig. 2b,

$$\varepsilon^* = \left[1/E^* - 1/E\right]\bar{\sigma}^T \tag{42}$$

8. THE CRACK SPACING

The interpretation of experimental data is rigorous when independent information is available concerning the matrix crack spacing $\bar{d}$. It is relatively straightforward to obtain $\bar{d}$ at the completion of a test, but it is difficult to measure the stress dependence. One approach is proposed here. Before failure, the crack spacing usually reaches (or closely approaches) the saturation value $\bar{d}_s$, at stress $\bar{\sigma}_s$ (Fig. 2a). This value can either be measured directly[10,11,14] (Fig. 9a) or it can be *estimated* from analysis of overlapping slip zones between neighboring cracks (Fig. 9b).[17,22] The latter suggests the scaling, $\bar{d}_s \sim \tau_o^{-2/3}$. Since $\bar{d}$ varies from 0 at the onset of matrix cracking to $\bar{d}_s$ at the saturation stress, $\bar{\sigma}_s$ (Fig. 2a); then the variation can be approximated by[7]

$$\bar{d}/\bar{d}_s \approx \frac{\left[\bar{\sigma}_s/\sigma_{mc} - 1\right]}{\left[\bar{\sigma}/\sigma_{mc} - 1\right]} \tag{43}$$

This linear interpolation between $\bar{\sigma}_s$ and $\bar{\sigma}_{mc}$ is compatible with existing experimental measurements[7] (Fig. 9). The 'Inelastic Strain Index' thus becomes;

$$\mathcal{H} \approx \frac{b_2(1 - a_1 f)^2 \bar{\sigma}_p^2 R\left[\bar{\sigma}_p/\sigma_{mc} - 1\right]}{4\tau_o E_m f^2 \bar{d}_s \left[\bar{\sigma}_s/\sigma_{mc} - 1\right]} \tag{44}$$

Consequently, it is only necessary to measure $\bar{d}_s$ (or $\bar{d}$ at one value of stress, $\bar{\sigma}_p$) in order to evaluate τ_o from the hysteresis measurements (Fig. 10).

9. SOME USEFUL INTERRELATIONSHIPS

The above results can be combined to form some additional relationships that facilitate data analysis. For LDE, the construction on Fig. 6b defines a stress, σ_0^T, which is related to the misfit stress by,

$$\bar{\sigma}^T = \left\{\Delta\varepsilon_o/2\left[1/E_0^* - 1/E\right]\right\} - \bar{\sigma}_0^T \tag{45}$$

Also, for LDE, there is a relationship between Σ_i and the strain differentials, given by

$$\Sigma_i = \Delta\varepsilon_p/\left[\Delta\varepsilon_0 + \Delta\varepsilon_p\right] \tag{46}$$

Also, Σ_i is related to the transition stresses Σ_{tu} and Σ_{tr} (Eqns. 24 and 27) at which slip is arrested at the debond.

10. SIMULATIONS

The experimental measurements described in the companion papers[8,9] and in prior work[7,10,11,14,27] give typical ranges for the constituent properties: τ_0 = 20–200 MPa, Γ_i = 0–5 Jm^{-2}, $\bar{\sigma}^T$ = 0–200 MPa. It is of interest to simulate stress/strain curves encompassing this range. Such simulations provide insight about the sensitivity of the inelastic strain to constituent properties. For this purpose, it is noted that $\bar{\sigma}_{mc}$, $\bar{\sigma}_s$ and $\bar{d}_s$ are also related to constituent properties.[5,7,10,21]

The results of some simulations are presented on Fig. 11. For these calculations, σ_{mc}^o and $\bar{\sigma}^T$ were fixed at 250 MPa and 100 MPa, respectively. The saturation stress $\bar{\sigma}_s$ was chosen to cover a typical range (from $1.5\bar{\sigma}_{mc}$ to $2\,\bar{\sigma}_{mc}$). The value of $\mathcal{B}$ represents a CMC with a fiber volume fraction, f = 0.5, and a modulus ratio E_f/E_m = 1 (Fig. 8). It

is apparent (Fig. 11) that both τ_o and Γ_i have a *substantial influence on the tensile stress/strain behavior*. As either of these parameters increase, the inelastic strains occur at higher stresses.

11. CONCLUDING REMARKS

The present analysis provides expressions that relate various characteristics of the inelastic strain measured on unidirectional CMCs to constituent properties. The results allow inelastic strain measurements made at stresses below the saturation stress, $\bar{\sigma}_s$, to be used to evaluate the constituent properties on *actual composites*. Moreover, with the constituent properties known, stress/strain curves may be *simulated* at stresses up to $\bar{\sigma}_s$. The analysis of the hysteresis loops allows separate evaluation of four quantities that govern the inelastic strain: E^*, $\mathcal{H}$, Σ_i and Σ^T. The first term E^*, which represents the effect of matrix cracks on the elastic modulus, can be readily determined. The second quantity $\mathcal{H}$, which is the non-dimensional parameter governing the contribution to the inelastic strain from interface slipping, can also be determined with good fidelity. The third term Σ_i, represents the resistance to interface debonding, that inhibits inelastic strain by interface debonding. When it is relatively large and has an important influence on the inelastic strain, it can be readily determined. The last term Σ^T is a residual stress parameters which can be obtained quite accurately when Σ_i is large. The details are elaborated in the companion paper.[8,9]

Information about the crack spacing $\bar{d}$ and how it relates to the matrix cracking stress, $\bar{\sigma}_{mc}$, as well as the saturation stress, $\bar{\sigma}_s$, is needed to evaluate τ, but is not required to determine either $\bar{\sigma}_i$ or $\bar{\sigma}^T$. Most critical is the accuracy with which $\bar{\sigma}_{mc}$, $\bar{\sigma}_s$ and $\bar{d}_s$ can be specified, because interpolation between these limits can be achieved in

several ways (such as Eqn. 43), with satisfactory precision.* Then, the crack spacing need only be measured at one value of the stress between $\bar{\sigma}_{mc}$ and $\bar{\sigma}_s$. In addition, models that relate $\bar{\sigma}_{mc}$, $\bar{\sigma}_s$ and $\bar{d}_s$ to constituent properties exist,[12,15-20] which are consistent with experimental measurements.[10-12] In principle, these models may be used to predict these parameters, but the matrix fracture energy, Γ_m, needs to be known. Methods for measuring Γ_m on actual composites are not well-established. Moreover, it is not generally acceptable to use values for the monolithic matrix, because of differing microstructures. Nevertheless, this does not represent a difficulty when the matrix is *fixed* and only the fibers or interfaces are changed, because the models then give the exact scaling.

One practical problem arises in some CMCs when the matrix crack surfaces come in contact upon unloading. When this behavior occurs, the unloading compliance increases as sketched in Fig. 12. One method for addressing this problem uses partial unloading, such that the minimum stress is above the closure stress (Appendix II).

* The designation of $\bar{\sigma}_{mc}$ and $\bar{\sigma}_s$ from the actual hysteresis data, because of the approximate linearity of E^* and $\mathcal{H}/\sigma_p^2$ with stress, $\bar{\sigma}_p$, provides an important simplification.

APPENDIX I

Synopsis of Sliding and Debonding Characteristics

To facilitate an understanding of the basic formulae presented in the text, schematics of the sliding characteristics are presented, with some relevant relationships. The emphasis is on the axial stresses in the fibers. Upon initial loading (Fig. A1a), there is a jump in the stress at the debond tip, located at ℓ_i, related to the debond energy, by[18]

$$\gamma \equiv \sigma_f^- - \sigma_f^+ = \frac{(1 - a_1 f)}{f c_1} \sqrt{\frac{E_m \Gamma_i}{R}} \qquad \text{(A1)}$$

For SDE material, reverse slip changes the stresses in the manner indicated on Fig. A1b, with ℓ_u and ℓ_r being the slip lengths for unloading and reloading, respectively. For LDE materials, there are additional considerations (Fig. A2). Upon unloading, when $\bar{\sigma}_u > 2\bar{\sigma}_i - 1$, the situation resembles that for SDE: case ① on Fig. A2a. However, when $\bar{\sigma}_u < 2\,\bar{\sigma}_i - 1$, reverse slip stops at the debond: case ② on Fig. A2a. There is an analogous situation upon reloading wherein reverse slip reaches the debond at $\bar{\sigma}_r = 2\,(\bar{\sigma}_p - \bar{\sigma}_i)$ (Fig. A2b).

APPENDIX II

Hysteresis With Partial Unloading

When a minimum stress $\bar{\sigma}_{min} > \bar{\sigma}_{c\ell}$ is used for hysteresis measurements, there are two different reloading regimes governed by the length of the reverse slip zone compared with the debond zone.‡ When $\bar{\sigma}_{min}$ is relatively large, such that the reverse slip zone is small, the reload strain is fully parabolic and given by ($\bar{\sigma}_{min} \geq 2\bar{\sigma}_i - \bar{\sigma}_p$)

$$\varepsilon_r = \mathcal{H}\left[4(1-\Sigma_i)\Sigma^T + 1 - 2\Sigma_i^2 + 2\Sigma_{min} - 2\Sigma_{min}\Sigma_r + \Sigma_r^2\right] + \bar{\sigma}_u/E^* + \varepsilon^* \qquad \text{(B1)}$$

where $\Sigma_{min} = \bar{\sigma}_{min}/\bar{\sigma}_p$. The hysteresis loop width can also be determined as

$$\delta\varepsilon = 2\mathcal{H}\left[1-\Sigma\right]\left[\Sigma - \Sigma_{min}\right] \qquad \text{(B2)}$$

with a maximum value

$$\delta\varepsilon_{max} = \left(\mathcal{H}/2\right)\left(1-\Sigma_{min}\right)^2 \qquad \text{(B3)}$$

at

28

$$\Sigma = \left(1+\Sigma_{min}\right)/2$$

‡ The unloading strains are unaffected.

At larger minimum stresses, $\bar{\sigma}_{c\ell} \le \bar{\sigma}_{min} \le 2\bar{\sigma}_i - \bar{\sigma}_p$, the hysteresis loop has both linear and parabolic portions. The inelastic strains are given by $[\bar{\sigma}_{min} \le \bar{\sigma}_r \le 2\bar{\sigma}_p - 2\bar{\sigma}_i + \sigma_{min}]$

$$\varepsilon_r = 2\mathcal{H}(1-\Sigma_i)\left[2\Sigma^T + (1-\Sigma_i) + 2\Sigma_{min}\right] + \mathcal{H}\left[\Sigma_r - \Sigma_{min}\right]^2 + \bar{\sigma}_r/E^* + \varepsilon^*$$

and $[2\bar{\sigma}_p - 2\bar{\sigma}_i + \bar{\sigma}_{min} < \bar{\sigma}_r < \bar{\sigma}_p]$

$$\varepsilon_r = 2\mathcal{H}(1-\Sigma_i)\left[2\Sigma^T - (1-\Sigma_i) + 2\Sigma_r\right] + \bar{\sigma}_r/E^* + \varepsilon^*$$

TABLE I

Constituent Properties of CMCs and Methods of Measurement

CONSTITUENT PROPERTY	MEASUREMENT METHODS	TYPICAL RANGE
Sliding Stress, τ (MPa)	• Push-Out Force • Pull-Out Length, $\bar{h}$ • Saturation Crack Spacing, $\bar{d}_s$ • 'Inelastic Strain Index,' $\mathcal{H}$ or $\mathcal{L}$	1–200
Characteristic Strength, S_c (GPa)	• Fracture Mirrors • Pull-Out Length, $\bar{h}$	1.2–3.0
Misfit Strain, Ω	• Bilayer Distortion • Permanent Strain, ε_o • Residual Crack Opening	0–2.10^{-3}
Matrix Fracture Energy, Γ_m (Jm^{-2})	• Monolithic Material • Saturation Crack Spacing, $\bar{d}_s$ • Matrix Cracking Stress, $\bar{\sigma}_{mc}$	5–50
Debond Energy, Γ_i (Jm^{-2})	• Permanent Strain, ε_o • Residual Crack Opening • Transition Stresses (LDE)	0–5

TABLE II

Summary of Constants (Type II Boundary Conditions)[18]

$$a_1 = E_f/E$$

$$a_2 = \frac{(1-f)E_f\left[1+E_f/E\right]}{\left[E_f+(1-2\nu)E\right]}$$

$$b_2 = \frac{(1+\nu)E_m\left\{2(1-\nu)^2E_f+(1-2\nu)\left[1-\nu+f(1+\nu)\right](E_m-E_f)\right\}}{(1-\nu)E_f\left[(1+\nu)E^*+(1-\nu)E_m\right]}$$

$$b_3 = \frac{f(1+\nu)\left\{(1-f)(1+\nu)(1-2\nu)(E_f-E_m)+2(1-\nu)^2E_m\right\}}{(1-\nu)(1-f)\left[(1+\nu)E^*+(1-\nu)E_m\right]}$$

$$c_1 = \frac{(1-fa_1)(b_2+b_3)^{1/2}}{2f} \qquad c_2 = \frac{a_2(b_2+b_3)^{1/2}}{2}$$

$$c_3 = \frac{E}{E_m}$$

$$c_1/c_2 = \frac{1-a_1f}{a_2f}$$

$$E^* = (1-f)E_f+fE_m$$

TABLE III

Relationships Between Residual Stresses and Misfit Stress‡

Axial Stress in Fiber, $q_f = -(a_2 c_1 / c_2)\sigma^T$

Axial Stress in Matrix, $q_m = (1/c_3)\sigma^T$

Stress Normal to Interface, $p = -(a_4 c_1 / c_2)\sigma^T$

---

‡ a_i and c_i are defined in reference (18).

REFERENCES

[1] J.J. Brennan and K.M. Prewo, "Silicon Carbide Fiber-Reinforced Glass-Ceramic Matrix Composites Exhibiting High Strength and Toughness," *J. Mater. Sci.*, **17** (1982) 2371–83.

[2] S. Mall, D.E. Bullock and J.J. Pernot, *Tensile Fracture of Fiber Resistance Ceramic Composites With Hole*, to be published.

[3] C. Cady, T.J. Mackin and A.G. Evans, "SiC/CAS: A Notch Insensitivite Ceramic Matrix Composite," *J. Am. Ceram. Soc.*, in press.

[4] F.E. Heredia, S.M. Spearing, P. Mosher, A.G. Evans and W.A. Curtin, "Mechanical Properties of Continuous Fiber-Reinforced Carbon Matrix Composites and Relationships to Constituent Properties," *J. Am. Ceram. Soc.*, **75** (1992) 3017–25.

[5] G. Bao and Z. Suo, "Remarks on Crack Bridging," *Appl. Mech. Rev.*, **54** (1992) 355.

[6] A.G. Evans and F.W. Zok, "Cracking and Fatigue of Fiber-Reinforced Metal and Ceramic Matrix Composites," *Topics In Fracture and Fatigue* (ed. A.S. Argon) 1992, pp. 271–308.

[7] A.G. Evans, J.-M. Domergue and E. Vagaggini, "A Methodology for Relating the Tensile Constitutive Behavior of Ceramic Matrix Composites to Constituent Properties," J. *Am. Ceram. Soc.*, in press.

[8] J.-M. Domergue, E. Vagaggini, A.G. Evans and J.M. Parenteau, "Relationships Between Hysteresis Measurements and the Constituent Properties of Ceramic Matrix Composites. II: Experimental Studies on Unidirectional Materials," *J. Am. Ceram. Soc.*, submitted.

[9] J.-M. Domergue, F.E. Heredia, A.G. Evans, "Relationships Between Hysteresis Measurements and the Constituent Properties of Ceramic Matrix Composites. III: Application to 2-D CMCs" *J. Am. Ceram. Soc.*, to be submitted.

[10] D. Beyerle, S.M. Spearing, F.W. Zok and A.G. Evans, "Damage and Failure in Unidirectional Ceramic Matrix Composites, *J. Am. Ceram. Soc.*, **75** (1992) 2719–25.

[11] D. Beyerle, S.M. Spearing and A.G. Evans, "Damage Mechanisms and the Mechanical Properties of a Laminated 0/90 Ceramic/Matrix Composite," *J. Am. Ceram. Soc.*, **75** (1992) 3321–30.

[12] M.Y. He, B.-X. Wu, A.G. Evans and J.W. Hutchinson, "Inelastic Strains Caused by Matrix Cracking in Fiber-Reinforced Composites," *Mech. of Mtls.*, to be published.

[13] K.S. Turner, J.S. Speck and A.G. Evans, "The Mechanisms of Deformation and Failure in Carbon Matrix Composites Subject to Tensile and Shear Loading," *J. Am. Ceram. Soc.*, in press.

[14] L. Guillaumat, Ph.D. Thesis, Laboratoire des Composites Thermostructuraux,' Domaine Universitaire, Bordeaux.

[15] J. Aveston, G. Cooper and A Kelly, *The Properties of Fiber Composites* (1971) NPL Conference Proceedings, pp. 15–21.

[16] D.B. Marshall, B.N. Cox and A.G. Evans, "The Mechanics of Matrix Cracking in Brittle Matrix Fiber Composites," *Acta Metall.*, **33** (1985) 2013.

[17] F.W. Zok and S.M. Spearing, "Matrix Crack Spacing in Brittle Matrix Composites," *Acta Metall. Mater.*, **40** (1992) 2033.

[18] J.W. Hutchinson and H. Jensen, "Models of Fiber Debonding and Pull-Out in Brittle Composites with Friction," *Mech. of Mtls.*, **9**, (1990) 139–163.

[19] C. Xia, R.R. Carr and J.W. Hutchinson, "Transverse Cracking in Fiber-Reinforced Brittle Matrix, Cross-Ply Laminates," Acta *Metall. Mater.*,**41** (1993) 2365.

[20] C. Xia and J.W. Hutchinson, "Micromechanics of the Tensile Behavior of Laminated Fiber-Reinforced Ceramic Matrix Composites," *Intl. Jnl. Solids Structures*, in press.

[21] W.A. Curtin, "Theory of Mechanical Properties of Ceramic Matrix Composites," *J. Am. Ceram. Soc.*, **74** (1991) 2837–45.

[22] S.M. Spearing and F.W. Zok, " Stochastic Aspects of Matrix Cracking in Brittle Matrix Composites,"*J. Eng. Mat. Tech.*, **115** (1993) 314.

[23] D.B. Marshall, "Analysis of Fiber Debonding and Sliding Experiments in Brittle Matrix Composites," *Acta Metall. Mater.*, **40** (1992) 427–41.

[24] D.B. Marshall and W. Oliver, "Measurements of Interfacial Mechanical Properties in Fiber Reinforced Ceramic Composites," *J. Am. Ceram. Soc.*, **70** (1987) 542-48.

[25] P.D. Jero, R.J. Kerans and T.A. Parathasarthy, "Effect of Interfacial Roughness on the Frictional Stress Measured Using Pushout Tests," *J. Am. Ceram. Soc.*, **74** (1991) 2793.

[26] T.J. Mackin, P. Warren and A.G. Evans, "The Effects of Fiber Roughness on Interface Sliding Properties," Acta *Metall. Mater.*, **40**, (1992) 1251–57.

[27] R. Rebaillat, J. Lamon and A.G. Evans, "A Microcomposite Test to Measure the Interface Properties of Ceramic Matrix Composites," *J. Am. Ceram. Soc.*, in press.

[28] D. Rouby and P. Reynaud, *High Temperature Ceramic Matrix Composites* (Ed. R. Naslain *et al.*) Woodhead Cambridge (1993) pp. 499–513.

[29] T.J. Kotil, J.W. Holmes and M. Cominou, "Origin of Hysteresis Observed During Fatigue of Ceramic Matrix Composites," *J. Am. Ceram. Soc.*, **73** (1990) 1879.

[30] R. M. McMeeking and A.G. Evans, "Matrix Fatigue Cracking in Composites," *Mech. of Mtls.*, 2 (1990) 217.

[31] B. Budiansky, J.W. Hutchinson, J.M. Domergue and A.G. Evans, "Effect of Debond Energy on the Matrix Cracking Stress of Ceramic Matrix Composites," to be published.

[32] A.W. Pryce and P. Smith, "Modelling the Stress/Strain Behavior of Unidirectional Ceramic Matrix Composite Laminates," *J. Mater. Sci.*, 27 (1992) 2695–2704.

[33] S. Baste, R.E. Guerjouma and B. Audoin, "Effect of Microcracking on the Macroscopic Behaviour of Ceramic Matrix Composites: Ultrasonic Evaluation of Anisotropic Damage," *Mech. of Mtls.*, 14 (1992) 15–31.

FIGURE CAPTIONS

Fig. 1. a) The tensile stress/strain curves for two unidirectional CMCs. The SiC/SiC is made by chemical vapor infiltration (CVI). In this material, composite failure precedes matrix crack saturation.[12,14] The SiC/CAS material has been produced by hot pressing. Also shown are typical hysteresis loops for the materials.

b) The tensile stress/strain curves for three 0/90 CMCs. The SiC/CAS is a cross-ply laminate, whereas the SiC/SiC and SiC/C are woven. The SiC/SiC material has been produced by CVI at SEP in France. It fails at a stress about equal to the matrix crack saturation stress.[14] The SiC/C material was made by HITCO. The SiC/CAS was made by Corning.

c) Schematic of stress-strain curves for unidirectional and cross-ply CMCs.

Fig. 2. a) Behaviors obtained upon unloading and reloading indicating the various strain measurements that relate to constituent properties.

b) Behavior expected if there were no debonding/sliding at the interfaces.

Fig. 3. The basic cell model indicating interface sliding and debonding.

Fig. 4. The crack opening displacements that arise during an unload/reload cycle with the corresponding interface sliding and debonding behaviors indicated. The curves are simulated using the formulae from the text. A schematic is shown in the insert.

Fig. 5. A mechanism map illustrating the regimes that lead to inelastic strain by matrix cracking in CMCs. The $\bar{\sigma}_{mc}$ bound is sketched from formulae given in Reference (31).

Fig. 6. The hysteresis loop a) for a material with a small debond energy (SDE), b) for a material with a large debond energy (LDE). Also shown is the construction used to define the strain differences, $\Delta\varepsilon_o$ and $\Delta\varepsilon_p$.

Fig. 7. The maximum hysteresis loop width, $\delta\varepsilon_{max}$, and the strain differences, $\Delta\varepsilon_o$ and $\Delta\varepsilon_p$, plotted as functions of the non-dimensional debond energy, $\Sigma_i = \bar{\sigma}_i/\bar{\sigma}_p$. The SDE and LDE regimes are identified.

Fig. 8. Finite element calculations of the effect of matrix cracks on the elastic stiffness of 1-D composites[12] ($\nu_f = \nu_m = 0.25$). Experiments indicate that larger changes occur in practice.[12]

Fig. 9. a) Change in crack density, $R/\bar{d}$, with applied stress, $\bar{\sigma}$, measured in a SiC/CAS composite. Also shown is the linear interpolation between σ_{mc} and $\bar{\sigma}_s$.

b) Simulated changes in crack density with stress.[17]

Fig. 10. Hysteresis loop data obtained for a 1-D SiC/CAS and SiC/SiC composites[8] illustrating one method for evaluating τ_o.

Fig. 11. Simulated stress/strain curves for 1-D CMCs with a range of constituent properties.

Fig. 12. A schematic of the effects of matrix crack closure on the compliance at low loads.

Fig. A1. The axial stresses in fibers when matrix cracks exist.

a) Upon loading: note the stress jump at ℓ_i, the end of the debond zone: otherwise, the stress gradient is linear.

b) Upon partial unloading or partial reloading of an SDE (small debond energy) material.

Fig. A2. The axial stress in the fibers for LDE materials

a) partial unloading indicating the slip is arrested at the debond leading to a linear stress with an abrupt change at the end of the debond zone

b) partial reloading showing that the slip zone reaches the debond before the original load is reached.

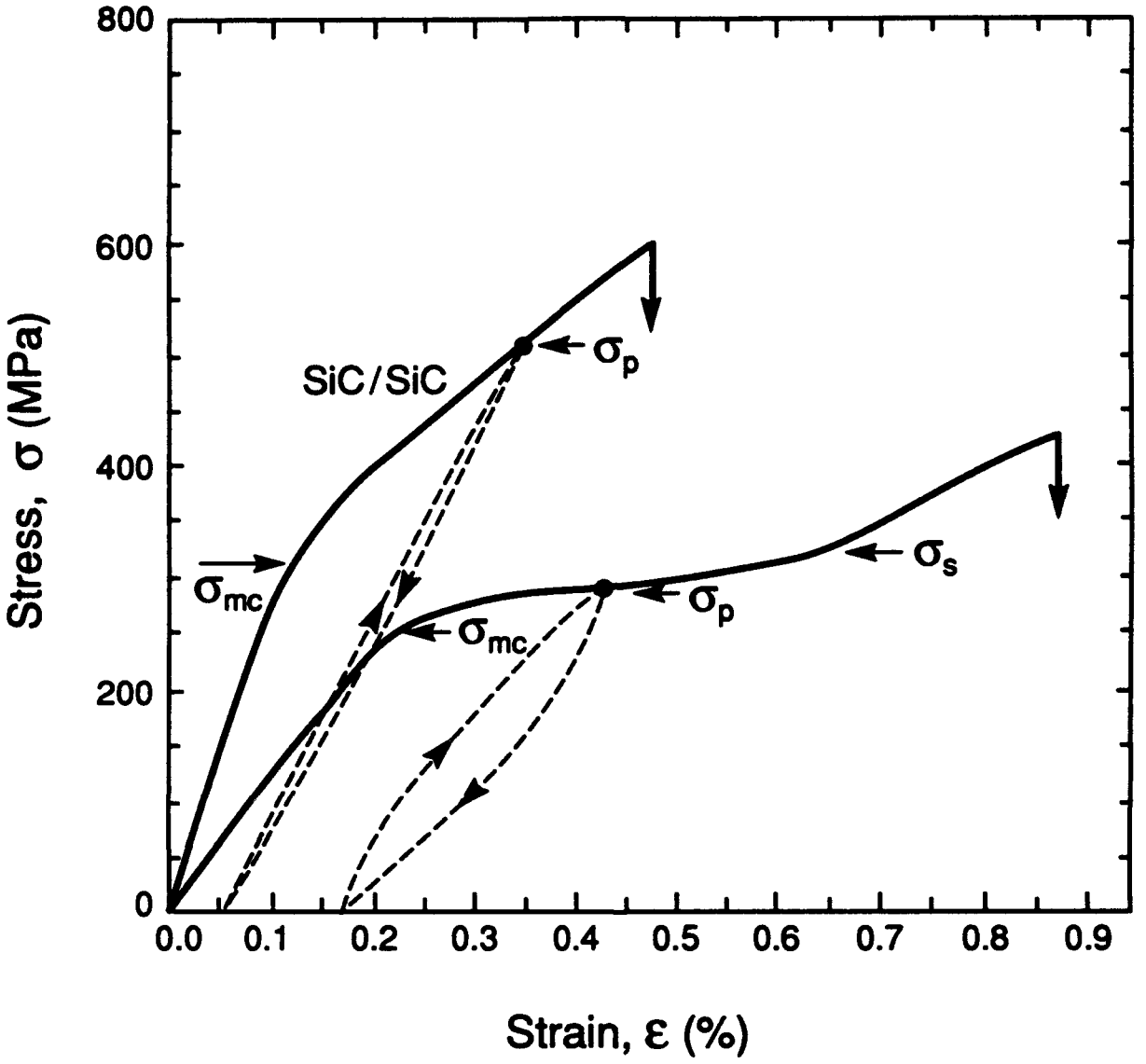
800
600
400
200
0
Stress, σ (MPa)
SiC/SiC
σp
σmc
σmc
σp
σs
0.0
0.1
0.2
0.3
0.4
0.5
0.6
0.7
0.8
0.9
Strain, ε (%)

Fig. 1a

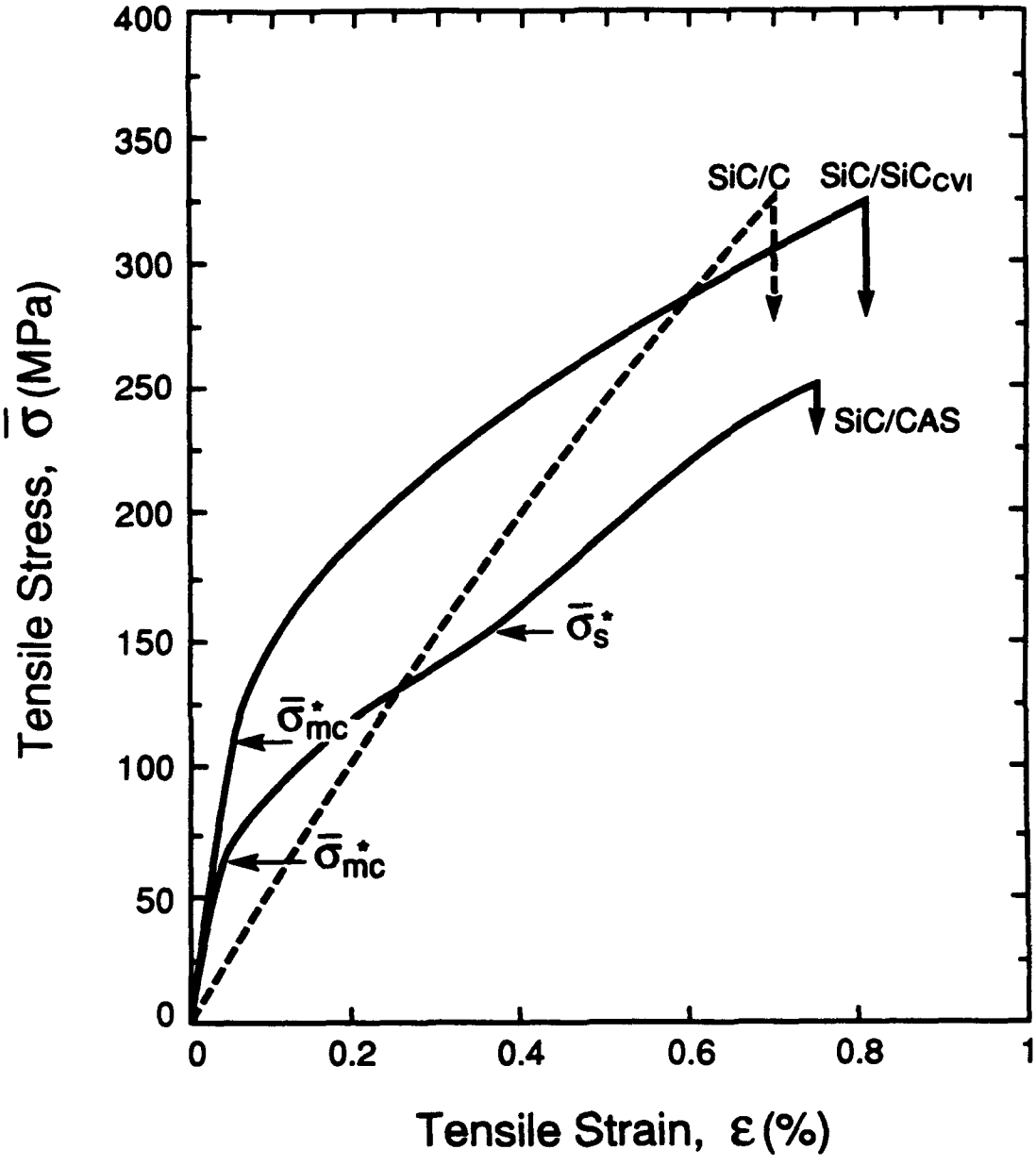

Fig. 1b. A summary of tensile stress / strain curves obtained for a variety of 2-D CMCs.

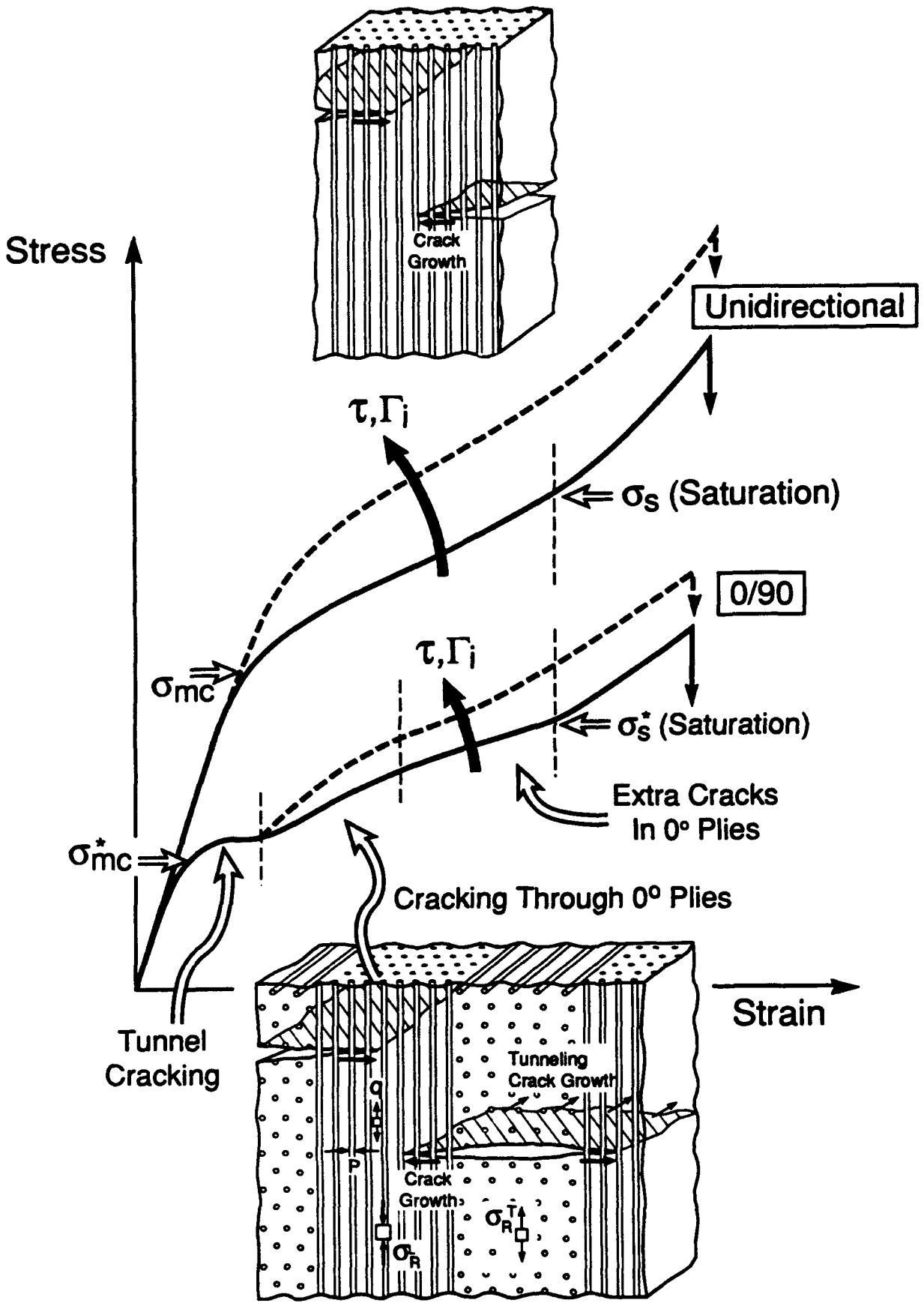
Crack Growth
Stress
Unidirectional
τ,Γi
σs (Saturation)
0/90
τ,Γi
σmc
σs* (Saturation)
Extra Cracks In 0° Plies
σ*mc
Cracking Through 0° Plies
Strain
Tunnel Cracking
Tunneling Crack Growth
Crack Growth
P
σR
σR

Fig. 1c

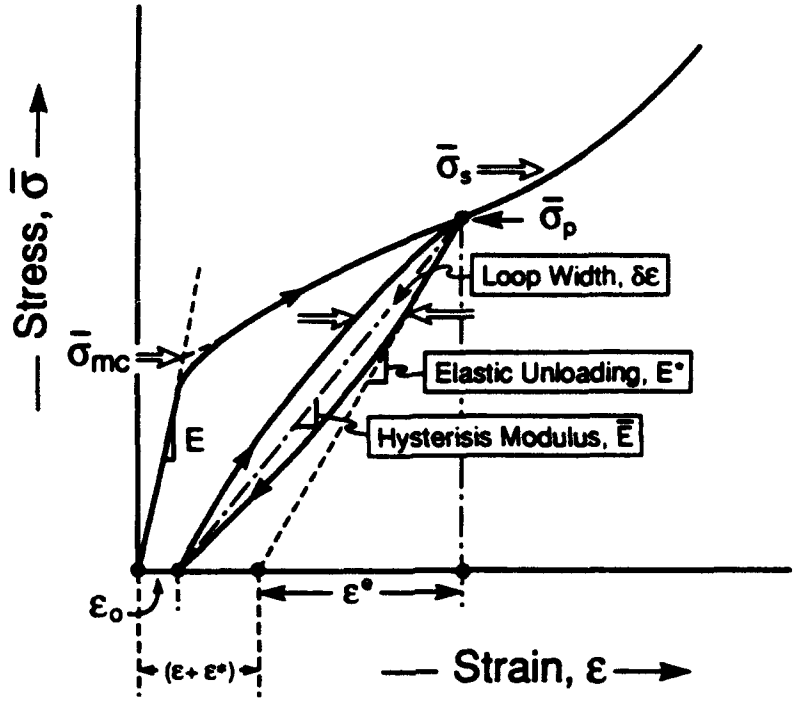

a) Debonding and Sliding Interface

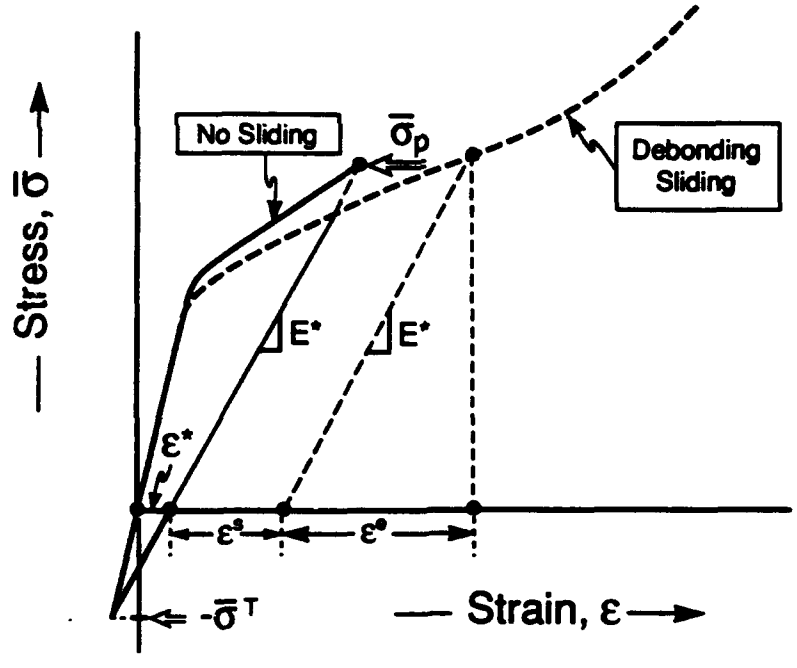

b) Behavior When Debonding Inhibited

Fig. 2. a) Behaviors obtained upon unloading and reloading indicating the various strain measurements that relate to constituent properties.
b) Behavior expected if there were no debonding / sliding at the interfaces.

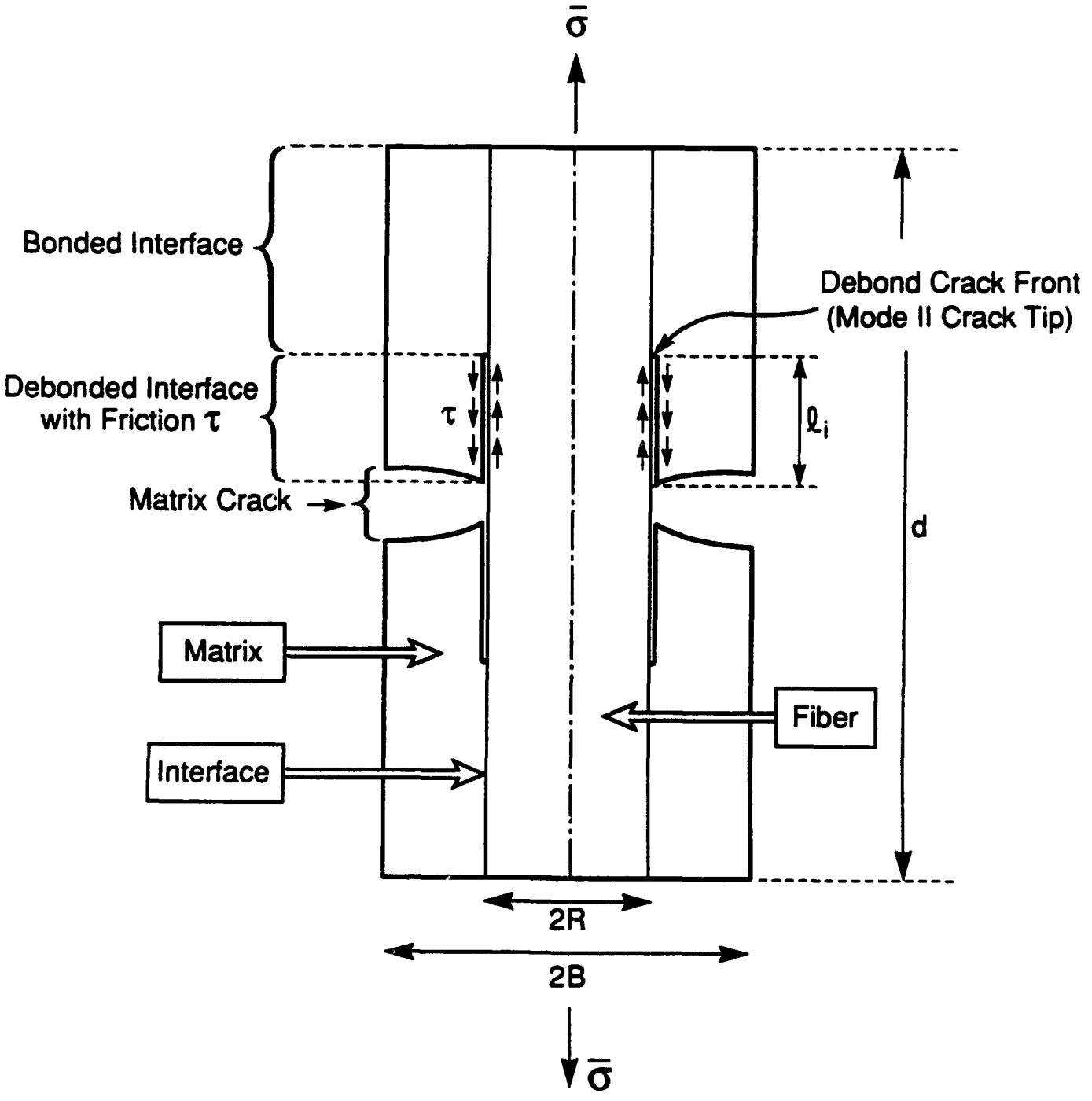

Figure 3 : Basic cell model

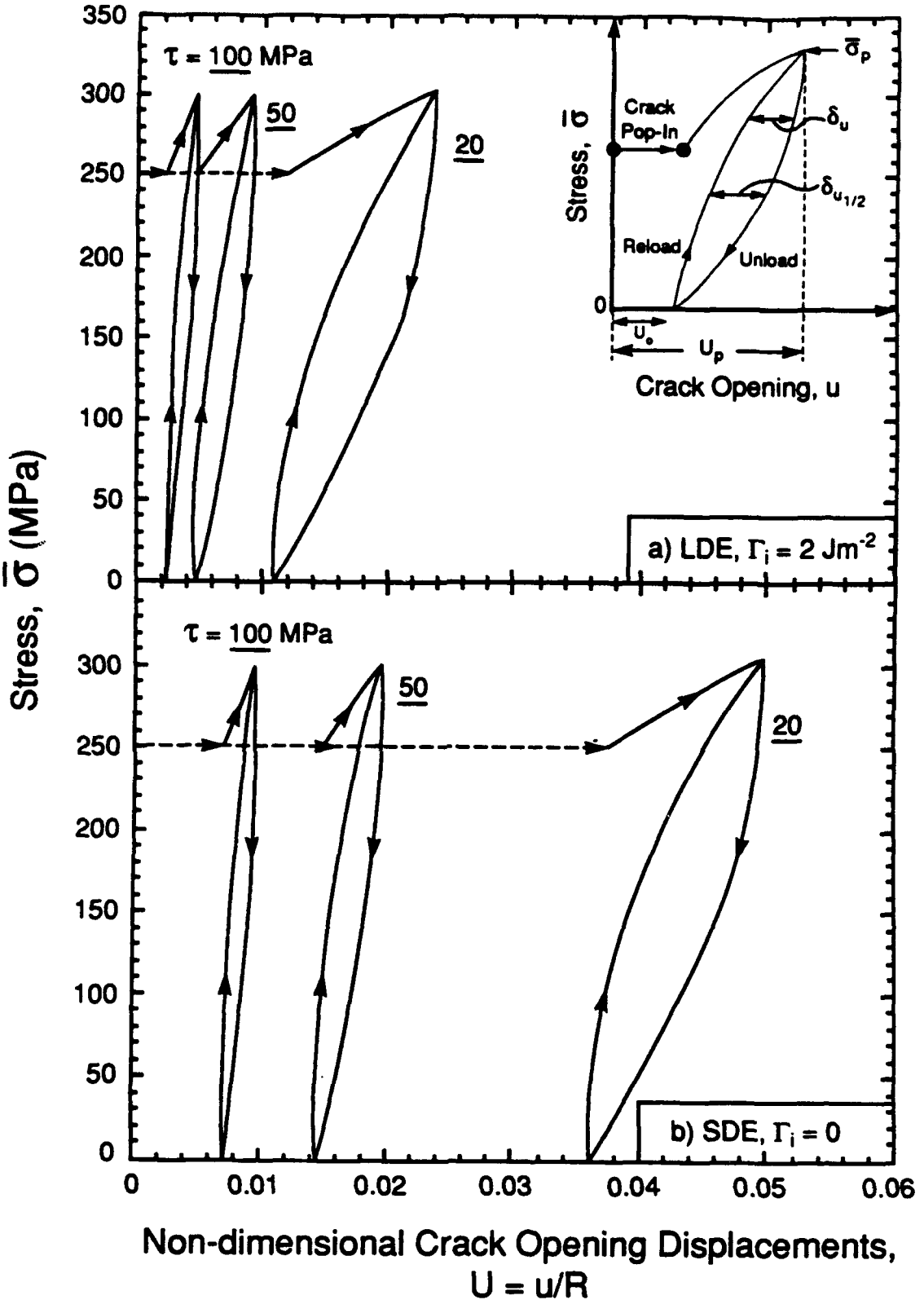
τ = 100 MPa
50
20
a) LDE, Γi = 2 Jm-2
τ = 100 MPa
50
20
b) SDE, Γi = 0
Stress, σ̄ (MPa)
Non-dimensional Crack Opening Displacements,
U = u/R
Crack Pop-In
σ̄p
δu
δu1/2
Reload
Unload
Uo
Up
Crack Opening, u

Figure 4

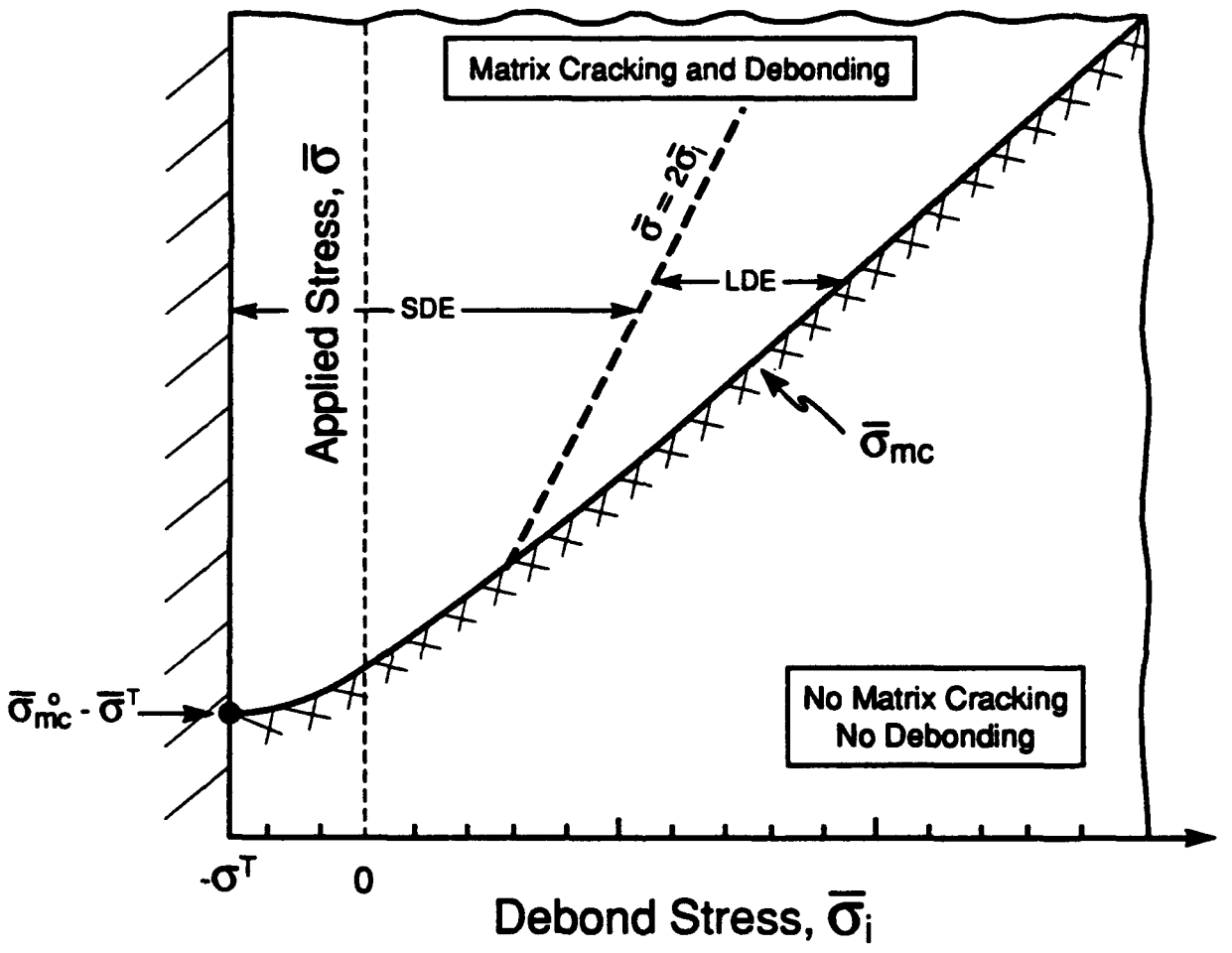
Matrix Cracking and Debonding
Applied Stress, $\bar{\sigma}$
$\bar{\sigma} = 2\bar{\sigma}_i$
SDE
LDE
$\bar{\sigma}_{mc}$
$\bar{\sigma}^{\circ}_{mc} - \bar{\sigma}^{T}$
No Matrix Cracking
No Debonding
$-\sigma^{T}$
0
Debond Stress, $\bar{\sigma}_i$

Figure 5

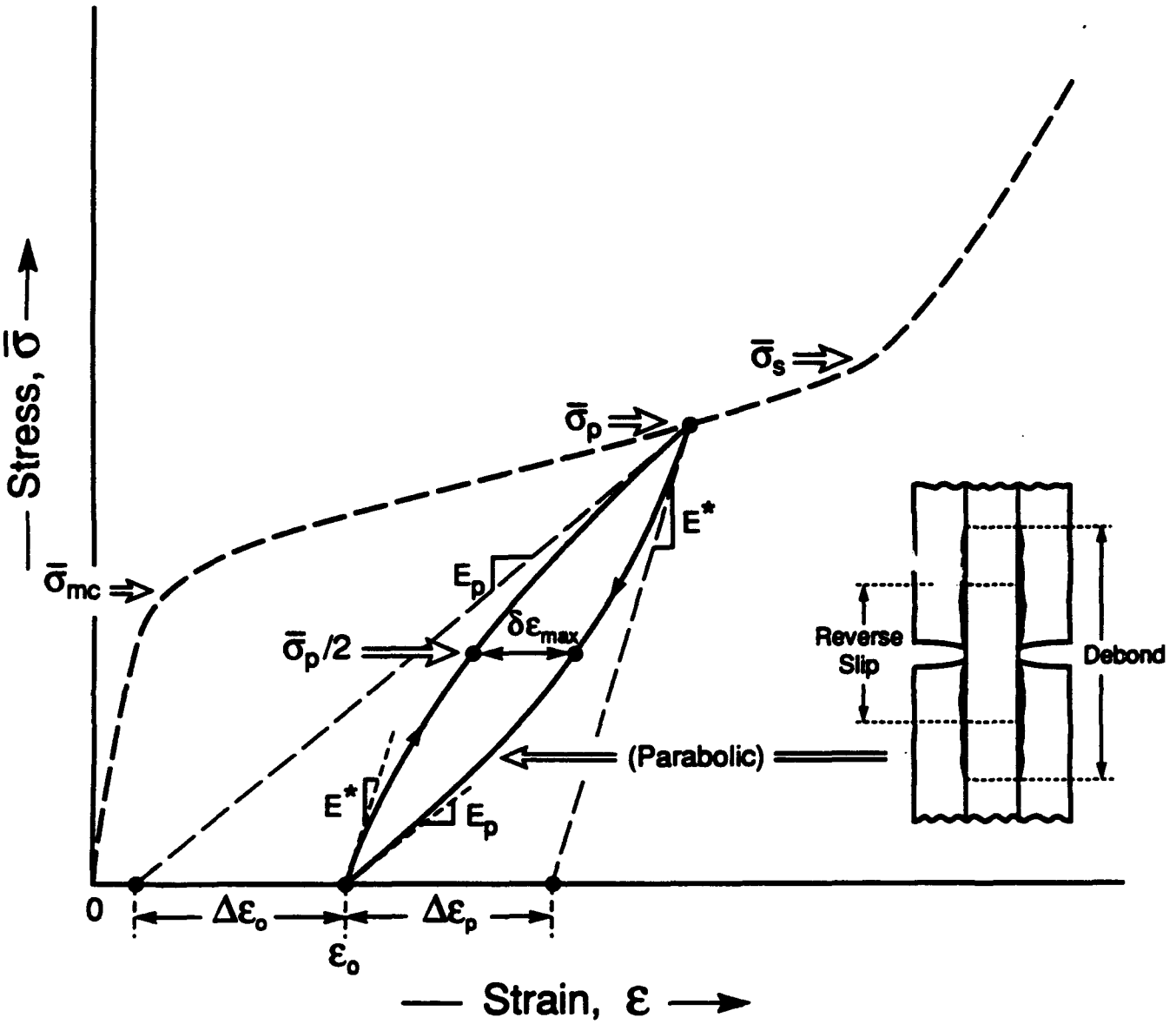

Fig. 6 a). The hysteresis loop for a material with a small debond energy (SDE).

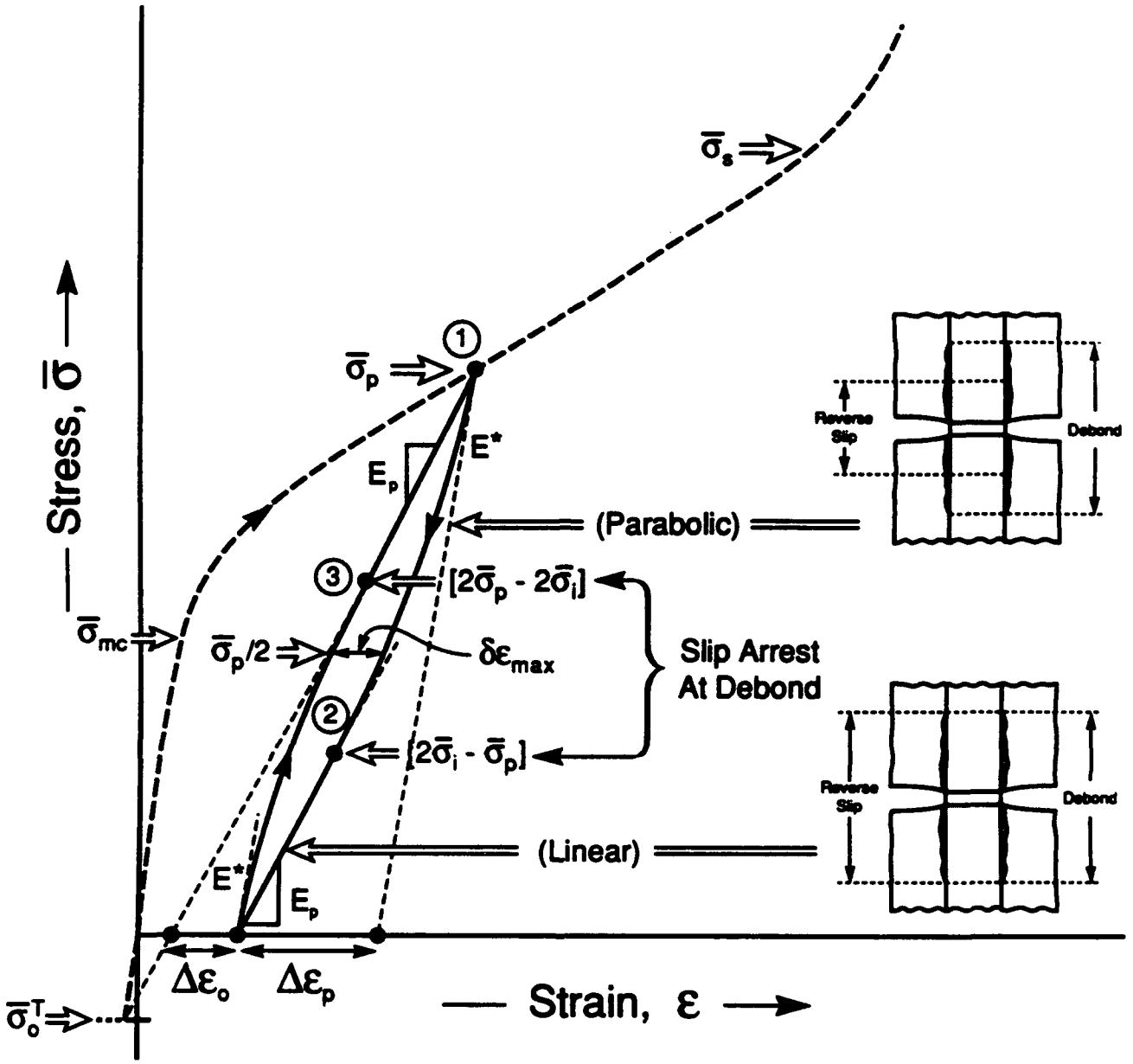

Fig. 6 b). The hysteresis loop for a material with a large debond energy (LDE).

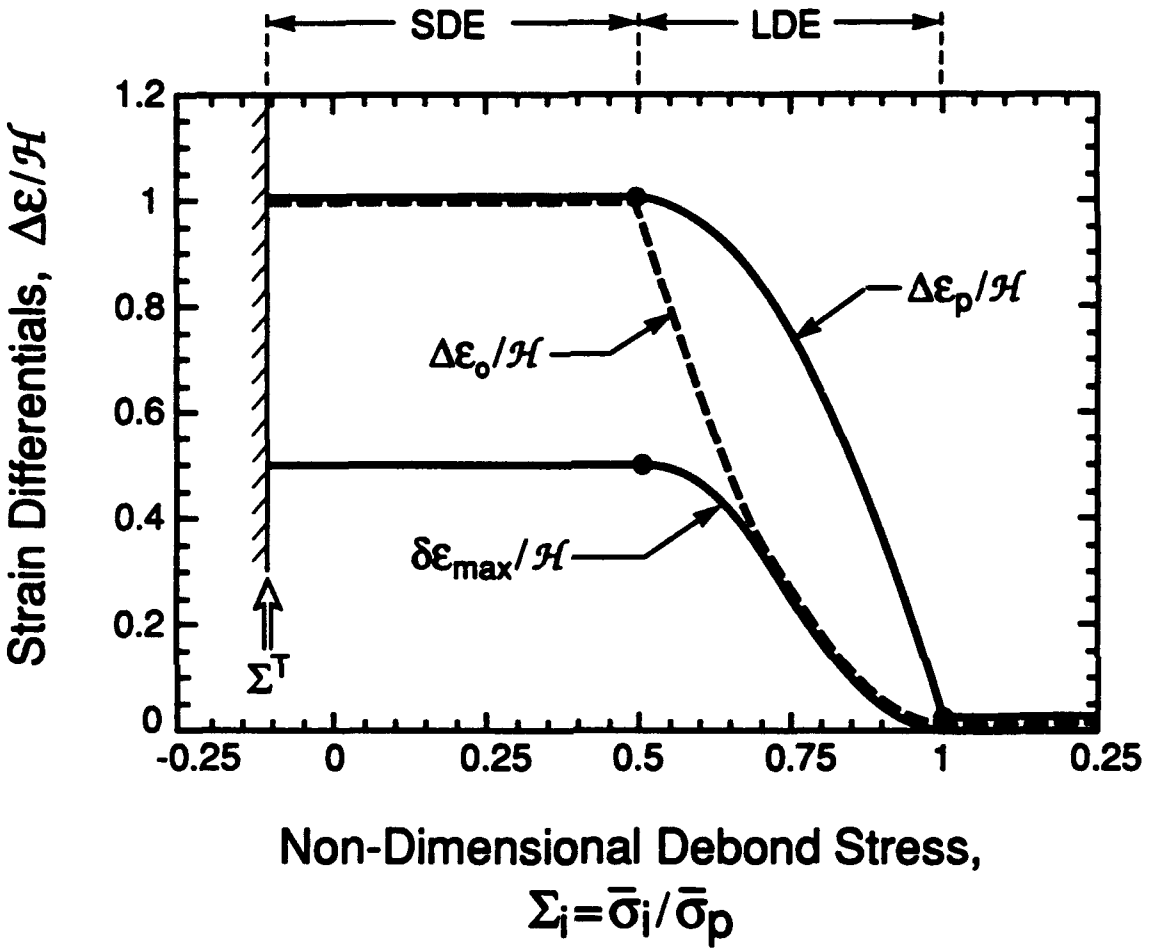
SDE
LDE
1.2
1
0.8
0.6
0.4
0.2
0
Strain Differentials, $\Delta\varepsilon/\mathcal{H}$
$\Delta\varepsilon_p/\mathcal{H}$
$\Delta\varepsilon_o/\mathcal{H}$
$\delta\varepsilon_{max}/\mathcal{H}$
Σ^T
-0.25
0
0.25
0.5
0.75
1
0.25
Non-Dimensional Debond Stress,
$\Sigma_i=\bar{\sigma}_i/\bar{\sigma}_p$

Figure 7

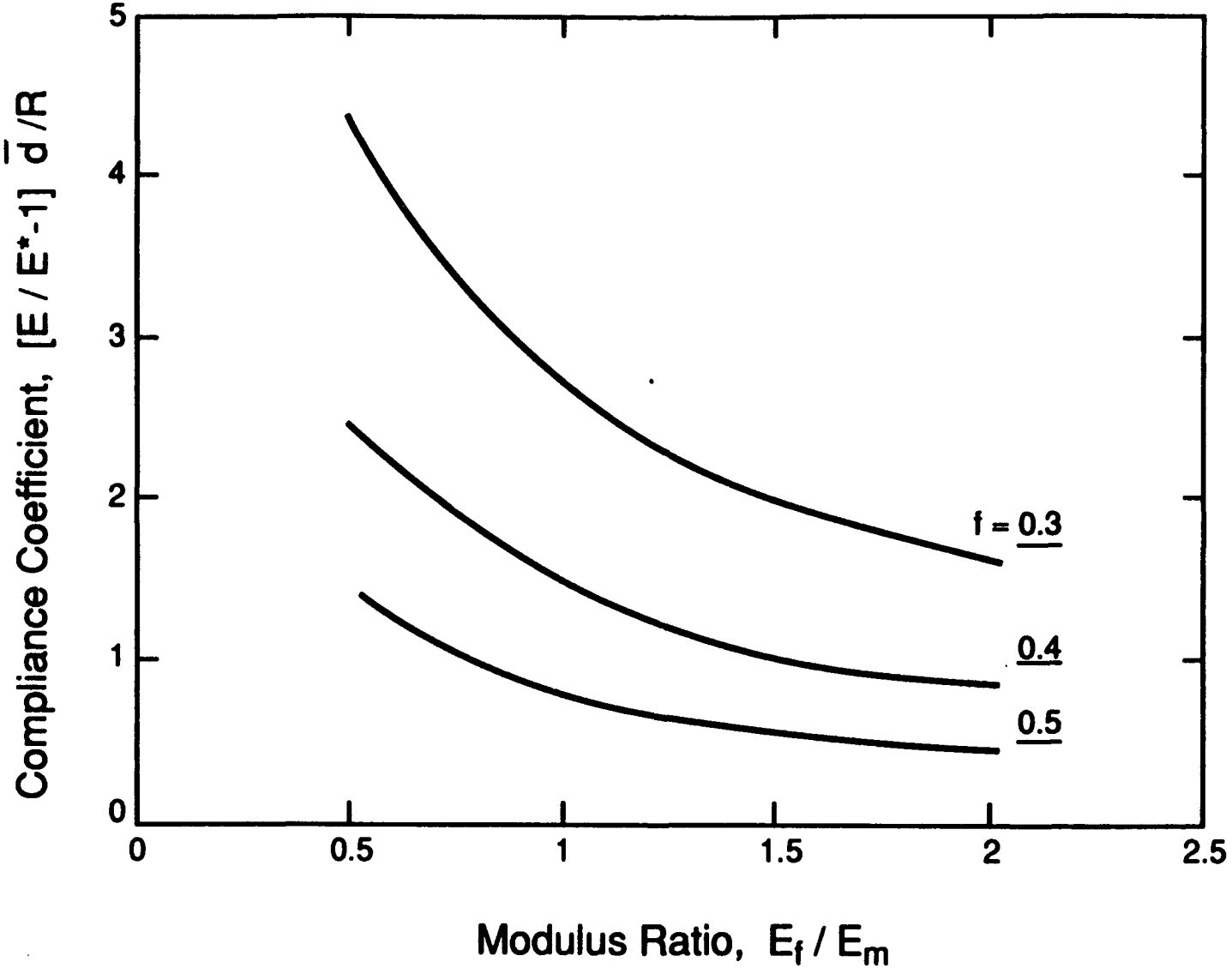
Compliance Coefficient, [E / E*-1] d̄ /R
Modulus Ratio, E_f / E_m
f = 0.3
0.4
0.5
0
0.5
1
1.5
2
2.5
0
1
2
3
4
5

Figure 8

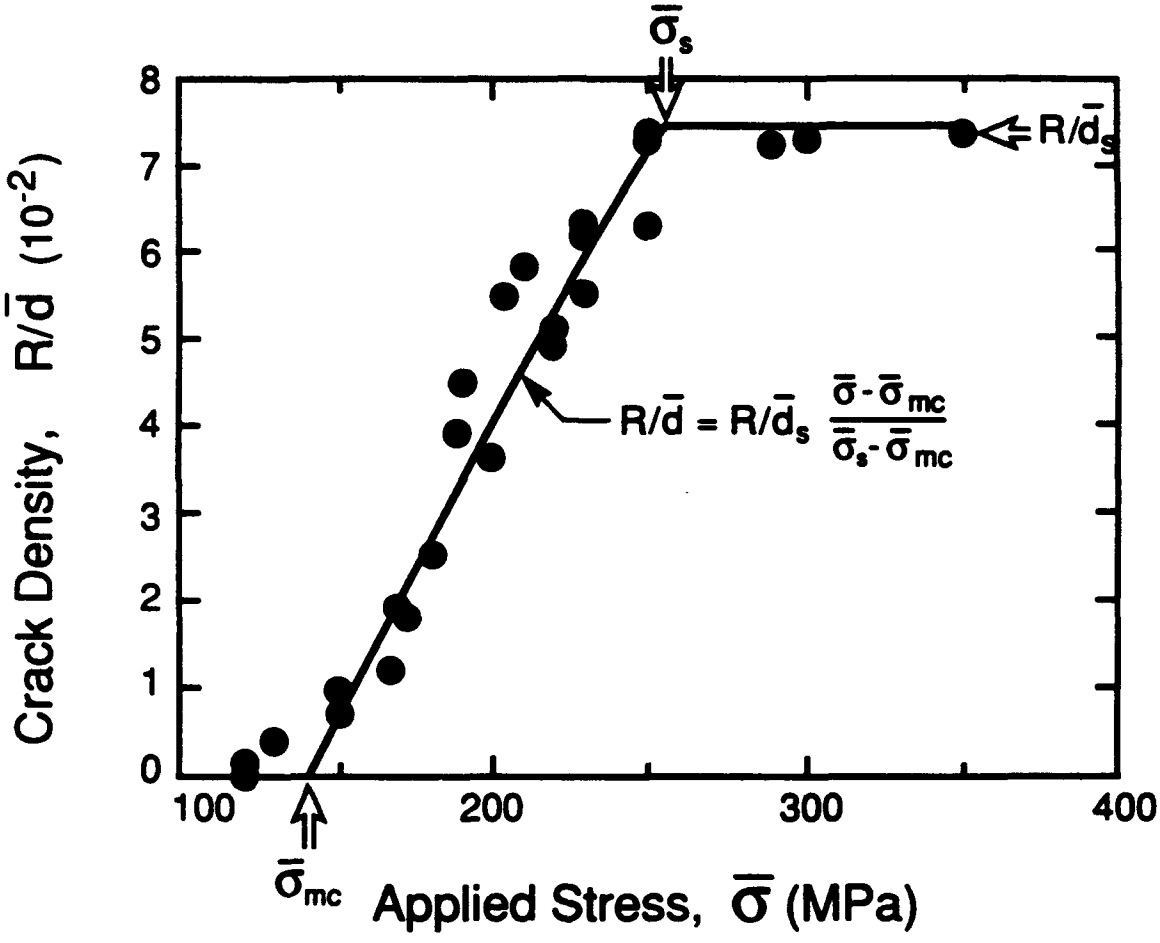
$\bar{\sigma}_s$
8
7
6
5
4
3
2
1
0
$R/\bar{d}_s$
$R/\bar{d} = R/\bar{d}_s \frac{\bar{\sigma}-\bar{\sigma}_{mc}}{\bar{\sigma}_s-\bar{\sigma}_{mc}}$
Crack Density, $R/\bar{d}$ (10^{-2})
100
200
300
400
$\bar{\sigma}_{mc}$
Applied Stress, $\bar{\sigma}$ (MPa)

Figure 9a

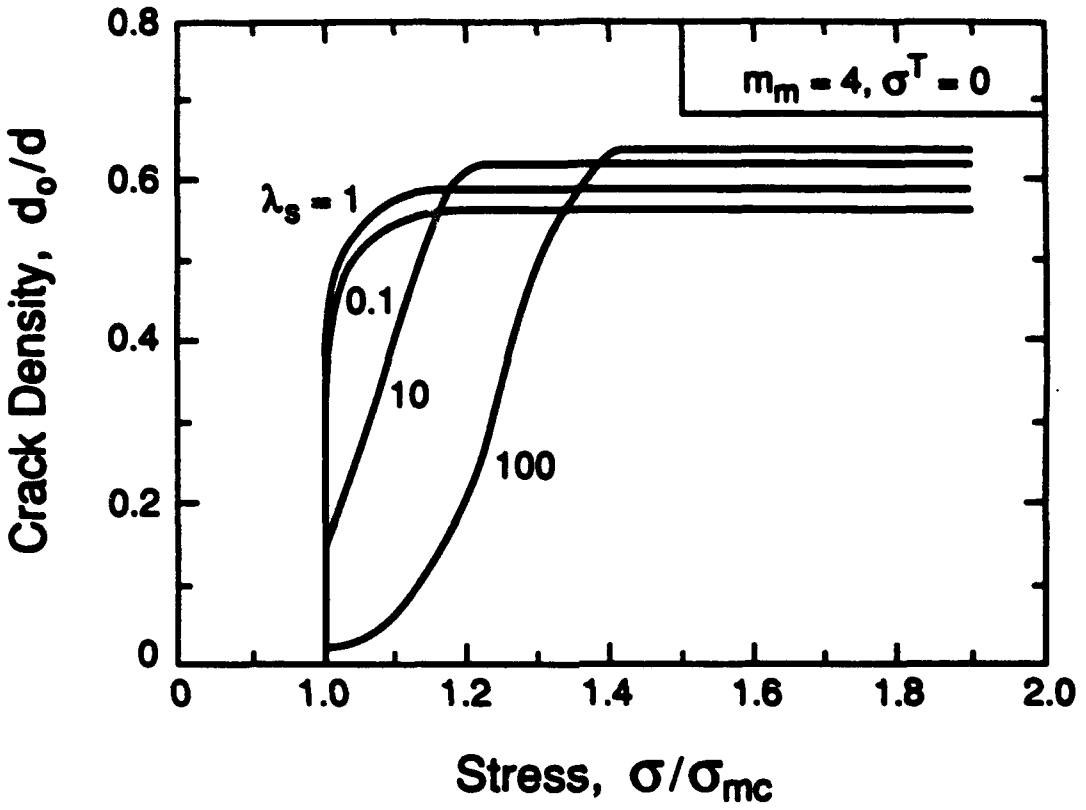
$m_m = 4, \sigma^T = 0$
$\lambda_s = 1$
0.1
10
100
Crack Density, $\bar{d}_o/\bar{d}$
Stress, σ/σ_{mc}
0.8
0.6
0.4
0.2
0
0
1.0
1.2
1.4
1.6
1.8
2.0

Figure 9b

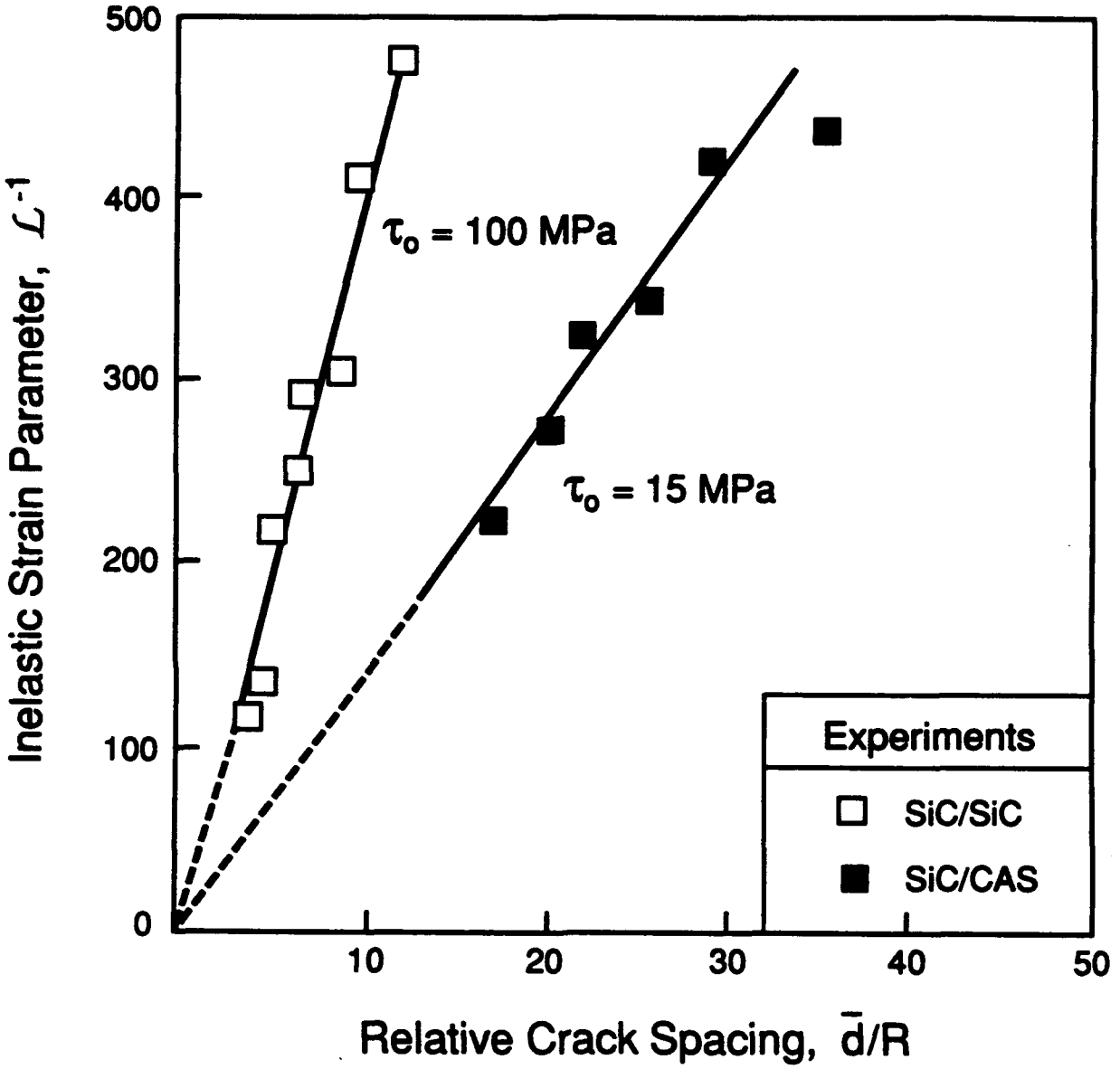
500
400
300
200
100
0
10
20
30
40
50
Inelastic Strain Parameter, $\mathcal{L}^{-1}$
Relative Crack Spacing, $\bar{d}/R$
τ_o = 100 MPa
τ_o = 15 MPa
Experiments
SiC/SiC
SiC/CAS

Figure 10

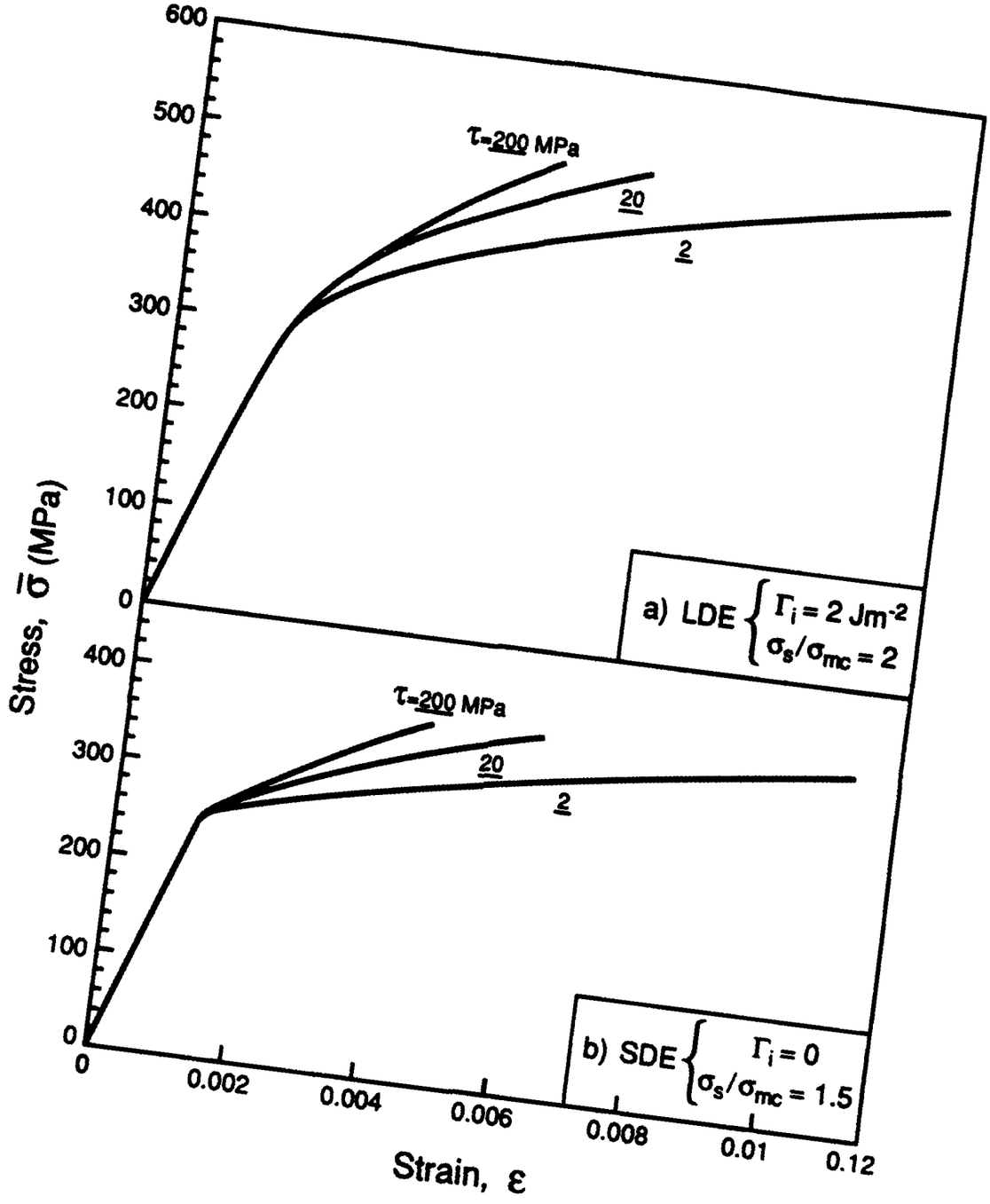
600
500
400
300
200
100
0
τ=200 MPa
20
2
a) LDE
$\Gamma_i = 2\ Jm^{-2}$
$\sigma_s/\sigma_{mc} = 2$
400
300
200
100
0
τ=200 MPa
20
2
b) SDE
$\Gamma_i = 0$
$\sigma_s/\sigma_{mc} = 1.5$
0
0.002
0.004
0.006
0.008
0.01
0.12
Stress, $\bar{\sigma}$ (MPa)
Strain, ε

Figure 11

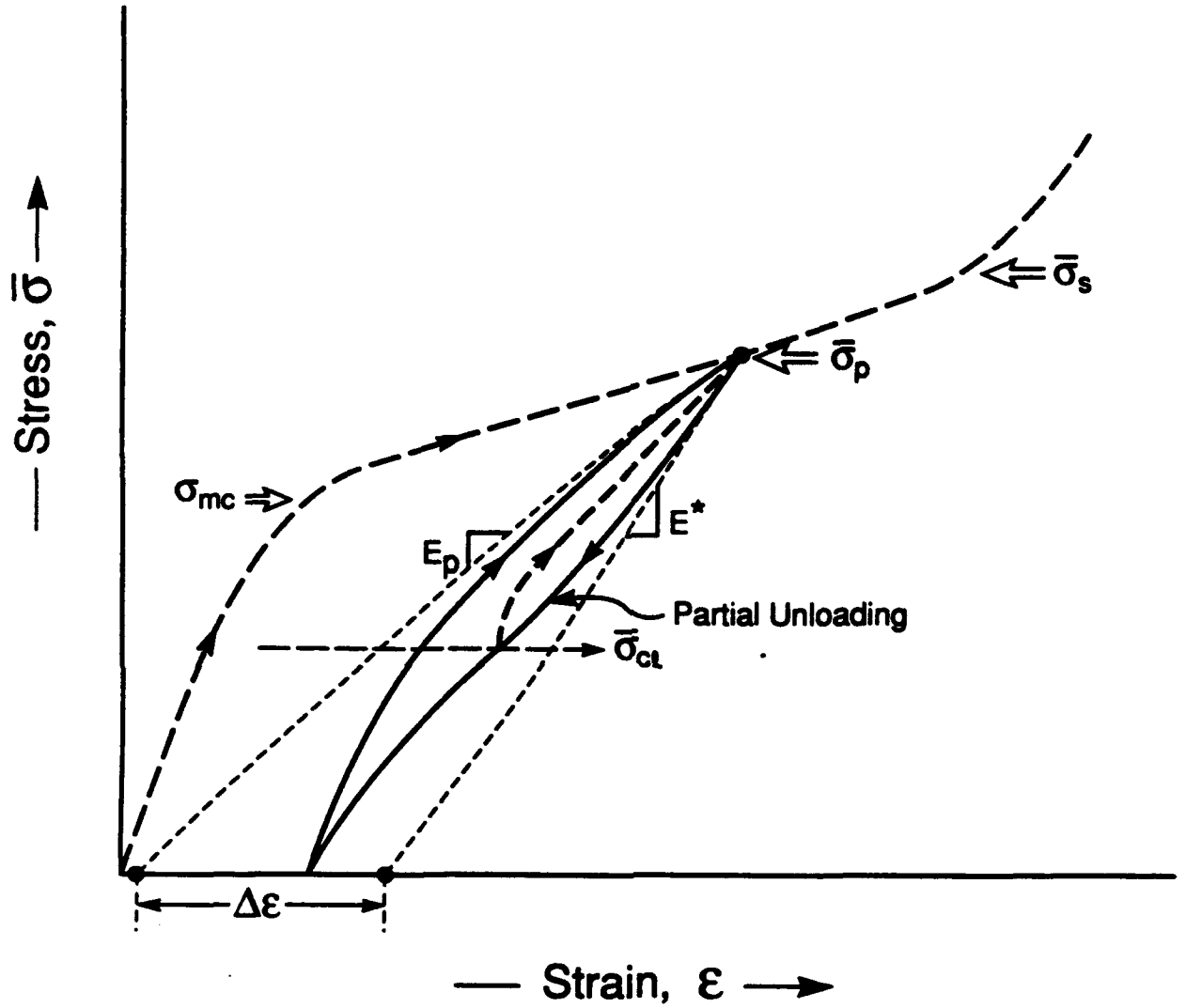
— Stress, $\bar{\sigma}$ →
$\bar{\sigma}_s$
$\bar{\sigma}_p$
σ_{mc}
E_p
E^*
Partial Unloading
$\bar{\sigma}_{ct}$
$\Delta\varepsilon$
— Strain, ε →

Figure 12

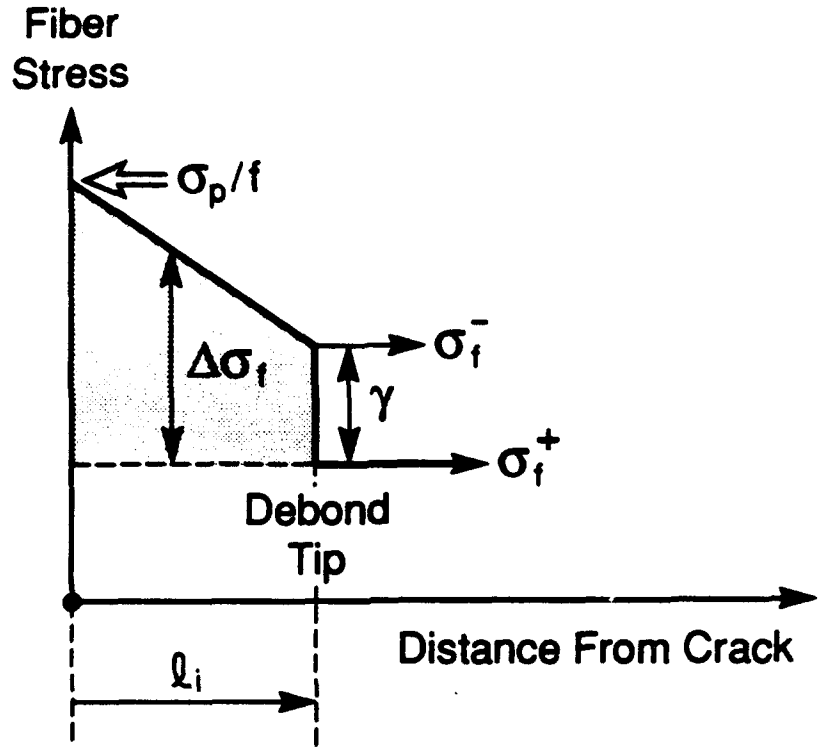

a) Loaded System

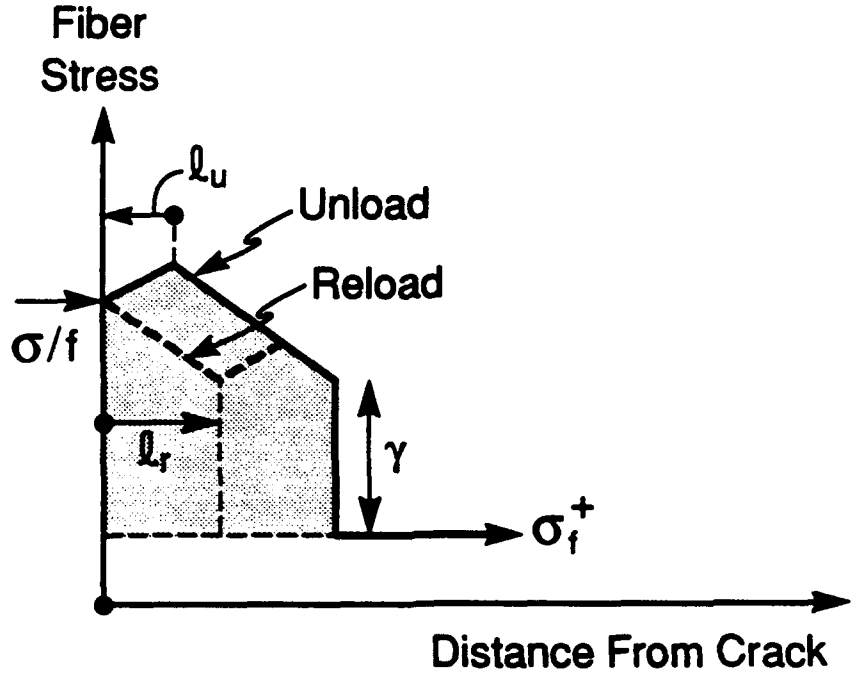

b) SDE Material Upon Partial Unloading or Reloading

Figure A1

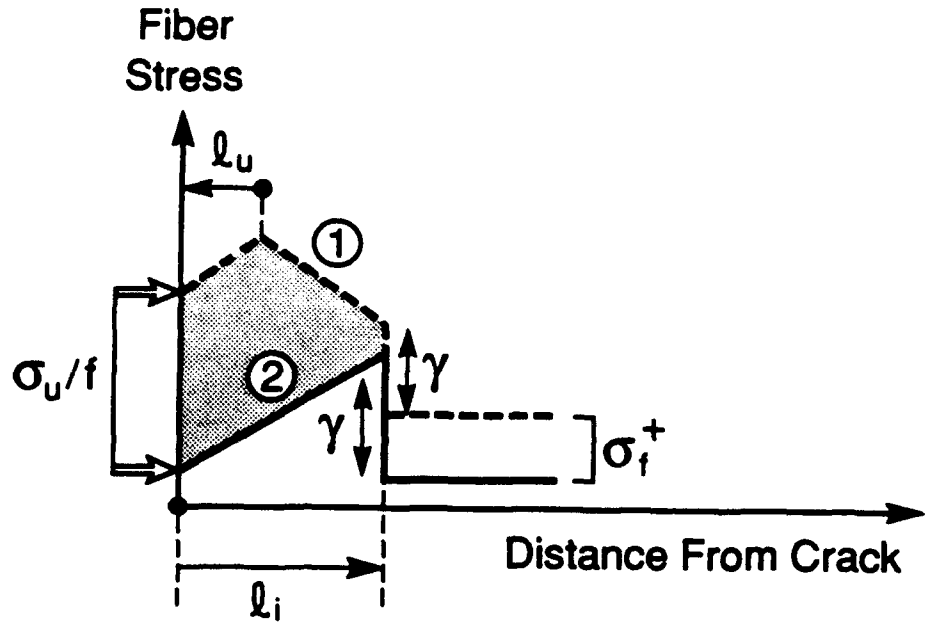

a) Unloading

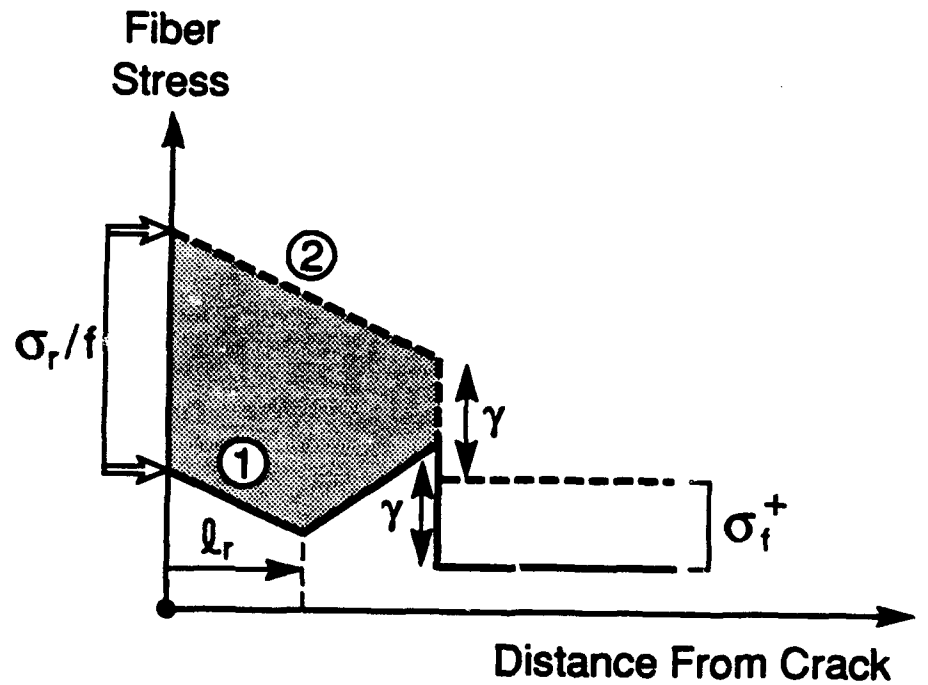

b) Reloading

Figure A2

MATERIALS

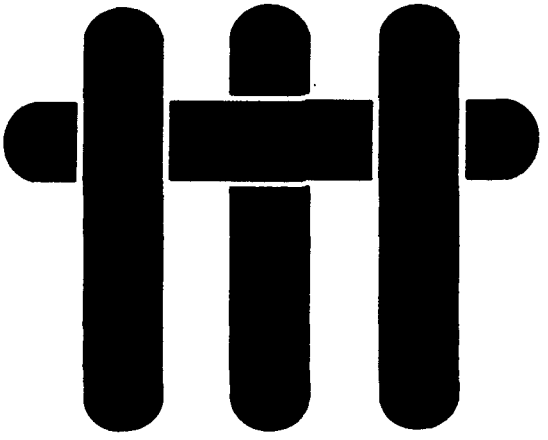

RELATIONSHIPS BETWEEN HYSTERESIS MEASUREMENTS AND THE CONSTITUENT PROPERTIES OF CERAMIC MATRIX COMPOSITES

II: EXPERIMENTAL STUDIES ON UNIDIRECTIONAL MATERIALS

by

J.-M. Domergue, E. Vagaggini, A.G. Evans
Materials Department
College of Engineering
University of California
Santa Barbara, California 93106-5050

and

Jean-Marie Parenteau
S.E.P.
Les 5 chemins, Le Haillan,
F-33160 Saint Médard en Jalles, France

KJS-Evans-16-TA-Ritnshp II 94/03/10-5:07 PM-3/10/94

ABSTRACT

The use of hysteresis loop measurements for assessing the constituent properties of unidirectional CMCs is evaluated, using basic theory described in a companion paper. Results are obtained on SiC/CAS and SiC/SiC composites. These materials exhibit very different hysteresis characteristics, reflected in differences in sliding stress, τ and debond energy, Γ_i. These interface properties are manifest in the respective tensile stress/strain curves.

1. INTRODUCTION

Ceramic matrix composites (CMCs) have attractive thermostructural characteristics because mechanisms exist that allow stress redistribution at strain concentration sites. The most important of these are matrix cracking[1-8] and stochastic fiber failure.[9,10] Both of these mechanisms cause inelastic strains that fundamentally control stress redistribution.[4,6,7-10] One of the challenges for the successful utilization of CMCs is the development of a methodology for relating these inelastic strains to the properties of the constituents (fiber, matrix, interface).[11] The successful development of such a methodology would allow the formulation of mechanism-based constitutive laws.[4,11] The basic matrix cracking and fiber failure models that underlie this methodology have already been developed and validated for some CMCs.[2-11] However, in addition to these models, the methodology must include experimental procedures for evaluating the constituent properties, summarized in Table I. Moreover, the procedures must be experimentally straightforward and their interpretation unambiguous. A methodology based on hysteresis measurements has been proposed for this purpose[11] and the theory presented in a companion paper[12] (Fig. 1). The application of the method to two unidirectional CMCs is described in this article. Results for cross ply laminates are presented elsewhere.[13]

Alternative methods for evaluating interface properties include fiber push-in and push-through tests,[14-17] as well as microcomposite tests.[18] These methods have the disadvantage that they are difficult to apply at high temperatures and have limited utility for assessing the fatigue degradation of the interface.[19] The measurements also involve single fibers, whereas average values over many fibers are relevant to composite behavior. The hysteresis method obviates these limitations.

The two CMCs chosen for this study have been selected because previous measurements[3,12,20] have suggested that they exhibit substantially different

stress/strain behaviors which must be related to differing interface properties. One material, SiC/CAS, has both a low sliding stress τ and a small debond energy Γ_i.[2,3] The other material, SiC/SiC, produced by chemical vapor infiltration (CVI) has both large τ and Γ_i.[20,21] Analysis of these materials thus represents a critical assessment of the methodology.

2. MATERIALS

Both the SiC/CAS and SiC/SiC materials use Nicalon fibers, having elastic modulus, E_f = 200 GPa. The matrix modulus is, E_m = 97 GPa.[3] The matrix cracks evolve with stress, as shown on Fig. 2. Fiber push-out experiments indicate a sliding resistance, $\tau \approx 17$ MPa[22] and a debond energy, $\Gamma_i \approx 0$. Beam bending and matrix dissolution measurements have established a fiber/matrix misfit stress,[3] $\sigma^T \approx 120$ MPa (Table I).

The SiC/SiC material has been made by chemical vapor infiltration, with a C fiber coating. The material has considerable porosity, distributed heterogeneously throughout the matrix, such that the matrix modulus, $E_m \approx 300$ GPa, is considerably less than that for dense SiC. Fiber push-in experiments indicate relatively high values of both τ and Γ_i, of order 50 → 200 MPa and 1 → 6 Jm^{-2}, respectively.[21] Thermal expansion measurements indicate a misfit stress,[23] σ^T in the range 150–250 MPa (Table I).

3. TEST PROCEDURES‡

Tensile tests are conducted with periodic unload/reload cycles. Emphasis is given to peak stresses below that at which matrix cracking saturates, $\sigma_p < \sigma_s$ (Fig. 1). The tension test methodology has been described elsewhere.[3] Briefly, displacements are measured using contact extensometers. Alignment is achieved using bonded tabs with friction grips. The information generated for each hysteresis cycle is stored on disc and the results analyzed in accordance with the procedures outlined below.

One practical problem concerns crack closure at small loads, $\sigma_{c\ell}$, upon unloading[12,24] (Fig. 1c). This phenomenon can invalidate the relationships between the inelastic strains and the constituent properties. It is manifest as a change in the unloading slope, as zero load is approached. The test procedure may include a minimum stress, σ_{min}, in the unload/reload cycle. This minimum stress is chosen to be above the matrix crack closure stress, $\sigma_{c\ell}$. Preliminary tests are conducted to evaluate $\sigma_{c\ell}$ as a function of the peak stress, σ_p.

Matrix crack densities are measured on both materials. For the SiC/SiC material, the matrix cracks are highlighted by using Murakami's etch.[20] The cracks can then be imaged in the scanning electron microscope, as illustrated on Fig. 3a. The average crack density is determined from line scans. For the SiC/CAS material, scanning electron microscopy is used to provide a direct image of the cracks[4] (Fig. 3b). The average crack spacing is again determined from line scans parallel to the loading axis.

---

‡ All the stresses presented in this analysis are those applied on the composite: therefore for simplicity, the bar superscript used in the companion paper[12] is omitted.

4. RESULTS

4.1 Strains

The hysteresis measurements indicate appreciable differences between the two materials (Fig. 4). For the SiC/CAS, the loop width and the permanent strain are much larger than for the SiC/SiC material. The loop shapes are also different. The unloading curves for SiC/CAS appear to be approximately parabolic, characteristic of composites with a small debond energy, designated SDE. The unloading strain for SiC/SiC has linear plus curved segments. Such effects are expected for materials with a relatively high debond energy, designated LDE. The present results for SiC/CAS indicate that the inelastic strains occur at stresses larger than those found in previous studies.[3] The difference is related to a lower residual stress in the current material, as explained below. There are crack closure effects (Fig. 4). However, the closure stress is quite small for both materials and much less than that found in certain other CMCs.[24] Consequently, there is minimal influence of closure on the hysteresis strains.

The influence of σ_p on the permanent strain, ε_o is plotted on Fig. 5. Substantially larger values are evident for SiC/CAS than for SiC/SiC.

4.2 Crack Densities

Crack density measurements made for the SiC/CAS method have been superposed onto Fig. 2. These results differ from previous measurements.[3] They show that the matrix cracking stress, $\sigma_{mc} \approx 285$ MPa and that matrix cracks saturate at $\sigma_s \approx 335$ MPa with spacing $\bar{d}_s = 125$ μm. A linear interpolation is used to represent the crack spacing ($\bar{d} < \bar{d}_s$)[11]

$$\bar{d} \approx \bar{d}_s \frac{[\sigma_s/\sigma_{mc} - 1]}{[\sigma/\sigma_{mc} - 1]} \qquad (1a)$$

or

$$\bar{d} = \bar{d}_o \left[\frac{\sigma_o/\sigma_{mc} - 1}{\sigma/\sigma_{mc} - 1} \right] \tag{1b}$$

as indicated on Fig. 2, with σ_o being any stress (between σ_{mc} and σ_s) and $\bar{d}_o$ the crack spacing measured at that stress. The difference in $\bar{d}$ (σ) from previous results[3] is consistent with the larger stresses needed to cause inelastic deformation, noted above, and will be shown to reside in a reduced misfit stress, σ^T (Table II).

For the SiC/SiC composite, measurements have been made at three different stresses above σ_{mc}, which is estimated to be ~ 270 MPa (Fig. 2). It is apparent that composite failure *precedes* matrix crack saturation, such that σ_s and d_s cannot be obtained. However, for further analysis, it is sufficient to use the values at composite failure.

5. THE HYSTERESIS METHODOLOGY

The companion paper gives all of the basic formulae for evaluating τ, Γ_i and σ^T from the hysteresis measurements.[12] Here, the results found to be most robust experimentally are emphasized. It will be noted that much of the requisite information can be gained without having explicit information about the crack spacing, $\bar{d}$. In fact, $\bar{d}$ is only needed to determine, τ. Even then, a single value obtained between σ_{mc} and σ_s suffices.

5.1 The Unloading Strain

The differential $\Delta\varepsilon_u$ between strains measured at the peak σ_p and upon unloading, at stress σ_u, is given for initial unloading (Fig. 1a) by,[12]

$$\Delta\varepsilon_u \equiv \varepsilon_p - \varepsilon_u = \mathcal{L}\left(\sigma_p - \sigma_u\right)^2 + \left(\sigma_p - \sigma_u\right)/E^* \tag{2a}$$

where E^* is the elastic modulus, and $\mathcal{L}$ the inelastic strain index given by[25]

$$\mathcal{L} = \frac{b_2\left(1 - a_1 f\right)^2}{4 f^2 \tau E_m}\left(R/\bar{d}\right)$$

or (2b)

$$\mathcal{L} \equiv \left(R/\bar{d}\right)\left(\beta/\tau E_m\right)$$

with R being the fiber radius, f the fiber volume fraction, E_m the matrix Young's modulus, a_i, b_i are the coefficients defined by Hutchinson and Jensen [25] (HJ) and β is non-dimensional. Upon combining Eqn. (2b) with Eqn. (1), it is evident that there should be an approximate linear dependence of $\mathcal{L}$ on σ_p,

$$\mathcal{L} \approx \mathcal{L}_s\left[\left(\sigma_p/\sigma_{mc} - 1\right)/\left(\sigma_s/\sigma_{mc} - 1\right)\right] \tag{2c}$$

where

$$\mathcal{L}_s \equiv \left(R/\bar{d}_s\right)\left(\beta/\tau E_m\right)$$

This behavior may be used to determine τ. Differentiation of Eqn. (2a) to obtain the initial unloading tangent modulus E_u gives

$$1/E_u \equiv -d\Delta\varepsilon_u/d\sigma_u = 1/E^* + 2\mathcal{L}\left(\sigma_p - \sigma_u\right) \tag{3}$$

This behavior obtains *down* to a transition stress, σ_{tu} (Fig. 6), given by[12]

$$\sigma_{tu} = 2\sigma_i - 1 \tag{4}$$

where σ_i is the non-dimensional debond stress, defined as[25]

$$\begin{aligned} \sigma_i &= (1/c_1)\sqrt{E_m \Gamma_i / R} - \sigma^T \\ &\equiv \sigma_D - \sigma^T \end{aligned} \tag{5}$$

At smaller unload stresses ($\sigma_u < \sigma_{tu}$),[12]

$$\Delta\varepsilon_u = 4\mathcal{L}(\sigma_p - \sigma_i)(\sigma_p - \sigma_u) + (\sigma_p - \sigma_u)/E^* \tag{6}$$

such that the tangent modulus is constant and given by,

$$1/E_p = 1/E^* + 4\mathcal{L}(\sigma_p - \sigma_i) \tag{7}$$

This unloading behavior expected for LDE material is schematically summarized on Fig. 6. There is an intercept at $\sigma_u = \sigma_p$, having magnitude E^{*-1} (Eqn. 3). The initial unloading behavior associated with the reverse slip process is linear, with slope, $2\mathcal{L}$ (Eqn. 3). Then, a transition occurs at σ_{tu}, coincident with the reverse slip zone being stopped at the debond. The stress σ_{tu} gives the debond stress σ_i (Eqn. 4). At lower stresses, E_u is *constant* and equal to E_p (Eqn. 7). This constant value has a coupled dependence on $\mathcal{L}$ and σ_i .‡ For SDE material, there is no transition to a constant region when $\sigma > 0$.

---

‡ If matrix crack closure occurs, E_u^{-1} decreases as $\sigma_u \to 0$, illustrated by the dotted line on Fig. 6.

5.2 The Reloading Strain

The reload tangent moduli (Fig. 6) are governed by a transition stress,[12]

$$\sigma_{tr} = 2\left(\sigma_p - \sigma_i\right) \tag{8}$$

When $\sigma_r < \sigma_{tr}$,

$$1/E_r = 1/E^* + 2\mathcal{L}\sigma_r \tag{9}$$

and when $\sigma_r > \sigma_{tr}$,

$$\begin{aligned} 1/E_r &= 1/E^* + 4\mathcal{L}\left(\sigma_p - \sigma_i\right) \\ &\equiv 1/E_p \end{aligned} \tag{10}$$

Note that this latter, constant modulus, region has *exactly* the same magnitude as that for unloading (Eqn. 7). The reloading strain may be analyzed in the same manner as the unloading strain, described above.

5.3 The Elastic Modulus

The elastic modulus has an explicit linear dependence on crack density, given by $(\bar{d} < \bar{d}_s)$,[4]

$$\begin{aligned} \left(E/E^* - 1\right) &= \mathcal{B}R/\bar{d} \\ &= \mathcal{D} \end{aligned} \tag{11}$$

where $\mathcal{B}$ is a constant for a particular composite (fixed f and E_f/E_m) and $\mathcal{D}$ is designated the matrix damage parameter. Upon combining with Eqn. (1) to eliminate $\bar{d}$, (at $\sigma_{mc} < \sigma \leq \sigma_s$),

$$\left(E/E^* - 1\right) = \left[E/E_s^* - 1\right]\left[\sigma_s/\sigma_{mc} - 1\right]\left(\sigma_p/\sigma_{mc} - 1\right) \tag{12}$$

where E_s^* is the modulus at matrix crack saturation. This relationship is particularly useful for analysis of matrix damage.

5.4 The Misfit Stress

For LDE materials, the moduli E_p and E^* are related to the misfit stress σ^T through the formula,[12]

$$\sigma^T = \frac{\left[1/E_p - 1/E^*\right]^2}{8\mathcal{L}\left(1/E_p - 1/E\right)} - E\sigma_p\left(1/E_p - 1/E_s\right) \tag{13a}$$

where E_s is the secant modulus, given by

$$E_s = \sigma_p/\varepsilon_p \tag{13b}$$

Hence, with $\mathcal{L}$, E^* and E_p already determined, the misfit stress can be calculated. Alternatively, $\mathcal{L}$ may be eliminated by combining Eqn. (13a) with Eqn. (7) and σ^T evaluated from the moduli and the debond stress.

The misfit stress for SDE materials may be evaluated from the permanent strain ε_o, given by[12]

$$\varepsilon_o/\mathcal{L} \;=\; 4\sigma^T\left(\sigma_p-\sigma_i\right)+\sigma_p^2-2\sigma_i^2+\varepsilon^*/\mathcal{L} \tag{14}$$

where ε^* is the misfit relief strain given by[4,12]

$$\varepsilon^* \;=\; \left[1/E^*-1/E\right]\sigma^T \tag{15}$$

The procedure is formalized by eliminating ε^*. This is achieved by using Eqn. (2c) for $\mathcal{L}$ and Eqn. (11) for E/E^* to give

$$\varepsilon^*/\mathcal{L} \;=\; \mathcal{B}\beta(E_m\tau/E)\sigma^T$$

or

$$\varepsilon^*/\mathcal{L} \;\equiv\; \sigma_\tau\sigma^T \tag{16}$$

A similar equation in terms of $\mathcal{L}_S$ and E_*^* can be obtained by using Eqns. (2c) and (12). Then, upon inserting Eqn. (16) into Eqn. (14), there is an explicit dependence of $\varepsilon_o/\mathcal{L}$ on σ^T,

$$\varepsilon_o/\mathcal{L}-\sigma_p^2 \;=\; 4\sigma^T\sigma_p+\sigma_\tau\sigma^T-4\sigma_i\sigma^T-2\sigma_i^2$$

or

$$\varepsilon_o/\mathcal{L}-\sigma_p^2 \;\equiv\; \xi_1\sigma_p+\xi_2 \tag{17}$$

Hence, by plotting $[\varepsilon_o/\mathcal{L}-\sigma_p^2\,]$ against σ_p, the slope,

$$\xi_1 \;=\; 4\sigma^T, \tag{18}$$

gives the misfit stress directly. With σ^T known, Eqn. (14) can be used to estimate the debond stress, σ_i.

5.5 Some Useful Interrelationships

An interface sliding stress index, $\mathcal{T}$, may be obtained by combining Eqns. (2c) and (12) to give

$$\mathcal{T} \equiv \mathcal{L}\left(E/E^{*}-1\right)^{-1} = \frac{\beta\left(R/\bar{d}_{o}\tau E_{m}\right)}{\left(E/E_{o}^{*}-1\right)} \tag{19}$$

The index $\mathcal{T}$ is thus constant, provided that τ is a material property. This constancy yields a procedure for assessing the *admissibility* of the data, described below.

Other formulae may be derived which can also be used to evaluate E^{*} and $\mathcal{L}$. It is possible to define another modulus, designated the hysteresis modulus, $\bar{E}$, given by

$$\bar{E} = \sigma_{p}/\left(\varepsilon_{p}-\varepsilon_{o}\right). \tag{20}$$

Then, with Eqn. (7), for LDE

$$1/E^{*} = \left[\sigma_{p}/\bar{E}-\left(\sigma_{p}-\sigma_{i}\right)/E_{p}\right]\left(\sigma_{p}-\sigma_{i}\right)^{-1} \tag{21}$$

and

$$\mathcal{L} = \left(\frac{1}{\bar{E}}-\frac{1}{E_{p}}\right)\frac{\sigma_{p}}{2\left(\sigma_{p}-\sigma_{i}\right)\left(2\sigma_{i}-\sigma_{p}\right)} \tag{22a}$$

For SDE

$$\mathcal{L} = \left(\frac{1}{E} - \frac{1}{E^*}\right)\frac{1}{\sigma_p} \tag{22b}$$

6. ANALYSIS

6.1 Preliminary Considerations

The strains are first fit to a high level polynomial. The tangent moduli are then obtained from the derivative. Some basic data obtained using a seventh order polynomial fit are presented on Figs. 7a and 7b. Two issues evident from these plots will be addressed before proceeding with a detailed interpretation.

(i) In the SiC/CAS, matrix stress corrosion occurs[26] such that the crack spacing often changes during a hysteresis cycle. These crack density changes proceed at the higher stresses within the cycle. Consequently, when truncated at $\sigma_r/\sigma_p \approx 0.8$ (Fig. 7b), the data appear to exhibit well-behaved linearity.

(ii) Variability in the debond and sliding resistances among the interfaces obtains in SiC/SiC. A qualitative comparison of the unload and reload tangent curves for SiC/SiC (Fig. 7a) with the theoretical form (Fig. 6) provides insight about the debonding and sliding. There are four main factors. (i) The plateau and linear zones have consistently *better definition upon reloading* than unloading. (ii) A definitive plateau is not usually attained upon unloading, such that $1/E_u$ is *always smaller* than the plateau value $1/E_p$, obtained from reloading. (iii) The *elastic modulus* E^* obtained by extrapolation of the linear region *consistently smaller for reloading*. (iv) There is clear evidence of a *closure* effect in unloading, beginning at $\sigma_u/\sigma_p \approx 0.2$. Yet, the reload data in the same stress range appear to be well-behaved and devoid of the non-linearities expected from the presence of closure.

Various implications are made from these trends. The basic conclusion is that for SiC/SiC composites, greater reliance is placed on the *reload* data. The absence of an abrupt onset of a plateau upon unloading in contrast with the definitive plateau found upon reloading suggests that there is a *distribution* of debond and sliding resistances at the interfaces. Upon unloading, this distribution causes slip to arrest at some interfaces but not at others. This process continues as unloading proceeds, resulting in a gradual approach to the nominal plateau. It is also speculated that there are some readjustments of the interfaces during this process, such that τ and Γ_i degrade at those interfaces having the larger values. As a result, there is greater interfacial uniformity when the reloading begins. This readjustment leads to a definitive transition stress, σ_{tr}, on reloading, which may be used to provide the best estimate of σ_i. The hypothesized τ and Γ_i distributions among the fibers are also consistent with the observation that the initial slope of the unloading modulus is always smaller than that found for reloading (smaller $\mathcal{L}$ signifies larger τ, Eqn. 2c). Moreover, these interface readjustments on unloading lead to the non-linearities in the initial unloading data, which create difficulties in the extrapolation used to evaluate, $1/E^*$. Finally, it is proposed that inelastic effects obtain during closure. Such deformations begin on unloading at stresses, $\sigma_r/\sigma_p \lesssim 0.2$, and cause some 'flattening' of the matrix crack surface contacts. Then, surface separation upon reloading occurs at appreciably smaller stresses, $\sigma_r/\sigma_p \approx 0.1$. The consequence is that the initial reload data are consistent with the behavior expected *solely from interface sliding*.

Another general observation before proceeding is that the results at small peak stresses are more susceptible to error, because the inelastic strains are relatively small. In general, therefore, more credence is given to measurements obtained at larger σ_p. A method for assessing the σ_p range in which the measurements are *admissible* uses the shear stress index, $\mathcal{T}$ (Eqn. 9). Only those results for this index which are independent of σ_p, within an acceptable range, should be considered amenable to further analysis.

6.2 Data Analysis

Initial emphasis is given to the reloading data for SiC/SiC. The magnitudes of E_r^{-1} are plotted on Fig. 8. From these plots, the inelastic strain index, $\mathcal{L}$, and the matrix damage parameter, $\mathcal{D}$, are obtained by using Eqn. (3), according to the method of Fig. 6. These are plotted against σ_p (Figs. 9, 10). The shear stress index, $\mathcal{T}$, is plotted on Fig. 11. The *matrix damage* data (Fig. 9) appear to be well-behaved and have the expected linearity, with no evidence of matrix crack saturation. Moreover, the intercept on the stress axis, $\sigma_{mc} \approx 280$ MPa is consistent with σ_{mc} obtained from the matrix crack density measurements (Fig. 2). The results for $\mathcal{L}$ (Fig. 10) have a less systematic dependence on the stress. However, the plot of the shear stress index (Fig. 11) indicates that the data are *inadmissible* at stresses, $\sigma_p \lesssim 306$ MPa, because the experimental estimate of $\mathcal{T}$ is not invariant in this range. Further analysis focusses on the admissible results at higher stresses. Then, reasonable linearity is apparent (Fig. 10), especially when σ_{mc} obtained from the matrix damage plot (Fig. 9) is used as the *required intercept* on the stress axis. These data may be used with the matrix crack spacing measurements to obtain *the sliding stress*, by using Eqn. (2b). The values obtained are in the range, $\tau = 50 \pm 10$ MPa, with no systematic dependence on the specific value of $\bar{d}$. (It would thus be feasible to use a single $\bar{d}$ measurement to determine τ.) The *debond stress*, obtained from the measurements of σ_{tr}, is plotted against σ_p on Fig. 12. The insensitivity to σ_p constitutes a check on the consistency of the procedure, since σ_i should be independent of the applied stress. The values obtained are $\sigma_i = 270 \pm 20$ MPa. The *misfit stress* obtained from the measurements of E_p (Fig. 10) upon using Eqn. (13) are plotted against σ_p on Fig. 13. This stress should also be independent of σ_p. The variations reflect measurement errors and inadmissible data at small σ_p. Emphasizing the admissible results at large σ_p, the misfit stress is, $\sigma^T = 100$

$\pm$ 20 MPa. Based on the preceding estimations of σ_i and σ^T, the debond energy can be obtained from Eqn. (5) as, $\Gamma_i = 4 \pm 1.5\ Jm^{-2}$.

The procedure is repeated for SiC/CAS, using reload data in the range, $\sigma_r/\sigma_p \lesssim 0.8$, because of stress corrosion[26] (Fig. 14). In this case, there is not a definitive transition in $1/E_r$ to a plateau, and σ_i cannot be explicitly obtained from these data. Both $1/E_r$ and $1/E_u$ exhibit reasonable linearity and a linear fit may be used to obtain E^* and $\mathcal{L}$. At stresses, $\sigma_p \lesssim \sigma_s$, the unload and reload behaviors give equivalent values indicating that there is relative uniformity in the sliding and debonding resistances of the interfaces in this composite.

The damage matrix parameter, $\mathcal{D}$, is plotted against stress, σ_p, on Fig. 9 and $\mathcal{L}$ is plotted on Fig. 15. The shear stress index $\mathcal{T}$ is plotted on Fig. 16. Again, the *matrix damage* data exhibit high fidelity (Fig. 9), being linear with σ_p and having a stress intercept consistent with σ_{mc} from crack density measurements. The inelastic strain index (Fig. 15) is subject to error at smaller stresses. The admissible range (Fig. 16) is $\sigma_p \gtrsim 290$ MPa. With this restriction, there is acceptable linearity of $\mathcal{L}$ with σ_p, especially when connected to σ_{mc}, previously evaluated from the E^* data. Upon using the crack spacing, these $\mathcal{L}$ give an interface *sliding resistance*, $\tau = 20 \pm 3$ MPa. Again, there is no significant dependence on the value of $\bar{d}$ used; a single value would have sufficed.

The misfit stress is extracted from the permanent strain and from $\mathcal{L}$ by using Eqn. (17). The requisite plot (Fig. 17) indicates that there is considerable scatter in the data. A least square fit thus provides a low correlation coefficient. Additional measurement would be needed to obtain σ^T with acceptable confidence. The alternative approach used here is to ascertain whether the estimate of σ^T obtained from the crack density measurements can be used to fit the data and also provide a reasonable value for the debond stress. A linear fit with $\sigma^T = 25$ MPa is shown on Fig. 19. This fit gives $\sigma_i = 100 \pm 30$ MPa. Taken together, these stresses may be used with Eqn. (5) to give a

reasonable debond energy, $\Gamma_i = 0.5 \pm 0.3\ Jm^{-2}$. However, a more complete assessment of the method would require additional data.

7. DISCUSSION

A comparison of the present measurements of constituent properties (Table II) with values obtained by others using different methods (Table I) provides an important check on the hysteresis approach. The most comprehensive prior analysis has been on SiC/CAS, particularly measurements of τ. The present values agree closely with those obtained by multiple fiber push-out[22] ($\tau = 17 \pm 3$ MPa) and is similar to the average value obtained by single fiber push-in tests[27] ($\tau = 22 \pm 3$ MPa). The small debond energy is also consistent with estimates made from fiber push-in tests.[27] The misfit strain σ^T is considerably smaller than that found previously,[3] *consistent* with the larger stresses needed for matrix cracking (Fig. 2) and the larger stresses needed to cause inelastic deformation (Fig. 4). It is surmised that different consolidation conditions where used to prepare the present material, resulting in a lower residual stress.

The comparisons for SiC/SiC are less conclusive because of the wide range of constituent properties reported in the prior literature. The present values lie within the reported range. However, further judgments might be made upon assessing the quality of the literature data. The most complete and precise measurements of τ and Γ_i have been obtained from fiber push-in tests.[21] These tests gave values, $\tau \approx 60$ MPa, comparable to the present measurements (Table II). These same tests gave debond energies in the range 2–6 Jm^{-2}, again similar to the present data. The thermal expansion coefficient for Nicalon fibers and vapor deposited SiC indicates a mismatch,[23] $\Delta\alpha \approx 0.8 \times 10^{-6}C^{-1}$. With this choice and a temperature change from CVI,[23] $\Delta T \approx 1000°C$, the misfit stress can be estimated as $\sigma^T \approx 120$ MPa, similar to the present

estimate. Consequently, the constituent property measurements appear to be compatible with the values expected from the literature.

It has been possible to obtain consistent determination of the constituent properties of the SiC/SiC composite with relatively few hysteresis loop measurements obtained in a single tensile test. Similar consistency has not been found for the SiC/CAS composite. Although the matrix damage parameter $\mathcal{D}$ and the sliding resistance τ could be obtained with acceptable precision from a small number of hysteresis measurements, made in a single test, there are problems with estimation of the debond stress and the misfit stress. There are two reasons for the problems. One concerns the occurrence of stress corrosion cracking[26] which affects the data at higher stresses. This problem could be overcome by testing in a dry atmosphere. The other limitation seems to be associated with SDE materials. For these materials, permanent strain and tangent modulus data need to be *combined* in order to obtain σ^T and σ_i, leading to an accentuation of the measurement errors. Additional tests are thus needed to provide determinations that have acceptable precision.

Finally, some remarks are made about the permanent strains found in the SiC/CAS material (Fig. 5). These strains should be constant after matrix crack saturation when $\mathcal{L}$ and E^* become constant (Eqn. 14). Yet, they continue to increase at strains above σ_s. Such behavior would appear to be at variance with the $\mathcal{L}$ and E^* measurements. This discrepancy is not yet understood, but probably relates to the incidence of fiber failure. Other work on this material[4,9,22] has shown that premature fiber failures occur and contribute to the inelastic strain, such that the composite modulus after saturation is significantly lower than the expected value, $f E_f$. Such behavior would cause the permanent strain to continue increasing at stresses above σ_s, in qualitative agreement with the present data (Fig. 5). However, fiber failure should also cause E^* and $\mathcal{L}$ to change. The magnitudes of these changes are not known. They

may be within the measurement uncertainties indicated on Figs. 9 and 15, such that small changes in $\mathcal{L}$ and E^* exist at stresses above σ_s. This area requires further work.

8. CONCLUSION

Hysteresis measurements made upon the tensile testing of CMCs have been demonstrated as a method for evaluating several constituent properties, such as the stiffness loss, E_*, the interface resistances to sliding τ and debonding Γ_i and the misfit (or residual) stress, σ^T. This approach is particularly straightforward for CMCs having relatively large Γ_i (LDE), such as a SiC/SiC. Then, consistent information about E_*, τ, Γ_i and σ^T can be obtained from a few hysteresis loops measured in a single tensile test. For materials with smaller Γ_i (SDE), τ and E_* can still be obtained from a relatively few loops measured in one test. However, Γ_i and σ^T estimations seemingly require additional data, because the procedure needed to obtain these properties involves the combination of two separate measurements. Further studies of the associated errors and of alternate data treatments are in progress.

The methodology has been developed in a manner that minimizes the need for independent crack density measurements. It has been found that the matrix cracking stress σ_{mc} can be determined with good precision from measurement of the stiffness loss, E_*. This finding has allowed τ to be obtained using the crack spacing at a *single* stress above σ_{mc} and below the saturation stress, σ_s.

TABLE I

Range of Constituent Properties For SiC/CAS and SiC/SiC Obtained From The Literature

Property	Material	
	SiC/CAS	SiC/SiC
Interface Sliding Stress, τ (MPa)[3,14,18,22,27]	15–25	50–150
Interface Debond Energy Γ_i (Jm^{-2})[14,18,21]	0–1	2–6
Misfit Stress σ^T (MPa)[3,23]	120	150–250
Matrix Modulus (GPa)[3,20,23]	97	300

TABLE II

Constituent Properties Obtained From Present Hysteresis Analysis

Property	Material	
	SiC/CAS	SiC/SiC
Matrix Cracking Stress σ_{mc} (MPa)	285 ± 5	270 ± 5
Saturation Stress, σ_s (MPa)	335 ± 6	—
Interface Sliding Stress, τ (MPa)	20 ± 3	50 ± 10
Debond Stress σ_i (MPa)	120 ± 30	260 ± 20
Misfit Stress σ^T (MPa)	(25)	100 ± 20
Debond Energy, Γ_i (Jm^{-2})	0.5 ± 0.3	4 ± 1.5

REFERENCES

[1] J. Aveston, G. A. Cooper and A. Kelly, "Single and Multiple Fracture," pp. 15–26 in *Properties of Fiber Composites*, Conference Proceedings of the National Physical Laboratories, IPC Science and Technology Press Ltd., Surrey, England, 1971.

[2] A. Pryce and P. Smith, "Behaviour of unidirectional and crossply ceramic matrix composites under quasi-static tensile loading," *J. Mater. Sci.*, 27 2695–2704 (1992).

[3] D.S. Beyerle, S.M. Spearing, F.W. Zok and A.G. Evans, 1992. "Damage, Degradation and Failure in a Unidirectional Ceramic-Matrix Composite," *J. Am. Ceram. Soc.*, 75, [10] 2719-2725.

[4] M.Y. He, B.-X. Wu, A.G. Evans and J.W. Hutchinson, "Inelastic Strain Due To Matrix Cracking In Unidirectional Fiber Composites," *Mech. of Mtls.*, in press.

[5] R.Y. Kim and N. Pagano, "Crack Initiation in Unidirectional Brittle Matrix Composites," *J. Am. Ceram. Soc.*, 74[5] 1082–90 (1991).

[6] P. Ladeveze, "Damage Mechanics For Composites," *Proc. JNCS* (Ed. Pluralis) pp. 667–83, Paris, 1986.

[7] W. Curtin, "Theory of Mechanical Properties of Ceramic-Matrix Composites," *J. Am. Cer. Soc.*, 74(11), 2837 (1991).

[8] S.M. Spearing and F.W. Zok, "Matrix Crack Spacing in Brittle Matrix Composites," *Acta Metall. Mater.*, 40 [8] 2033–2043 (1992).

[9] W.A. Curtin, "Multiple Matrix Cracking in Brittle Matrix Composites," *Acta Metall. Mater.*, 41 (1993) 1369.

[10] F. Hild, J.-M. Domergue, F.A. Leckie and A.G. Evans, "Tensile and Flexural Ultimate Strength of Fiber-Reinforced Ceramic-Matrix Composites," *Intl. Jnl. Solids Structures*, in press.

[11] A.G. Evans, J.-M. Domergue and E. Vagaggini, "A Methodology for Relating the Tensile Constitutive Behavior of Ceramic Matrix Composites to Constituent Properties," *J. Am. Ceram. Soc.*, in press.

[12] E. Vagaggini, J.-M. Domergue and A.G. Evans, "Relationships Between Hysteresis Measurements and the Constituent Properties of Ceramic Matrix Composites I: Theory," submitted to the *J. Am. Ceram. Soc.*

[13] J.-M. Domergue and A.G. Evans, "Relationships Between Hysteresis Measurements and the Constituent Properties of Ceramic Matrix Composites III: Cross-Ply Materials," in preparation.

[14] P.D. Jero , R.J. Kerans and T.A. Parthasarathy, "Effect of Interfacial Roughness on The Frictional Stress Measured Using Push-out Tests," *J. Am. Cer. Soc.*, 74(11), 2793, 1991.

[15] T.J. Mackin, P.D. Warren and A.G. Evans, "The Effects of Fiber Roughness on Interface Sliding in Composites," *Acta Metall. Mater.*, **40** [6] 1251–57 (1992).

[16] D.B. Marshall and W. Oliver, "Measurement of Interfacial Mechanical Properties in Fiber-Reinforced Ceramic Composites," *J. Am. Ceram. Soc.*, **70**[8] 542–48 (1987).

[17] D.B. Marshall, "Analysis of Fiber Debonding and Sliding Experiments in Brittle Matrix Composites," *Acta Metall. Mater.*, Vol. 40, No. 3 (1992) pp. 427–441.

[18] F. Rebaillat, J. Lamon and A.G. Evans, "A Microcomposite Test Procedure For Evaluating the Interface Properties of Ceramic Matrix Composites, *J. Am. Ceram. Soc.*, in press.

[19] P. Reynaud, G. Fantozzi and M. Bourgeon, *High Temperature Ceramic Matrix Composites*, (Ed. R. Naslain) pp. 659–66.

[20] X. Aubard, Thèse de Doctorat de L'Université de Paris (Nov. 1992), "Modélisation et Identification du Comportement Mecanique des Materiaux Composites 2D SiC-SiC."

[21] M. Parlier, B. Passilly and O. Sudre, "Caratérisation Micromécanique des Composites," *Introduction of Ceramics Into Aerospace Composites*, Agard Report 795 (1993) pp. 5.1–5.8.

[22] T.J. Mackin and F.W. Zok, "Fiber Bundle Pushout: a Technique for the Measurement of Interfacial Sliding Properties," *J. Am. Ceram. Soc.*, **75** (1992) 3169–71.

[23] J.L. Bobet, J. Lamon and J.L. Lebrun, "Thermal Residual Stress Field in Ceramic Matrix Composites," *High Temperature Ceramic Matrix Composites*, (Ed. R. Naslain *et al.*) Woodhead, U.K. (1993) pp. 515–22.

[24] T.J. Kotil, J.W. Holmes and M. Comninou, "Origin of Hysteresis Observed During Fatigue of Ceramic-Matrix Composites," *J. Am Ceram. Soc.*, **73**[7], 1879–83, 1990.

[25] J.W. Hutchinson and H. Jensen, "Models of Fiber Debonding and Pullout in a Brittle Composite with Friction," *Mech. Mtls.*, **9**, 139–63, 1990.

[26] S.M. Spearing, F.W. Zok and A.G. Evans, "Stress Corrosion Cracking In Unidirectional Ceramic Matrix Composites, *J. Am. Ceram. Soc.*, **77** (1994) 562.

[27] M.H. Lewis, A. Chamberlain, A.M. Daniel, M.W. Pharoah, A.G. Razzell and S. Sutherland, *Introduction of Ceramics Into Aerospace Composites*, Agard Report 795 (1993) pp. 5.1–5.8.

FIGURE CAPTIONS

Fig. 1. Hysteresis loops and the associated parameters a) LDE materials, b) SDE materials, c) The effect of crack closure on unloading.

Fig. 2. Effect of stress on crack evolution in SiC/SiC and SiC/CAS. The results on SiC/CAS are from Beyerle *et al.*,[3] as well as the present study. The difference is related to the residual stress, σ^T.

Fig. 3. SEM images of matrix cracks in: a) SiC/SiC, b) SiC/CAS.

Fig. 4. Stress/strain curves and hysteresis loops obtained for the two composites. a) SiC/SiC, b) SiC/CAS. The numbering on the latter is used to help identify the loops.

Fig. 5. Variations of permanent strain, ε_o, with applied stress, σ_p, for SiC/SiC and SiC/CAS.

Fig. 6. A schematic showing the forms of the inverse unloading tangent moduli in the LDE regime: E_u^{-1} against unloading stress σ_u and E_r^{-1} against reloading stress σ_r.

Fig. 7. Typical tangent modulus plots for the two composites (a) SiC/SiC, (b) SiC/CAS (the dashed lines represent the extrapolated behavior).

Fig. 8. Reload tangent moduli plots for SiC/SiC.

Fig. 9. Effect of applied stress on the matrix damage parameter, $\mathcal{D}$ for both SiC/SiC and SiC/CAS.

Fig. 10. The inelastic strain index for SiC/SiC. The open data are in the inadmissible range and are not used for the data fit.

Fig. 11. The interface sliding stress index for SiC/SiC indicating the admissible range.

Fig. 12. A plot of the debond stress σ_i against applied stress σ_p for SiC/SiC.

Fig. 13. A plot of the misfit stress σ^T against σ_p for SiC/SiC.

Fig. 14. Tangent modulus data for SiC/CAS at six initial stress levels.
a) unloading, b) reloading.

Fig. 15. The inelastic strain index for SiC/CAS. The open points are in the inadmissible range.

Fig. 16. The interface sliding stress index for SiC/CAS, showing the admissible range.

Fig. 17. A plot of the permanent strain parameter used for evaluating the misfit stress for SiC/CAS.

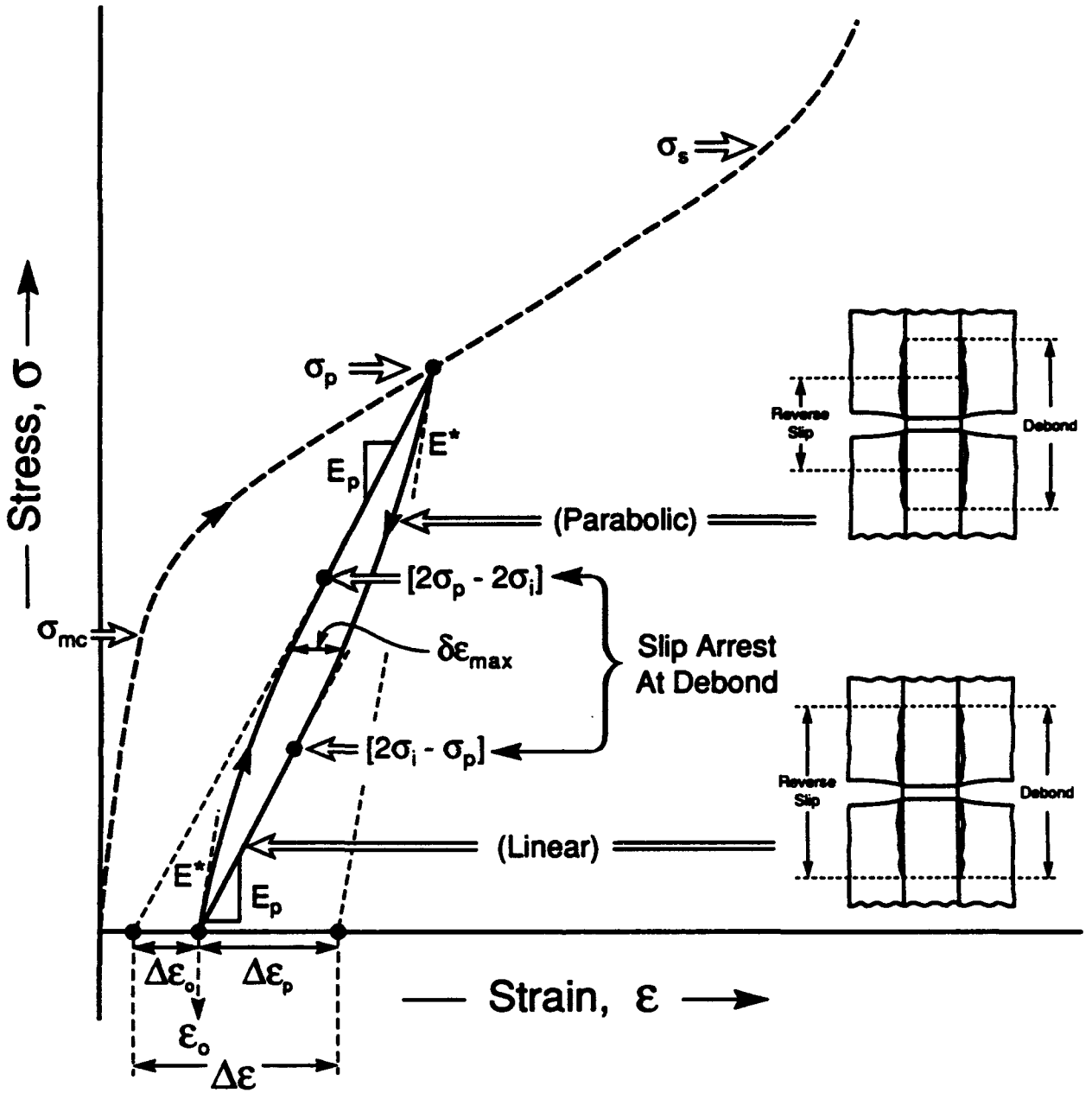

Fig. 1 a). The hysteresis loop for a material with a large debond energy (LDE).

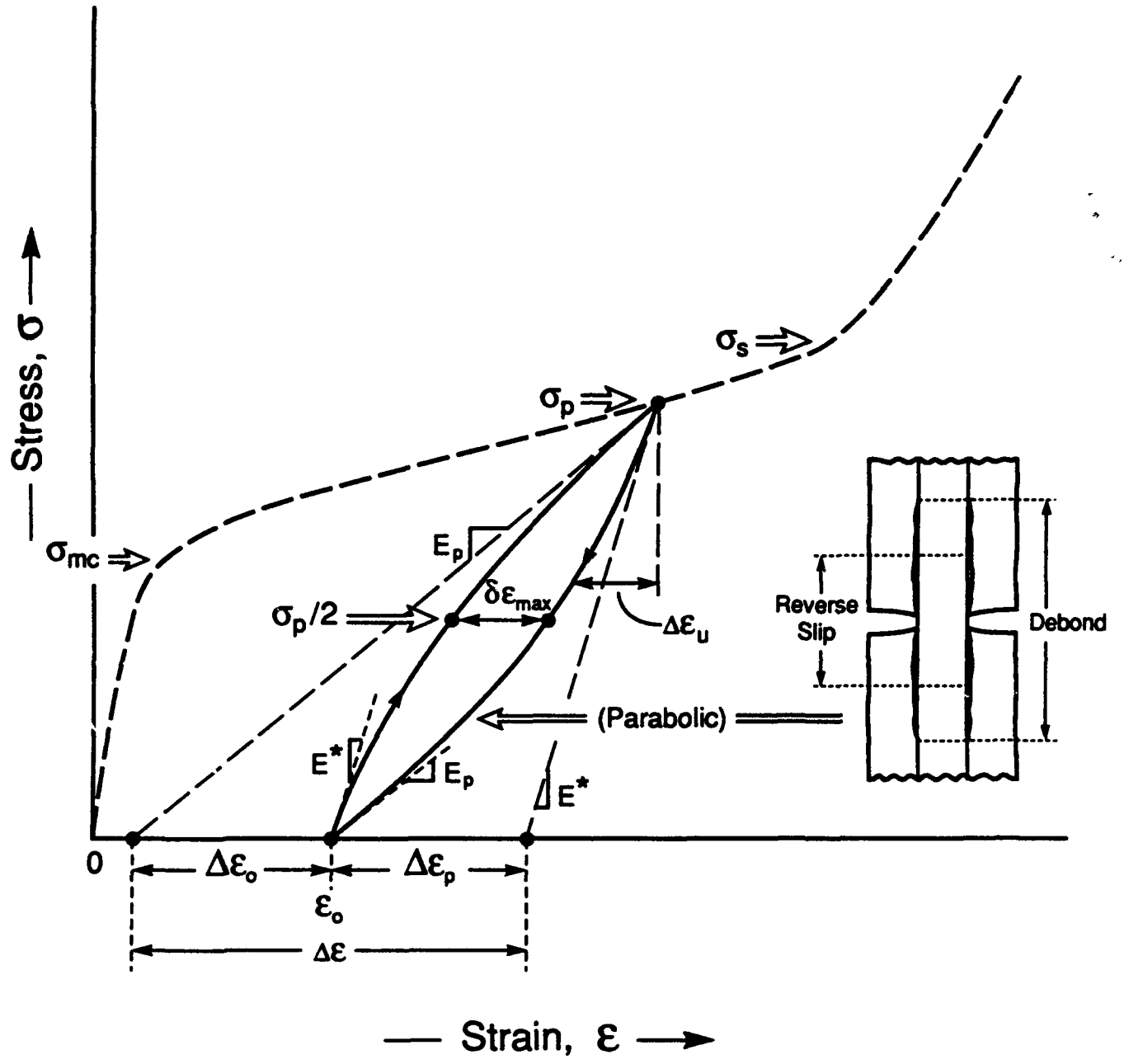

Fig. 1b). The hysteresis loop for a material with a small debond energy (SDE).

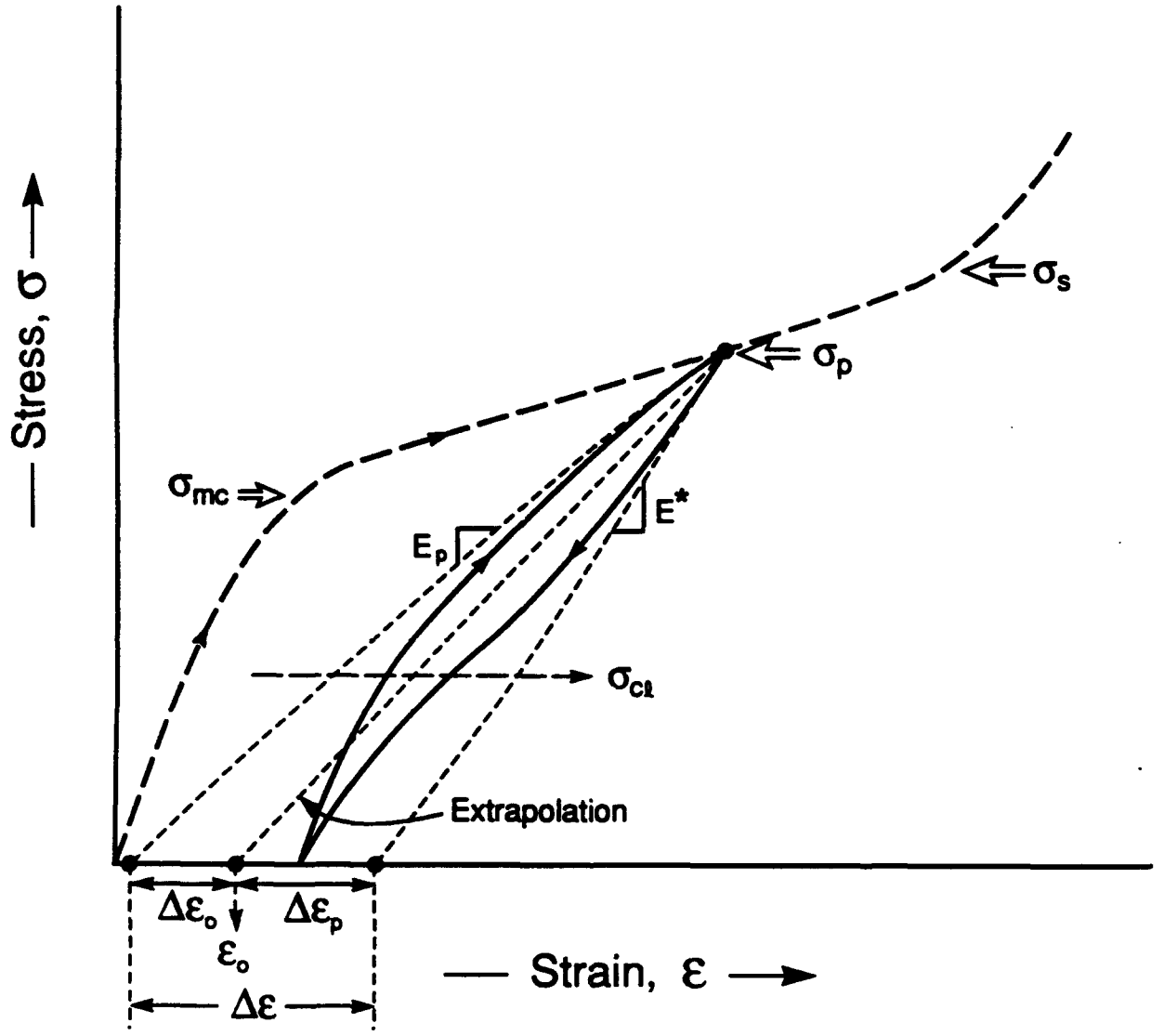
— Stress, σ →
σs
σp
σmc
E*
Ep
σcℓ
Extrapolation
Δεo
Δεp
εo
Δε
— Strain, ε →

Figure 1c

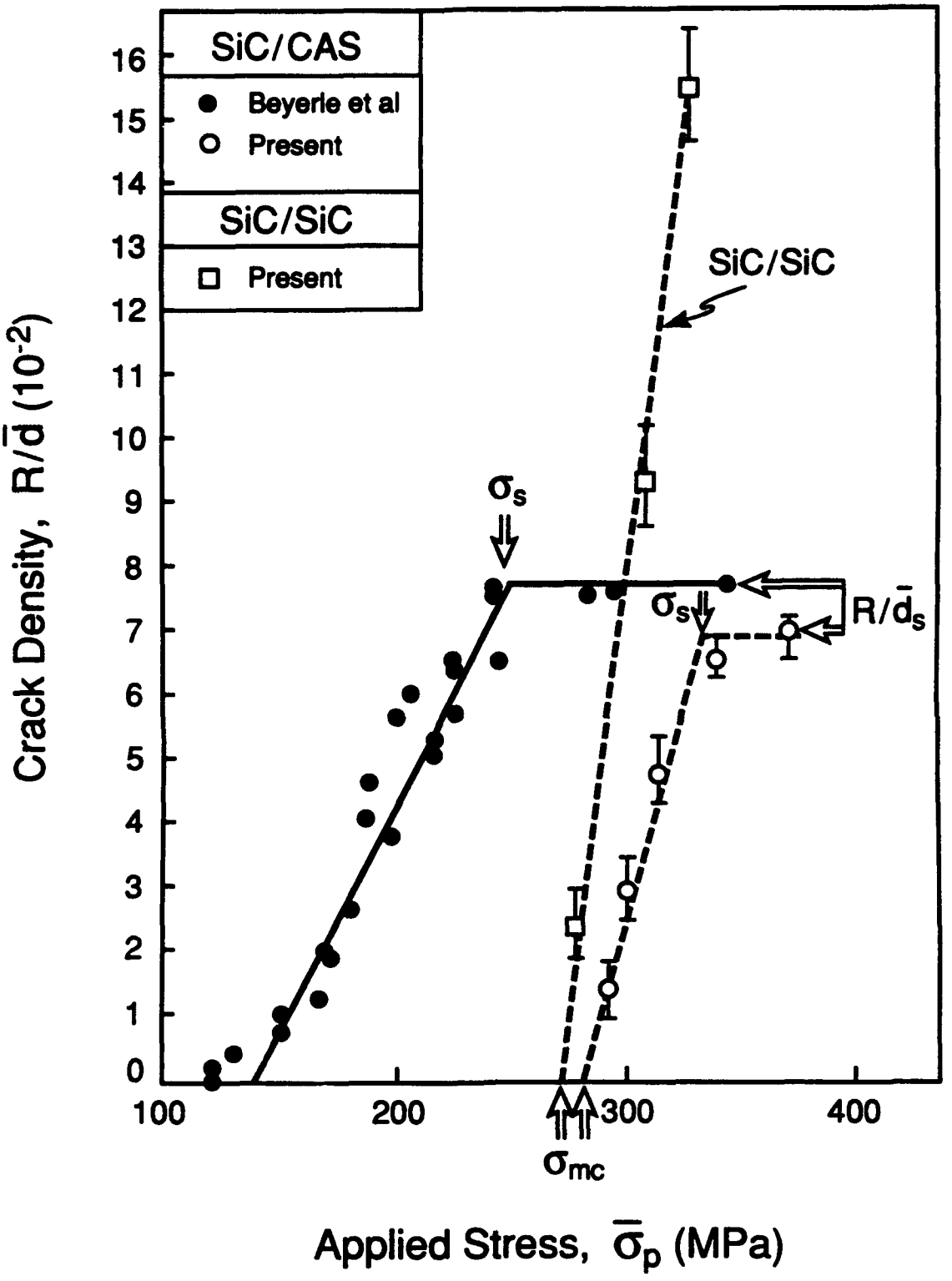
SiC/CAS
Beyerle et al
Present
SiC/SiC
Present
SiC/SiC
σ_s
σ_s
$R/\bar{d}_s$
σ_{mc}
Crack Density, $R/\bar{d}$ (10^{-2})
Applied Stress, $\bar{\sigma}_p$ (MPa)
0
1
2
3
4
5
6
7
8
9
10
11
12
13
14
15
16
100
200
300
400

Figure 2

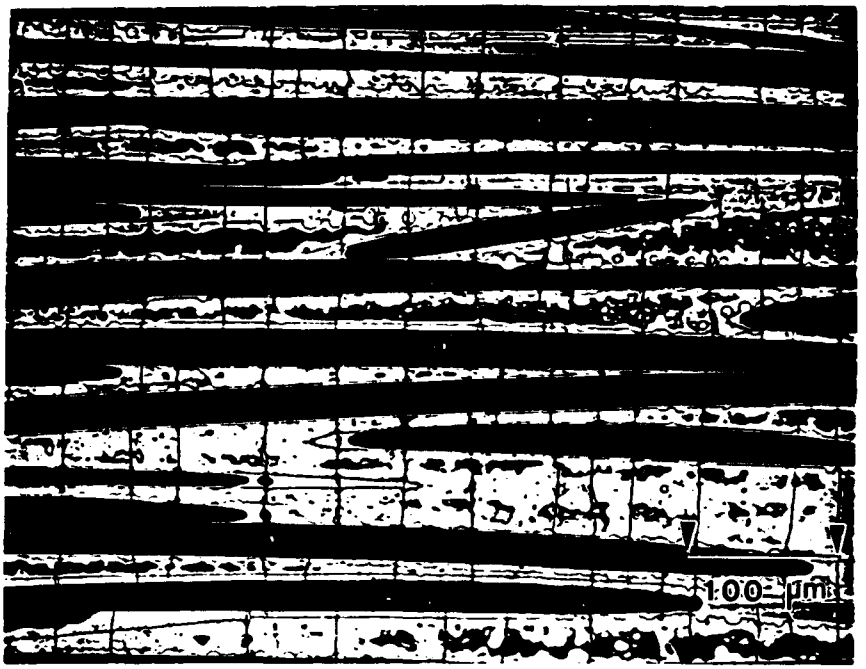

a) SEM observation of matrix cracking in SiC/SiC

b) SEM observation of matrix cracking in SiC/CAS

Figure 3

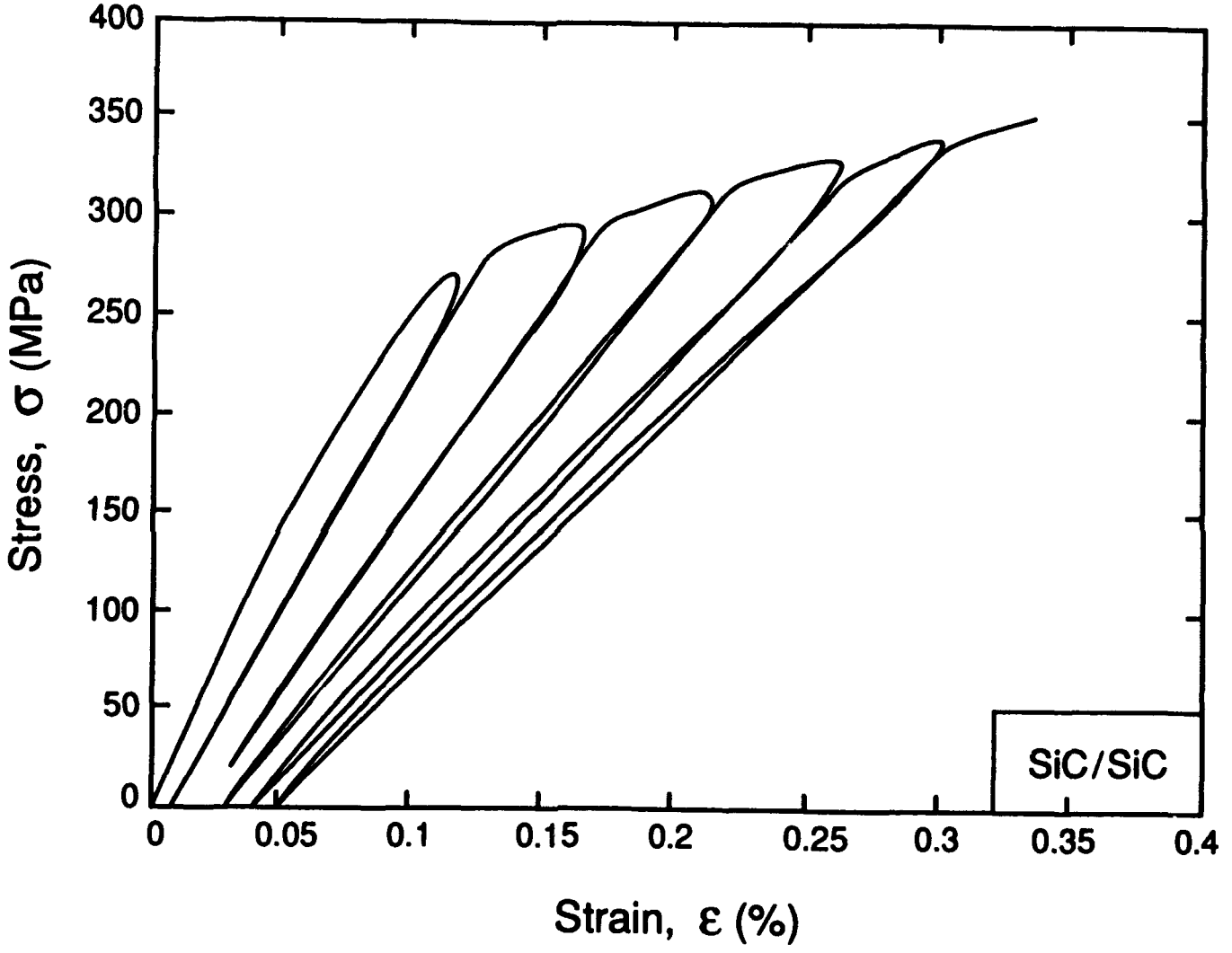
400
350
300
250
200
150
100
50
0
Stress, σ (MPa)
0
0.05
0.1
0.15
0.2
0.25
0.3
0.35
0.4
Strain, ε (%)
SiC/SiC

Figure 4a

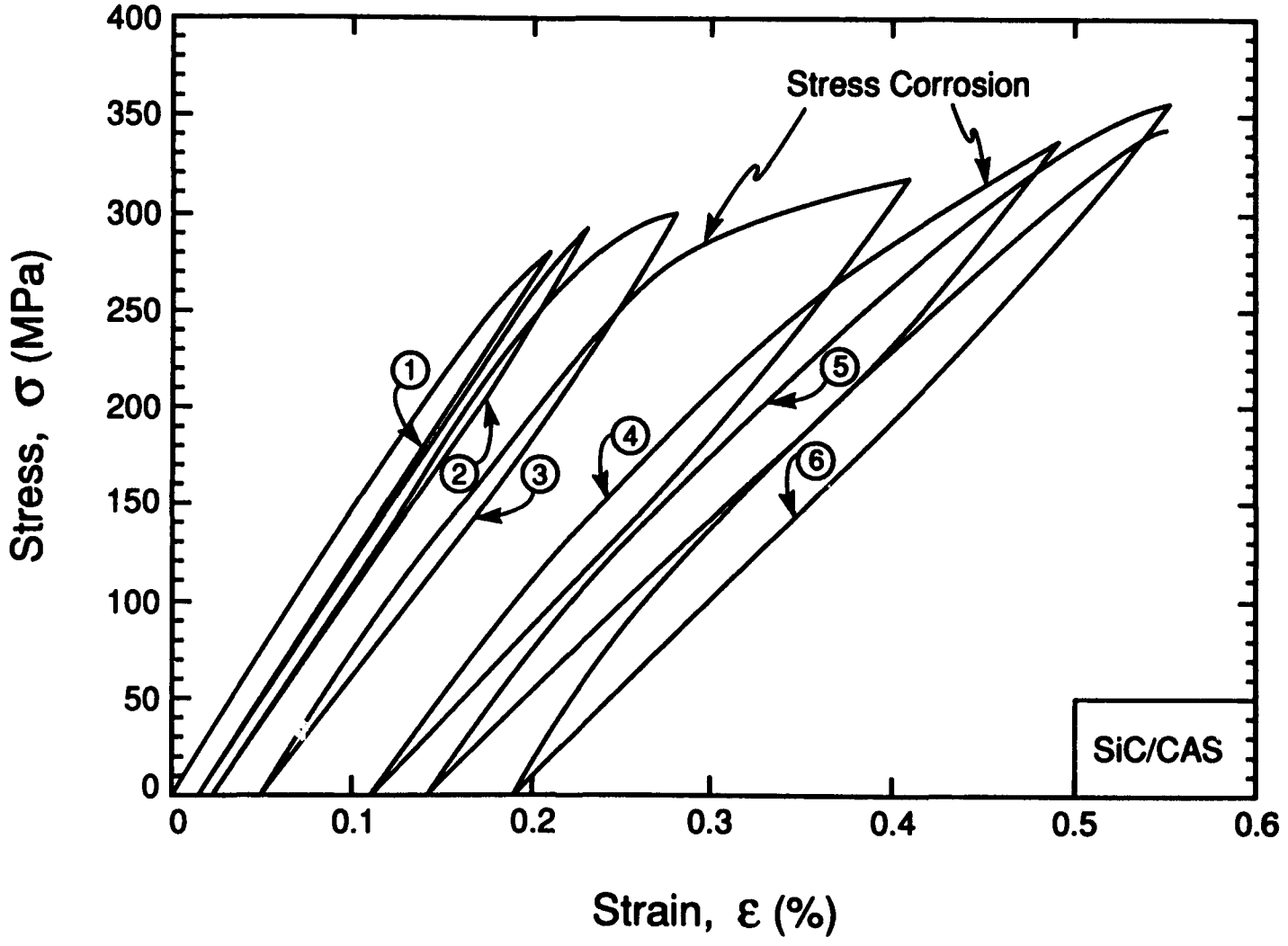
Stress Corrosion
SiC/CAS
Stress, σ (MPa)
Strain, ε (%)
400
350
300
250
200
150
100
50
0
0
0.1
0.2
0.3
0.4
0.5
0.6
1
2
3
4
5
6

Figure 4b

Figure 5

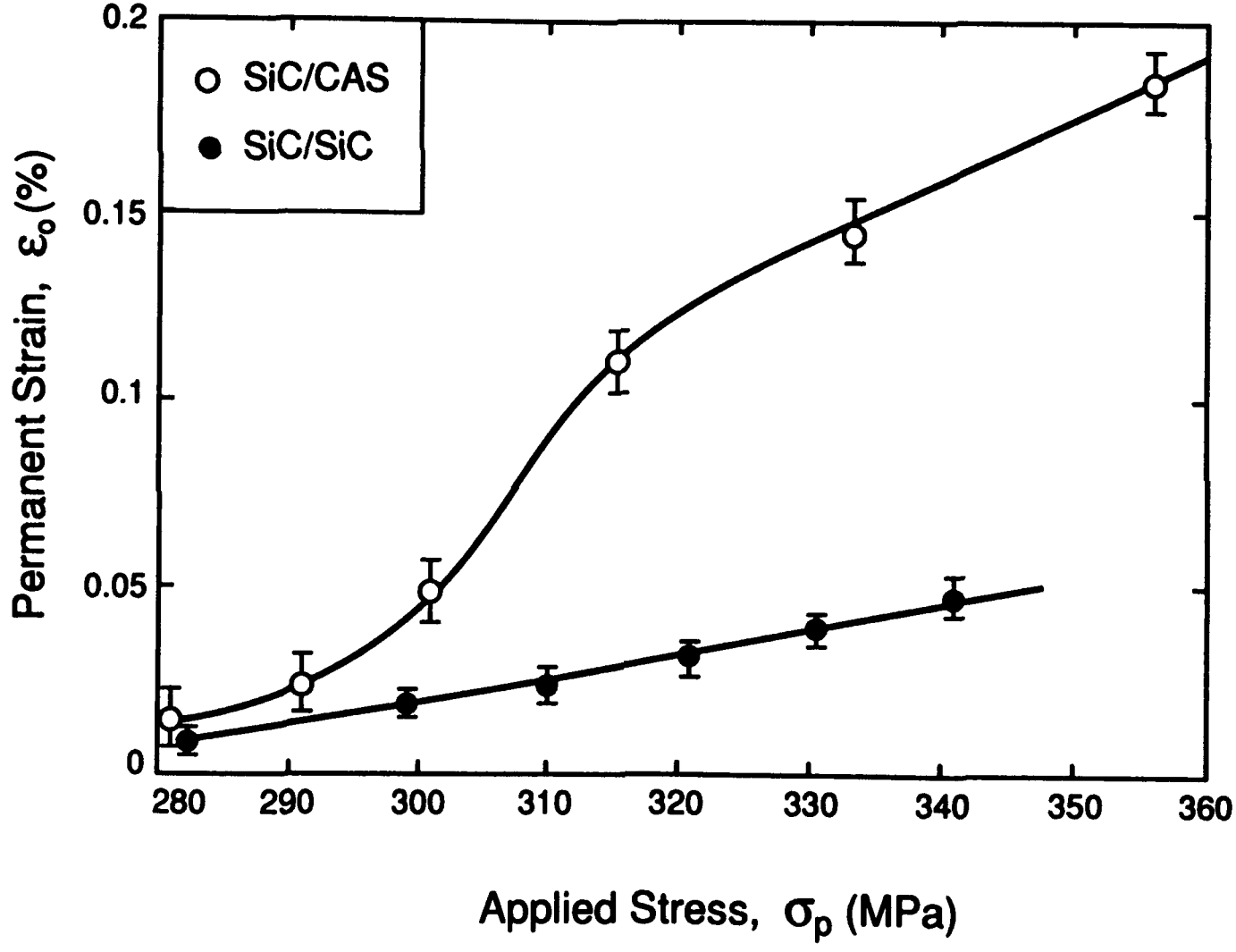
SiC/CAS
SiC/SiC
Permanent Strain, ε_o (%)
0.2
0.15
0.1
0.05
0
280
290
300
310
320
330
340
350
360
Applied Stress, σ_p (MPa)

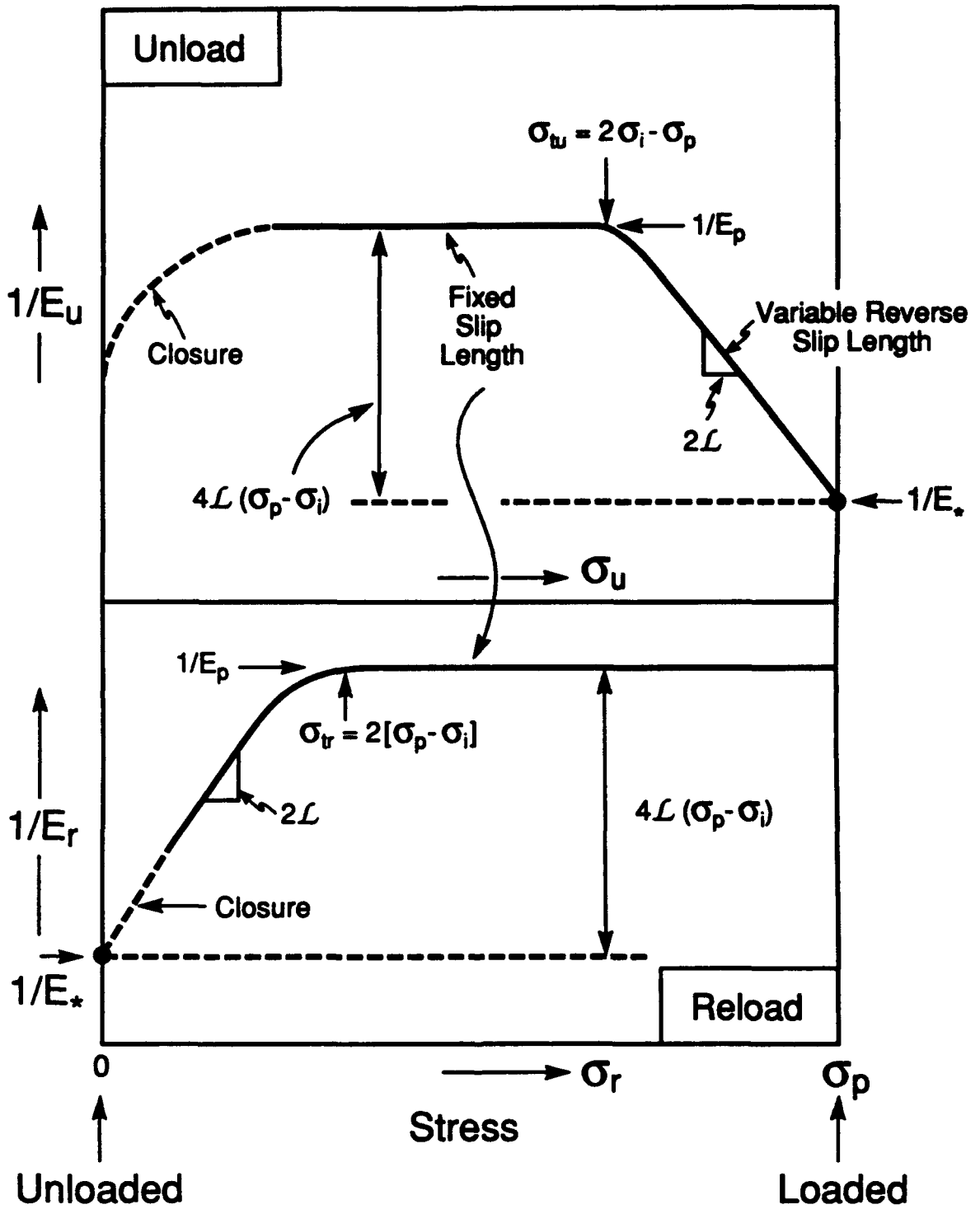
Unload
$\sigma_{tu} = 2\sigma_i - \sigma_p$
$1/E_p$
$1/E_u$
Closure
Fixed Slip Length
Variable Reverse Slip Length
$2\mathcal{L}$
$4\mathcal{L}(\sigma_p - \sigma_i)$
$1/E_*$
σ_u
$1/E_p$
$\sigma_{tr} = 2[\sigma_p - \sigma_i]$
$1/E_r$
$2\mathcal{L}$
$4\mathcal{L}(\sigma_p - \sigma_i)$
Closure
$1/E_*$
Reload
0
σ_r
σ_p
Stress
Unloaded
Loaded

Figure 6

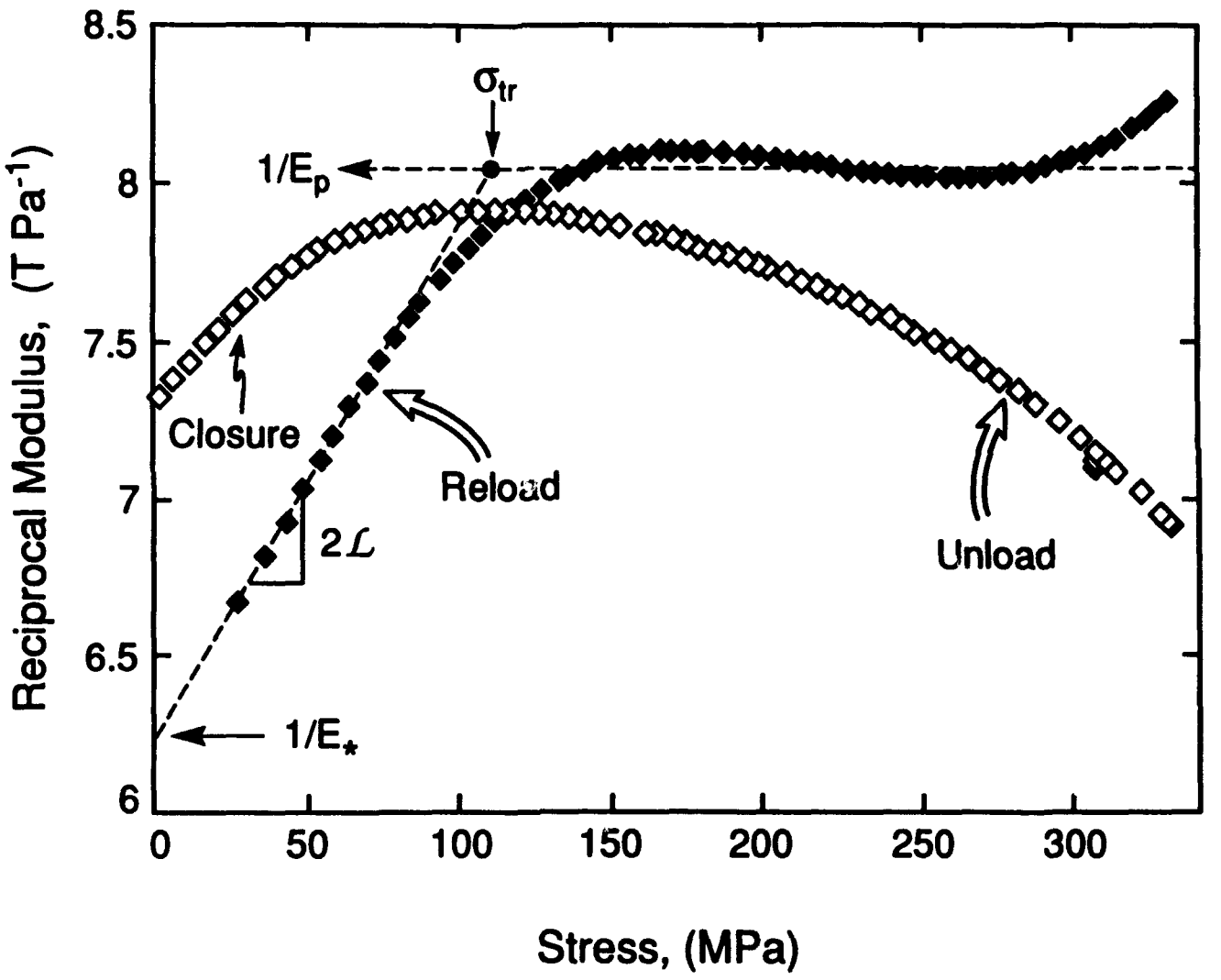
8.5
8
7.5
7
6.5
6
0
50
100
150
200
250
300
σ_{tr}
$1/E_p$
$1/E_*$
$2\mathcal{L}$
Closure
Reload
Unload
Reciprocal Modulus, (T Pa^{-1})
Stress, (MPa)

Figure 7a

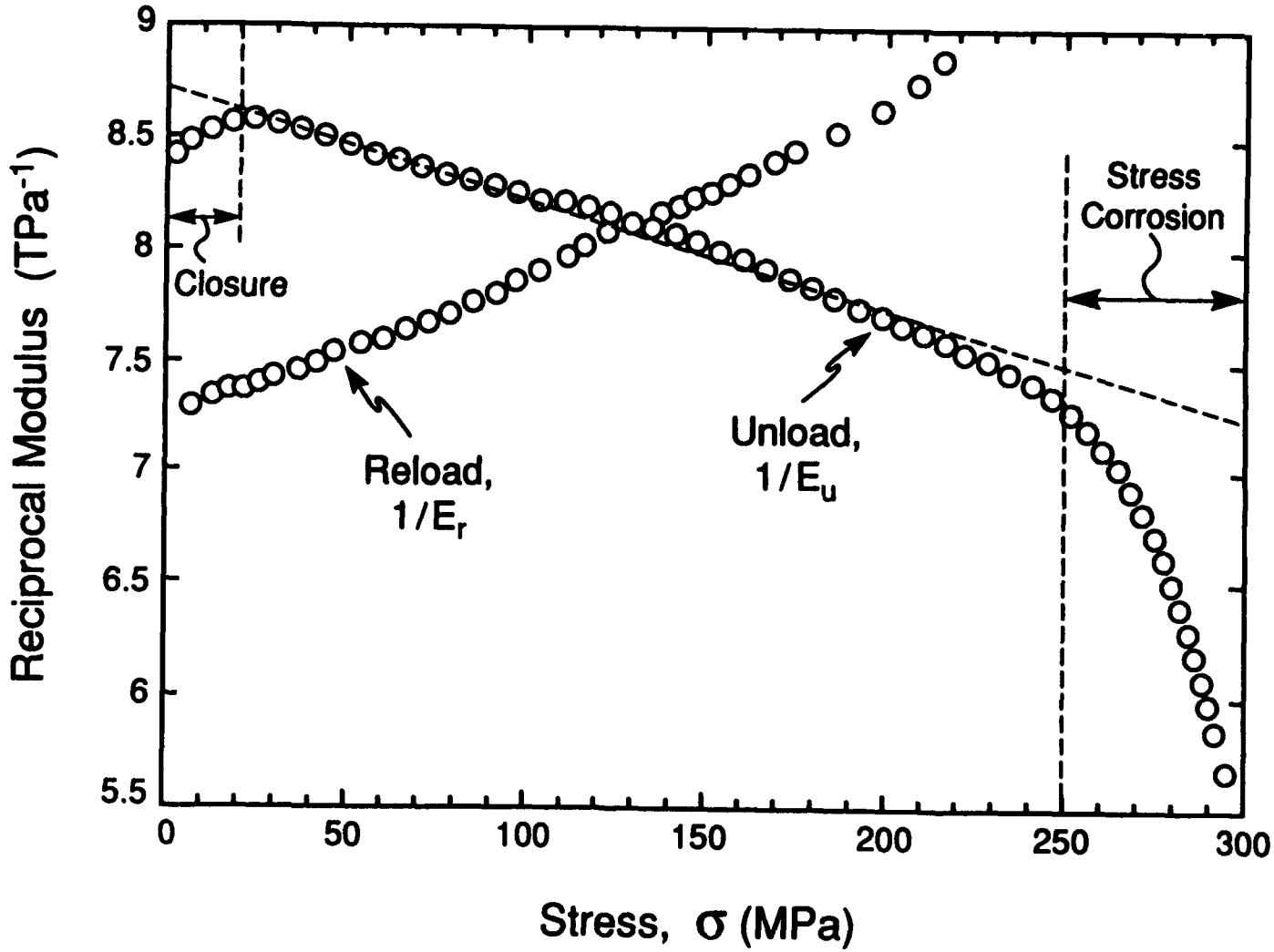
Reciprocal Modulus (TPa^{-1})
9
8.5
8
7.5
7
6.5
6
5.5
0
50
100
150
200
250
300
Stress, σ (MPa)
Closure
Stress Corrosion
Reload, 1/E$_r$
Unload, 1/E$_u$

Figure 7b

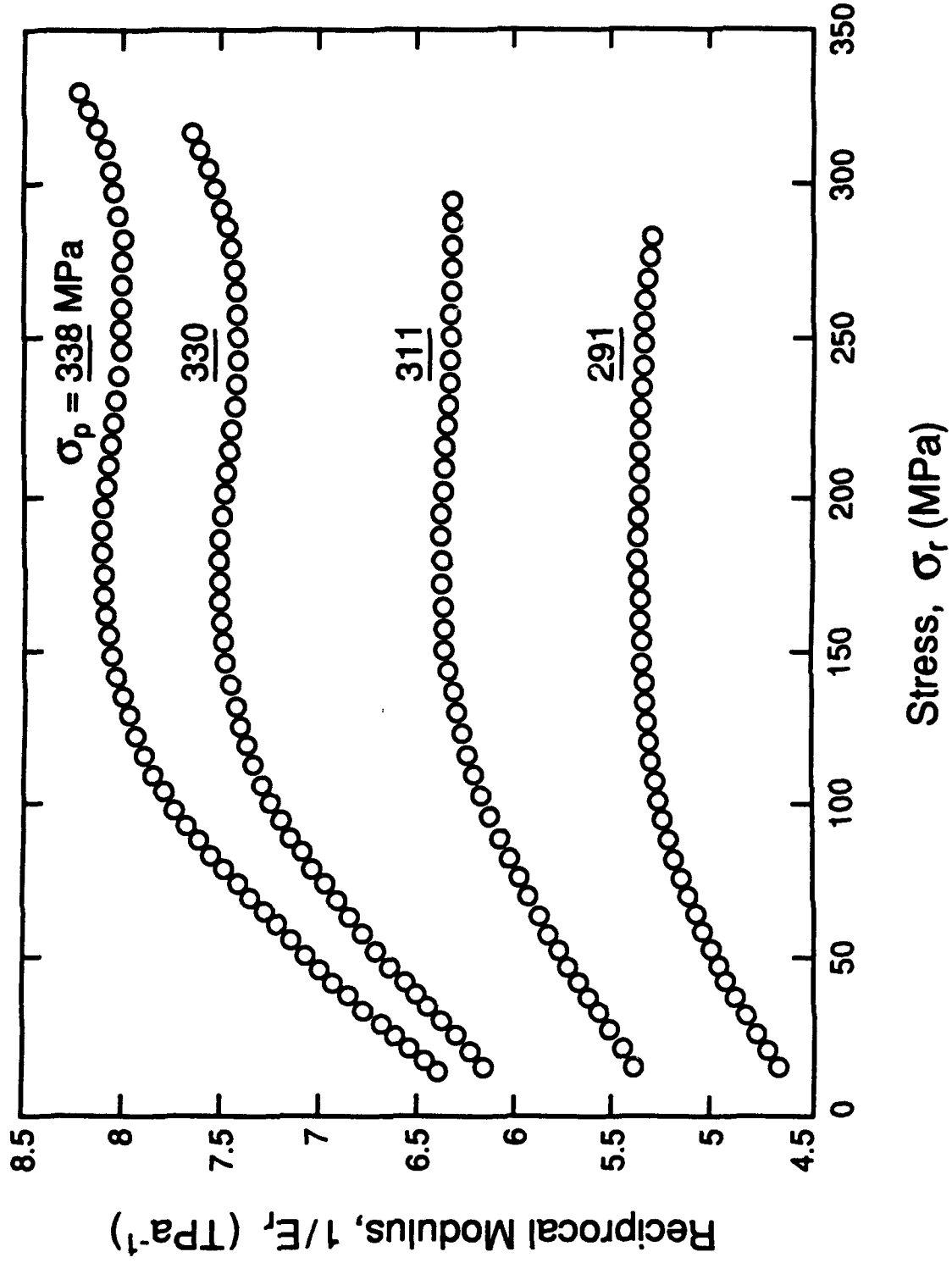

Figure 8

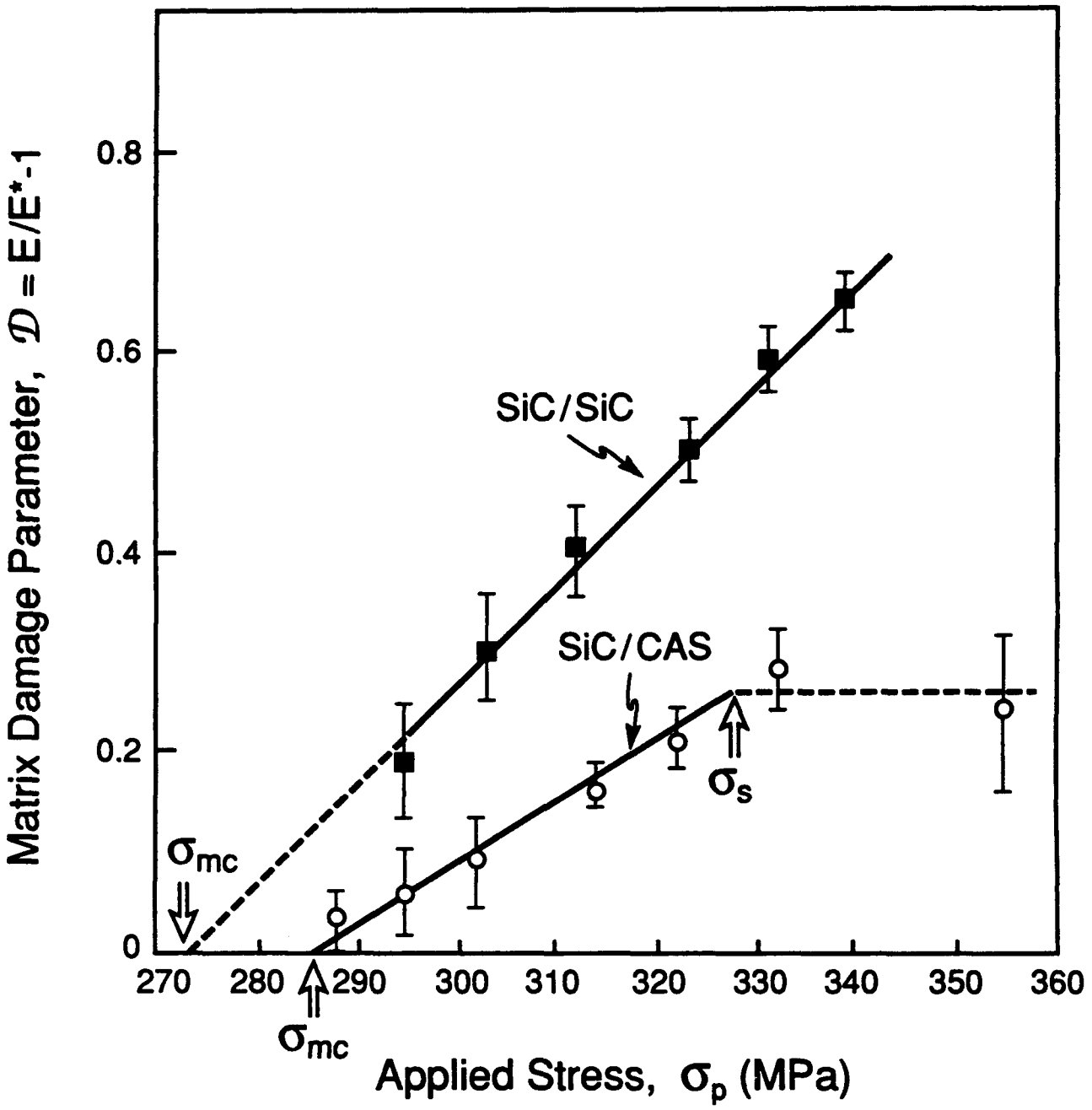
Matrix Damage Parameter, $\mathcal{D} = E/E^* - 1$
0.8
0.6
0.4
0.2
0
SiC/SiC
SiC/CAS
σ_{mc}
σ_{mc}
σ_s
270
280
290
300
310
320
330
340
350
360
Applied Stress, σ_p (MPa)

Figure 9

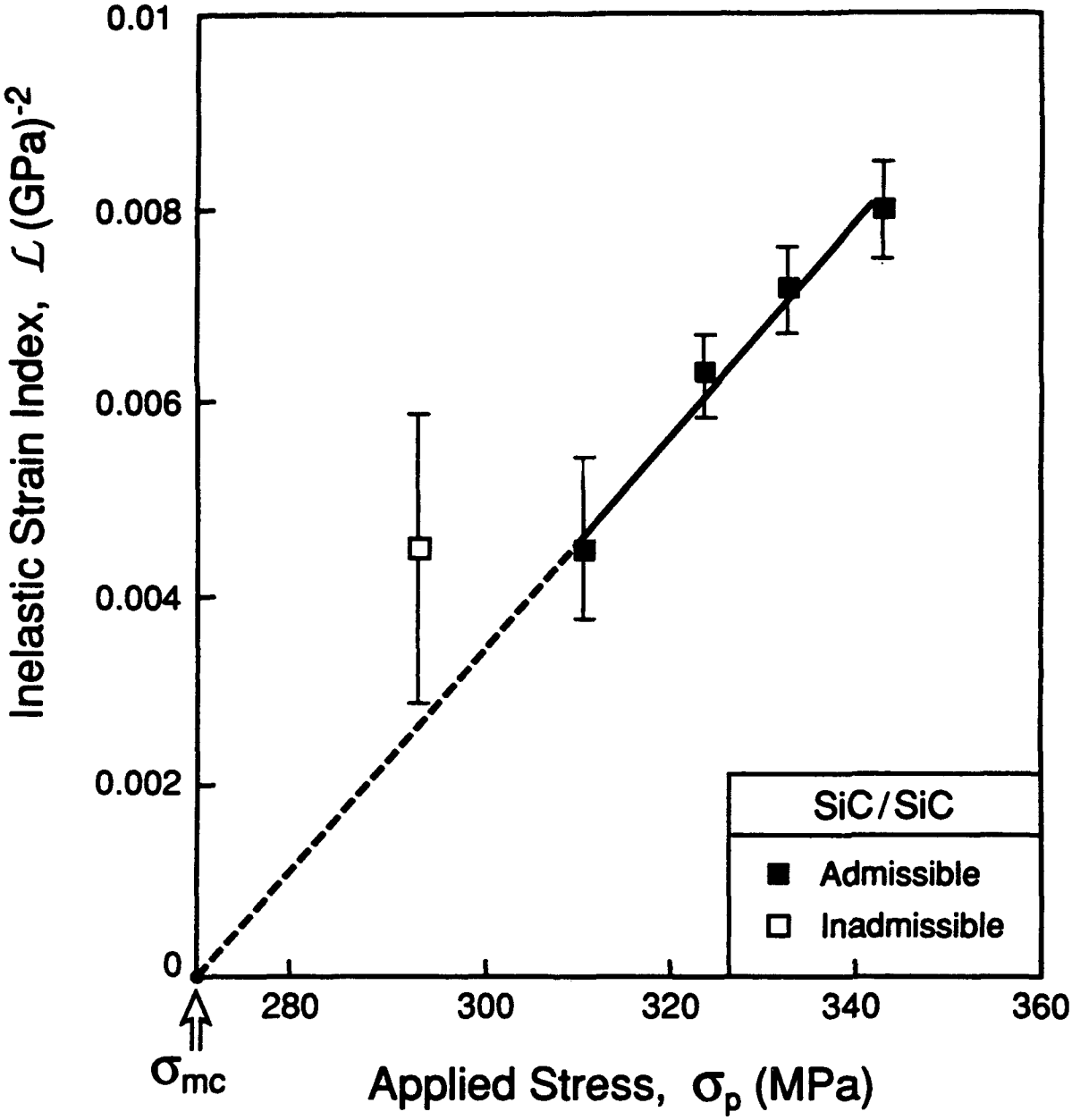
0.01
0.008
0.006
0.004
0.002
0
Inelastic Strain Index, $\mathcal{L}$ (GPa)$^{-2}$
280
300
320
340
360
σ_{mc}
Applied Stress, σ_p (MPa)
SiC/SiC
Admissible
Inadmissible

Figure 10

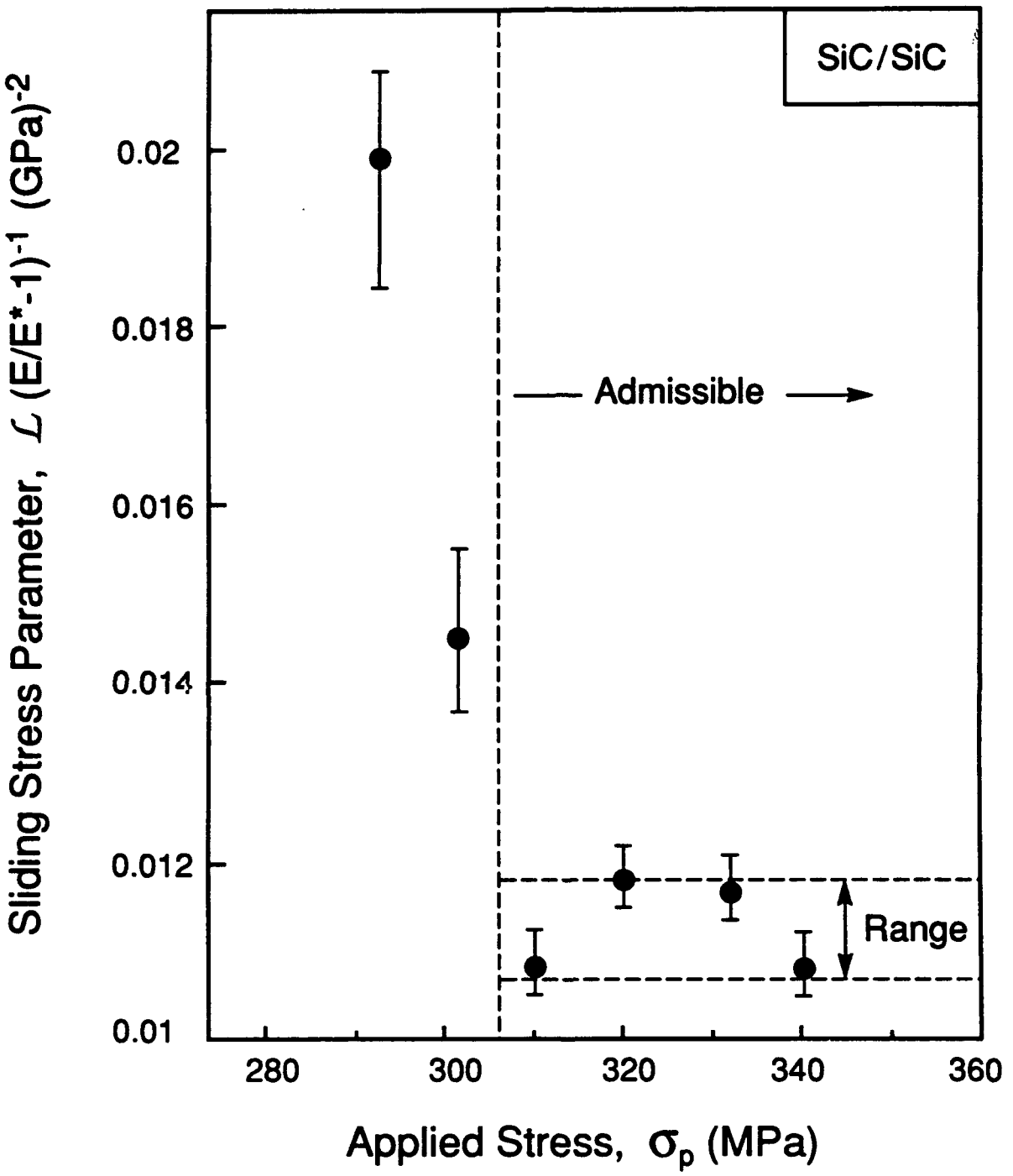
SiC/SiC
Admissible
Range
Sliding Stress Parameter, $\mathcal{L}$ $(E/E^*-1)^{-1}$ $(GPa)^{-2}$
0.02
0.018
0.016
0.014
0.012
0.01
280
300
320
340
360
Applied Stress, σ_p (MPa)

Figure 11

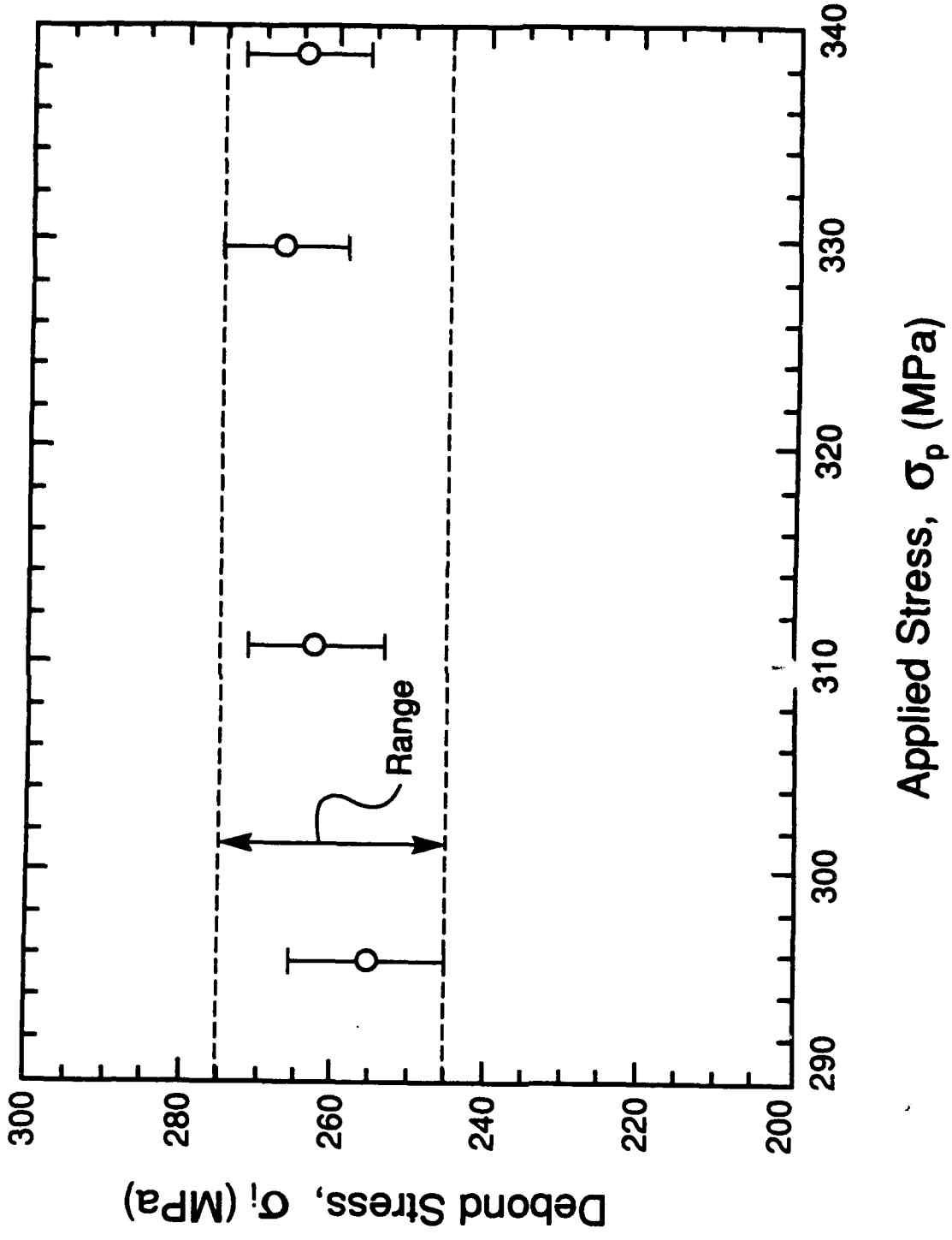
Debond Stress, σ_i (MPa)
300
280
260
240
220
200
Range
290
300
310
320
330
340
Applied Stress, σ_p (MPa)

Figure 12

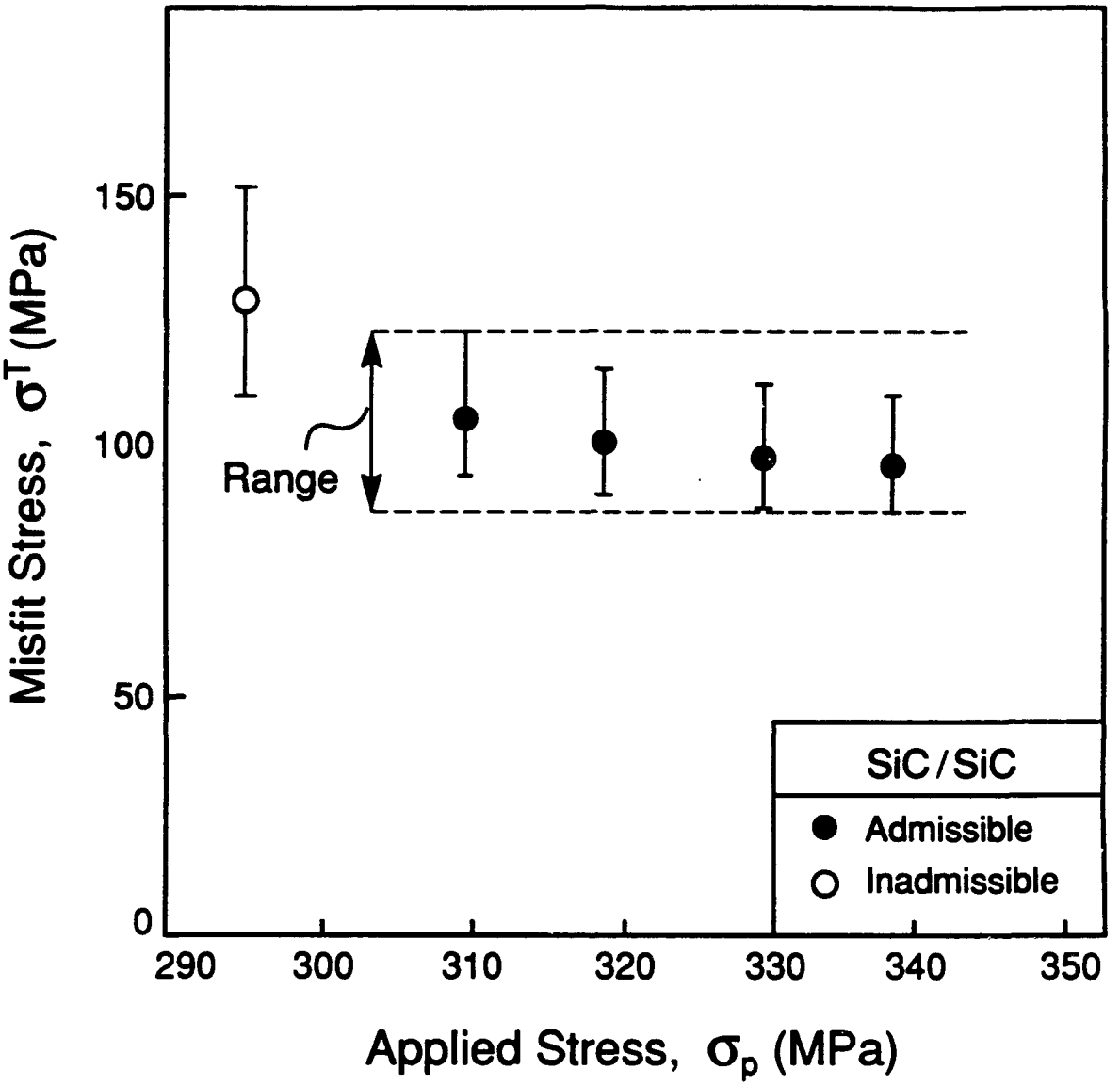
Misfit Stress, σ^T (MPa)
150
100
50
0
Range
SiC / SiC
Admissible
Inadmissible
290
300
310
320
330
340
350
Applied Stress, σ_p (MPa)

Figure 13

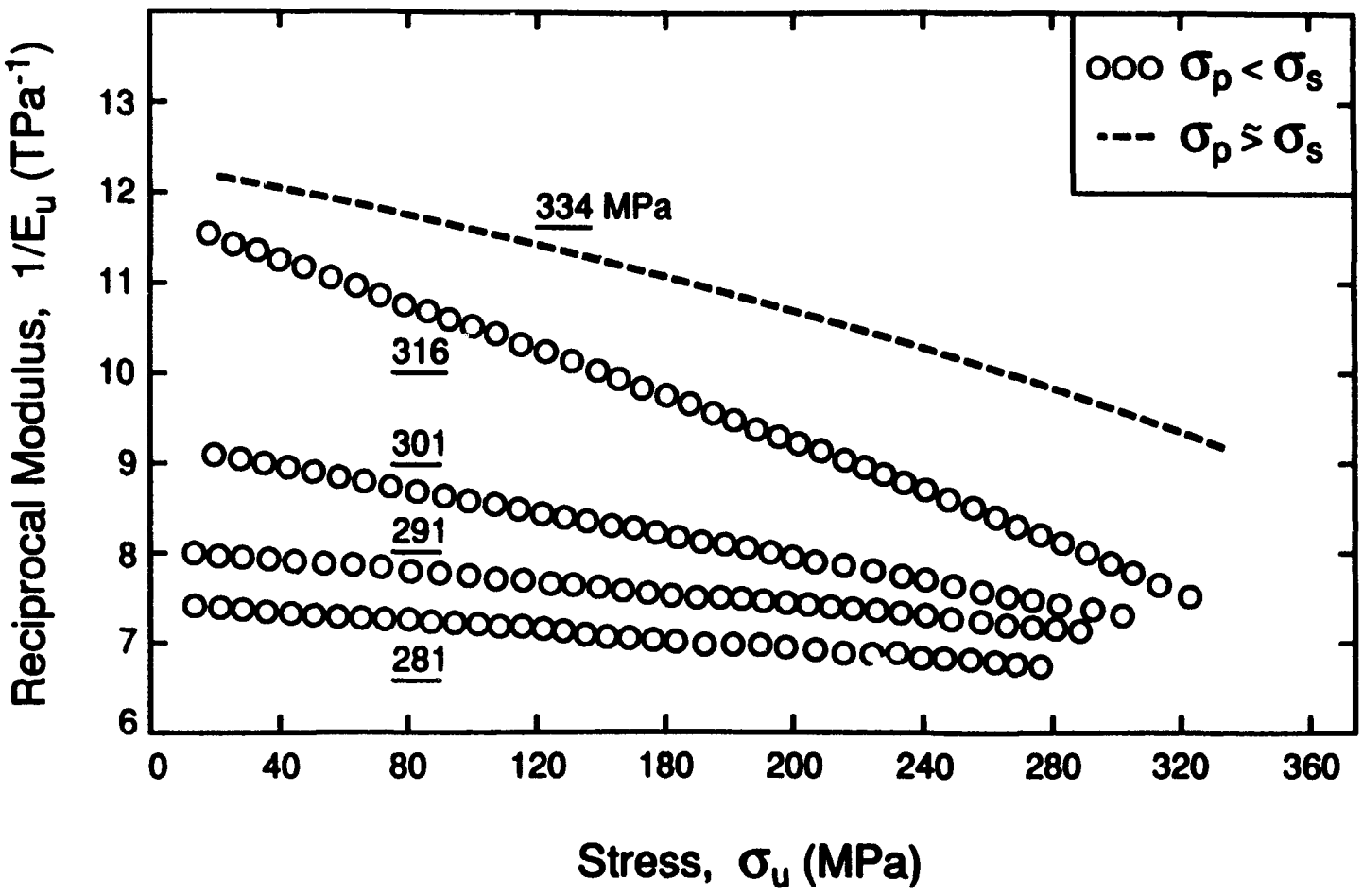
Reciprocal Modulus, $1/E_u$ (TPa^{-1})
Stress, σ_u (MPa)
$\sigma_p < \sigma_s$
$\sigma_p \gtrsim \sigma_s$
334 MPa
316
301
291
281
13
12
11
10
9
8
7
6
0
40
80
120
180
200
240
280
320
360

Figure 14a

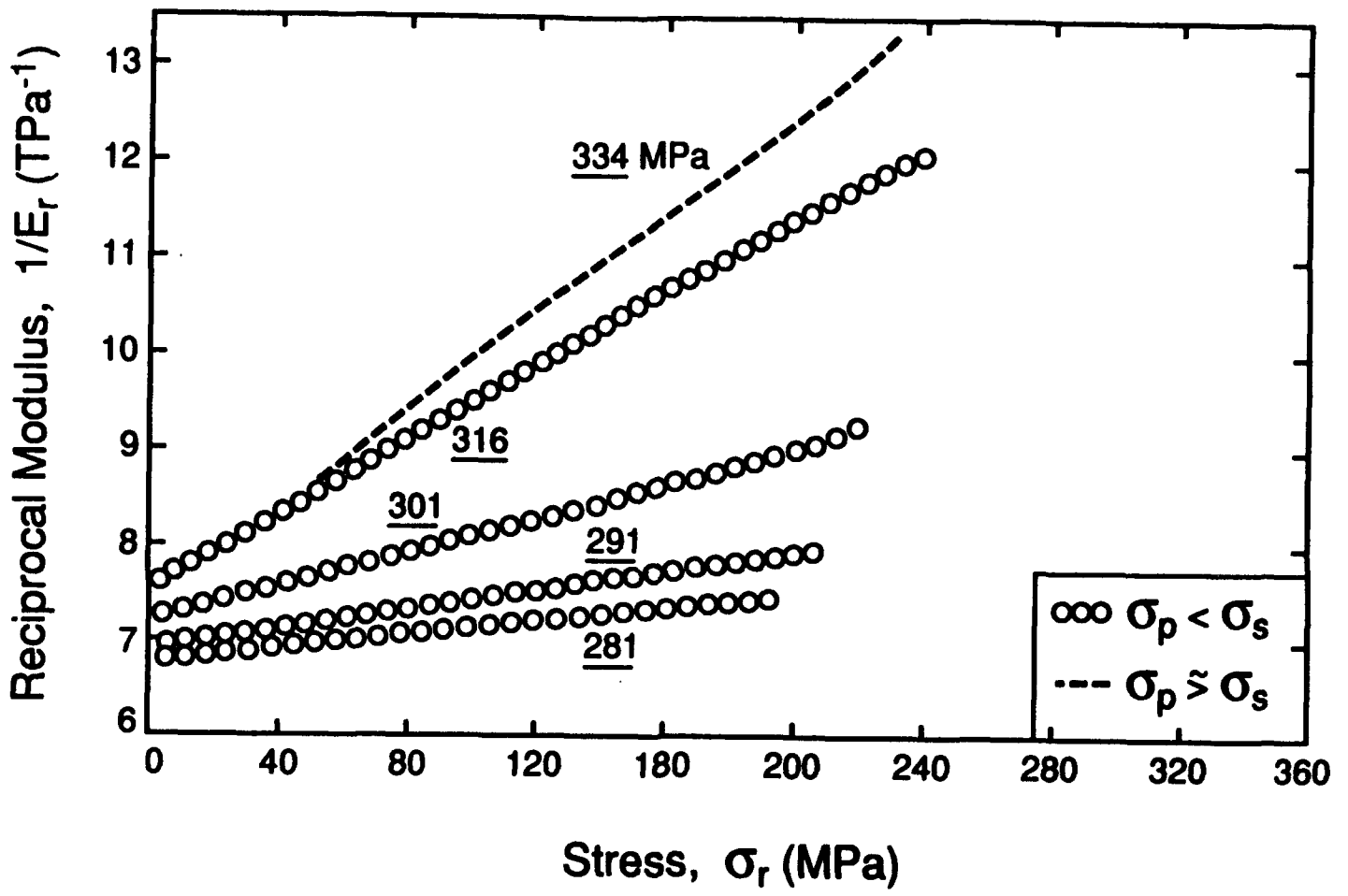
Reciprocal Modulus, $1/E_r$ (TPa^{-1})
13
12
11
10
9
8
7
6
0
40
80
120
180
200
240
280
320
360
Stress, σ_r (MPa)
334 MPa
316
301
291
281
$\sigma_p < \sigma_s$
$\sigma_p \gtrsim \sigma_s$

Figure 14b

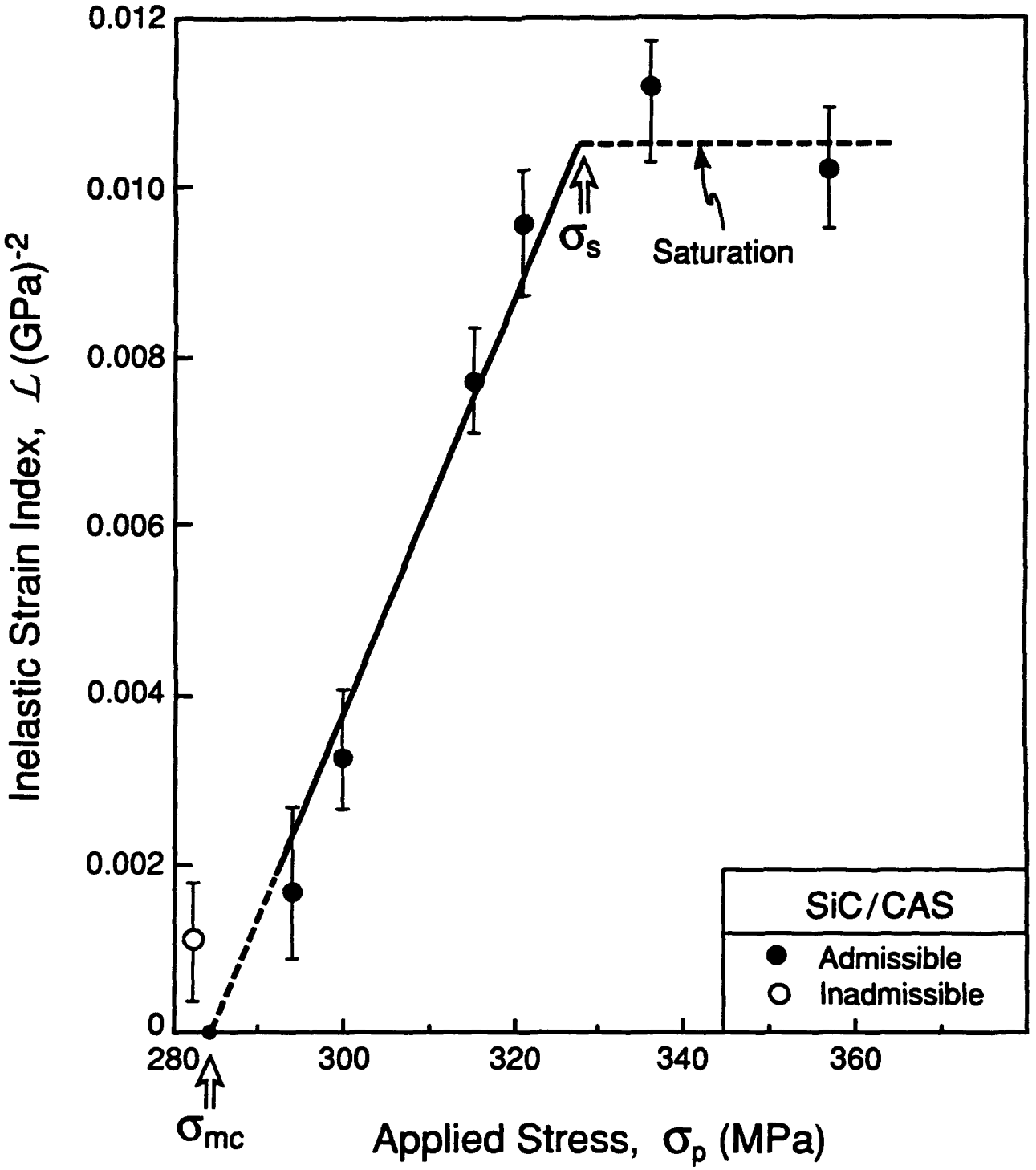
0.012
0.010
0.008
0.006
0.004
0.002
0
Inelastic Strain Index, $\mathcal{L}$ (GPa)$^{-2}$
280
300
320
340
360
σ_{mc}
σ_s
Saturation
Applied Stress, σ_p (MPa)
SiC/CAS
Admissible
Inadmissible

Figure 15

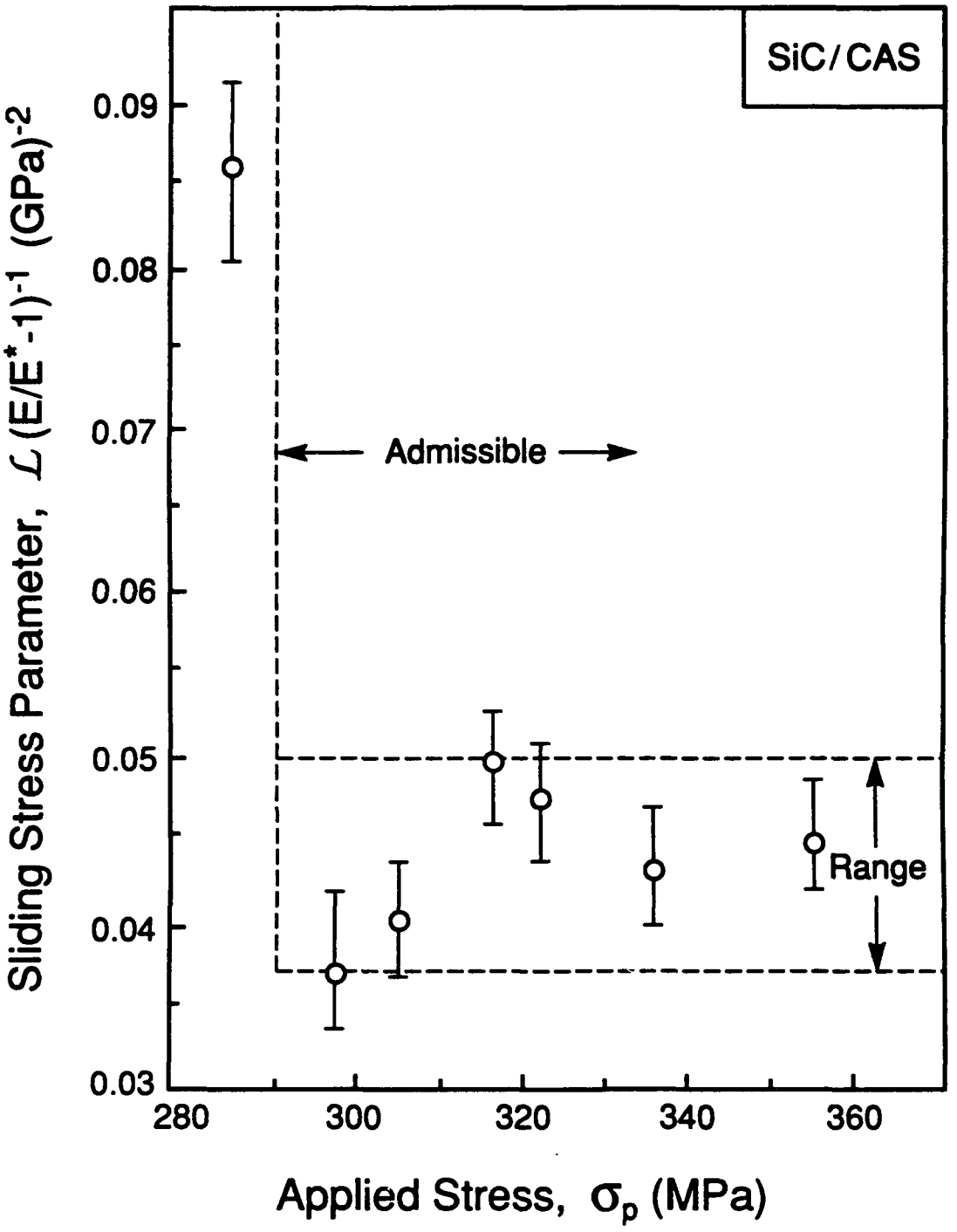

Figure 16

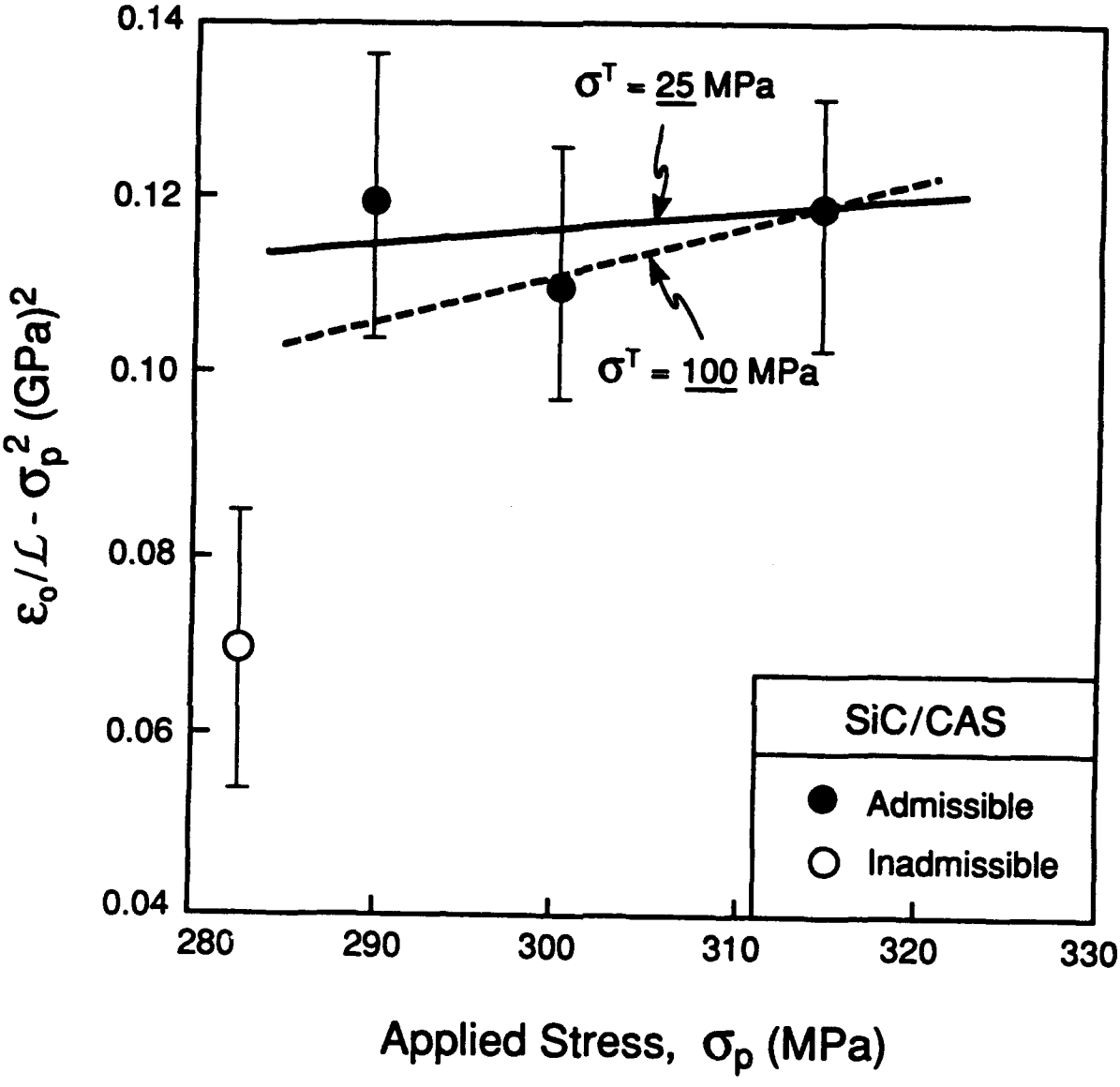
0.14
0.12
0.10
0.08
0.06
0.04
280
290
300
310
320
330
σ^T = 25 MPa
σ^T = 100 MPa
SiC/CAS
Admissible
Inadmissible
$\varepsilon_o/\mathcal{L} - \sigma_p^2$ (GPa)^2
Applied Stress, σ_p (MPa)

Figure 17

Composites Engineering, Vol 4, No. 1, pp. 67-80, 1994.
Printed in Great Britain.

0961-9526/94 $6.00 + .00

THE EFFECT OF FIBER-MATRIX REACTIONS ON THE INTERFACE PROPERTIES IN A SCS-6/Ti-24Al-11Nb COMPOSITE

PAUL E. CANTONWINE and HAYDN N. G. WADLEY†
Department of Material Science and Engineering, University of Virginia, Charlottesville, VA 22903, U.S.A.

(*Received* 14 *July* 1993; *final version accepted* 15 *August* 1993)

Abstract—The interfacial structure/property relationships of a representative composite system consisting of SiC (SCS-6) fibers in a Ti_3Al + Nb intermetallic alloy have been investigated. Two samples were fabricated at 1040°C with different exposure times in order to vary the amount of fiber-matrix reaction. This resulted in samples with reaction zone thicknesses (δ) of 1.1 and 1.7 μm, while ensuring roughly the same residual stress state. A pushout test was used to determine the debond strength (τ_d) and sliding resistance (τ_s) of both interfaces. An increase in the interface debond strength and sliding resistance with reaction zone thickness was observed and has been correlated with a change in debond path. Pushout analysis of the δ = 1.1 μm sample (where debonding occurred between the fiber's SCS carbon coating and the reaction product) revealed a debond fracture energy, Γ_i = 0–0.9 J m^{-2}, a coefficient of friction (assuming simple Coulomb friction), μ = 0.5–0.95, and a radial residual stress, σ_r = 100–190 MPa. A similar analysis on the δ = 1.7 μm sample proved unsuccessful using either a simple Coulomb or Coulomb plus constant friction law. This is believed to be due to multiple debond path branching between the SiC/inner SCS, inner SCS/outer SCS and outer SCS/reaction product interfaces. The transition to this mode of sliding is deleterious to composite properties and suggests the importance of minimizing the integrated thermal exposure associated with the consolidation process.

INTRODUCTION

Many of the mechanical properties of high-performance composites (i.e. metal, intermetallic and ceramic matrices reinforced with continuous ceramic fibers) can be predicted from the properties and volume fractions of their constituents and from the properties of the interface between them (Hashin, 1983; He *et al.*, 1993; Thouless *et al.*, 1988). The interfacial properties play a particularly important role in micromechanics-based models for predicting composite strength and toughness. For instance, when multiple matrix cracking and fiber pullout occur, the toughness of the more brittle (e.g. intermetallic and ceramics) matrix composites is substantially enhanced over that of the constituents alone (i.e. of a rule-of-mixtures prediction) (Phillips, 1972; Evans and McMeeking, 1986; Budiansky *et al.*, 1986). The conditions for this to happen have been shown to depend on the debond fracture energy (Γ_i) and the sliding resistance (τ_s) of the debonded interface between the fiber and matrix (Budiansky *et al.*, 1986; Beyrle *et al.*, 1993). Recent analysis of the fiber pushout test has led to a convenient experimental method for the estimation of these interface parameters, provided the interfacial sliding obeys either a Coulomb friction or Coulomb plus constant friction law (Marshall, 1992; Liang and Hutchinson, 1993).

It is anticipated that these debond and sliding properties depend upon the local microstructure of the interface which is affected by processing. One expects that fiber/matrix debonding (along the weakest path at the interface) depends upon the reaction products formed at the interface during processing and the distribution of defects. Fiber sliding properties have been shown to depend on the topology (roughness) of the two sliding surfaces (Kearns and Parthasarthy, 1991; Mackin *et al.*, 1992), and we would expect this to also depend upon the reaction products at the interface. The significant difference in the coefficient of thermal expansion between the fiber and matrix also results in large residual stresses at the interface upon cooling from the normally high temperatures used in processing (Pindera *et al.*, 1992; Chawla, 1987). The resulting compressive

† To whom all correspondence should be addressed.

axial and radial stresses in the fiber also affect the interfacial debonding and sliding behavior by acting to clamp the fiber in place.

Both the residual stresses and interface structure are controlled by fiber coatings and the processing conditions. Engineering of the fiber coatings to control the interface properties has been investigated (Mackin *et al.*, 1993; Cantonwine and Wadley, to be published). However, the effect of fiber/matrix reactions during processing upon the interface properties have not been systematically investigated and could, in light of the above, be significant. The work reported here begins to explore the potential importance of fiber/matrix reactions to the parameters Γ_i and τ_s. Pushout tests have been conducted on two samples of a representative system consisting of SCS-6 (SiC) fibers and a Ti_3Al + Nb intermetallic alloy. Both samples were processed at 1040°C to ensure essentially equal residual stress states. Only the time of exposure at the processing temperature was varied in order to change the interfacial structure. This, it will be shown, resulted in significantly different interface microstructures, debond paths, and interface mechanical properties.

EXPERIMENTAL

(a) *Sample preparation*

A foil/fiber/foil method was used to fabricate the composite samples. Plasma-sprayed Ti-24Al-11Nb (at%) foil was supplied by GE Aircraft Engines (Lynn, MA). The plasma-spray process deposits molten matrix material onto a spinning drum where it is rapidly solidified and cooled (Siemers and Jackson, 1991; Gigerenzer and Wright, 1991; Groves, 1992). The resulting foil was about 250 μm thick and had one rough side and one smooth side. To avoid fiber damage during subsequent consolidation (Groves, 1992), the rough surface was ground to a 180 grit finish. The SiC fiber (SCS-6) was produced by Textron Specialty Corp. using a chemical vapor deposition (CVD) process. The fiber diameter was 140 μm. It had dual carbon-rich coatings (SCS layers) whose structure and thickness vary from lot to lot, but typically the total thickness was between 3 and 5 μm (Wawner, 1988). These coatings are designed to protect the load-bearing SiC from matrix reactions (Wawner, 1988), and they help to ensure easy debonding and sliding.

Foil/fiber/foil lay-ups with a small ($\approx$ 10%) fiber volume fraction were consolidated under uniaxial constrained compression in an Astro HP20 vacuum hot-press (VHP). A 60–100 mtorr vacuum was maintained during temperature ramping at a rate of 4–5°C per min to the consolidation temperature. When the consolidation temperature of 1040°C was reached, a 100 MPa pressure was applied to densify the lay-up. One sample was processed for 30 min and the second for 240 min. The samples were sectioned, polished and lightly etched in 10% HF, 5% HNO_3, 85% H_2O solution for 10–20 s at ambient temperature. A JOEL 840 scanning electron microscope (SEM) was used to measure the reaction zone thicknesses (Cantonwine, 1993). Sample 1, processed for 30 min, had a 1.1 μm reaction zone thickness whilst sample 2, processed for 240 min, had a 1.7 μm reaction zone thickness.

(b) *Pushout tests*

The loads required to debond and slide the fiber past the matrix were measured using a pushout test. The apparatus used is schematically illustrated in Fig. 1 and was similar to that developed by Warren *et al.* (1992) except that the fiber displacement was not monitored. Pushout specimens were made by first cutting a thin ($\approx$ 500 μm) slice from each sample perpendicular to the fiber direction. Both sides of the slices were then polished to a 1 μm finish. The final specimen thickness was 450 μm and was chosen to (a) ensure that the relaxation of residual stresses at the free surfaces of the specimens did not dominate the pushout behavior (Liang and Hutchinson, 1993) and (b) minimize bending effects which can cause interfacial debonding to initiate at the specimen's bottom face during testing (Kallas *et al.*, 1992). The pushout specimen was then placed on a support base and centered over a support base hole. A small-diameter hole (about 220 μm) was

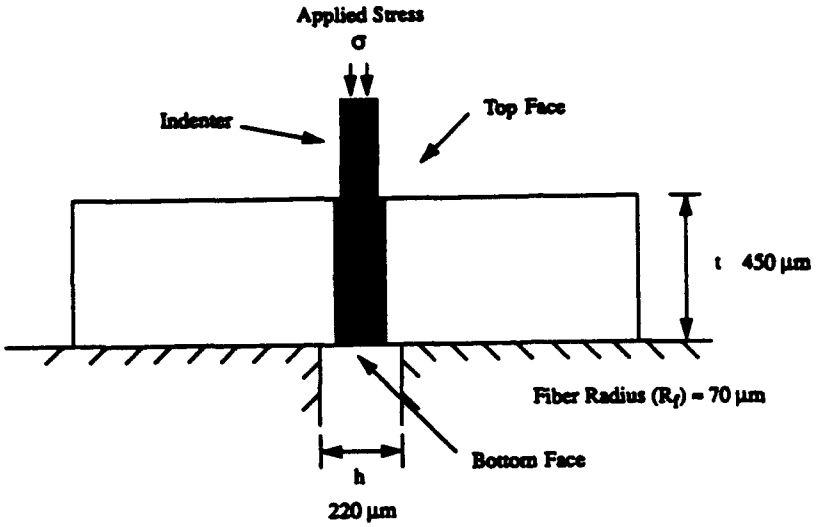

Fig. 1. Pushout test schematic: t is the specimen thickness ($\approx 450\,\mu$m), h is the diameter of the support-base hole ($\approx 220\,\mu$m).

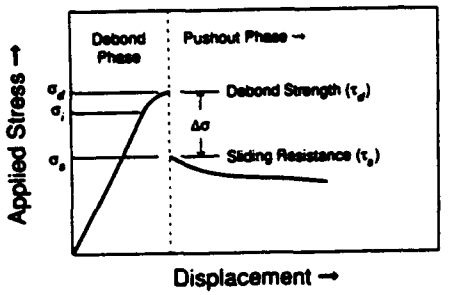

Fig. 2. Applied stress/displacement curve for a pushout test; σ_i is the applied stress needed to initiate a debond crack at the top face; σ_d measures the stress when catastrophic failure of the interface occurs (presumably when the crack tip is $1.5R_f$ from the bottom face).

chosen, again to reduce bending effects. A load was applied to the embedded fiber through a cylindrical indenter at a constant displacement rate of 0.5 μm sec^{-1}, and load vs time (displacement) curves obtained.

Figure 2 schematically presents typical pushout data in the form of applied stress (in the embedded fiber) vs fiber displacement. A model has recently been developed by Liang and Hutchinson (1993) to describe the result of a typical pushout test like that shown in Fig. 2. A debond crack is thought to initiate on the sample's top face at the initiation stress, σ_i, in Fig. 2. The nonlinear section of the curve between this crack-initiation point and the peak stress then represents stable debond crack growth down the interface. The peak pushout stress, which characterizes the debond strength ($\tau_d = R_f\sigma_d/2t$), is predicted to occur when the crack tip is $1.5R_f$ above the bottom face. At this point, the remaining interface catastrophically fails, resulting in a drop in the applied stress, $\Delta\sigma$ (or equivalently in the interfacial shear stress $\Delta\tau = R_f\,\Delta\sigma/2t$). The applied stress to cause further pushout is denoted σ_s. Provided fiber displacement has not exceeded about 1 μm following the load drop, σ_s characterizes the sliding resistance ($\tau_s = R_f\sigma_s/2t$) of the interface during the debond phase. According to the experimental work of Warren *et al.* (1992), fiber displacements after the load drop were about 1 μm.

RESULTS

(a) *Microstructure*

The microstructure of an as-consolidated composite (sample 1) is shown in Fig. 3. The matrix has an equaxed α_2 structure (4–8 μm grain diameter) with about a 10 volume

per cent β phase precipated at the α_2 grain boundaries. Radial matrix cracks were consistently observed around the fibers. The cracking around the fibers in sample 2 was more severe than for sample 1 (see Cantonwine, 1993, for a detailed characterization). A depletion of the β phase around the fiber was also observed (Fig. 3). Again, it was more severe in sample 2. Reactions between the fiber and matrix occurred, leading to the build-up of a reaction-product layer (or reaction zone) at the outer SCS surface (Figs 4 and 5). The two-phase reaction zone shown in Figs 4 and 5 has been reported to consist of a mixture of $(Ti, Nb)C_{(1-x)}$ + $(Ti, Nb, Al)_5Si_3$ in the inner zone and $(Ti, Nb)_3AlC$ + $(Ti, Nb, Al)_5Si_3$ in the outer zone (Bauman *et al.*, 1990). The growth of both the reaction and β-depleted zones is diffusion controlled and the rate of reaction exhibits parabolic kinetics (Gundel and Wawner, 1989; Gundel, 1991; Cantonwine, 1993; Bauman *et al.*, 1990). However, the detailed mechanisms of their evolution are presently unknown. The reaction-zone thickness, δ, was measured as a convenient parameter to describe the extent of the fiber/matrix reaction. For sample 1, $\delta = 1.1\,\mu m$, whilst for sample 2, $\delta = 1.7\,\mu m$.

(b) *Interfacial mechanical behavior*

Typical pushout data for both specimens are shown in Fig. 6. Notice the slightly greater load needed to cause debonding in sample 2 and the distinct difference in the pushout behavior during the pushout phase (fiber sliding after the load drop). In sample 1, the load gradually decreases after the load drop, consistent with a decrease in the area of fiber/matrix contact. However, in sample 2, the load initially increased, reached a maximum and only then decreased. This type of behavior has been observed in other systems when interface roughness (topology) controls frictional sliding behavior during the pushout phase (Mackin *et al.*, 1992, 1993; Warren *et al.*, 1992).

The debond strength (τ_d) and the sliding resistance (τ_s) for the two specimens are compared in Table 1. Sample 2 ($\delta = 1.7\,\mu m$) exhibited both a higher debond strength and sliding resistance compared to sample 1 ($\delta = 1.1\,\mu m$). Average values of τ_d and τ_s are reported from three tests (sample 1) and five tests (sample 2). The standard deviations are also given.

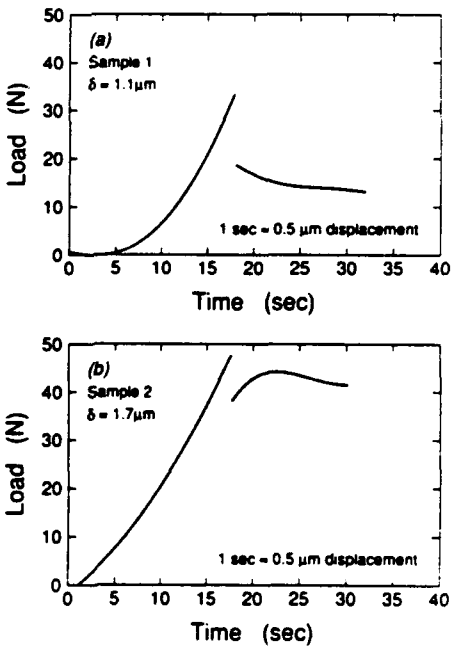

Fig. 6. Typical variations of load with time for SCS-6 fibers representing different debond properties (τ_d and τ_s). The response after the load drop measures the sliding property of large fiber displacements.

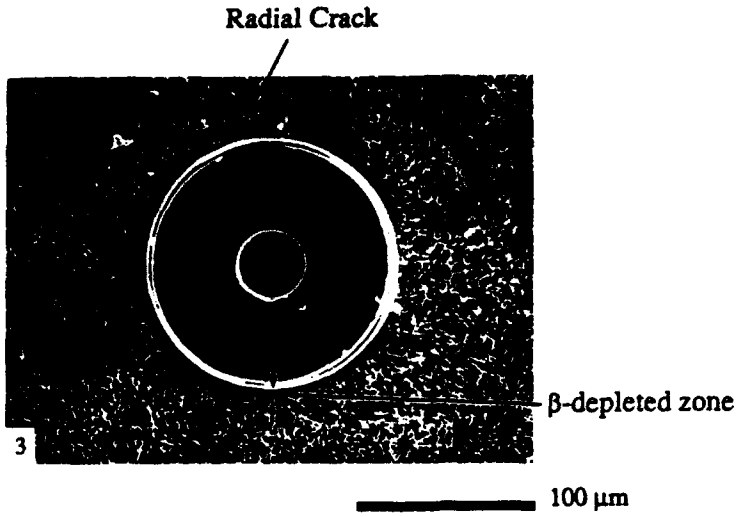

Fig. 3. SCS-6/Ti-24Al-11Nb composite; VHP consolidated at 1040°C/100 MPa/30 min.

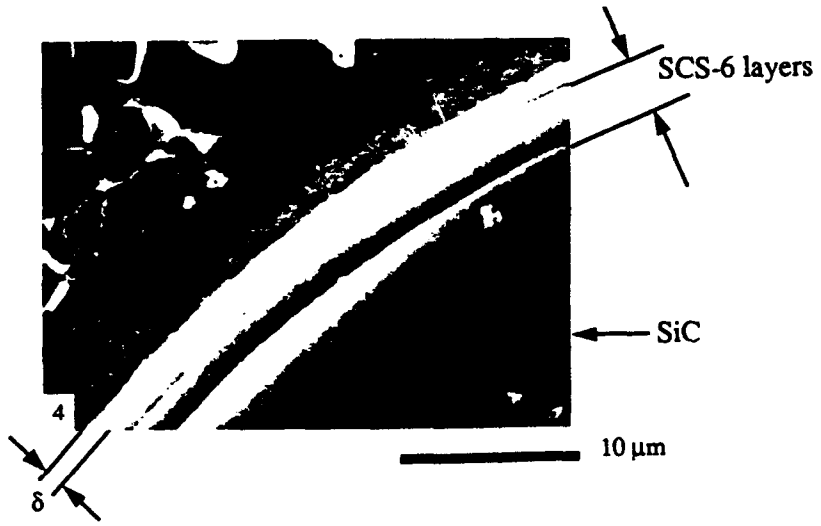

Fig. 4. Interface of the SCS-6/Ti-24Al-11Nb composite; VHP consolidated at 1050°C/100 MPa/30 min (δ = 1.1 μm).

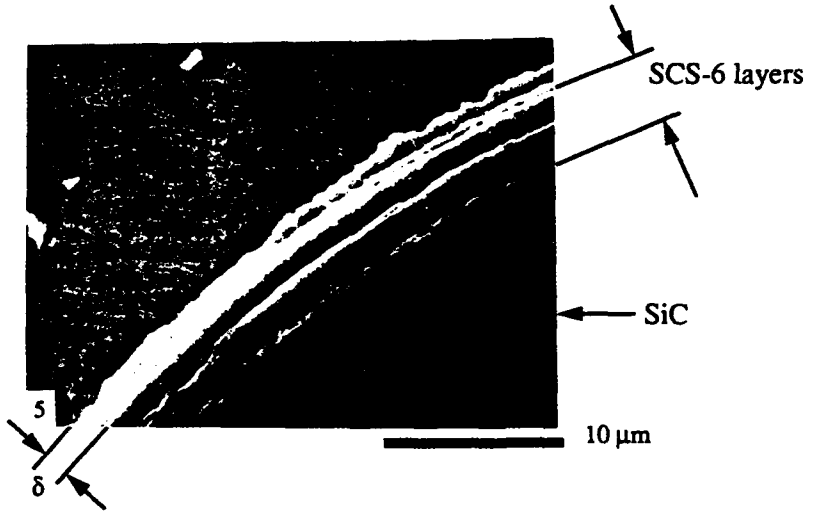

Fig. 5. Interface of the SCS-6/Ti-24Al-11Nb composite: VHP consolidated at 1050°C/100 MPa/240 min (δ = 1.7 μm).

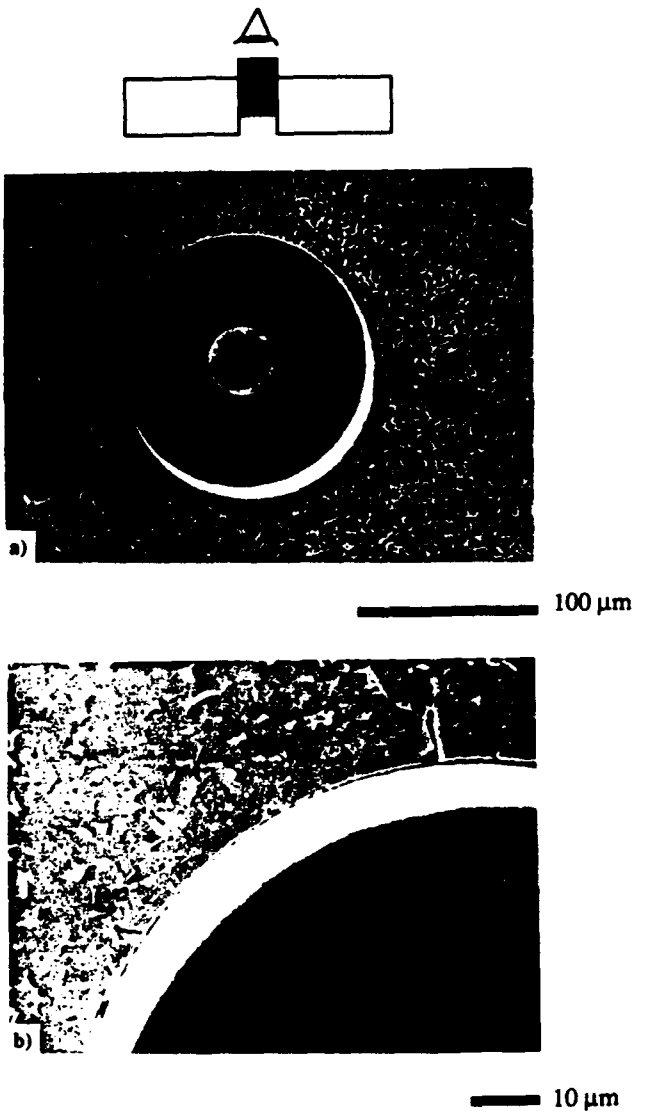

Fig. 7. Bottom face of pushout test sample 1 (δ = 1.1 μm); the SCS layers adhered to the fiber indicating the debond interface is between the outer SCS layer and the reaction product.

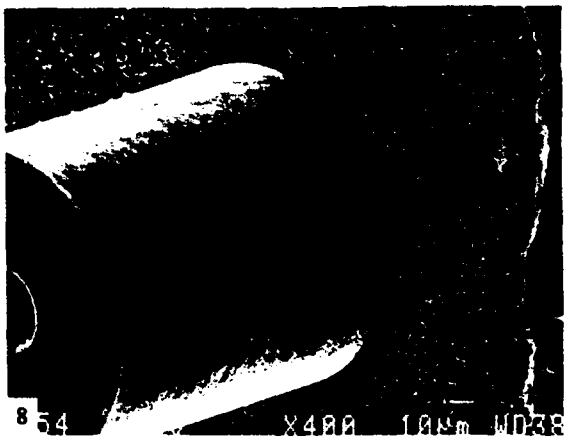

Fig. 8. The bottom face of pushout test sample 1 (δ = 1.1 μm) after a very large fiber displacement. Note the SCS layers are bonded to the fiber and the reaction product to the matrix.

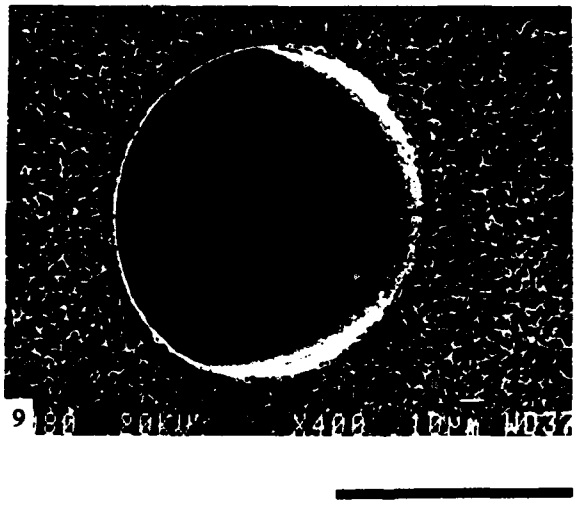

Fig. 9. The top face of pushout test sample 1 (δ = 1.1 μm); the inner surface of the hole left by the fiber mirrors the pushed out fiber in Fig. 8.

Fig. 10. The bottom face of pushout test sample 2 (δ = 1.7 μm) after a very large fiber displacement. Note the damage to the SCS layers in some regions of the fiber surface.

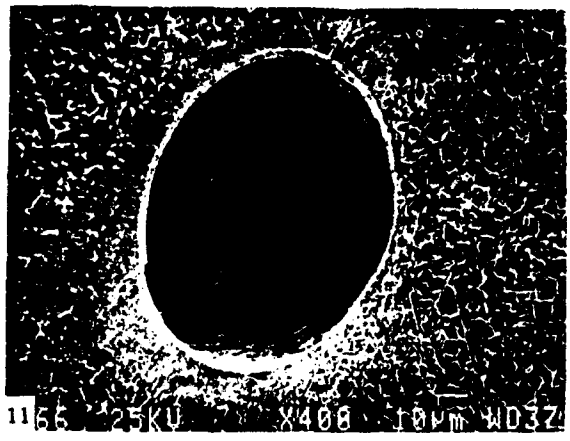

Fig. 11. The top face of pushout test sample 2 (δ = 1.7 μm) shows the inner surface to have a considerably different morphology to that in Fig. 9. An extensive amount of the SCS layers adhered to the reaction product rather than to the fiber.

Table 1. Pushout test data for SCS-6/Ti-24Al-11Nb

Sample	Reaction zone thickness (δ) (μm)	Debond strength τ_d (MPa) (standard deviation)	Sliding resistance τ_s (MPa) (standard deviation)
1	1.1	150 (12)	95 (8)
2	1.7	240 (20)	206 (12)

The debond surfaces of both specimens were examined using the SEM. Figure 7 shows the etched bottom face of pushout sample 1 ($\delta = 1.1\,\mu$m). It can be seen that the reaction product adhered to the matrix while the SCS layers adhered to the fiber. Thus, debonding occurred at the outer SCS/reaction product interface. This is somewhat surprising, since it is well known that the interface between the inner and outer SCS coatings is weak in as-received fibers, and was thought by Kantzos *et al.* (1992) to be the primary debond interface. A much rougher debond surface was observed in sample 2 ($\delta = 1.7\,\mu$m; Figs 10–11). In this case, debonding occurred locally, probably at all three interfaces (i.e. the outer SCS/reaction product, inner SCS/outer SCS and SiC/inner SCS interfaces). Kantzos *et al.* (1992), Roman and Jero (1991) and Eldridge *et al.* (1991) have also reported debonding along a similar path. Thus, extending the processing time results in a transition in the debond interface which has been correlated with a change in interfacial mechanical properties.

PUSHOUT ANALYSIS

The sliding resistance (τ_s) of a debonded interface can most simply be modeled by a Coulomb friction law:

$$\tau_s = \mu\sigma_r \tag{1}$$

where σ_r is the (thermal residual) radial stress acting on the interface (compression defined here as positive), and μ is a constant coefficient of friction, assumed to be independent of the sliding displacement. This model of sliding resistance ignores the effects of large-scale (5–10 μm amplitude) roughness seen in some fiber systems (Mackin *et al.*, 1992; Jero and Kearns, 1990). It has been rationalized as a valid description of these systems though, because the initial fiber displacement that accompanies debonding is very small ($< 1\,\mu$m) and results in a roughness-independent friction coefficient (Liang and Hutchinson, 1993; Mackin *et al.*, 1992). Equation (1) allows direct evaluation of the fundamental parameter (μ) from τ_s provided the radial compressive stress at the fiber/matrix interface is known.

Two expressions for the debond fracture energy (Γ_i) can also be deduced from the pushout test data (τ_d and $\Delta\tau$) using the model developed by Liang and Hutchinson (1993) (again assuming a Coulomb friction law):

$$\Gamma_i(\tau_d) = \frac{B_2 R_f}{E_f}\left[\left[\frac{2t}{R_f}\tau_d - \sigma_z - \frac{\sigma_r}{B_1}(e^{\zeta'} - 1)\right]\frac{1}{2e^{\zeta'}}\right]^2 \tag{2}$$

$$\Gamma_i(\Delta\tau) = \frac{B_2 R_f}{E_f}\left[\left[\frac{2t\,\Delta\tau}{R_f e^{\zeta''}} - \sigma_z - \frac{\sigma_r}{B_1}(e^{-3\mu B_1} - \right]\frac{e^{3\mu B_1}}{2}\right]^2 \tag{3}$$

where

$$B_1 = \frac{\nu_f E}{(1-\nu_f)E + (1+\nu)E_f} \tag{4}$$

$$B_2 = \frac{(1+\nu_f)(1-2\nu_f)E + (1+\nu)E_f}{(1-\nu_f)E + (1+\nu)E_f} \tag{5}$$

$$\zeta = \frac{2B_1\mu l}{R_f} \tag{6}$$

where R_f is the fiber radius (70 μm); t is the specimen thickness (450 μm); E_f, ν_f are the Young's modulus (410 GPa) and Poisson's ratio (0.3) of the fiber; E, ν are the Young's

Table 2. Material properties for SCS-6 and Ti-24Al-11Nb

Temperature (°C)	Tangent CTE SCS-6† 10^6 °C^{-1}	Tangent CTE Ti-24Al-11Nb‡ 10^6 °C^{-1}	Young's modulus SCS-6† (GPa)	Young's modulus Ti-24Al-11Nb‡ (GPa)	Yield strength Ti-24Al-11Nb‡ (MPa)
21	3.53	9.9	410	110	370
200	3.62	10.1	410	100	400
425	3.9	11.2	410	75	370
600	4.2	12.8	410	86	290
650	4.28	13.3	410	70	270
815	4.5	15.4	410	40	160
1040§	4.8	19.2	410	15	50

† Textron Specialty Corp. (1992).
‡ Brindley, NASA Lewis Research Center, 105438 (1990) and 105802 (1992).
§ Extrapolated data.

modulus (100 GPa) and Poisson's ratio (0.3) of the matrix; σ_z is the axial residual stress in the fiber; σ_r is the radial residual stress normal to the interface; and τ_d and $\Delta\tau$ are measured from the pushout test. For ζ' in eqn (2) (at the peak stress), the debond crack length (l) is thought to equal $t - 1.5R_f$, whilst for ζ'' in eqn (3), l is taken equal to t.

Since only positive values of Γ_i are physically meaningful, eqns (2) and (3) are constrained so that:

$$\frac{2t}{R_f}\tau_d - \sigma_z - \frac{\sigma_r}{B_1}(e^{t'} - 1) \geq 0 \tag{7}$$

$$\frac{2t\,\Delta\tau}{R_f e^{t''}} - \sigma_z - \frac{\sigma_r}{B_1}(e^{-3\mu R_1} - 1) \geq 0. \tag{8}$$

Equations (2) and (3) allow one to relate either the measured debond strength (τ_d) or the load drop ($\Delta\tau$) of the pushout test to the fundamental parameter (Γ_i), provided that the residual stresses σ_r and σ_z are known. Ideally, the residual stresses should be directly measured, but techniques for this are only just emerging (Kuntz *et al.*, 1993; Hough, 1993; Ma and Clark, 1993). Instead, continuum mechanics models are usually used to estimate these stresses. One model developed by Pindera *et al.* (1992) allows for both elastic and plastic deformations of the matrix. Using the Pindera model (and assuming cooling from 1040 to 25°C) together with the coefficient of thermal expansion (CTE), Young's modulus and yield strength data in Table 2, we have calculated σ_r and σ_z to be 340 and 1590 MPa, respectively. Using $\tau_d = 150$ MPa and $\Delta\tau = 55$ MPa, these values of residual stress lead to negative values in eqns (7) and (8), which is clearly non-physical.

One reason for this could be that the residual stresses present in the pushout specimen are lower than those predicted from Pindera's model. There are several potential reasons for this. One is the relaxation of stresses at the two free surfaces of the samples. This has been shown by Liang and Hutchinson (1993) and experimentally verified by Ma and Clark (1993) to extend about a fiber radius below the free surfaces. Therefore, only about 300 μm of the 450 μm specimen thickness would experience the full residual stress state. Other reasons include the possibility of stress relaxation by creep and matrix radial cracking during cooling from the processing temperature.

To obtain a better estimate of the true state of the residual stress, and thus the debond fracture energy, a relationship between σ_r and σ_z can be defined and used to reduce eqns (2) and (3) to two equations and two unknowns (Γ_i, σ_r). As a first approximation, we assume that the ratio of the stress is the same as that predicted by the Pindera model, i.e.

$$\sigma_z = \frac{1590}{340}\sigma_r. \tag{9}$$

Substituting eqn (9) into eqns (2) and (3) yields expressions for both $\Gamma_i(\tau_d)$ and $\Gamma_i(\Delta\tau)$ as a function of only σ_r. These are plotted in Fig. 12 for sample 1 using $\tau_d = 150$ MPa and $\Delta\tau = 55$ MPa. It can be seen that the expressions intersect when σ_r is between 150 and

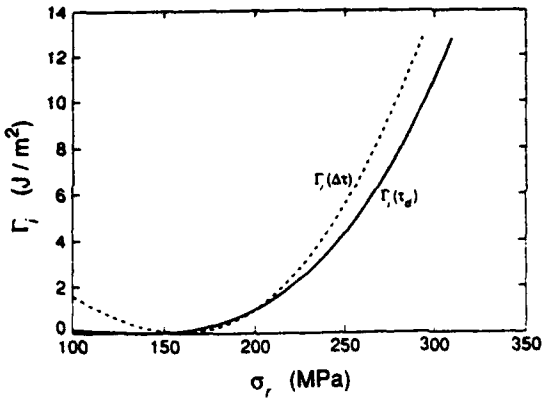

Fig. 12. $\Gamma_i(\tau_d)$ and $\Gamma_i(\Delta\tau)$ plotted vs σ_r for sample 1 (δ = 1.1 μm). There is good agreement when σ_r is between 150 and 190 MPa (Γ_i varies from 0 to 0.9 J m^{-2}).

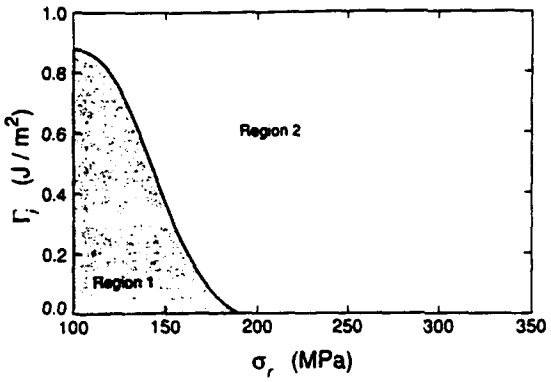

Fig. 13. Region 1 defines a set of points (Γ_i, σ_r) that give predicted values within a standard deviation of the measured values of both τ_d and $\Delta\tau$. In region 2 the predicted values are not within a standard deviation of both τ_d and $\Delta\tau$.

190 MPa. In this regime of residual stress, the debond fracture energy (Γ_i) varies between 0 and 0.5 J m^{-2}. When variability in the measured τ_d and $\Delta\tau$ values is considered (Table 1), a region (1) in Γ_i–σ_r space can be defined (see Fig. 13) where combinations of Γ_i and σ_r can be substituted into eqns (2) and (3) to give agreement between the predicted and measured values of τ_d and $\Delta\tau$.

Once the effective radial residual stress is known, the coefficient of friction, μ, can then be estimated using eqn (1). For example, using σ_r = 175 Mpa, μ for sample 1 would be about 0.54 while for sample 2 it is about 1.2. However, the simple Coulomb friction law may not be valid for sample 2, as discussed below.

A similar analysis to the above was attempted for sample 2 in order to deduce Γ_i and μ. It was found that there exists no simultaneous solution for eqns (2) and (3) (using τ_d = 240 MPa and $\Delta\tau$ = 34 MPa) for any realistic range of residual stress. One possible explanation is that the simple Coulomb friction law [eqn (1)] is no longer realistic. The Liang and Hutchinson (1993) analysis was therefore repeated assuming a friction law that included both Coulomb and constant friction (τ_0) terms†

$$\tau_s = \tau_0 + \mu\sigma_r. \tag{10}$$

This results in a system of three equations [(2), (3) and (10)] and three unknowns (μ, Γ_i and σ_r). However, no combination of μ, Γ_i and σ_r could be found to give agreement between the predicted and measured values of both τ_d and $\Delta\tau$. The implication of this is that both friction laws are inadequate, and a more complex law describing the behavior of sample 2-type debond interfaces may be needed.

† Note the measured value of τ_s was substituted for $\tau_0 = \mu\sigma_r$ in the form of eqns (2) and (3) when assuming a Coulomb plus constant friction law. See Liang and Hutchinson (1993) for the correct form.

Evidence for the existence of a more complex friction law can be seen in Fig. 6. If either eqn (1) or (10) defined the friction law as the fiber is being pushed out (after the load drop), one would expect a gradual decrease in the load as seen in sample 1 (δ = 1.1 μm). However, this is not observed in sample 2 (δ = 1.7 μm), where there is an initial increase, followed by a subsequent decrease in the load. This type of behavior has been observed in a SCS-6/β-Ti (15-3-3) composite by Mackin *et al.* (1992), where the load rise was thought to be caused by the presence of asperities (or roughness) at the debonded interface.

Mackin *et al.* (1992) have likened the effect of the asperities to an additional misfit pressure that adds to that of the residual stress. An entirely Coulombic friction law was defined:

$$\tau_s = \mu(\sigma_r + p) \tag{11}$$

where p is the additional pressure induced by asperity deformation which will vary with fiber displacement. This model successfully predicts a load rise during the post-debond sliding. However, because the fiber displacements are small immediately after unstable debonding ($< 1\ \mu$m), the fiber and matrix were thought to be in near-perfect registry until significant sliding began. This means the asperity pressure (p) is small enough to ignore. Thus, eqn (11) simply reduces to eqn (1), and does not explain the difficulties we observed in applying the Liang and Hutchinson analysis to sample 2.

It appears that another process affects the sliding behavior during the debond phase of sample 2. Examination of Figs 10 and 11 provide a clue to this. They show that the debond interface of sample 2 varied along the debond path and was either between the SCS/reaction product interface or within the SCS layers (probably between the inner/outer SCS or the SiC/inner SCS interface). From this evidence one surmises that as the debond crack tip propagates down the pushout specimen, the debond interface jumps from one interface to another. Ledges would then be created to connect the various debonded interfaces. Figure 14 schematically illustrates this and compares it to the case of sample 1-type debonding. It can be seen that these ledges resist even the small fiber

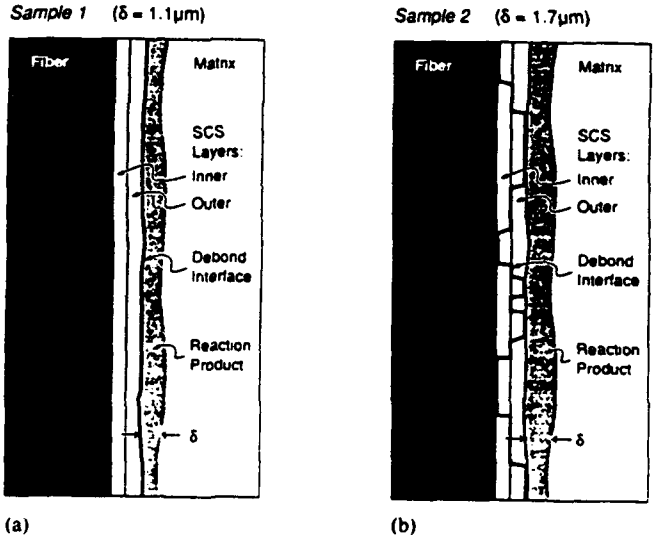

Fig. 14. (a) Debonding path at the outer SCS/reaction product interface found in sample 1. (b) Debonding at the outer SCS/reaction product, inner SCS/outer SCS or the SiC/inner SCS interface in sample 2 causes ledges between the interfaces. These ledges affect the small-fiber displacement ($< 1\ \mu$m, i.e. debond phase) behavior, while the overall interface topology (roughness) affects the large-fiber displacements (pushout phase).

displacements of the debond phase. This restraining force can be overcome by either elastic distortion of the stepped asperity or its debonding, and it is presumably this which gives rise to the interfacial hardening/softening seen in the post-debond sliding of sample 2. These observations suggest that there is a need to extend the micromechanical models for sliding to include these multiple-crack behaviors in order to develop a more detailed description of the effect of processing on interfacial sliding.

SUMMARY

(1) It has been shown that the interface properties (debond strength and sliding resistance) are a function of the fiber/matrix reactions in a SCS-6/Ti-24Al-11Nb composite, which in turn depend on processing.

(2) The changes in the interface mechanical properties are correlated with a change in the debond path. Debonding occurred along the outer SCS/reaction product interface in samples with a thin reaction product ($\delta = 1.1\,\mu m$). However, it alternated between the outer SCS/reaction product, inner/outer SCS and SiC/inner SCS in samples with thicker reaction products ($\delta = 1.7\,\mu m$).

(3) Analysis of the pushout data from the samples with a thin reaction zone using a Coulomb friction law indicated that the debond fracture energy (Γ_i) ranged from 0 to $0.9\,J\,m^{-2}$, the radial residual stress (σ_r) from 100 to 190 MPa, and the coefficient of friction (μ) from 0.5 to 0.95.

(4) Analysis of samples with the thicker reaction product indicated an increased difficulty of debonding and sliding. Both a simple Coulombic and a Coulomb plus constant friction law were inadequate to describe the experimental behavior of sample 2. The observation that debonding occurred along several interfaces leads us to speculate that ledges connecting the debond interfaces complicate the frictional response during the initial fiber displacement ($<1\,\mu m$). This type of debond mechanism also results in asperity-controlled sliding during the pushout phase (similar to that analyzed by Mackin *et al.*, 1992, 1993).

(5) Whilst further work is needed to elucidate the fundamental processes that cause the observation transitions in fiber/matrix debond behavior, it is clear that they are the source of deleterious changes to the sliding properties. They are induced by prolonged high-temperature processing, which for some creep-resistant titanium alloy composites is necessary in order to avoid fiber fracture (Groves *et al.*, 1993). The work reported here shows that a trade-off must be made in process temperature and time in order to avoid fiber fracture and excessive interfacial reaction and to optimize the composite performance. This trade-off could be simplified by careful functional grading of the fiber coating prior to processing in order to retard the reaction kinetics.

Acknowledgements—We are grateful to Professors A. Evans, D. Elzey, M. Pindera and especially T. Mackin for their most helpful discussions and advice throughout the entirety of this work. Support has been provided by the Advanced Research Projects Agency through two programs. One was supported by NASA (NAGW-1692, Program manager Dr R. Hayduk), and the second was through the UCSB URI (contract number—NO 0014-92-J, 1808 managed by Dr Steve Fishman of the Office of Naval Research).

REFERENCES

Bauman, S. F., Brindley, P. K. and Smith, S. D. (1990). Reaction zone microstructure in a Ti_3Al + Nb/SiC composite. *Metall. Trans.* **21A**, 1559–1568.

Beyrle, D. S., Spearing, S. M., Zok, F. W. and Evans, A. G. (1993). Damage and failure in unidirectional ceramic-matrix composites (in press).

Bowden, D. M., O'Neal, J. E., Deffeyes, J. E., Schwartze, D. S. and Peterman, D. J. (1991). Effect of matrix chemistry on interface development in α_2 + β titanium aluminide alloys containing SCS-6 (SiC) reinforcements. In *Titanium Aluminide Composite Workshop* (WL-TR-91-4020) (Edited by P. R. Smith, S. J. Balsone and T. Nicholas).

Brindley, P. (1990, 1992). NASA Lewis Research Center, published in NASA Technical Memoranda 105438 (1990) and 105802 (1992).

Budiansky, B., Hutchinson, J. W. and Evans, A. G. (1986). Matrix fracture in fiber-reinforced ceramics. *J. Mech. Phys. Solids* **34**(2), 164.

Cantonwine, P. E. (1993). The effect of processing on the interface structure/property relationships in a Ti-24Al-11Nb (at%) composite. Masters Thesis, University of Virginia.

Cantonwine, P. and Wadley, H. N. G. (to be published). The effect of coatings on interface properties in a SiC reinforced titanium aluminide composite.
Chawla, K. (1987). *Composite Materials: Science and Engineering*, Chapter 10. Springer, New York.
Eldridge, J. I., Bhatt, R. T. and Kiser, J. D. (1991). Investigation of interfacial shear strength in SiC/Si_3N_4 composites. *Ceram. Engng Sci. Proc.* **12**(7-8), 1152-1171.
Evans, A. G. and McMeeking, R. M. (1986). On the toughening of ceramics by strong reinforcements. *Acta Metall. Mater.* **34**, 2435.
Gigerenzer, H. and Wright, P. K. (1991). Plasma sprayed SCS-6/titanium aluminide composite test panels. In *Titaneium Aluminide Composite Workshop* (WL-TR-91-4020) (Edited by P. R. Smith, S. J. Balsone and T. Nicholas), pp. 251-264.
Groves, J. F. (1992). Fiber damage during the consolidation of metal matrix composites. Masters Thesis, University of Virginia.
Groves, J. F., Elzey, D. and Wadley, H. N. G. (submitted 1993). Fiber fracture during the consolidation of metal matrix composites. *Acta Metall. Mater.*
Gundel, D. B. (1991). Investigation of the interaction between silicon carbide fibers and titanium alloys. Masters Thesis, University of Virginia.
Gundel, D. B. and Wawner, F. E. (1989). Interfacial reaction kinetics of coated SiC fibers with various titanium alloys. *Scripta Metall.* **25**, 437-441.
Hashin, Z. (1983). Analysis of composite materials—a survey. *J. Appl. Mech.* **50**, 481.
He, M. Y., Evans, A. G. and Curtin, W. A. (1993). The ultimate tensile strength of metal matrix and ceramic matrix composites. *Acta Metall. Mater.* **41**(3), 871.
Hough, H. (1993). Masters Thesis, University of Virginia.
Jero, P. D. and Kearns, R. J. (1990). The contribution of interfacial roughness to sliding friction of ceramic fibers in a glass matrix. *Scripta. Metall.* **24**, 2315-2318.
Kallas, M. N., Koss, D. A., Hahn, H. T. and Hellman, J. R. (1992). Interfacial stress state present in a "thin slice" fibre pushout test. *J. Mater. Sci.* **27**, 3821-3826.
Kantzos, P., Eldridge, J. I., Koss, D. A. and Ghosn, L. J. (1992). The effect of fatigue loading on the interfacial shear properties of SCS-6/Ti-based MMCS. In *Proc. Symp. Materials Research Society*, Vol. 273, pp. 135-142.
Kearns, R. J. and Parthasarthy, T. A. (1991). Theoretical analysis of fiber pullout and pushout tests. *J. Am. Ceram. Soc.* **74**(7), 1585-1596.
Kuntz, T. A., Wadley, H. N. G. and Black, D. R. (1993). Residual strain gradient determination in MMCs by synchotron X-ray energy dispersive diffraction. *Metall. Trans.* **24A**, 1117-1124.
Liang, C. and Hutchinson, J. W. (1993). Mechanics of the fiber pushout test. *Mech. Mater.* **14**, 207-221.
Ma, Q. and Clark, D. R. (1993). Measurement of residual stresses in sapphire fiber composites using optical fluorescence. *Acta Metall. Mater.* **41**(6), 1817-1823.
Mackin, T. J., Warren, P. D. and Evans, A. G. (1992). Effects of fiber roughness on interface sliding in composites. *Acta Metall. Mater.* **40**(6), 1251-1257.
Mackin, T. J., Yang, J. Y., Levi, C. G. and Evans, A. G. (1993). Environmentally compatible double coating concepts for sapphire fiber-reinforced γ-TiAl. *Mater. Sci. Engng* **A161**, 285-293.
Marshall, D. B. (1992). Analysis of fiber debonding and sliding experiments in brittle matrix composites. *Acta Metall. Mater.* **40**, 427.
Phillips, D. C. (1972). *J. Mater. Sci.* **7**, 1175.
Pindera, M. J., Freed, A. D. and Arnold, S. M. (1992). Effects of fiber and interfacial layer architectures on the thermoplastic response of metal matrix composites. NASA Technical Memorandum 105802.
Roman, I. and Jero, J. D. (1992). Interfacial shear behavior of two titanium-based SCS-6 model composites. In *Proc. Symp. Materials Research Society*, Vol. 273, pp. 337-342.
Siemers, P. A. and Jackson, J. J. (1991). Ti_3Al/SCS-6 MMC fabrication by induction plasma deposition. In *Titanium Aluminide Composite Workshop* (WL-TR-91-4020) (Edited by P. R. Smith, S. J. Balsone and T. Nicholas), pp. 233-250.
Textron Specialty Corp. (1992). Published in NASA Technical Memorandum 105802.
Thouless, M. D. and Evans, A. G. (1988). The effect of pull-out on the mechanical properties of ceramic-matrix composites *Acta. Metall. Mater.* **36**(3), 517.
Warren, P. D., Mackin, T. J. and Evans, A. G. (1992). Design, analysis and application of an improved push-through test for the measurement of interface properties in composites. *Acta Metall. Mater.* **40**(6), 1243-1249.
Wawner, F. E. (1988). In *Fibre Reinforcements for Composite Materials* (Edited by A. R. Bunsell), pp. 371-424.

M A T E R I A L S

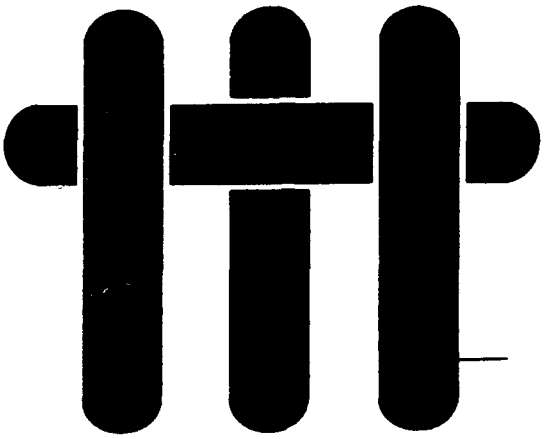

FATIGUE CRACK GROWTH AND STRESS REDISTRIBUTION AT INTERFACES

by

M.C. Shaw,[†,‡] D.B. Marshall,[‡] B.J. Dalgleish,[*] M.S. Dadkhah,[‡] M.Y. He,[†] and A.G. Evans[†]

[†]Materials Department
College of Engineering
University of California, Santa Barbara
Santa Barbara, California 93106–5050

[‡]Rockwell Science Center
Camino Dos Rios
Thousand Oaks, California 91360

[*]Department of Materials Science
University of California, Berkeley
Berkeley, California 94720

KJS 12/2/93

Submitted to Acta Metallurgica and Materialia

ABSTRACT

The role of the interface in redistributing stress around cracks in multilayered ceramic/metal composites is investigated. The emphasis is on the different effects of interfacial debonding or of plastic slip in the metal phase adjacent to strongly bonded interfaces. The experiments are conducted on alumina/aluminum multilayered composites. Monotonic loading precracked test pieces causes plastic shear deformation within the aluminum layer at the tip of the notch without debonding. However, interfacial debonding can be induced by cyclic loading, in accordance with a classical fatigue mechanism. Measurements of the stress around the crack demonstrate that debonding is much more effective than slip at reducing the stress ahead of the crack.

1. INTRODUCTION

In layered materials with alternating ductile and b' 'e constituents, various modes of crack growth are possible.[1-6] Under in-plane loading, cracks form in the brittle layers. A crack in one layer may induce cracks in an adjacent layer. Whether or not this occurs depends upon the nature of the stress concentration transmitted across the intervening ductile material. If this stress concentration is large, a series of near-coplanar cracks form, which can be viewed as a single, *dominant crack*. Conversely, a weakened stress concentration allows *distributed damage*. The stress concentration may be reduced either by debonding at the interface between the brittle and ductile layers or plastic slip within the ductile layers. An asymptotic calculation[6] (Fig. 1) predicts that debonding is more effective than slip at reducing the peak stress in the intact brittle layers and hence, should suppress crack renucleation. This prediction has yet to be verified by experiment.

The incidence of debonding, as opposed to slip adjacent to interfaces is influenced by the loading history. Interfaces that remain bonded upon monotonic loading may debond upon cyclic loading.[7] Moreover, the ratio of mode II (shear) to mode I (tensile) loading acting upon an interface crack may affect the relative tendencies for debonding and slip.[8]

The three objectives of this study are as follows. (i) Contrast the debonding and sliding characteristics of interfaces subject to monotonic and cyclic loads. (ii) Examine the validity of models for the role of debonding and sliding on stress redistribution. This is achieved by comparing predicted stresses with measured stresses. For this purpose, the fluorescence spectroscopy method is used with aluminum oxide/Al multilayers. (iii) Establish the basic mechanism of cyclic debonding (fatigue) at metal/ceramic interfaces.

2. EXPERIMENTAL METHODS

2.1 Materials

Multilayered composites of Al and Al_2O_3 were prepared by diffusion bonding.[1,4] For this purpose, thin discs of sapphire and polycrystalline Al_2O_3 were mechanically polished with diamond, to produce planar, parallel surfaces, which were then heat treated in air at 1000°C for 1 h to remove carbon based impurities. Thin sheets of Al (40, 100 or 250 μm thick) were prepared from 99.99% pure foils by cold rolling. These were interspersed between the sapphire and Al_2O_3 plates, with a sapphire layer on one outside surface and Al_2O_3 layers elsewhere. The layers were then vacuum hot pressed at temperatures of 640°C at a compressive stress of ~ 5 MPa for 48 h, resulting in a diffusion bond with essentially no residual porosity.

The diffusion-bonded discs were cut into beams suitable for flexural testing (dimensions ~ 3 x 3.5 x 50 mm) by using a diamond saw. Both side surfaces were polished to an optical finish to facilitate observations of interfacial debonding and crack growth, as well as for stress measurements.

2.2 Mechanical Tests

The location of the dominant crack in each specimen was pre-determined by placing a row of 50 N Knoop indentations, 500 μm apart, into the sapphire surface (Fig. 2). Direct observation of the specimen, using a long focal length optical microscope, revealed that these indentations produced precracks approximately 50-100 μm in length. The specimen was then loaded in four-point flexure with the indented surface in tension, within a fixture that permitted *in situ* monitoring of the side surfaces of the beams by using an optical microscope (Fig. 2). At a critical load, the flaws coalesced into a crack that propagated unstably, but arrested at the metal/sapphire interface.

These precracked specimens were loaded either monotonically or cyclically in four-point flexure. During each cyclic loading experiment, the range of load, ΔP, and the peak load, P_{max}, were kept constant. The tests were interrupted after 1000, 5000 and 20,000–50,000 cycles to allow observation of the interface between the sapphire and the first aluminum layer. Interfacial debond cracks (Fig. 3a, b) were characterized by viewing through the transparent sapphire using an optical microscope. The growth rates of interfacial cracks were also determined in this manner. Following the cyclic experiments, the interfacial cracks were characterized further by scanning electron microscopy, after removal of the sapphire layer by fracture of the specimen.

2.3 Stress Measurement

After cycling, some specimens were reloaded in flexure, using a fixture located on the stage of a Raman microprobe.† This apparatus allows stress measurement by fluorescence spectroscopy within the Al_2O_3.[9] The loads were monitored using a miniature load cell. Chromium fluorescence spectra were collected at sites within the intact Al_2O_3 layer ahead of the precrack, as indicated in Fig. 2, with the specimen in both the loaded and unloaded states. Analysis of these spectra gave fluorescence peak locations that provided a measure of the stress in the Al_2O_3 layer: the relation between peak shift and stress was obtained from a separate series of calibration experiments (Section 4.1). In polycrystalline alumina, the method has ~ 20 MPa stress resolution and 100–200 μm spatial resolution.[9-11]

In some cases, the precrack was extended into the underlying Al_2O_3 layers by monotonic loading. Again, cyclic loading experiments were conducted and the responses of the intervening Al layers were characterized by using both optical and scanning electron microscopy (SEM).

---

† Instruments SA, Model U1000.

3. INTERFACE RESPONSE

Monotonic loading of precracked specimens caused plastic slip within the metal layer at the tip of the precrack, prior to crack renucleation in the next Al_2O_3 layer. The characteristics of such plasticity have been measured using high-resolution strain mapping techniques.[4] Cracks formed sequentially in adjacent polycrystalline Al_2O_3 layers, with increasing load. Each crack was nearly coplanar with the precrack. By considering this assembly as a dominant, mode I crack and by measuring its length, a nominal crack growth resistance, K_R, was determined from the applied loads (Fig. 4).

Cyclic loading of similar precracked specimens gave a different response. When the peak load was below that at which a crack renucleated in the next Al_2O_3 layer, *stable debonding* occurred along the sapphire/Al interface (Fig. 3). The crack growth rate, da/dN, was found to decrease slightly with increase in crack length, L_s, for a given load range, ΔP (typically by a factor of 2–4 after 20,000–50,000 cycles). After fracturing the specimen to remove the sapphire from the region above the interface fatigue crack, classical fatigue striations were observed by scanning electron microscopy on the Al crack surface (Fig. 5). In the case shown in Fig. 5, the striation spacing is about equal to the crack extension per cycle (~ 1 μm/cycle). Moreover, the striations are strongly affected by crystallography, having different orientations in different grains (Fig. 5b). The basic crack growth mechanism thus appears to be similar to that occurring in monolithic alloys.[12-15]

The range of energy release rates, $\Delta\mathcal{G}$, applicable to each cyclic loading experiment was estimated from the load range, ΔP, by using a previous analysis of the flexural geometry (Fig. 2).[16,17] The analysis provides solutions for steady-state cracks ($L_s/a_o > 0.4$) in homogeneous elastic beams with no residual stress.[17] The estimates were obtained by neglecting the effect of residual stress and plasticity in the metal on $\mathcal{G}$

and by using the steady-state formulae. The present results were obtained for $0.2 < L_s/a_o < 4.0$, except for the lower left point in Fig. 6, where $L_s/a_o \sim 0.04$. Note that these results refer to mixed-mode cyclic debonding[16] with a mode mixity, $\psi \approx 50°$. These values of ΔG, in conjunction with the crack growth rates per cycle, da/dN, allow comparison with fatigue data for monolithic aluminum alloys obtained from the literature (Fig. 6 and Table I).[18-20] It is evident that the rates of cyclic interfacial debonding exceed the mode I fatigue crack growth rates for monolithic alloys, at all ΔG used during the present investigation. Therefore, *mixed-mode* fatigue crack growth can occur along strongly bonded metal/ceramic interfaces in preference to mode I crack growth through the alloy. These interface measurements complement data obtained previously in mode I.[7]

Conversely, in specimens that had been loaded monotonically to grow a crack through *several*, successive Al_2O_3 layers, subsequent cyclic loading caused rapid fatigue failure of the intervening, intact Al layers. This occurred by mode I cyclic growth emanating from cracks in the adjacent alumina layers (Fig. 7). Similar results have been reported for multilayered intermetallic/metal composites.[21]

4. STRESS MEASUREMENTS AND COMPARISON WITH THEORY

4.1 Piezospectroscopic Calibration

The relationship between the applied stress, σ_{ij}, and the fluorescence peak shift, $\Delta\nu$, is a tensorial relation,[10]

$$\Delta\nu = \Pi_{ij}\,\sigma_{ij} \qquad (1)$$

where Π_{ij} are the piezospectroscopic coefficients. It has been shown that the off-diagonal components of Π_{ij} are negligibly small for the fluorescence peaks of chromium

in aluminum oxide.[10] This expression may be further simplified for a polycrystalline material to[10]

$$\Delta\nu = Q\sigma_{kk} \tag{2}$$

where $Q = 1/3\,(\Pi_{11} + \Pi_{22} + \Pi_{33})$ and σ_{kk} is the sum of the principal stresses, $\sigma_{kk} = \sigma_{11} + \sigma_{22} + \sigma_{33}$.

The coefficient, Q, for the stress dependence of the R_2 chromium fluorescence peak in the alumina used in the present case was calibrated by collecting spectra from the side surface of a polished alumina beam subjected to various levels of four-point flexural loading. These spectra were analyzed to yield the relative peak position as a function of applied stress (Fig. 8). From these results, $Q = 2.48 \pm 0.05$ cm^{-1}/GPa: consistent with values previously reported for alumina (2.46–2.52 cm^{-1}/GPa).[10]

4.2 Stresses

The distributions of stress before and after monotonic and cyclic loading were measured by optical fluorescence. In each specimen, the measurements were obtained from the first intact Al_2O_3 layer along a line 20 μm from the interface with the metal layer. Typical results are shown in Fig. 9. The stress distribution during monotonic loading (at $K = 7\ \text{MPa}\sqrt{\text{m}}$) exhibited a broad maximum ahead of the crack front. After unloading, the stress along the same line exhibited a minimum ahead of the crack front (Fig. 9). The measured peak stress at the maximum load is similar to that given by the solution for a homogeneous elastic body (Appendix A), consistent with previous measurements in other ceramic/metal multilayered composites.[4,11] These have shown that slip in the metal layer does not diminish the σ_{yy} stress in the ceramic layer ahead of the crack tip (Fig. 1) significantly, unless the relative slip length, L_p/h, is large (> 10).[6]

After cyclic loading to attain a debond length, $L_s > 2$ mm,‡ the stress concentration ahead of the crack was found to be eliminated, within the sensitivity of the fluorescence measurements (Fig. 9). Comparison of this result with analysis is complicated by finite geometry effects: because of the large values of the ratio: debond length/precrack length, $L_s/h \approx 5$, the asymptotic solution (Fig. 1) is not relevant. A finite element solution has thus been obtained for the specific flexural geometry used in these tests. The solution (Fig. 10) establishes that, for $L_s/a_o \approx 5$, the stress concentration ahead of the precrack is, indeed, eliminated. These measurements and calculations directly confirm that debonding is more effective than plastic slip at reducing the stress ahead of a crack in ceramic/metal multilayers.

5. FATIGUE CRACK TRAJECTORIES

Two trajectories are possible for a fatigue crack arrested at the interface (Fig. 11). The crack may propagate into the metal under essentially mode I conditions (Fig. 7). Alternatively, it may deflect and propagate along the interface (Fig. 3). The parameters controlling the choice between these two trajectories are the relative strain energy release rate ranges, $\Delta\mathcal{G}$, the crack growth rates, da/dN and the mode mixity, Ψ. For a surface crack, $\Delta\mathcal{G}$ for mixed mode growth along the interface is *less* than $\Delta\mathcal{G}$ for mode I growth through the Al alloy (Appendix B). Nevertheless, in flexural loading, for which $\psi \approx 50°$ [8] (Section 3), growth along the interface is preferred for both the Al/sapphire and the Al/polycrystalline alumina interfaces. This behavior arises because at given $\Delta\mathcal{G}$, the mixed-mode interfacial crack growth rate, da/dN is *larger* than the mode I growth rate through the alloy (Fig. 12), as elaborated in Appendix B.

---

‡ ($\Delta K = 5\ MPa\sqrt{m}$ and $K_{max} = 7\ MPa\sqrt{m}$)

The preference for fatigue crack growth through the metal rather than along the interface when the metal layer is one of the intact ligaments remaining after monotonic cracking of several ceramic layers, as in Fig. 7, now remains to be explained. The relative values of ΔG for interfacial debonding and growth through the Al alloy are essentially the same as for the surface crack (Appendix B). One significant difference, however, is the mode mixity. For interfacial debonding at metal ligaments, the loading is mode II[8] (Ψ = 90°). It is likely that mode II cyclic debond rates are considerably lower than those measured in mixed mode, because of crack face contact.[22,23] It is plausible that the debond rate is reduced to such a level that mode I ligament failure is preferred. If these arguments are correct, the effect of mode mixity on the cyclic debonding of the interface has major implications for the fatigue performance of multilayers.

The basic mechanisms that determine the different cyclic crack growth rates are governed by the cyclic stresses and strains that occur near the crack tip. For a crack near a bimaterial interface, the cyclic shear stresses can exceed those expected in a monolithic alloy.[24] These large stress amplitudes should coincide with a larger cyclic growth rate near the interface, at the equivalent loading mode. However, a comprehensive analysis that relates these stress amplitudes to crack growth for a range of mode mixities is needed to rationalize the behaviors found in this study.

6. CONCLUDING REMARKS

Two competing mechanisms of fatigue cracking have been observed in Al_2O_3/Al multilayers. Mixed-mode cracks extend along the metal/ceramic interfaces, normal to the tip of a main crack, in accordance with a classical fatigue mechanism. Conversely, intact metal ligaments rupture rapidly by mode I fatigue crack growth. The interfacial cracking at the crack tip has the *beneficial* effect of reducing the stresses ahead of the

main crack and thereby suppressing further growth of that crack. The rupture of ligaments in the crack wake is detrimental, because it reduces the crack tip shielding imparted by the bridging ligaments. This duality in fatigue behavior might be exploited in order to optimize the fatigue resistance of metal/ceramic multilayers.

The mixed mode fatigue crack growth rate along the Al/Al_2O_3 interface exceeds the mode I rate in monolithic Al alloys. The large growth rate arises because of the enhanced shear stress amplitude at the tip when the crack is at a bimaterial interface.[25] Further analysis of the relationship between the growth rates in the interface and the alloy is in progress.

The experimental measurements of the relative effects of slip and debonding on stress redistribution ahead of a mode I crack are consistent with calculations.[6] Debonding was found to be substantially more effective than slip at reducing the stress. The development of interfaces that experience controlled debonding upon either cyclic loading or monotonic loading thus represents an opportunity for achieving fracture and fatigue-resistant layered materials.

APPENDIX A

Fluorescence Measurements And Probe Size Effects

The signal intensity at a given frequency within a fluorescence spectrum of a stress-sensitive material is influenced by the state of stress of the material throughout the volume sampled by the probe. If stress gradients are significant within this volume, calculation of the fluorescence peak position requires a somewhat complicated calculation of the entire spectrum. To obtain an estimate of probe size effects in the present experiments, a simpler calculation, which assumes that the measured peak position is a weighted average of the peak positions from each element within the sampling volume, was used:

$$\sigma'_{kk}(x_o, y_o) = \int_{-y^*}^{y^*}\int_{-x^*}^{x^*}\sigma_{kk}(x,y)R(x_o - x, y_o - y)\,dx\,dy \Big/ \int_{-y^*}^{y^*}\int_{-x^*}^{x^*}R(x,y)\,dx\,dy \qquad \text{(A1)}$$

where $R(x-x_0, y-y_0)$ is the probe response function, $\sigma_{kk}(x, y)$ is the local stress field and x^* and y^* represent the boundaries of the region from which the probe collects information.

Previous studies have established that the stresses of interest for layered materials with strongly bonded interfaces are given to a good approximation by the asymptotic elastic field around a crack in a homogenous body.[2,4] For mode I loading, the stress, $\sigma_{kk}(x, y)$ is, therefore,[25]

$$\sigma_{kk}(x,y) = \left[K\sqrt{\left(2\Big/\left(\pi\left(x^2+y^2\right)^{1/2}\right)\right)}\right]\cos\left(\tan^{-1}\left(y/x\right)/2\right) \qquad \text{(A2)}$$

where x and y are the Cartesian coordinates measured from the crack tip. In the present analysis, the measured stress is compared with this solution at the location directly opposite the precrack ($x = h_m$, $y = 0$), where Eqn. (A2) becomes

$$\sigma_{kk} = \frac{2K_I}{\sqrt{2\pi h_m}}. \qquad \text{(A3)}$$

The response function was characterized experimentally by placing the probe on a horizontal surface of a thick beam of alumina, at a location immediately adjacent to a vertical free surface. The intensity of the signal was measured as the probe was translated away from the vertical surface, until the signal reached a level that did not change appreciably with further movement of the probe.The results were consistent with a response function of the form

$$R(x,y) = \exp\left[-\left(x^2 + y^2\right)/b^2\right] \qquad \text{(A4)}$$

where b is a measure of the size of the volume of material sampled by the probe. The value of b ($\approx$ 200 μm) is much larger than the area illuminated on the specimen surface (spot size ~ 2 μm); indirect illumination from internal scattering determined the volume from which the fluorescence signal was collected.

With the parameters pertinent to the data of Fig. 9 (K_I = 7.0 MPa$\sqrt{m}$, h_m = 250 μm), the stress directly opposite the crack tip is, from Eqn. (A3), $\sigma_{kk}(h_m, 0)$ = 350 MPa. The stress given by Eqn. (A1), with the center of the probe at $(x_0, y_0) = (h_m, 0)$ is significantly lower: 325 MPa. However, both values are reasonably close to the value in Fig. 9 deduced from the measured peak shift (360 ± 20 MPa), consistent with the findings of previous studies.[4,11]

APPENDIX B

Fatigue Crack Trajectory

The preferred path taken by a fatigue crack depends on the ratio of energy release rate ranges, $\Delta\mathcal{G}$, compared with the ratio of crack growth rates at the relevant phase angle, Ψ, for the different possible trajectories. For a surface crack, an interface debond is mixed mode ($\Psi \approx 50°$).[16] The comparison is thus made for mixed mode crack growth along the interface and mode I growth through the alloy (Fig. 6). The energy release rate range for mode I growth through the alloy is[26]

$$\Delta\mathcal{G} \approx 1.26\pi a\left(\sigma_{max}^2 - \sigma_{min}^2\right)/E \tag{B1}$$

where a is one-half the ceramic layer thickness, σ_{max} and σ_{min} are the maximum and minimum stresses applied during load cycling and E is the modulus of the ceramic. For mixed-mode growth along the interface, upon initial cyclic debonding[27]

$$\Delta\mathcal{G}_{I/II} \approx 0.3\pi a\left(\sigma_{max}^2 - \sigma_{min}^2\right)/E. \tag{B2}$$

Then, upon further growth, when steady state is reached ($\Delta\mathcal{G} = \Delta\mathcal{G}_{ss}$),[16]

$$\Delta\mathcal{G}_{I/II}^{ss} \approx 0.5a\left(\sigma_{max}^2 - \sigma_{min}^2\right)/E. \tag{B3}$$

The ratio of energy release rates for mode I growth into the alloy and for mixed mode I/II growth along the interface, is thus in the range 4.2–2.5 π. Imposing this ratio onto the crack growth curves dictates whether interface debonding is preferred or vice versa

(Fig. 12). The present data for Al_2O_3/Al (Fig. 6) indicate that interface crack growth is preferred, at least for ΔG in the range, $10 \rightarrow 10{,}000\ Jm^{-2}$.

For intact metal ligaments, the ΔG ratio is similar, with a somewhat larger value for mode I,[26]

$$\Delta G_1 \approx 2b\left(\sigma^2_{max} - \sigma^2_{min}\right)\left[\tan\left(\pi a/2b\right)\right]/E. \qquad \text{(B4)}$$

where 2(b – a) is the ligament thickness. More importantly, the loading for an interface debond crack is now mode II. It is expected that the mode II debond growth rate, da/dN, is appreciably lower than that in mixed mode. Such reductions arise because of frictional contacts along the debond faces, as found in monolithic alloys in fatigue,[22] and for monotonic interface debonding.[23] In this case, mode I growth through the alloy is preferred over interface debonding.

TABLE I

Interface Fatigue Crack Growth for Al/Al_2O_3

Metal Layer Thickness (μm)	Energy Release Rate Range, ΔG (Jm^{-2})	Average Crack Growth Range, $d\bar{a}/dN$ (m/cycle)
40	13	2.9×10^{-8}
	144	1.0×10^{-8}
	180	1.5×10^{-6}
100	13	1.4×10^{-9}
	139	2.2×10^{-8}
250	4	2.8×10^{-9}
	130	3.4×10^{-8}

REFERENCES

[1] B.J. Dalgleish, K.P. Trumble and A.G. Evans, "The Strength and Fracture of Alumina Bonded with Aluminum Alloys," *Acta Metall.*, **37**[7] (1989) 1923–31.

[2] H.C. Cao and A.G. Evans, "On Crack Extension in Ductile/Brittle Laminates," *Acta Metall. Mater.*, **39**[12] (1991) 2997–3005.

[3] M.Y. He, F.E. Heredia, M.C. Shaw, D.J. Wissuchek and A.G. Evans, *Acta Metall. Mater.*, **41** (1992) 369.

[4] M.C. Shaw, D.B. Marshall, M.S. Dadkhah and A.G. Evans, *Acta Metall. Mater.*, **41**[11] (1993) 3311–22.

[5] A.G. Evans and B.J. Dalgleish, *Acta Metall. Mater.*, **40** (1992) S295.

[6] K.S. Chan, M.Y. He and J.W. Hutchinson, *Mat. Sci. Eng.*, in press.

[7] R.M. Cannon, B.J. Dalgleish, R.H. Dauskart, T.S. Oh and R.O. Ritchie, *Acta Metall. Mater.*, **39**, (1991) 2145.

[8] J.W. Hutchinson and Z. Suo, *Appl. Mech. Rev.*, **28** (1991).

[9] S.E. Molis and D.R. Clarke, *J. Am. Ceram. Soc.*, **73** (1990) 3189.

[10] Q. Ma and D.R. Clarke, *J. Am. Ceram. Soc.*, **76** (1993) 1433.

[11] M.C. Shaw, A.G. Evans, D.B. Marshall, D.R. Clarke and Q. Ma, to be published.

[12] R.M. Pelloux, *Trans. Quart.*, ASM, **62**[1] (1969) 281.

[13] R.W. Hertzberg and P.C. Paris, *Proceedings, International Fracture Conference*, Sendai, Japan, **1** (1965) 459.

[14] R.C. Bates and W.G. Clark, Jr., *Trans. Quart.*, ASM **62**[2] (1969) 380.

[15] P.C. Paris, *Fatigue—An Interdisciplinary Approach*, Proceedings 10th Sagamore Conference, Syracuse University Press, Syracuse, NY (1964) p. 107.

[16] P.G. Charalambides, J. Lund, R.M. McMeeking and A.G. Evans, *J. Appl. Mech.*, **56** (1989) 77–82.

[17] P.G. Charalambides, H.C. Cao, J. Lund and A.G. Evans, *Mech. of Mtls.*, **8**[4] (1990) 269–83.

[18] S.R. Swanson, F. Cicci and W. Hoppe, ASTM *STP 415* (1967) 312.

[19] P.C. Paris and F. Erdogan, *J. Basic Eng. Trans.*, ASME, Series D, **85**[4] (1963) 528.

[20] Society of Materials Science, Japan, "Data Book on Fatigue Crack Growth Rates of Metallic Materials," [1] (1983).

[21] K.T. Rao, R.O. Ritchie and G.R. Odette, *Acta Metall. Mater.*, **40** (1992) 353.

[22] R.O. Ritchie, F.A. McClintock, H. Nayeb-Hashemi and M.A. Ritter, "Mode III Fatigue Crack Propagation in Low Alloy Steel," *Met. Trans. A*, Vol. **13A**, 1, 1982, pp. 101–110.

[23] A.G. Evans and J.W. Hutchinson, *Acta Metall.*, **37** (1989) 909.

[24] C. Woeltjen, C.F. Shih and S. Suresh, *Acta Metal. et Mater.*, **41** (1993) 2317.

[25] B.R. Lawn and T. Wilshaw, *Fracture of Brittle Solids*, Cambridge Univ. Press (1975).

[26] H. Tada, P.C. Paris and G.R. Irwin, *The Stress Analysis of Cracks Handbook*, Paris Productions (1985).

[27] M.Y. He and J.W. Hutchinson, *Intl. Jnl. Solids Structures*, **25**[9] (1989) 1053–67.

FIGURE CAPTIONS

Fig. 1. Effects of slip and debonding on the stress ahead of a semi-infinite crack.[6]

Fig. 2. The specimen configuration and the locations used for stress measurement.

Fig. 3. a) Optical micrographs of two Al/Al_2O_3 beams, the top beam subjected to a single load cycle, the lower beam subjected to 50,000 cycles of flexural fatigue.
b) Optical micrograph of an interface debond created from the precrack by cyclic loading, as viewed through the transparent outer sapphire layer.

Fig. 4. Crack growth resistances measured for the multilayers used in the present study.

Fig. 5. Scanning electron micrographs of fatigue striations observed in the aluminum layer after debonding and removal of the upper sapphire layer: a) within one grain, b) different orientations in different grains.

Fig. 6. Plot of the average crack growth rate, $d\bar{a}/dN$ vs. ΔG for multilayers with different metal layer thicknesses. Also shown are data for Type 7075-T6 and 1100-TO aluminum alloys, taken from References 7 and 18–20.

Fig. 7. Scanning electron micrograph of an aluminum ligament that failed in fatigue.

Fig. 8. Piezospectroscopic calibration curve for the alumina used in the present investigation.

Fig. 9. Stress ahead of precrack with load applied (nominal $K = 7\,MPa\sqrt{m}$) and unloaded. Comparison with and without debonding.

Fig. 10. Effect of debonding in a flexural configuration on stresses ahead of the surface precrack.

Fig. 11. Schematic illustrating possible fatigue crack trajectories: a) Mode I extension of cracks from cracked ceramic layers into the intervening metal layer and b), c) Extension of mode II cracks along the interface.

Fig. 12. Schematic of the effect of mode mixity on the relative crack growth rates for different crack trajectories. Also shown is the ratio of ΔG's. For this case, interface debonding is preferred over mode I growth into the alloy.

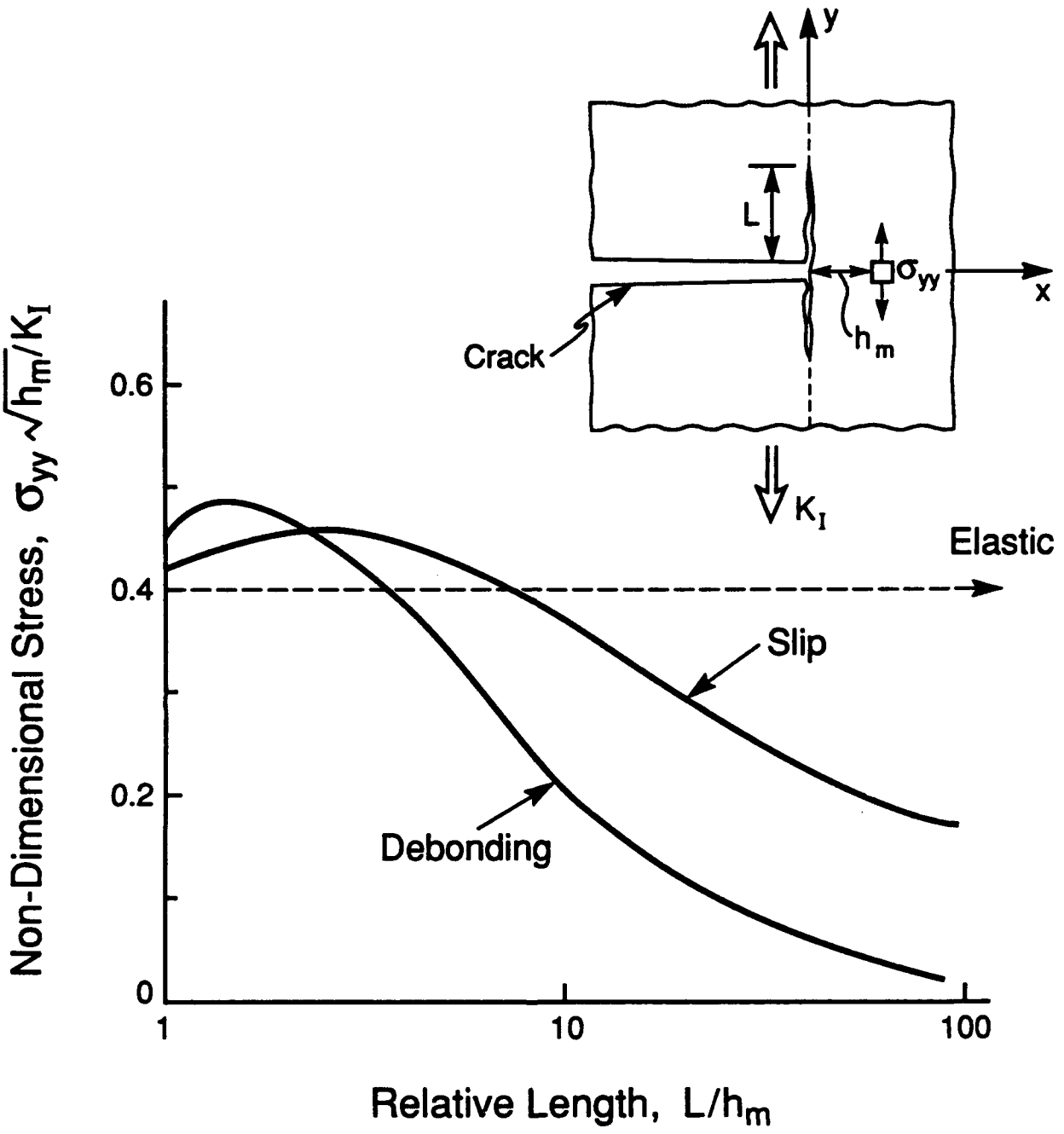
y
L
σ_{yy}
x
Crack
h_m
K_I
Elastic
Slip
Debonding
Non-Dimensional Stress, $\sigma_{yy}\sqrt{h_m}/K_I$
0.6
0.4
0.2
0
1
10
100
Relative Length, L/h_m

Figure 1

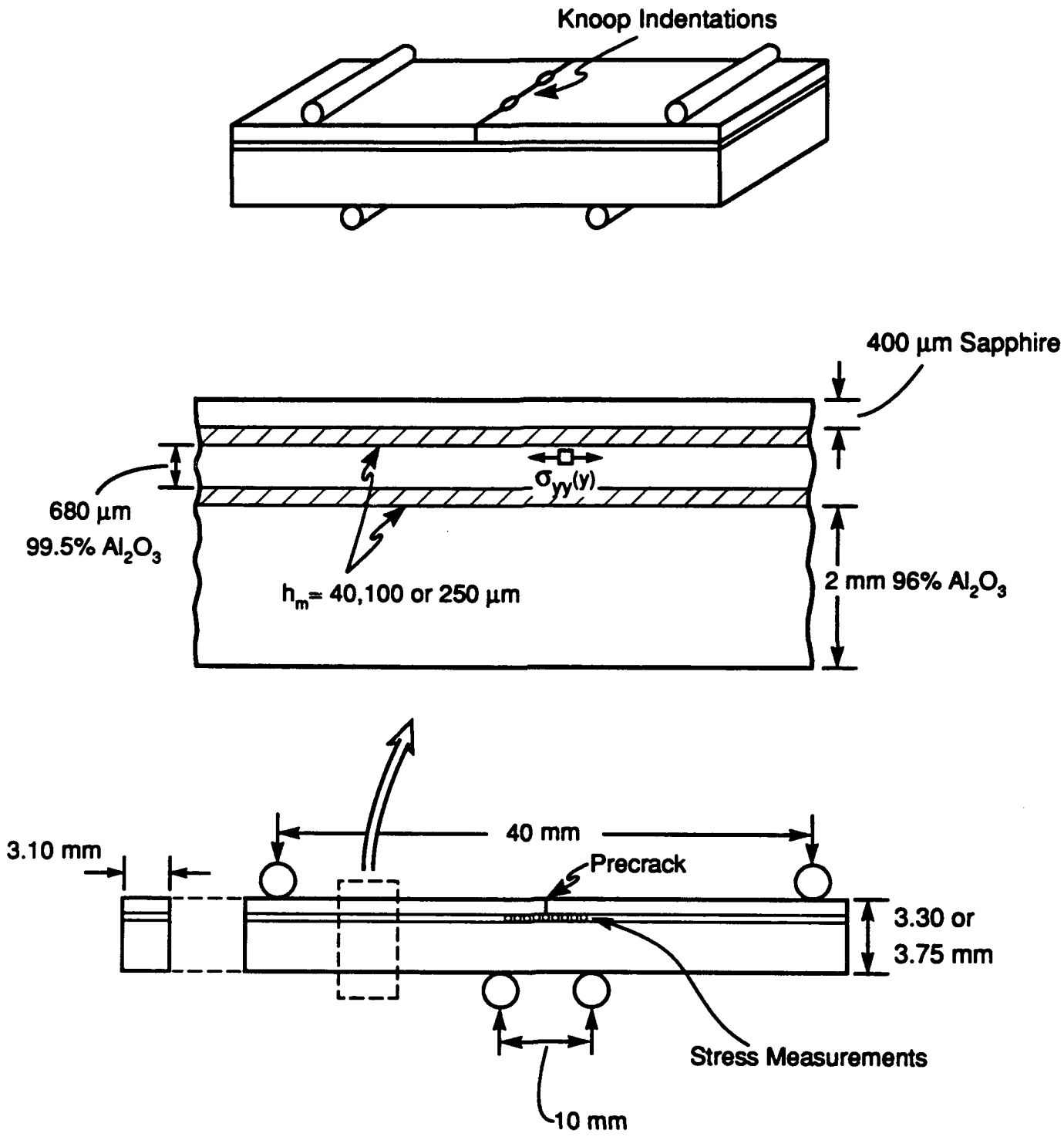
Knoop Indentations
400 μm Sapphire
680 μm
99.5% Al_2O_3
$\sigma_{yy(y)}$
h_m= 40,100 or 250 μm
2 mm 96% Al_2O_3
3.10 mm
40 mm
Precrack
3.30 or
3.75 mm
Stress Measurements
10 mm

Figure 2

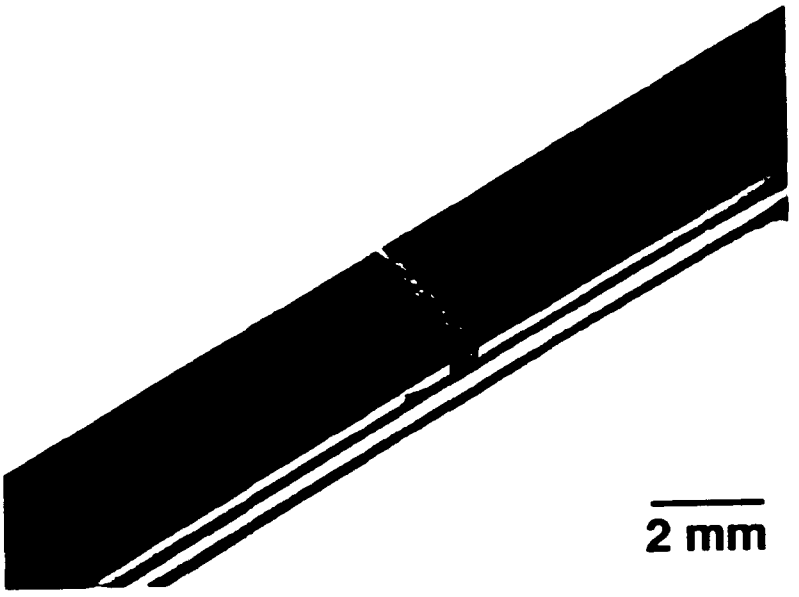

1 Load Cycle

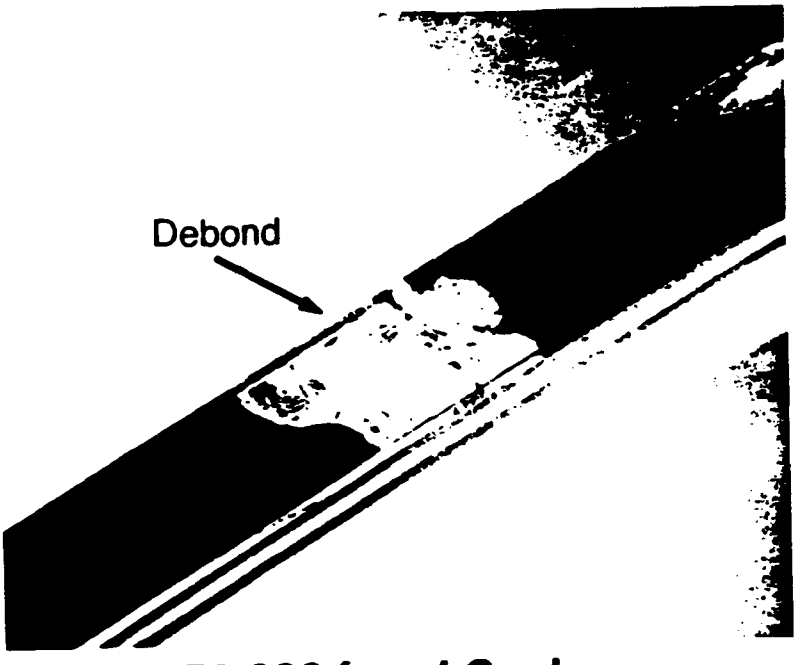

50,000 Load Cycles

Figure 3(a)

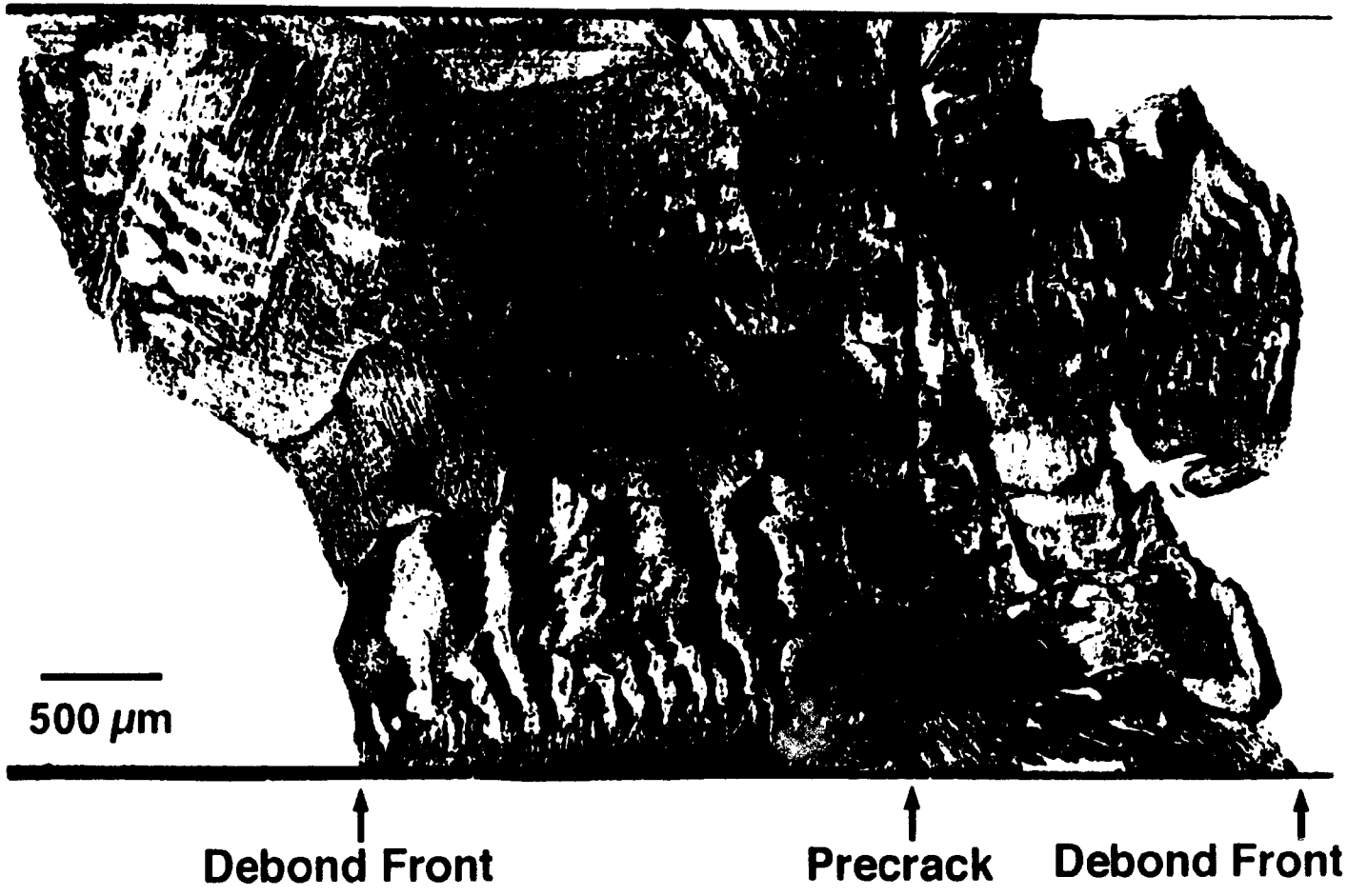

Figure 3(b)

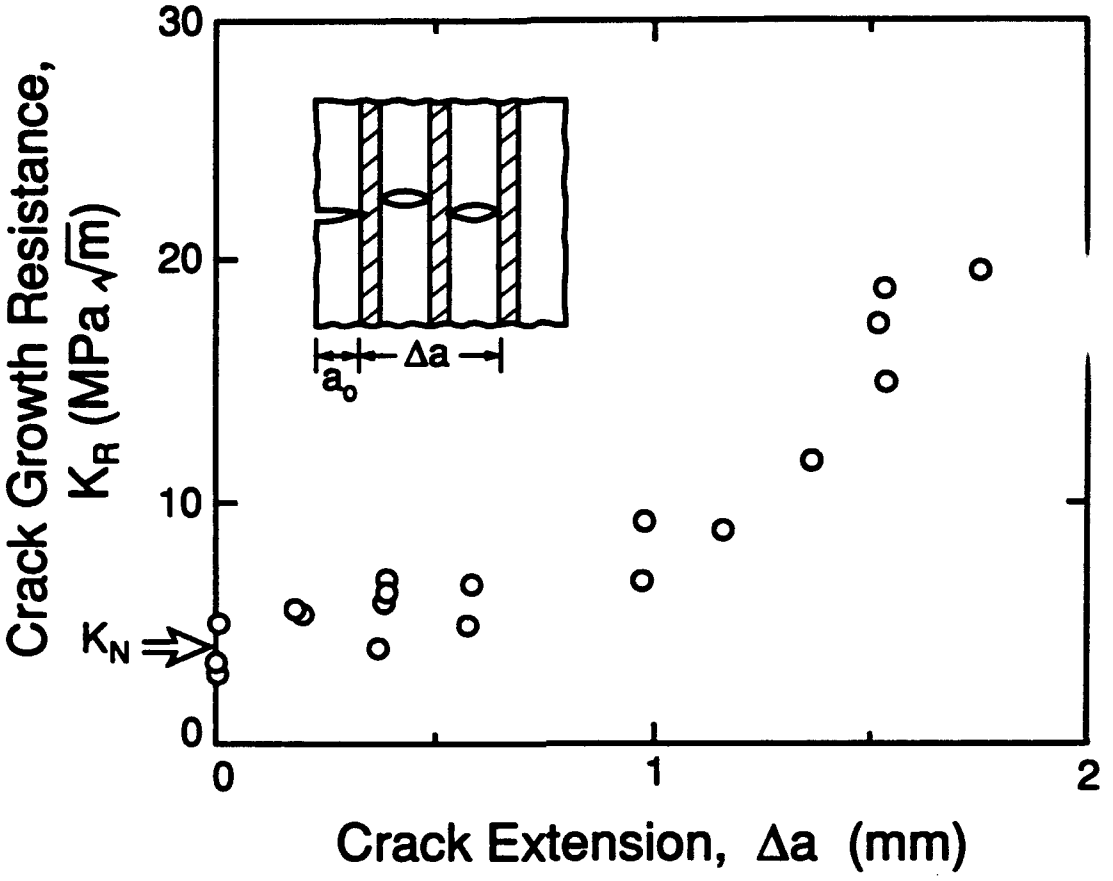
Crack Growth Resistance, K_R (MPa$\sqrt{m}$)
30
20
10
0
K_N
0
1
2
Crack Extension, Δa (mm)
Δa
a_o

Figure 4

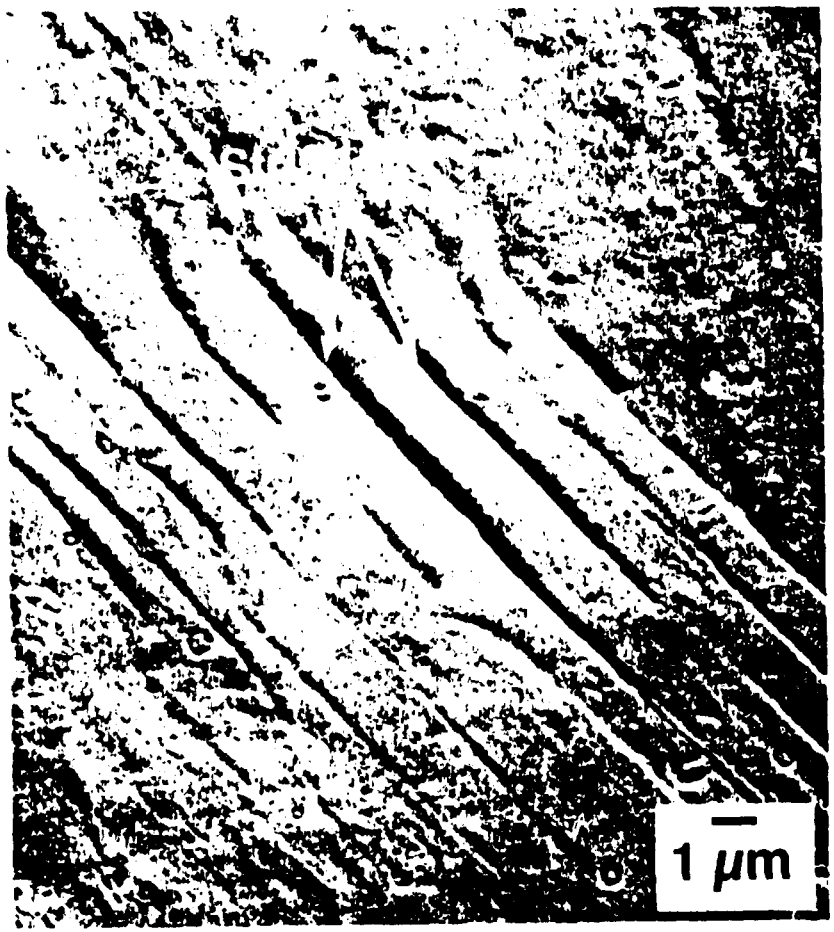

(a)

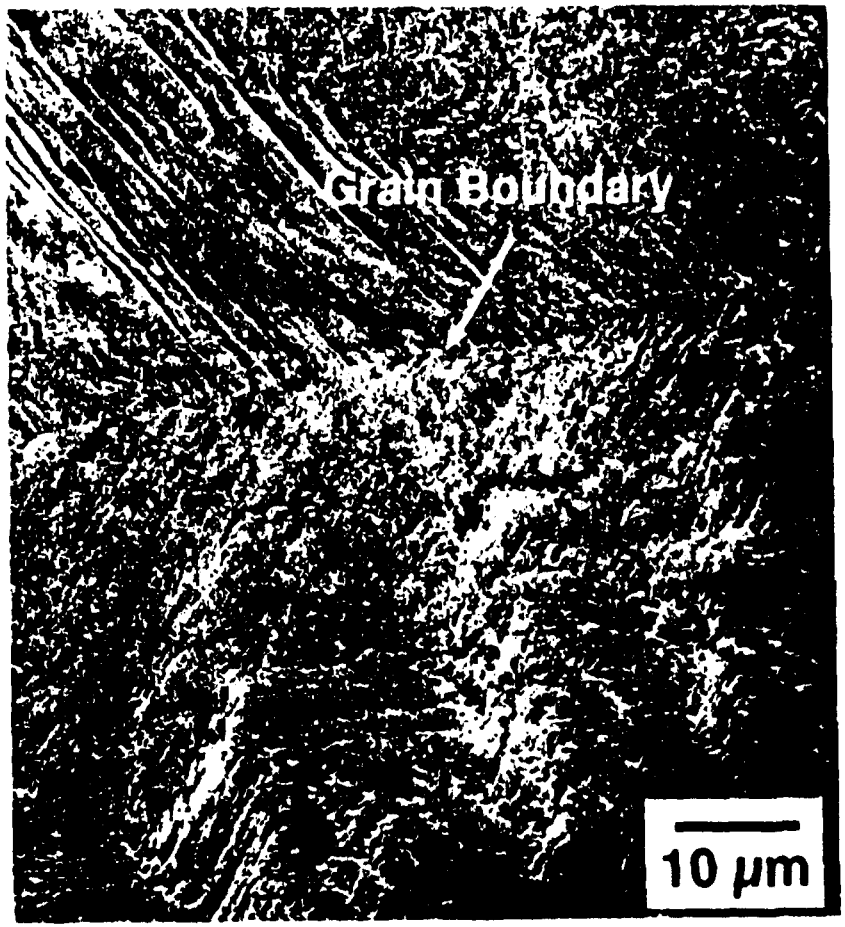

(b)

Figure 5

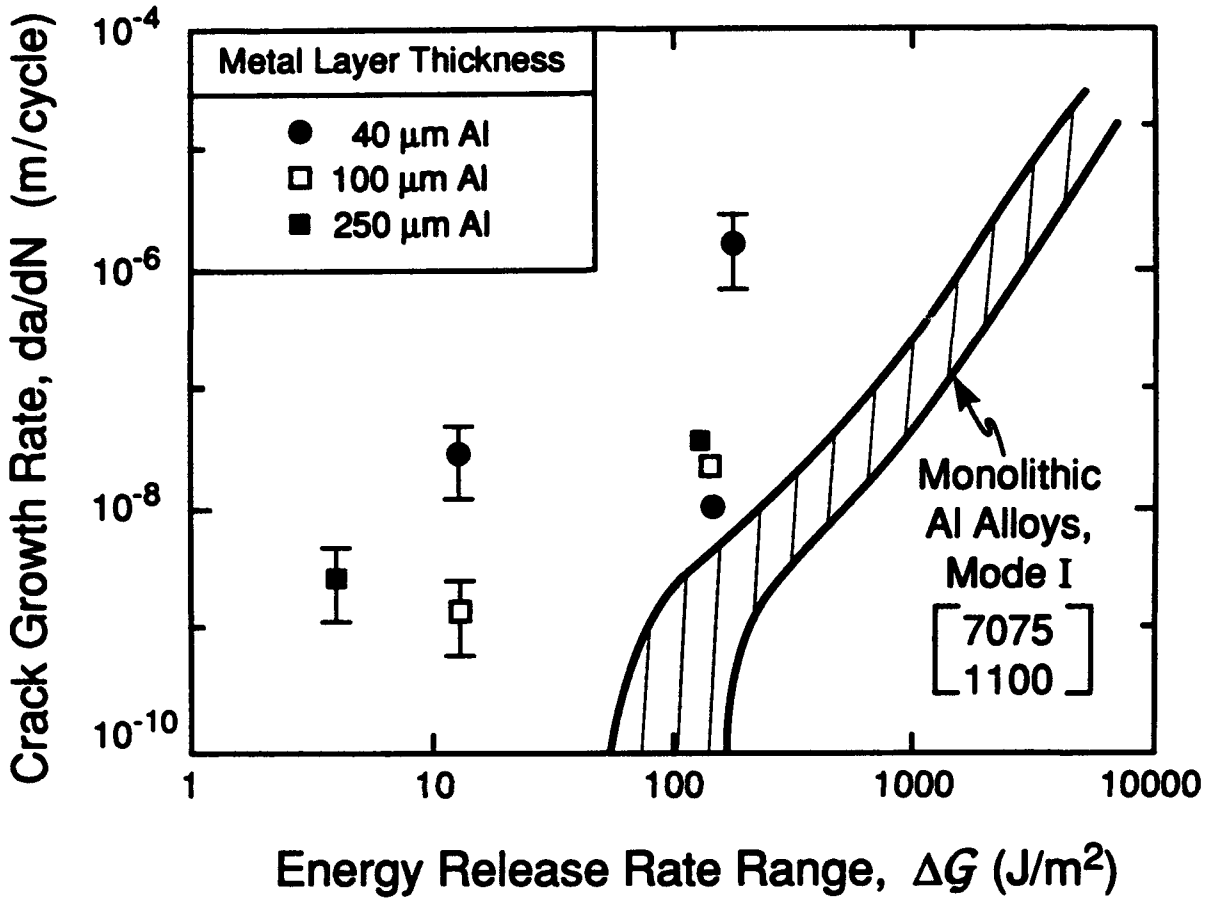
Metal Layer Thickness
40 μm Al
100 μm Al
250 μm Al
Monolithic
Al Alloys,
Mode I
7075
1100
Crack Growth Rate, da/dN (m/cycle)
10-4
10-6
10-8
10-10
1
10
100
1000
10000
Energy Release Rate Range, ΔG (J/m2)

Figure 6

Figure 7

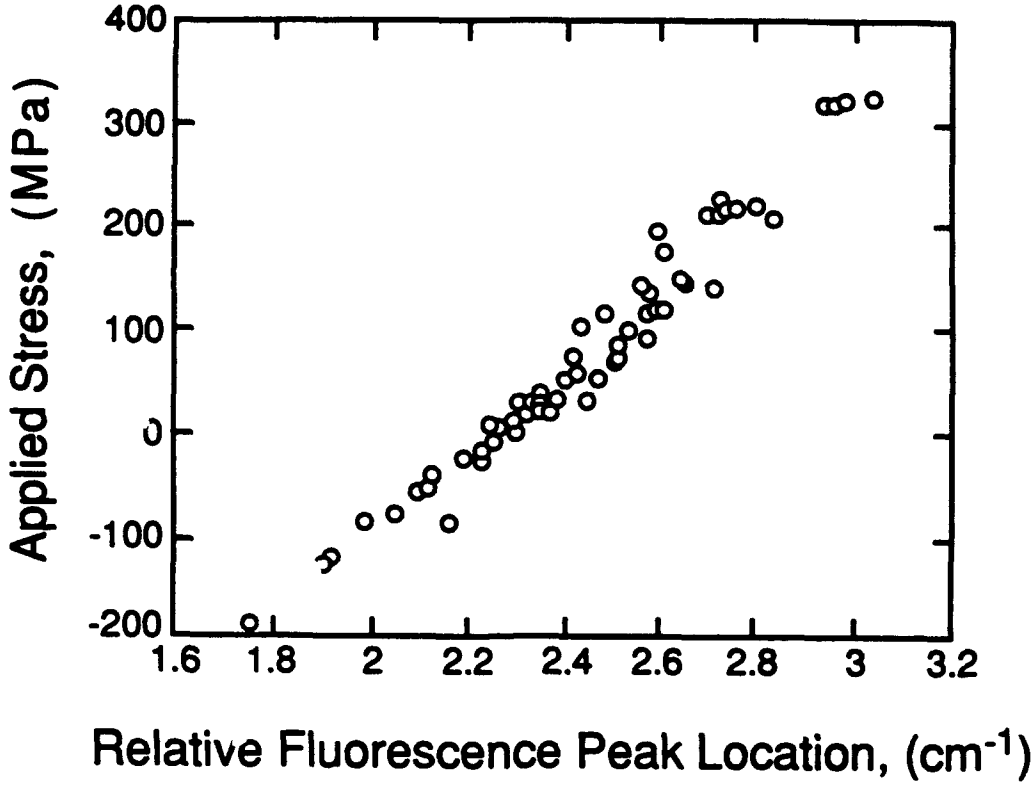
Applied Stress, (MPa)
400
300
200
100
0
-100
-200
1.6
1.8
2
2.2
2.4
2.6
2.8
3
3.2
Relative Fluorescence Peak Location, (cm-1)

Figure 8

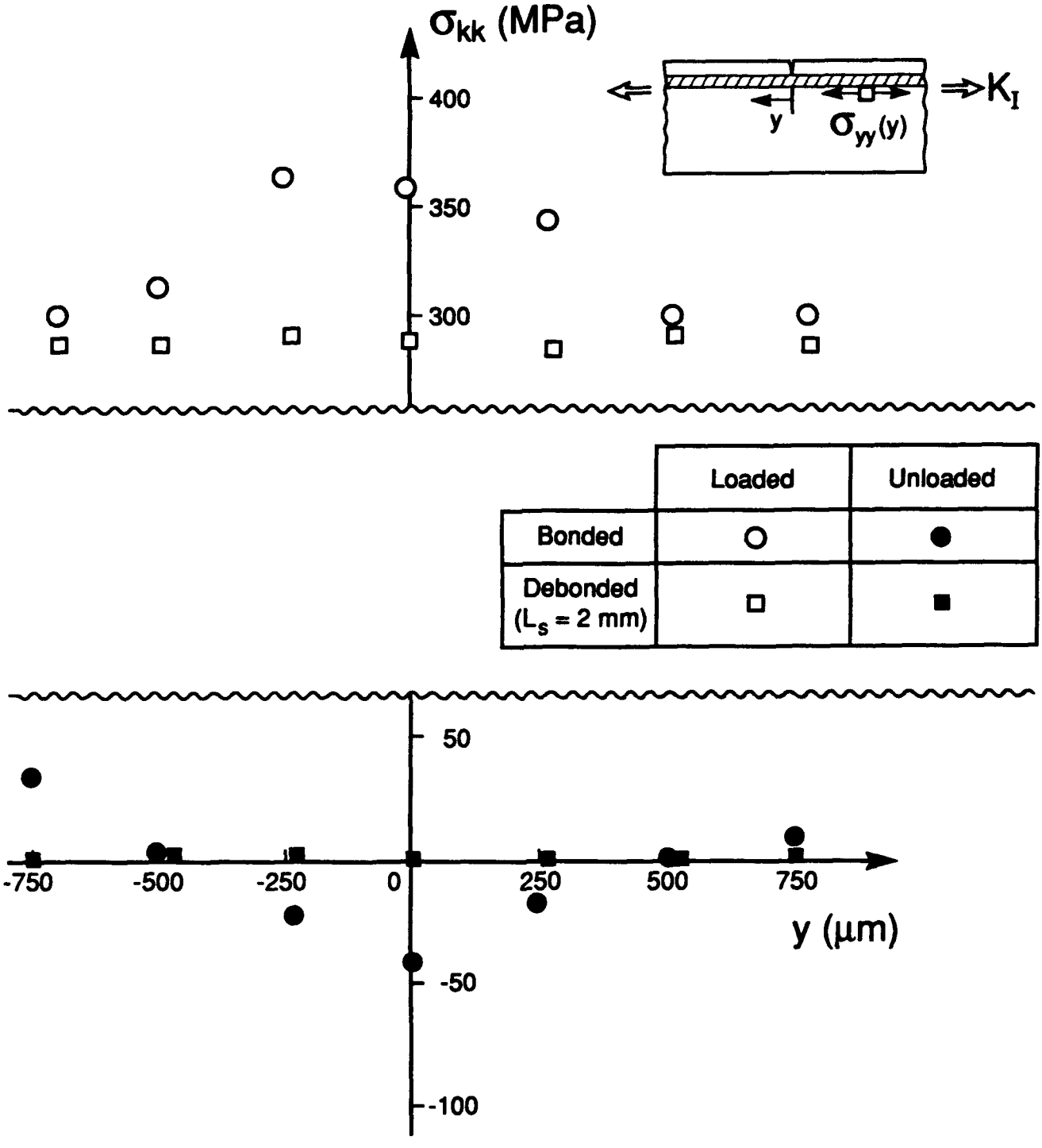
σkk (MPa)
400
350
300
y
σyy(y)
KI
Loaded
Unloaded
Bonded
Debonded
(Ls = 2 mm)
50
-50
-100
-750
-500
-250
0
250
500
750
y (μm)

Figure 9

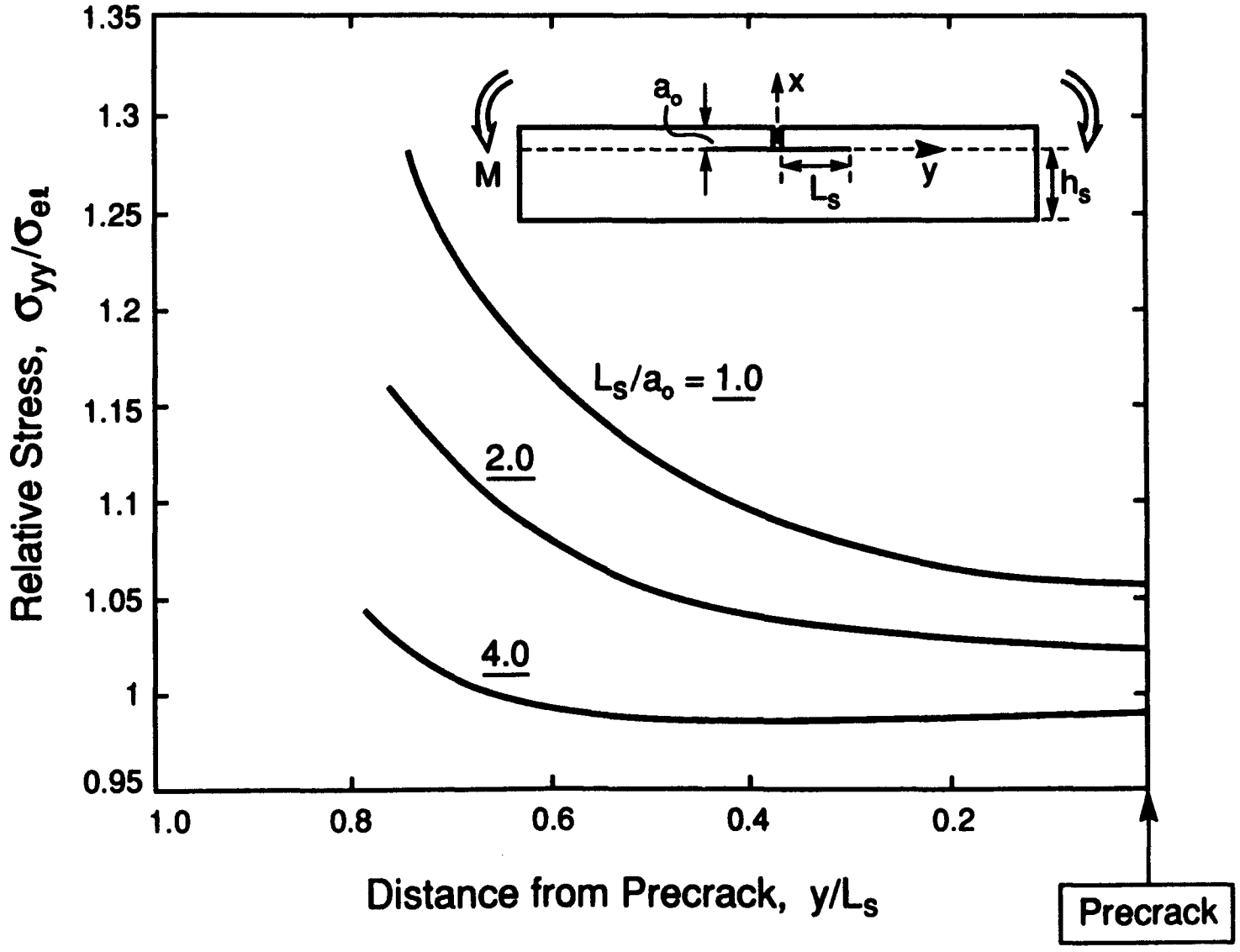
1.35
1.3
1.25
1.2
1.15
1.1
1.05
1
0.95
Relative Stress, σ_{yy}/σ_{el}
1.0
0.8
0.6
0.4
0.2
Distance from Precrack, y/L_s
a_o
x
M
y
L_s
h_s
$L_s/a_o = 1.0$
2.0
4.0
Precrack

Figure 10

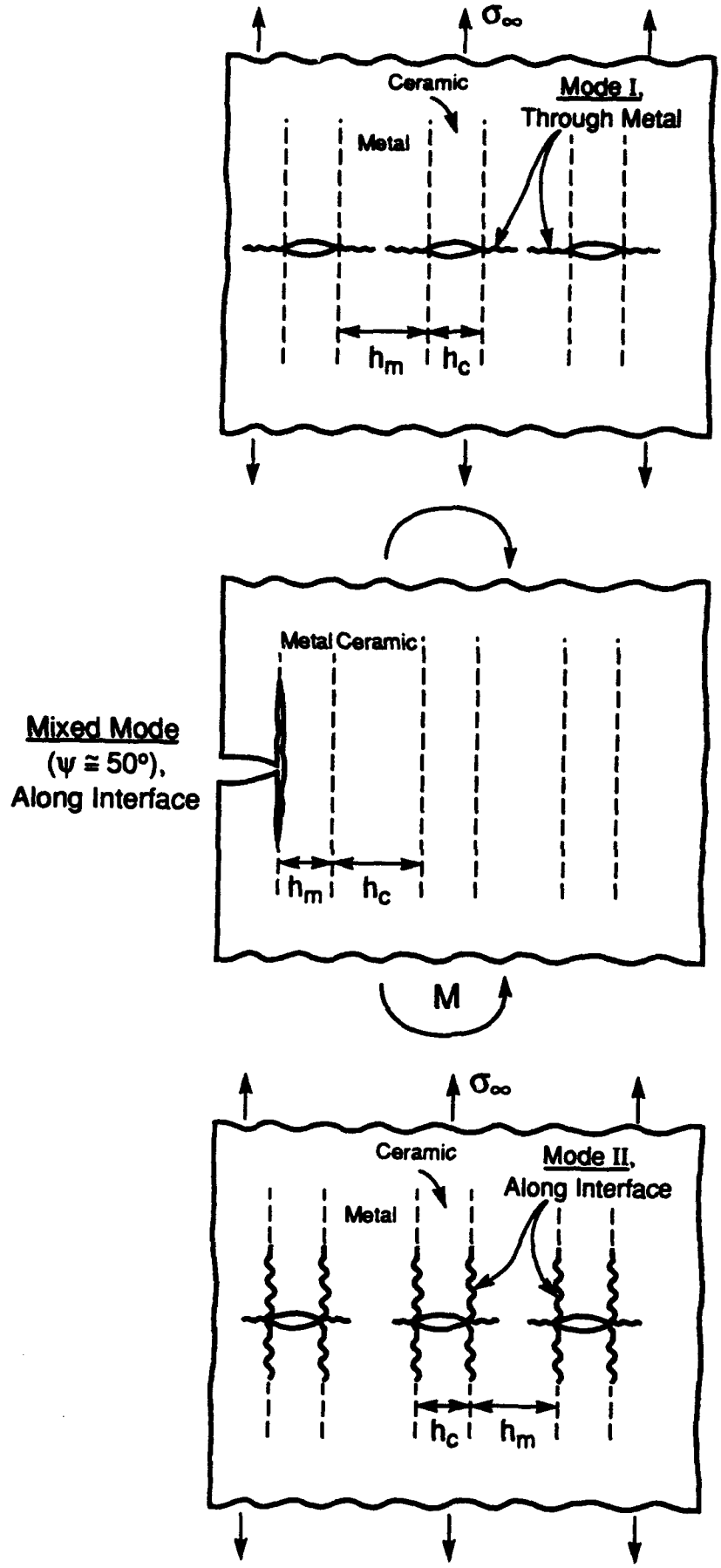

Shaw.Evans.URI-10/93-emk-0361217-4

Figure 11

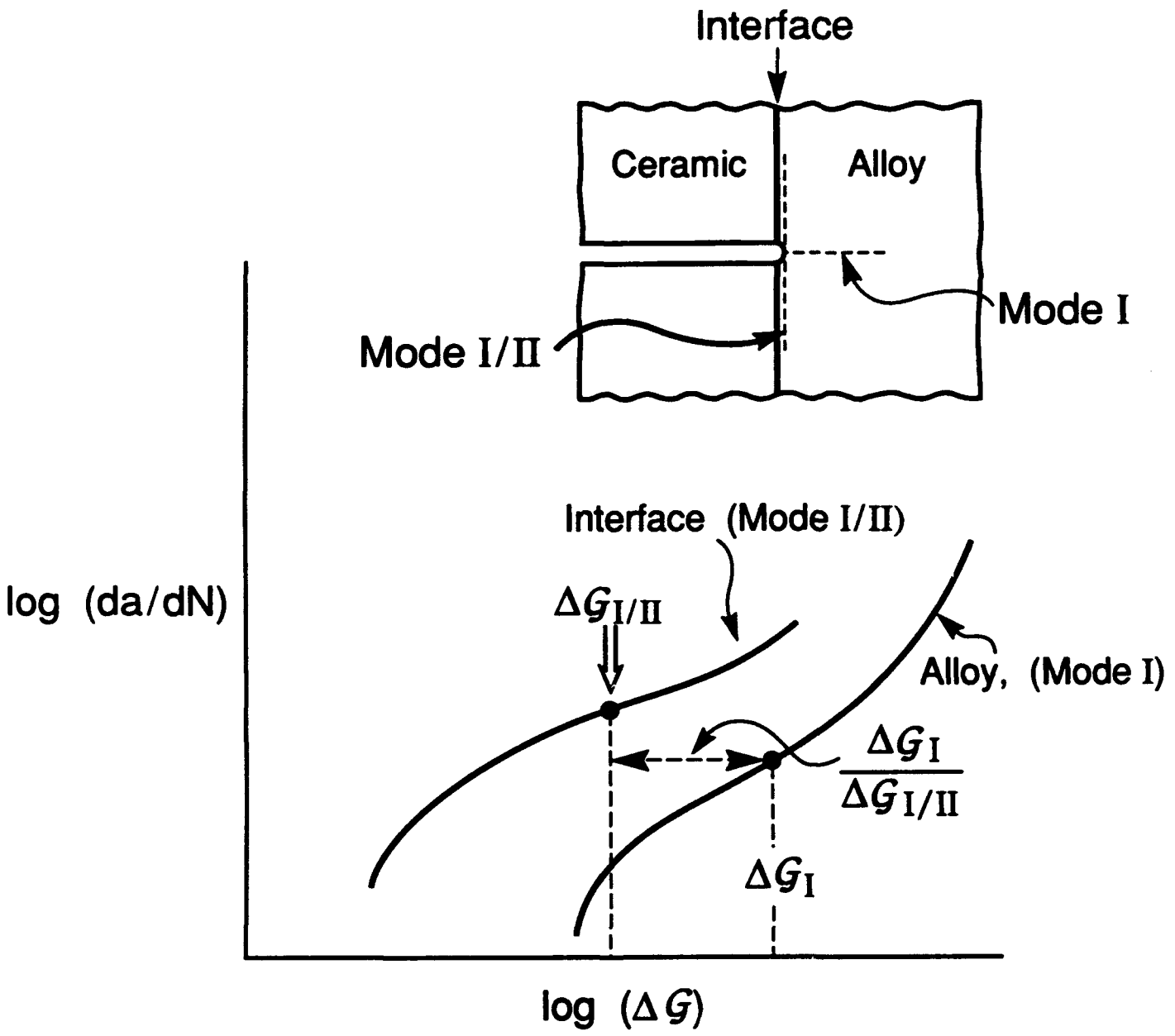
Interface
Ceramic
Alloy
Mode I
Mode I/II
Interface (Mode I/II)
log (da/dN)
$\Delta G_{I/II}$
Alloy, (Mode I)
$\frac{\Delta G_I}{\Delta G_{I/II}}$
ΔG_I
log (ΔG)

Figure 12

Dislocations, Steps and Disconnections at Interfaces

by

J.P. Hirth

Mechanical and Materials Engineering Department

Washington State University, Pullman, WA 99164-2920

Abstract

Line defects at interfaces, excluding disclinations, are classified as dislocations, steps and disconnections. A Burgers circuit procedure is described to determine the vector describing the geometry of each of these defects. Applications to several cases of phase transformations are discussed.

1. Preface

It is a great pleasure to participate in these proceedings honoring R.W. Balluffi. I have had the pleasure of collaborating with him and have found his seminal work on interface structures to be an inspiration throughout my career.

2. Introduction

Formally, the Burgers vector **b** of a dislocation can be defined in terms of the Burgers circuit, introduced by Frank[1] or by general symmetry theory as described by Pond[2]. Ledges on free surface are topologically connected with dislocations: indeed superposing a perfect surface onto an equivalent one containing a right-angled ledge creates a pure edge dislocation. Steps with ledge-like character can also exist at internal interfaces (we use ledge for free surfaces and steps for internal interfaces to distinguish

between the two cases). Some attention has been given to the dual step/dislocation character of line defects at interfaces[3-5]. However, no formal definition of a step vector equivalent to the Burgers vector has been presented.

Here we present a circuit procedure that defines a ledge or step vector ℓ. Several examples of defects with pure step character, pure dislocation character and mixed character are presented. Because the latter defect has partial dislocation and partial step character, it is neither a pure dislocation nor a pure step. We propose the name disconnection for this defect. This usage would be consistent with the discussion by Kröner[6] of the crystallographic theory of connectivity at interfaces.

3. Surface Ledges

Consider the ledge in Fig. 1a on a simple cubic crystal. There may be local relaxations of a dipole nature near the ledge[7] but in general there is no ambiguity about the atom positions near the ledge, unlike the dislocation case, where nonlinear strains near the core are so large that a "bad" region near the core is excluded from Burgers circuit operations[1]. Hence, we can start and end a circuit at a ledge and we prescribe that this be the case. Analogous to the dislocation case, a sense vector ξ is assigned to the ledge. A right-hand circuit relative to ξ is then completed, starting at S ending at F as in Fig. 1a. The same circuit is constructed in a perfect reference lattice, Fig. 1b, thereby suppressing elastic and thermal vibrational strains. The closure vector **FS** is the ledge vector ℓ and the convention **FS/RH** is the same as that for a dislocation.

In the example of Fig. 1b, the ledge vector is normal to the terrace surface, and $\ell = h$, the ledge height. This need not be the case. Fig. 1c shows a circuit in a monoclinic crystal where ℓ has components ℓ_1 and ℓ_2 with $\ell_1 = h$ and $\ell_2 = m$. In general $\ell = (\ell_1, \ell_2, \ell_3)$ with $\ell_3 = s$. If one pasted a crystal with coincident symmetry and a planar surface onto Fig. 1c, the dislocation of Fig. 1d would be created, with Burgers vector components $\mathbf{b} = (b_i$.

b_2, b_3) and b_1=*h*, b_2=*m*, b_3=*s*. The designation *h* is related to ledge height, *m* to the misfit component of dislocations at interfaces and *s* to the screw component of dislocations at interfaces. Fig. 1e shows a ledge converting to a dislocation: continuity of circuit vector is maintained at the dislocation-ledge junction and the circuit vector content is conserved. In low symmetry crystal where there are several possible ledge descriptions, Fig. 1f, that with the shortest ledge vector is selected.

4. Interfacial Defects

a. Misfit Dislocation

Both circuit procedures and the symmetry/dichromatic complex methods[2] for identifying Burgers vectors are discussed by Pond and Hirth[5]. An example is given in Fig. 2 for a (5/6) [100] misfitting (010) surface for a tetragonal crystal. Figure 2a represents the incommensurate interface. Figure 2b represents the crystals strained to the coherent or commensurate state. A circuit drawn in Fig. 2b and then repeated in the unstrained reference state of Fig. 2c gives the total Burgers vector content [100] (referred to α) of the coherent interface. this content can be thought of as being partitioned on coherency dislocations $\frac{1}{5}$[100] distributed on the interface as shown in Fig. 2b. For this case, the dislocations $\frac{1}{5}$[100] are the minimum size dislocations of the dichromatic complex[2], i.e. the superposition of the α and β lattices. The coherency strain can be removed by superposing a misfit dislocation with Burgers vector equal and opposite to that of the coherency dislocations, Fig. 2d. Alternatively one could imagine straining Fig. 2d to the equal lattice parameter state of α Fig. 2e and performing a conventional Burgers circuit to determine its Burgers vector $[100]_\alpha$.

The configuration of Fig. 2d is conventionally viewed as a positive dislocation with its extra half-plane residing in α, although it could equally well be regarded as a negative

dislocation with its missing half plane in β. We adopt the former view for convenience in defining a procedure for the circuits in the following cases.

b. Disconnections

In the procedure for steps, misorientation dislocations and disconnections, we wish to suppress effects associated with coherency and misfit strains. Therefore in the subsequent treatment, we use the coherently strained reference states of Fig. 2b and e. Any necessary misfit dislocations can be determined separately from the defects now considered. To form a disconnection we imagine two crystals with opposing ledges as in Fig. 3a. Conventionally, we choose α as the crystal with the largest ledge height since we wish to associate the step height of the disconnection with the height of the β ledge. The ledge vectors l_α and l_β are determined by the procedure described previously. The crystals are rigidly brought into contact, Fig. 3b, leaving a gap to the right of the step. The gap is closed, Fig. 3c, creating a disconnection with both step character, the contact region in Fig. 3b, and dislocation character, arising from the gap closure. With, these prescriptions, the Burgers vector **b** and step vector l of the disconnection are, respectively

$$\mathbf{b} = l_\alpha + l_\beta$$

$$l = -l_\beta$$

For the example of Fig. 3a, the step vector is normal to the surface and the step height is $h = |l_\beta|$. If one defines a vector **n** normal to the α surface in Fig. 3a, one can make a connection with the signs of steps as discussed by Pond and Hirth[5]. In their convention a step is positive if the step translates the terrace in the direction of **n** when traversing the step in the $\xi \times \mathbf{n}$ direction. This convention is seen to hold for the example of Fig. 3a.

The formation of a less simple step is illustrated in Figs. 3 d-f. In this case, the ledge vector l_β is inclined to the terrace normal of β so the ledge height is the projected length. Also the step height is now $h = l \cdot \mathbf{n}$ In closing the gap of Fig. 3e both displacements

parallel and perpendicular to the interface are needed as indicated by the dashed lines in the figure. As a consequence, the disconnection has both components $b_1=h$ and $b_2=m$. The latter component serves to either increase or decrease any necessary misfit accomodation. In general a component b_3 could be present. Since it is not simple to depict in two dimensions but is easy to envision in three dimensions, we do not explicitly show this case.

c. Pure Steps

Figure 4 shows the formation of a pure step. In this case $t_\alpha = -t_\beta$ in Fig. 4a so that the resulting defect, Fig. 4b, has no dislocation character. The defect in this case is a pure step, one limiting form of the disconnection.

d. Misorientation Dislocations

Figure 5 depicts the formation of a pure misorientation dislocation. In this case $t_\beta = 0$ in Fig. 5a. The resulting defect, Fig. 5b, has pure dislocation character, the other limiting form of the disconnection. Interface dislocations of this type are misorientation dislocations in the sense that their presence produces a rotation of β with respect to α. By symmetry, evidently the misorientation dislocations can have their extra half-phases in α, Fig. 5b, or in β, Fig. 5c.

5. Discussion

The description of the step and dislocation character of interfacial defects has several interesting applications. Defects at interfaces must have translational character t with t being a vector of the dichromatic complex[1] if the presence of the defect is not to also entail a stacking fault being present. In the interface context this means that t must equal $(\mathbf{b}+\ell)$. Such disconnections are important in phase transformations and prescribe

conditions that must be fulfilled when they act as so called translational dislocations and/or structural ledges.[8-10]

Another case of interest is that of oxidation where misfit dislocations, misorientation dislocations, and disconnections all have different behavior as point defect sources and sinks.[11-13] The dislocation character of all three defects is important in the mechanism of introducing interface control into scaling kinematics by means of pinning of interfacial defects.[14]

The above description is valid for the homogeneous, isotropic, linear elastic case. More generally, the true definitions of $\mathbf{b}$ and ℓ in the perfect reference lattices as defined here remain valid. However, the local definitions can differ. For example, the reference lattice for the true $\mathbf{b}$ for Fig. 2e is the perfect unstrained α lattice. The local $\mathbf{b}$ in Fig. 2d can be thought of as belonging to neither lattice. In a simple treatment, the local $\mathbf{b}$ can be taken as the geometrical mean of $[100]_\alpha$ and $[100]_\beta$ unless the lattice parameter of α and β differ drastically, in which case a more detailed treatment is needed.[15] Of course, these small variations of $\mathbf{b}$ imply also variations in ℓ since $\mathbf{t} = \mathbf{b} + \ell$ is fixed by the ideal reference dichromatic complex. Also, the strain fields in α and β are modified in the inhomogeneous case by the presence of image dislocations. These effects can be viewed as second-order in nature, important only in the limit of large differences in elastic constants or misfit.

6. Summary

A circuit procedure is described to define step and dislocation vector components of interfacial defects called disconnections. Examples of a variety of cases illustrate the utility of the method. The description should have applications in descriptions of interfaces in local equilibrium, in shear and diffusional phase transformations, and in particular in the modeling of scaling reactions.

Acknowledgment

The author is grateful for the support of this research under the Advanced Research Projects Agency, University Research Initiative at the University of California, Santa Barbara, under Office of Naval Research Contract No. 00014-93-I-0213; and to R.C. Pond: discussions with him were crucial to the development of the concepts presented here.

References

(1) Frank, F.C., *Philos. Mag.*, **42**, 809 (1951).

(2) Pond, R.C., Dislocations in Solids, Vol. 8, p. 1 (edited by F.R.N. Nabarro), North-Holland, Amsterdam (1989).

(3) King, A.H., *Acta Metall*, **30**, 419 (1982).

(4) Hirth, J.P., and Tiller, W.T., *J. Appl. Phys.*, **56**, 9471 (1984).

(5) Pond, R.C. and Hirth, J.P., *Solid State Phys*, in press.

(6) Kröner, E., Dislocations and Properties of Real Crystals, p. 67 (edited by B. Eyre), Oxford University Press, Oxford (1985).

(7) Chen, S.P, Voter, A.F. and Srolovitz, D.J., *Phys. Rev. Lett.*, **57**, 1308 (1986).

(8) Christian, J.W., Proceedings of the ASM Conference on Bainitic Phase Transformations, *Metall. Trans. A*, in press.

(9) Aaronson, H.I., ibid.

(10) Hirth, J.P., ibid.

(11) Tiller, W. A., *J. Electrochem. Soc.*, **127**, 625 (1980).

(12) Pierragi, B. and Rapp, R. A. , *Acta Metall.*, **36**, 1281 (1988).

(13) Hirth, J. P. , *Metall. Trans.*, **22A**, 1331 (1991)

(14) Pieraggi, B., and Rapp, R.A., *J. Electrochem Soc.*, in press.

(15) Dregia, S.A. and Hirth, J.P., *J. Appl. Phys.*, **69**, 2169 (1991).

Figure Captions

Fig. 1 The sense vector ξ points out of the page for (a) - (d): (a), ledge on simple cubic crystal and circuit; (b) circuit of (a) in perfect reference crystal; (c) ledge on monoclinic crystal; circuit of (c) in perfect reference crystal; (e) ledge changing into dislocation.

Fig. 2 ξ points out of the page: (a), incommensurate interface in tetragonal crystal; (b), reference lattice strained to lattice parameter of α; (c) circuit of (b) in relaxed reference; (d) lattice of (b) relaxed in presence of misfit dislocation; lattice of (d) with both phases strained to normal lattice parameter of α.

Fig. 3 ξ points out of the page: (a), crystals of α and β with ledges; (b), crystals in (a) rigidly brought into contact; (c) relaxed version of (b); (d), crystals of α and β with ledges.; (e) crystals in (c) rigidly brought into contact; (f), relaxed version of (e).

Fig. 4 ξ points out of the page: (a) crystals of α and β with ledges; (b) crystals brought into contact forming pure step.

Fig. 5 ξ points out of the page: (a) crystal of α, with ledge, and β; (b) crystals brought into contact forming misorientation dislocation; (c) another version of misorientation dislocation.

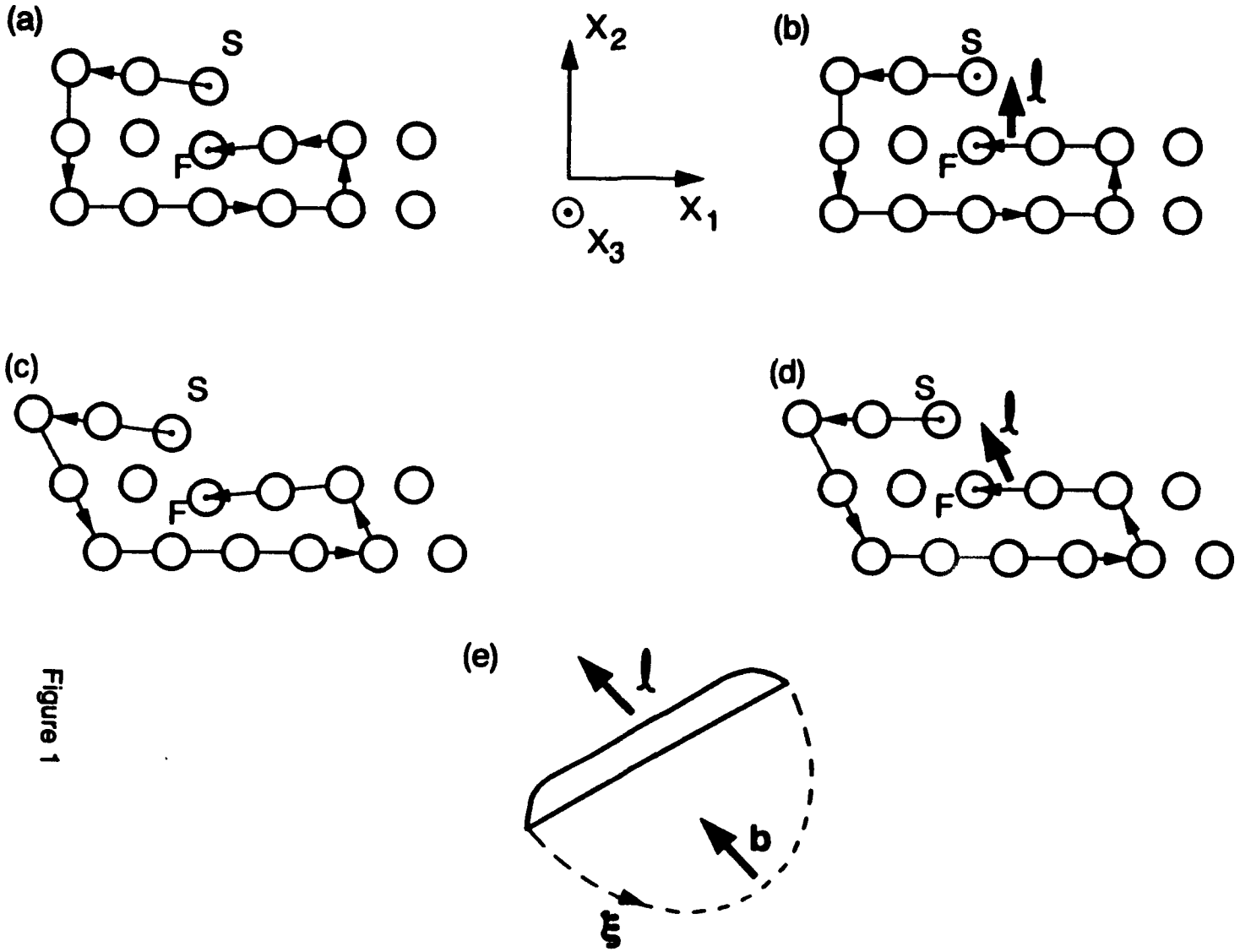

Figure 1

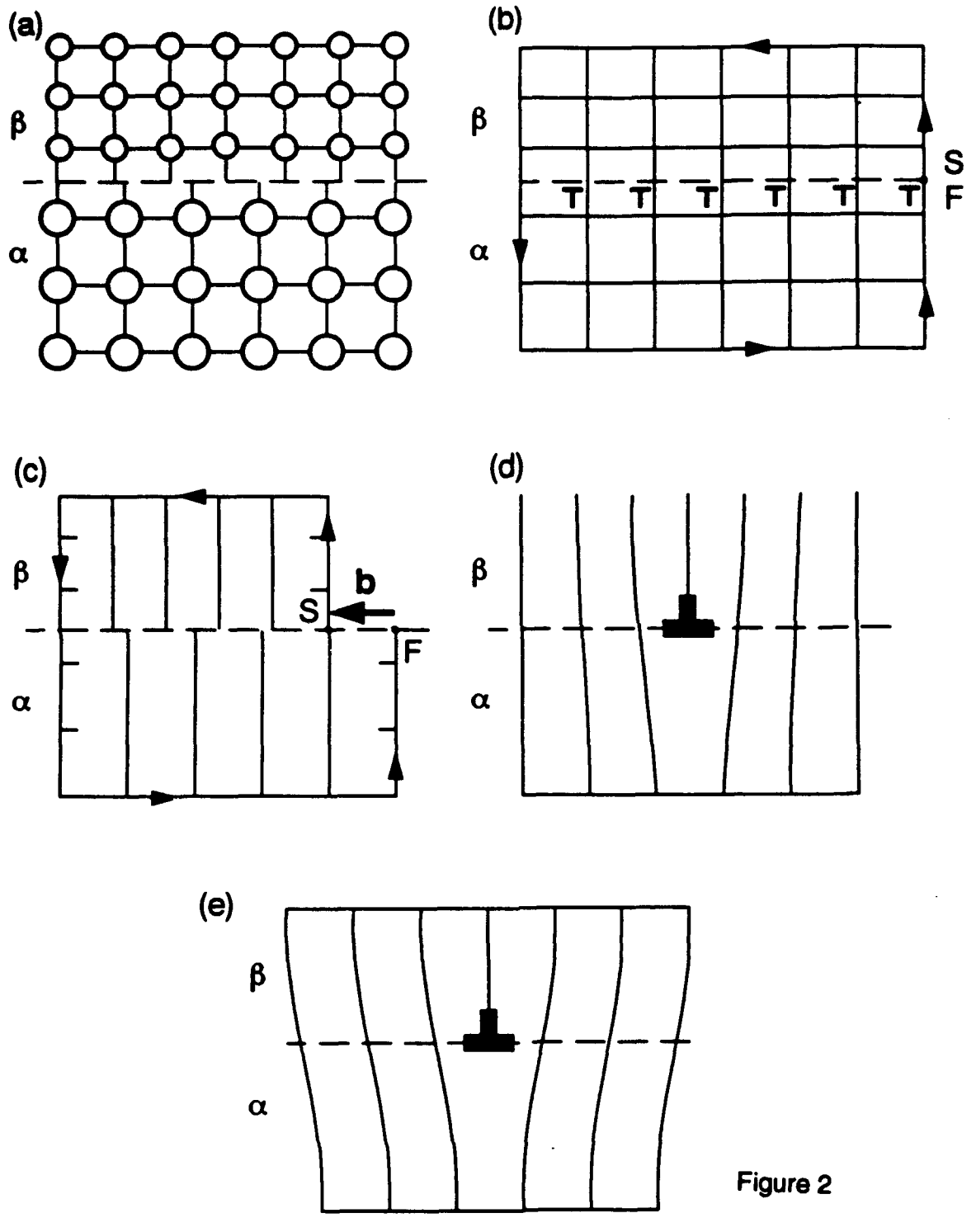

Figure 2

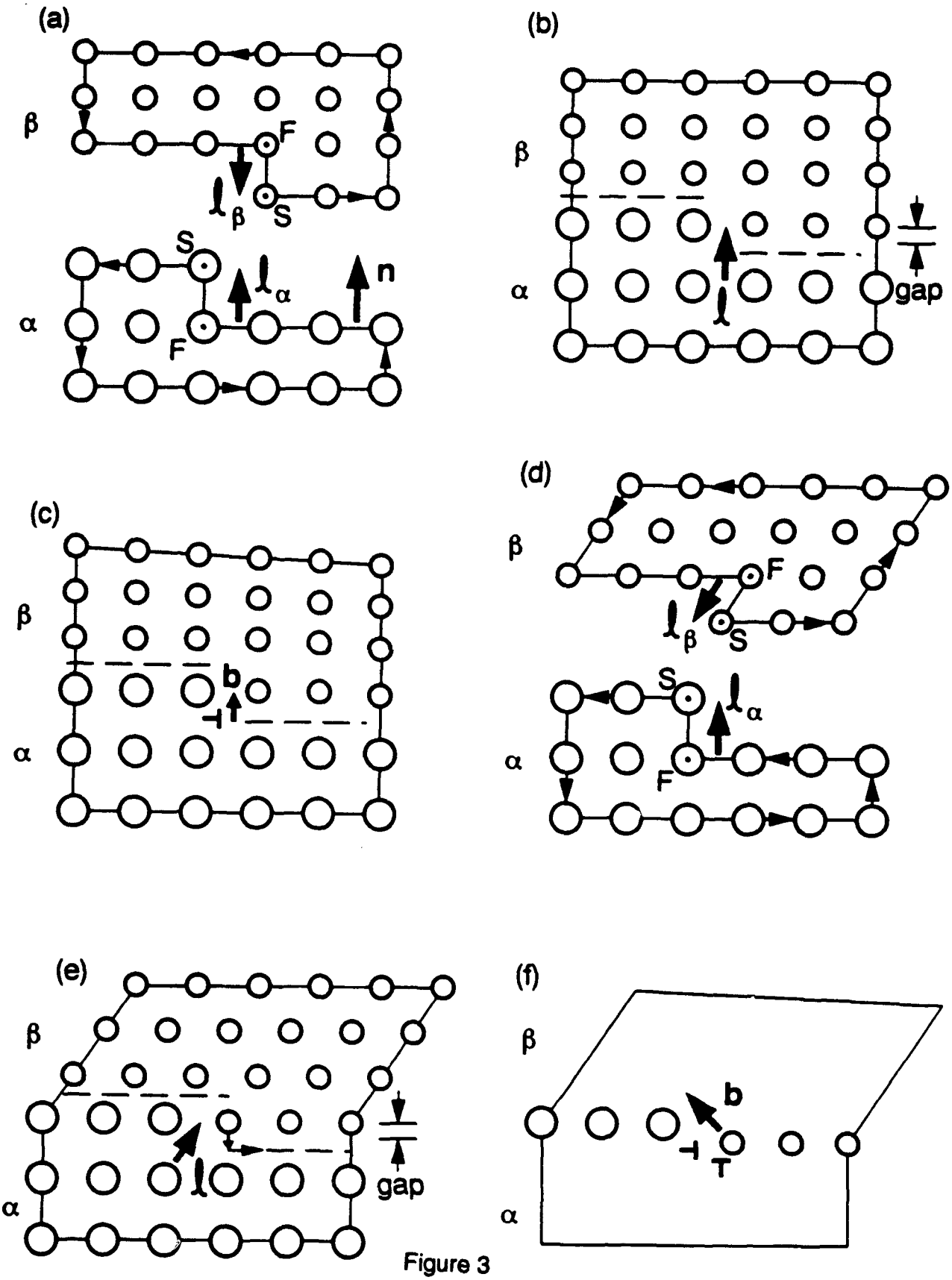

Figure 3

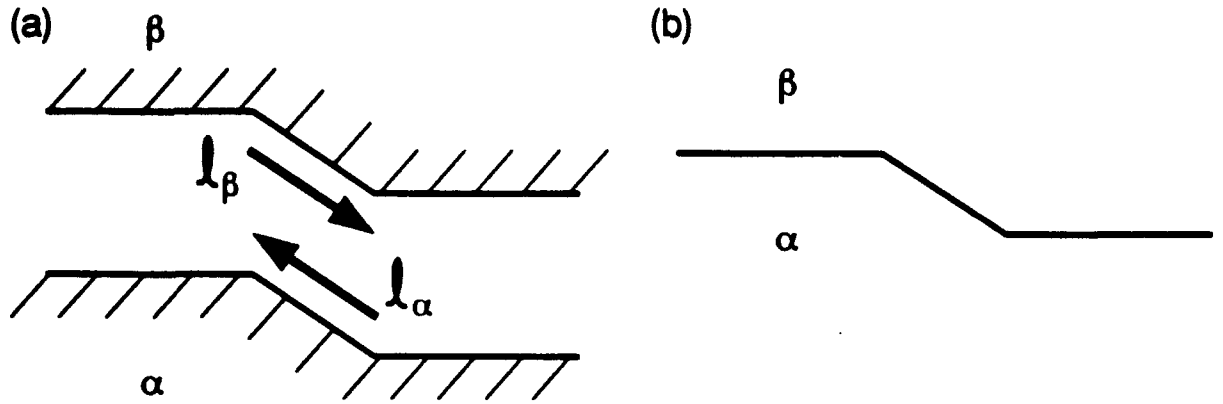

Figure 4

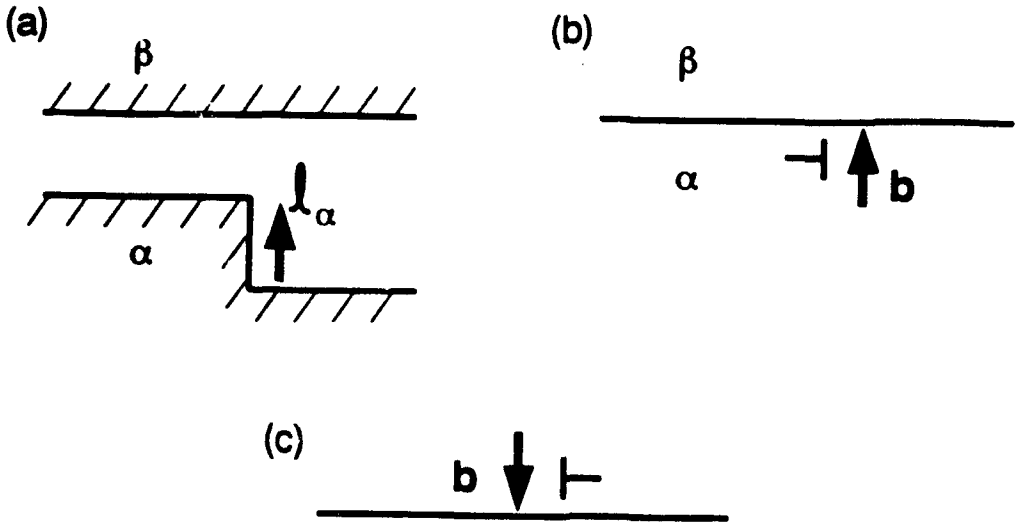

Figure 5

ON THE DIRECTIONALITY OF INTERFACIAL CRACKING IN BICRYSTALS AND THE LOADING PHASE ANGLE DEPENDENCE

Jian-Sheng Wang
Division of Applied Sciences, Harvard University, Cambridge, MA 02138.
and
Glenn E. Beltz
Department of Mechanical and Environmental Engineering, College of Engineering, University of California, Santa Barbara, CA 93106.

ABSTRACT: Experimental evidence on the direction and loading phase angle dependence of interfacial cracking in bicrystals of Cu and Fe-Si alloys, and in metal/sapphire bimaterial systems, is presented. The response of a stressed interfacial crack depends not only on the structure of the interface, but also on the direction of the crack propagation and the local loading conditions. This directionality of interfacial cracking and the loading phase angle effect seem explainable in terms of the competition between dislocation emission from the crack tip and decohesion of the interface, and relate to the asymmetrical angular orientation of slip planes relative to the interface.

It has not been well acknowledged so far, that the interfacial cracking behavior for a given interface between solids may depend on the direction of the crack propagation. *I. e.*, a crack may propagate in a ductile manner in one direction, while in the opposite direction it may cleave leading to brittle decohesion. Thus, the response of a stressed interfacial crack tip is not only structurally dependent, it is also directionally dependent.

The directionality of interfacial cracking in bicrystals was first quantified by the modified Rice-Thomson model[1] and supported by Wang and Anderson's experimental results : $\Sigma 9$ [110]/$(2\bar{2}1)$ copper bicrystals

[2]. With the intent of extending the R-T model to the behavior of interfacial cracks in dissimilar materials, Rice, Suo and Wang[3] predicted that this directionality occurs also in bimaterials. A remarkable result of that prediction is that the ductile direction under mode I loading in the copper bicrystal mentioned above is the brittle direction in a bend test in the copper/sapphire bimaterials system when the copper $(2\bar{2}1)$ plane is bonded to sapphire. This prediction was recently verified experimentally[4] and the change of the directional behavior may be attributed to the effect of the loading phase angle[3].

Due to the importance of the directional dependence in understanding failure in advanced materials, both theoretically and practically, a detailed discussion is in demand. In this paper, experimental evidence is first presented. Then, we discuss the energetics of dislocation emission from the tip of an interfacial crack, so that a possible interpretation of this phenomenon may be reached. The discussion is initially based on the modified R-T model of Anderson and Rice[1] and Rice, Suo and Wang[3]. It is valuable due to its simplicity and ability of qualitative prediction. A brief introduction to a recent, and more realistic, approach [5, 6], which evaluates the energetics of the nucleation of an incipient dislocation from a crack tip using the Peierls concept, follows. In the third part of the paper experimental results will be discussed based on the models.

EXPERIMENTAL EVIDENCE

The Directional Dependence of Interfacial Cracking in Copper Bicrystals

In a study of the fracture behavior of Cu bicrystals[2] contaminated with sulphur the $\Sigma 9$ [110]/$(2\bar{2}1)$ symmetric tilt bicrystal showed the directional dependence of crack propagation. The bicrystal was first uniformly strainhardened by fatigue in a way that would not form persistent slip bands[7, 8]. Then it was divided into two specimens and a notch was made by spark erosion along the boundary with the tip parallel to the [110] and co-planar with the $(1\bar{1}\bar{1})$ or $(1\bar{1}1)$ slip planes. The notches were cut so that in one specimen the crack would potentially propagate in the $[\bar{1}14]$ direction, while in the other, in the opposite direction, $[\bar{1}14]$. The two notched specimens were further tested by tension-compression fatigue with R=-1.

At the resolved shear stress of 28 MPa, unstable crack propagation along the interface of the specimen with the cracking direction of $[1\bar{1}4]$ occurred at $6x10^3$ cycles. An intergranular brittle fracture surface with cleavage tongues was obtained (Fig.1a) and sulphur-bearing particles were observed on the fracture surfaces. In contract, the specimen with the potential cracking direction of $[\bar{1}14]$ underwent stable fatigue cracking for 6.5×10^4 cycles without fracture. It was then broken at a monotonic tensile loading corresponding to a resolved shear stress of 76.7 MPa. The fracture surfaces showed a well developed striation structure (Fig.1b). No sulphide particles were found on the fracture surface, indicating a transgranular fracture. Since the only difference between these two specimens is the directions of crack propagation, the different behavior can only be interpreted as the directional dependence of the ductile versus brittle response of the interface.

Cracking Direction Effects in Copper/Sapphire Interfaces

In the spirit of testing the idea that the competition between dislocation emission and cleavage decohesion controls the ductile versus brittle behavior of a metal/ceramic interface and that the crack response is directionally dependent, Wang and Beltz[4] studied the fracture behavior of a copper/sapphire interface.

Rectangular pieces of Cu single crystals were cut via EDM with the basal surfaces parallel to $(2\bar{2}1)$ or (001) crystallographic planes and the side surfaces parallel to (110) planes. The $(2\bar{2}1)$ or (001) surface was bonded to the $(11\bar{2}0)$ plane of a commercially-obtained sapphire slide by diffusion bonding. TEM examination showed that there was no intermediate interaction layer in the interface and good atomic bonding was achieved[9]. A pre-notch was made at the midpoint of the sapphire layer and then the specimen was subjected to a bend load to initiate an interfacial crack. The pre-cracked specimen was loaded under four-point bending until a nonlinear load versus deflection relation was noted and then was unloaded and reloaded several times to let the crack grow.

In all but one of the $Cu(2\bar{2}1)$/sapphire specimens tested the interfacial crack propagated only in the $[\bar{1}14]_{Cu}$ direction causing interfacial debonding, while plastic deformation occurred in the

opposite direction, $[\overline{1}\overline{1}4]_{Cu}$, as shown in Fig.2. In one specimen the crack propagated in the $[\overline{1}\overline{1}4]_{Cu}$ direction a small amount, but in the $[\overline{1}\overline{1}4]_{Cu}$ direction an unstable cracking occurred causing half the sapphire layer to detach entirely from the copper crystal. On the $(110)_{Cu}$ side surface, dense slip traces appeared near the tip area in the $[\overline{1}\overline{1}4]_{Cu}$ direction, exhibiting the emission of dislocations from the tip during bending, while in the opposite direction the slip traces were much less. The results showed a strong directional dependence of interfacial cracking in the Cu$(2\overline{2}1)$/sapphire interface. The interface was brittle in the $[\overline{1}\overline{1}4]$ direction and ductile in the $[\overline{1}\overline{1}4]$ direction, opposite to that in the $\Sigma 9$ [110]/$(2\overline{2}1)$ bicrystals.

This directional dependence did not appear in the Cu(001)/sapphire specimens. There, the interfacial crack grew in the both directions by debonding and deformation. Slip traces were observed on the $(110)_{Cu}$ surfaces, indicating dislocation processes during debonding.

Corrosion Fatigue and Stress Corrosion Cracking in Fe-2.7wt.%Si Bicrystals

Fe-Si bicrystals are known to be susceptible to intergranular corrosion fatigue [10] and stress corrosion cracking (SCC) in $(NH_4)_2CO_3$ and $(Na_2CO_3+NaHCO_3)$ solutions [11]. The processes of corrosion fatigue and SCC can be described by a simple slip step dissolution model, in which crack growth is assumed to proceed by alternate dislocation emission and film rupture and dissolution. A directional dependence of crack growth might thus be anticipated when there is an asymmetry of dislocation activity at opposite crack tips.

In a study of the influence of localized slip on the nucleation and growth of intergranular stress corrosion cracking (IGSCC), Vehoff and his colleagues found a directional effect upon IGSCC in [010] symmetric tilt bicrystals of an Fe-2.7wt.%Si alloy [11]. Their results are replotted in terms of a brittleness parameter, $a_n = Ctg(\alpha/2)$, where α is the crack tip opening angle, versus the tilt angle of the bicrystal in Fig.3. A higher value of a_n represented more susceptible to IGSCC. The authors believed that the cracking directional dependence was due to the asymmetry of the shear stresses on the active slip planes near the crack tip in opposite directions.

The directional dependence of corrosion fatigue and SCC was studied by Wang in detail with Σ5[100]/(021) bicrystals of an Fe-2.7wt.% Si alloy [12]. Single edge cracked tension specimens (SECT) in dimensions of 5x6x30 mm were cut by EDM to allow the interface to be perpendicular to the specimen axis. Notches were made along the boundaries in opposite directions, $[0\bar{1}2]$ and $[01\bar{2}]$, respectively. For convenience, the $[0\bar{1}2]$ direction was designated the positive direction and $[01\bar{2}]$, the negative. Fatigue and SCC tests were carried out in a standard three-electrode cell in a solution of 2M $(NH_4)_2CO_3$ at 343 K under potentiostatic control. The specimens, except the notched area, were coated with lacquer to prevent general corrosion of the surfaces.

Corrosion fatigue

The fatigue tests were conducted under a constant load control model with the initial ΔK_I=6.5 MPa$\sqrt{m}$, the mean level 7 MPa$\sqrt{m}$ and the load frequency 1 Hz. The working potential was -587 mV relative to the SCE cell, and the current density was measured to be about 100 mA/m^2.

The specimen with a positive crack failed at $6x10^3$ cycles. Figure 4a shows the fracture surface with striations in the $[4\bar{1}2]$ direction and secondary cracks along (100) cleavage planes. The final failure of the specimen occurred by cleavage along (010) planes at the tensile half of the last cycle. A large amount of persistent slip bands (PSB's), in spacing of about 100 μm along the [012] direction, were observed on the (100) surface. They were identified to originate from the $(12\bar{1})[\bar{1}\bar{1}1]$ slip system. PSB's along the $[0\bar{1}1]$ direction were also found on the side surface, suggesting (211) or (011) systems were also activated during fatigue.

Only a small amount of crack propagation was detected after $3x10^4$ cycles for the specimen with negative crack (Fig.4b). The specimen finally cleaved along the (010) cleavage plane under a monotonic loading of σ=228.5 MPa and K_{IC}=37 MPa$\sqrt{m}$. A small amount [012] slip traces was found on the (100) side surface of the specimen accompanying with cleavage. No slip traces originating from (211) or (011) slip systems were detected. The result showed that dislocations were not active at the crack tip.

Stress corrosion cracking and corrosion fatigue

Another pair of specimens was tested under repeated sustained and cyclic loading to evaluate the SCC behavior of the bicrystal. A tension load of 5700 N (initially K_I=18 MPa$\sqrt{m}$) sustained for 1.8×10^3 seconds and then fatigue of 300 cycles in load control model followed. This procedure was repeated until failure. The working potential was kept at -700 mV relative to the SCE cell. The initial current density was about 50 mA/m^2.

The specimen with a positive crack, $[0\bar{1}2]$, failed after two successions of sustained plus cyclic loadings. The crack growth rate was higher under cyclic loading than at sustained loading. At the second course of fatigue when the maximum K_I reached about 44 MPa$\sqrt{m}$ and the growth rate reached 12.5 μm/cycle unstable crack growth occurred resulting in a ductile failure. Figure 5a shows striations developed during second course of fatigue. Microscopically, the cracking direction is deviated about 60° away from the macroscopic cracking direction, $[0\bar{1}2]$ and the striations followed the $[4\bar{1}2]$ direction.

In contrast, the specimen with a negative crack failed by cleavage along (010) during sustained-loading (Fig.5b). No slip traces were found on the (100) side surface. The results show again that dislocation emission from the negative crack tip is difficult.

THE ENERGETICS OF DISLOCATION-LOOP EMISSION FROM A CRACK TIP ALONG AN INTERFACE

The directionality of interfacial cracking may be understood in terms of the competition between dislocation emission from the crack tip and decohesion of the interface, as proposed by Armstrong [13] and Kelly, Tyson and Cotrell [14] in 1960's and later modelled by Rice and Thomson [15] and recently advanced by Rice *et.al.* [1,3,5,6]. In the model, the energy release rate for dislocation emission from the crack tip, G_{disl}, and the energy release rate for cleavage, G_{cleav}, were compared. If $G_{disl} < G_{cleav}$ dislocations were assumed to emit from the crack tip, blunting the tip, before interfacial decohesion. The interface was predicted to be intrinsically ductile. If, on the other hand, $G_{disl} > G_{cleav}$, decohesion was assumed to occur before dislocation

emission and the interface was intrinsically brittle. While G_{cleav} is relatively insensitive to the misorientation of the crystal involved[3], G_{disl}, being mainly determined by the resolved shear stress on the slip plane, may change dramatically with the changing of the inclination angle of the slip plane with respect to the interface. Due to the geometrical asymmetry of the slip plane configurations at the crack tip in opposite directions, the energy release rate for dislocation emission from the crack tip in opposite directions may differ significantly.

In the first part of this section we will develop a model for the emission of a dislocation loop from the interfacial crack tip in bimaterials based on the Rice-Thomson approach. Then, we will give a brief description of a newer approach which treats the processes of incipient dislocation nucleation from a crack tip based on the Peierls-Nabarro concept.

The Rice-Thomson Approach

The Rice-Thomson type approach developed by Anderson and Rice for bicrystals [1] and by Rice, Suo and Wang for bimaterials [3] takes into account the balance of the work done by the applied stress and the energy of a dislocation emanating from the crack tip. This procedure evokes a dislocation core cutoff, a poorly defined parameter in the continuum elastic dislocation theory and, in essence, it deals only with emission of dislocations from the crack tip, not dislocation nucleation. We combine the model in [3] with that in [1] so that the treatment of loop emission criterion for symmetric bicrystals can be applied for bimaterials and asymmetric bicrystals.

Let us consider an interface in a bimaterial system, where the crack front lies along the intersection of the slip plane and the interface, a semicircular dislocation loop is assumed to emit into material 1 from the crack tip and material 2 is assumed to be elastic. The total energy of the dislocation loop as a function of the loop radius, r, consists of three terms:

$$E_{total}(r) = E_{self} + E_{ledge} - W_{stress} \qquad (1)$$

where E_{self} is the self energy of the loop, E_{ledge} is the energy of the ledge created by crack-tip blunting due to dislocation emission, and

W_{stress} is the Peach-Koehler type work done by the local crack-tip stress field to expand the loop. Evaluations of the three terms follow.

The near-tip stress field for an interfacial crack between dissimilar isotropic materials has the singular form [3]

$$\sigma_{\alpha\beta} = \frac{1}{\sqrt{2\pi r}}[\mathrm{Re}(Kr^{i\varepsilon})\Sigma^{I}_{\alpha\beta}(\theta) + \mathrm{Im}(Kr^{i\varepsilon})\Sigma^{II}_{\alpha\beta}(\theta)] \qquad (\alpha, \beta = x, y) \tag{2}$$

For simplicity, forms for 2-D conditions are presented. Here the angular functions $\Sigma_{\alpha\beta}(\theta)$ of superscripts *I* and *II* (given by [3]) correspond to tractions across the interface at $\theta = 0$ of tensile and in-plane shear, respectively, so that the complex stress intensity factor, *K*, is defined by

$$(\sigma_{yy}+i\sigma_{yx})_{\theta=0} = \frac{Kr^{i\varepsilon}}{\sqrt{2\pi r}} \tag{3}$$

In this expression θ is the angle made by the active slip plane and the interface. By definition, the parameter ε, the so-called oscillatory index, is given by

$$\varepsilon = \frac{1}{2\pi}\ln\left[\frac{(3-4\nu_1)/\mu_1 + 1/\mu_2}{(3-4\nu_2)/\mu_2 + 1/\mu_1}\right] \tag{4}$$

where μ is the shear modulus and ν the Poisson ratio, and subscripts refer to the two materials.

For most material pairs the parameter ε is small, in the range 0.01~0.04 so that $Kr^{i\varepsilon}$ is only a slow function of *r*. Therefore, in the case of the dislocation emission from the crack tip, for all *r* of order *b*, the Burgers vector of the dislocation loop in consideration, we have $Kr^{i\varepsilon} \cong Kb^{i\varepsilon}$. Based on this approximation, an atomic scale loading phase angle, ψ', might be defined by

$$Kb^{i\varepsilon} = |K|e^{i\psi'} \tag{5}$$

Here, the local phase angle ψ' is related to the applied loading phase angle, $\psi = \tan^{-1}[\mathrm{Im}(KL^{i\varepsilon})/\mathrm{Re}(KL^{i\varepsilon})]$ by $\psi' = \psi - \varepsilon\ln(L/b)$, where *L* is a characteristic length scale connected with the dimension of the specimen. We thus have

$$\mathrm{Re}(Kr^{i\varepsilon}) \equiv |K|\cos\psi' \text{ and } \mathrm{Im}(Kr^{i\varepsilon}) \equiv |K|\sin\psi' \tag{6}$$

The resolved shear stress acting on the slip plane, containing the crack front and making an angle θ with the interface, in the direction of the Burgers vector is given by

$$\begin{aligned}\tau &= \frac{b\cos\phi}{\sqrt{2\pi r}}[\,|K|\cos\psi'\Sigma^{I}_{r\theta}(\theta)+|K|\sin\psi'\Sigma^{II}_{r\theta}(\theta)\,] \\ &= |K|br^{-1/2}(S^{I}\cos\psi'+S^{II}\sin\psi')\end{aligned} \tag{7}$$

where the Schmid factors are

$$S^{I} = \frac{\cos\phi}{\sqrt{2\pi}}\Sigma^{I}_{r\theta}(\theta), \text{ and } S^{II} = \frac{\cos\phi}{\sqrt{2\pi}}\Sigma^{II}_{r\theta}(\theta) \tag{8}$$

with the angle ϕ between the Burgers vector and the normal to the crack front.

The Peach-Koehler force, τb, is integrated over the entire area of the semicircular loop of the dislocation[1] to obtain the work done by the applied stress

$$W_{stress} \equiv 3.5|K|br^{3/2}(S^{I}\cos\psi'+S^{II}\sin\psi') \tag{9}$$

The image force component opposing outward motion of a dislocation line, and drawing it back to the crack tip, has been solved by Rice[16] for the general case of joined anisotropic solids. It depends only upon the elastic properties of the material in which the dislocation resides, (material 1 in our case,) and is

$$f_{image} = \frac{1}{r}b_{\alpha}A_{\alpha\beta}b_{\beta} \tag{10}$$

where $A_{\alpha\beta}$ is the pre-logarithmic energy factor matrix of a straight dislocation line in that material[17]. Following the procedure of Anderson [1], the self energy of the dislocation loop emitted from the crack tip is

$$E_{self}=\pi r A_o \ln\frac{8mr}{e^2 r_o} \tag{11}$$

Here r_o is the dislocation core cutoff, the most poorly defined parameter in the model, and m is a geometric factor given by [18]

$$m \equiv \exp[1.23\cos^2\phi \ln m_2 + 0.86\sin^2\phi \ln(2\cos(\theta/2))] \tag{12}$$

where

$$m_2 = 2\cos\frac{\theta}{2}\exp\left(-\frac{1}{2}\sin\frac{\theta}{2}\sin\frac{3\theta}{2}\right).$$

A_o is the pre-logarithmic energy factor $b_\alpha A_{\alpha\beta} b_\beta$ for a straight dislocation with the same Burgers vector as the loop, averaged over all possible orientation angles ϕ of the line within the loop plane. For the isotropic case

$$A_o = \mu_1 b^2 \frac{2-\nu_1}{8\pi(1-\nu_1)} \tag{13}$$

The ledge energy created by crack-tip blunting due to dislocation emission is given by [15] as

$$E_{ledge} = \gamma_{ledge} b\cos\phi\sin\theta \tag{14}$$

where γ_{ledge} is the free energy of the ledge, which is usually a fraction of the surface free energy[2].

Claiming that spontaneous dislocation emission occurs when both the first and the second derivatives of the total energy of the loop, with respect to the loop radius equal to zero[1], the critical stress intensity factor for dislocation emitting from the crack-tip is thus derived as

$$|K|(S^I\cos\psi' + S^{II}\sin\psi') = 0.76\frac{A_o}{b}\sqrt{\frac{m}{r_o}}\exp\frac{E_{ledge}}{\pi A_o} \tag{15}$$

The Irwin-type energy release rate for the dislocation emission is given by

$$G = \frac{|K|^2}{E^* \cosh \pi\alpha} \tag{16}$$

where

$$\frac{1}{E^*} = \frac{1}{2}\left(\frac{1}{\bar{E}_1} + \frac{1}{\bar{E}_2}\right) \text{ and } \bar{E} = \frac{E}{1-\nu^2} = \frac{2\mu}{1-\nu}$$

define the plane strain Young's modulus.

The Approach of the Peierls-Nabarro Type

The methods for determining G_{disl} as discussed in the previous discussion treats a dislocation as an elastic singularity that exists ahead of the crack tip prior to loading. An unfortunate consequence of this usage is that a core cutoff parameter is present in the analysis. Argon [19] and, more recently Schöck [20] have recognized that a full dislocation is likely to emerge unstably from an incomplete, incipient dislocation at the tip, and an exact treatment has been given recently by Rice [5]. That treatment, discussed in further detail by Beltz and Rice [21, 22], solves the elasticity problem of a traction free crack with a Peierls-type stress versus displacement relation being satisfied as a boundary condition along a slip plane ahead of a crack tip. Once this problem is solved for a suitable constitutive relation for material sliding and perhaps opening along a slip plane, there is no need for the core cutoff parameter. This method allows for the existence of an extended dislocation core during nucleation, and eliminates uncertainty in choosing the core parameters. Numerical work by Beltz and Rice [22] agrees with the directional and phase angle effects given by the Rice-Thomson model [3] for the case of a metal/ceramic interface.

The P-N type approach requires a knowledge of the Peierls shear stress τ ($\equiv\sigma_{r\theta}$, on $\theta=0$ in the case now discussed) versus relative atomic displacement, Δ_r, relation. The simplest form of this is a sinusoidal relation. The τ/τ_{max} vs. Δ_r/b curve gives the shear stress needed to locally shear atoms with respect to one another on a given slip plane, and is the fundamental input to the Peierls-Nabarro dislocation model [23,24]. The initial slope of such a curve corresponds with an appropriate shear modulus. The parameter b, the magnitude of a Burgers vector, represents the periodicity of the stress-displacement relation. This type of data has been calculated through the use of pair

potentials, the embedded atom method, or density functional theory by several researchers [25-28]. The integral of such a curve from Δ_r=0 to the unstable equilibrium position at which the shear stress next vanishes (at Δ_r=$b/2$ in simple cases) is known as the unstable stacking energy, denoted γ_{us} [5]. An estimate of this solid state parameter for copper, based on Frenkel theory (which models the τ versus Δ_r curve as a sine wave), gives a value of about 0.22 J/m^2 [6].

A J-integral calculation may be used to derive the following result for a mode II shear crack with a coplanar slip plane (see [29] for details):

$$G_{disl} = \frac{1-\nu}{2\mu}\left(K_{II}^{disl}\right)^2 = \gamma_{us} \tag{17}$$

With the exception of the nonlinear behavior along the slip plane, the material in this simple case is taken as an isotropic, linear elastic solid with shear modulus μ and Poisson's ratio ν. As discussed below, G_{disl} may be calculated for more realistic situations involving inclined slip planes and mixed mode loadings, and also for bimaterial crack tip fields and taking into account the anisotropic effects; however, the above result illustrates a feature that pervades these complicated cases: the energy release rate for dislocation nucleation scales with the recently identified solid state parameter γ_{us}.

Further complexities arise when we include in the model the effects of normal tractions and dilatant opening across the slip plane. This situation occurs if a mode I-type loading is added to the mode II situation just discussed, or in more realistic cases when the slip plane is inclined with respect to the crack plane. There are no reasons to assume that a given τ versus Δ_r curve retains its shape if tension is superposed; hence the effect of superposed tension on the "effective" γ_{us} must be investigated. Argon [19] and Cheung et al.[30] have already noted the importance of softening in shear due to large tensile stresses across a slip plane. The effect of tension normal to the slip plane was treated recently by Rice et al.[5,21,22] by assuming a tensile stress versus normal component of separation relation consistent with the well-known fit, with energy proportional to $-(L+\Delta_\theta)exp(-\Delta_\theta/L)$, to the universal bonding correlation of Ferrante, et. al. [31]. The parameter L is the characteristic length associated with the decohesion process (the

tensile stress reaches a maximum, at Δ_r=0, when Δ_θ=L). The effects of the tension/shear coupling are represented by the dilation parameter p defined by $p=\Delta_\theta^*/L$, where Δ_θ^* is the relative atomic displacement in the opening direction when the shear displacement reaches the unstable value $\Delta_r=b/2$. Embedded atom method fit to material properties have been employed to estimate L/b, q ($=\gamma_{us}/2\gamma_s$) and p[26,28].

ANALYSES OF THE EXPERIMENTAL RESULTS

The energy release rates for dislocation emission for opposite cracking directions in the specimens tested are calculated with the two models.

Dislocation Nucleation and Emission from the Crack Tip in Copper Bicrystals

The critical mode I G_{disl} for dislocation nucleation in Cu bicrystals as a function of the slip plane inclination angle θ is calculated with the Eqn's 15 and 16 of the R-t type model. In the calculations, the core cutoff is assumed to equal the Burgers vector, the ledge energy per unit area created by dislocation emission is taken to be one tenth of the surface free energy of Cu [2] and an isotropic elasticity is presumed.

For [110] symmetric tilt bicrystals, where the crack front lies along the tilt axis, the likely dislocations to be activated are the partial dislocations with $b=a\langle 112\rangle/6$ and ϕ=60° and then ϕ=0° or the perfect dislocation with ϕ=30°. As discussed in [2] the critical energy release rate for dislocation emission is determined by the minimum value of G_{disl} required to nucleate the partials with ϕ=60°. The results are shown in Fig.6. In the figure results from the P-N type model (which neglects tension-shear coupling and takes γ_{us} =0.22 J/m^2 for Cu) are also displayed, which predicts the same G_{disl} vs. θ relation.

The directionality observed in Σ9 [110]/(2$\bar{2}$1) copper bicrystals might be understood by comparing predictions for opposite cracking directions. For cracking in the [$\bar{1}$14] direction, the most likely dislocations to be activated are partials on the (1$\bar{1}\bar{1}$) slip plane with θ=54.7°, ϕ=60° and G_{disl}=3.8 J/m^2. If the crack growth direction is

reversed, in the $[1\bar{1}4]$ direction, the most active slip systems remain the same, but in this case, θ=125.3° and the predicted value of G_{disl} is 8.3 J/m^2, more than twice that of the $[\bar{1}14]$ direction. Dislocation emission is preferred in the $[\bar{1}14]$ direction.

Dislocation Nucleation and Emission from the Interfacial Crack Tip in Copper/Sapphire Bimaterials

For the Cu/sapphire bimaterials system under the pure bend conditions the atomic scale phase angle is -79° [3]. Assuming the sapphire is purely elastic and dislocations can only be activated in Cu, the critical energy release rate for dislocation emission from the $[110]_{Cu}$ crack-tip vs. θ is presented in Fig.7. Several observations follow:

i. As the same as in bicrystals, G_{disl} is a strong function of θ with a minimum, but due to the mostly mode II loading conditions for the bimaterials the minimum value occurs at a larger θ angle ($\theta_{min} \cong 130°$).

ii. The minimum value of G_{disl} for the bimaterials is much lower than that for bicrystals, indicating a toughening effect of the interfacial crack by a rigid solid.

iii. The active slip systems have changed from the $(1\bar{1}1)$ slip plane with b=a[211]/6 or a$[\bar{1}21]$/6 and ϕ=60° to the $(\bar{1}\bar{1}1)$ slip plane with b=a[121]/6 or a$[\bar{2}11]$/6 and ϕ=60°. In this case the θ angle is 125.3° for cracking in the $[1\bar{1}4]$ direction and 164.2° for cracking in the $[\bar{1}14]$ direction, respectively. In contrast with bicrystals, G_{disl} for cracking in the $[1\bar{1}4]$ direction is two times lower than that for cracking in the $[\bar{1}14]$ direction and this may partially explain the directional dependence observed in the Cu/sapphire system.

The difference between G_{disl} in two opposite directions predicted by the R-T type model is not significant numerically, however. A check from the P-N type calculations is needed. Results based on those in [22] for a simplified set of slip plane constitutive relations for copper are now summarized. For the partials with ϕ=60° G_{disl}=1.08 J/m^2 when cracking in the $[1\bar{1}4]_{Cu}$ direction and G_{disl}=2.91 J/m^2 when cracking in the $[\bar{1}14]_{Cu}$ direction (here, effects of tension-shear coupling are not included.) There is a difference of more than a factor of two in G_{disl} for crack growth in the opposing directions as shown in Fig.7; hence, it is concluded that dislocation nucleation is preferred in the $[1\bar{1}4]_{Cu}$ direction, and blunting should be favored in this growth direction.

The tension-shear coupling reduces the energy release rate for dislocation nucleation as shown in Fig.8, where the applied energy release rate G/γ_{us} is plotted as a function of the atomic shear displacement δ_r^{tip}/b for the ϕ=0° partials for the two angles of interest. Here $\delta_r \equiv u_r^{(+)} - u_r^{(-)}$ denotes the displacement discontinuity on a mathematical cut coincident with the slip plane. The critical value for dislocation nucleation occurs at the maximum in the G/γ_{us}~δ_r^{tip}/b curve. For cracking in the $[1\bar{1}\bar{4}]_{Cu}$ direction, *i.e.*, θ=125.3°, unstable nucleation of the partial dislocation occurs at G/γ_{us}=1.839 for p=0 and G/γ_{us}= 1.715 for p=0.1. When cracking in the $[\bar{1}14]_{Cu}$ direction, *i.e.*, θ=164.2°, instability occurs at G/γ_{us}=12.55 for p=0 and G/γ_{us}=11.69 for p=0.1.

The switch of the active slip systems or the reverse of the cracking directionality in the Cu/sapphire specimens is attributable entirely to the phase angle effect. Here, the atomic scale phase angle ψ' is -79° against 0° for mode I loading in a symmetric tilt bicrystal. The phase angle effect is shown in Fig.9, which gives G_{disl} vs. ψ' for the various slip plane inclination angles. The solid lines correspond to angles associated with the $[\bar{1}14]_{Cu}$ direction, and the dashed lines correspond to angles associated with the $[1\bar{1}\bar{4}]_{Cu}$ direction. Comparison of the curves at ψ'=0 and ψ'=-79° shows that the favored direction for dislocation emission reverses when the phase angle is altered.

It is not surprising that the specimens with the $(001)_{Cu}$/sapphire interface did not show directional dependence, since configurations of slip systems at the crack-tips in opposite directions are symmetric.

Dislocation Nucleation and Emission from the Crack-Tip in Iron Bicrystals

For [100] symmetric tilt Fe bicrystals the likely dislocations to be activated from the crack-tip lying along [100] might be those with b=a<111>/2 and ϕ=35.26° on {110} planes. The critical mode I G_{disl} vs. θ curve predicted by the R-T type model is presented in Fig.10. Here, the core cutoff r_o=2/3 b, the ledge energy γ_{ledge}=.4γ_s[2] and an isotropic elasticity is presumed. Results from the P-N type model, where γ_{us}≅0.55 J/m^2 for Fe is assumed, are also shown in the figure. The trends predicted by both models are the same, though the P-N type model

predicts a lower value for dislocation emission.

For the Σ5[100]/(021) bicrystals with the macroscopic crack front lying along [100], the coplanar slip systems are $(011)[1\bar{1}1]$, $(011)[11\bar{1}]$, $(01\bar{1})[111]$ and $(01\bar{1})[\bar{1}\bar{1}\bar{1}]$ When the crack propagates in the negative direction, $[01\bar{2}]$, the active slip plane would be $(01\bar{1})$ with θ=71.57° and G_{disl}=6.3 J/m^2, as predicted by the model. In the positive direction, $[0\bar{1}2]$, the active slip plane (if it could ever be activated) would still be $(01\bar{1})$, but in this case θ=108.43° and G_{disl}=9.6 J/m^2, about twice that in the $[01\bar{2}]$ direction. In contrast to the experimental observations, the model predicts that dislocations are easier to emit from the crack-tip when cracking in the $[01\bar{2}]$ direction than that in the opposite direction, and slip traces or PSB's corresponding to the $(01\bar{1})$ slip planes could be observed for both cracking directions.

The puzzle of dislocations being more active at the crack-tip in the positive direction might be resolvable if we contemplate the microscopic direction of the crack propagation and the elastic incompatibility accompanied with it.

Microscopically, the crack front, as observed in our tests, was $[\bar{4}12]$ (Fig.4a) or $[4\bar{1}2]$ (Fig.5a) and the cracking direction was $[\bar{5}12]$ or $[5\bar{1}2]$ for the positive direction. Correspondingly, the coplanar slip systems were $(12\bar{1})[\bar{1}\bar{1}\bar{1}]$ or $(1\bar{2}1)[111]$, and the angle between the Burger's vector and the normal to the crack front is ϕ=22.21°, as if we have had a $[\bar{4}12]$ or $[4\bar{1}2]$ tilt bicrystal. Assuming isotropic elasticity and a zero atomic scale phase angle, the G_{disl} vs. θ relation for the $[\bar{4}12]$ tilt bicrystals is plotted in Fig.10 as a dashed curve. Compared with the solid curve, it shows that dislocations are more active in {112} type slip systems than in {110} type slip systems. This may partially explain the microscopic deviation of the cracking direction observed in the specimens. It cannot, however, explain why dislocations are easier to emit in the positive direction. In this case, when the $(12\bar{1})[\bar{1}\bar{1}\bar{1}]$ or $(1\bar{2}1)[111]$ slip system is activated, θ=123.21° and G_{disl}=13.2 J/m^2 for the positive direction, but θ=56.79° and G_{disl}=6.0 J/m^2 for the negative direction. Dislocations are predicted to nucleate easier in the negative direction than that in the positive direction, still in contradiction to the experimental results.

The directional dependence observed in the Σ5(100/[021] Fe bicrystals might be understandable if one recalls the effect of the atomic-scale phase angle and the fact that the directionality in Cu/sapphire bimaterials is reversed with respect to that in Cu bicrystals. Differing from [100] symmetric tilt bicrystals, the elastic incompatibility between the adjoining crystals in the imaginary $[4\bar{1}2]$ tilt bicrystals will inevitably produce a mode II component, and this mixed mode loading condition will shift the G_{disl} vs. θ relation. A similar reverse, as observed in Cu/sapphire bimaterials, may thus occur in the Σ5[100]/(021) bicrystals, when the crack propagates in the <512> direction microscopically. A detailed analysis will appear in work in progress [121].

CONCLUSION

1. A directional dependence of crack growth in bicrystals of fcc and bcc metals, and in bimaterials, as well as effects of the atomic scale phase angle were experimentally observed.

2. The cracking directionality and phase angle effects may be understood in terms of the competition between cleavage decohesion of the interface and dislocation emission from the crack tip.

3. The experimental observations are significant both theoretically in verifying the idea that the competition processes aforementioned may control the ductile versus brittle transition in solids and interfaces, and practically in understanding interfacial failure in complex solid systems.

ACKNOWLEDGEMENT

Supported by DARPA through the University Research Initiative Program, coordinated by University of California at Santa Barbara and NSF through the MRL at Harvard. JSW is grateful to B. Schaff with Max-Planck Institut für Eisenforschung GmbH for providing him with Fe-2.7%Si bicrystals.

REFERENCES

[1] Anderson, P.M. and Rice, J.R., Scripta metallurgica Vol. 20, 1986, pp 1467-1472, and Anderson, P.M., "Ductile and Brittle Crack Tip Response", Ph.D. thesis, Harvard University, Cambridge, Mass.,1986.

[2] Wang, J.-S. and Anderson, P.M., Acta metallurgica et materialia Vol. 39, 1991, pp 779-792.

[3] Rice, J.R., Suo, Z. and Wang, J.-S., Metal-Ceramic Interfaces, Acta Scripta Metallurgica Proceedings Series, Vol. 4, edited by M. Rühle, A.G. Evans, M. F. Ashby, and J.P. Hirth, Pergamon Press, Oxford, 1990, pp 269-294.

[4] Wang, J.-S. and Beltz, G E., Structure and Properties of Interfaces and Materials, edited by W. A. T. Clark, U. Dahmen and C. L. Briant, Proceeding of Materials Research Society, Vol. 238, Materials Research Society, Pittsburgh, 1992, pp 405-410, Beltz, G E. and Wang, J.-S., Acta metallurgica et materialia, Vol. 40, 1992, pp 1675-1683 and Wang, J.-S., unpublished work.

[5] Rice, J.R., Journal of the Mechanics and Physics of Solids, Vol. 40, 1992, pp 239-271.

[6] Rice, J.R., Beltz, G E. and Sun, Y., Topics in Fracture and Fatigue, edited by A.S. Argon, Springer-Verlag, 1992, pp 1-58.

[7] Wang, J.-S., Journal of Materials Research, Vol. 3, 1988, pp 16-28.

[8] Yan, B. and Laird, C., Materials Science and Engineering, Vol. 76, 1986, pp 71-76.

[9] Kim, M. J., private communication.

[10] Waltersdorf, J., and Vehoff, H., Scripta metallurgica, Vol. 23, 1989, pp 513-518.

[11] Vehoff, H., Stenzel, H. and Neumann, P., Zeitschrift für Metallkunde, Vol. 78, 1987, pp 550-558.

[12] Wang, J.-S., unpublished work.

[13] Armstrong, R.W., Materials Science and Engineering, Vol. 1, 1966, pp 251-256.

[14] Kelly, A., Tyson, W. and Cottrell, A., Philosophical Magazine, Vol. 15, 1967, pp 567-586.

[15] Rice, J.R. and Thomson, R., Philosophical Magazine, Vol. 29, 1974, pp 73-97.

[16] Rice, J.R., Fundamentals of Deformation and Fracture (Eshelby Memorial Symposium), edited by Bilby, B.A. Miller, K.J. and Willis, J.R., Cambridge University Press, 1985, pp 33-56.

[17] D. J. Bacon, D. M. Barnett and R. O. Scattergood, Progress in Materials Science, Vol. 23, 1979, pp 51-265.

[18] Cao, H. and Rice, J.R., Journal of the Mechanics and Physics of Solids, Vol. 37, 1989, pp 155-174.

[19] Argon, A. S., Acta metallurgica. Vol. 35, 1987, pp 185-196.

[20] Schoeck, G., Philosophical Magazine, Vol. A 63, 1991, pp 111-120.

[21] Beltz, G. E. and Rice, J.R., Modeling the Deformation of Crystalline Solids: Physical Theory, Application, and Experimental Comparisons edited by Lowe, T. C. and Rollett, A.D., Follansbee, P.S. and Daehn, G.S.,TMS, 1991, pp 457-480.

[22] Beltz, G. E. and Rice, J.R., Acta metallurgica et materialia, Vol. 40, 1992, pp S321-S331.

[23] Peierls, R. E., The Proceedings of the Physical Society, Vol. 52, 1940, pp 34-37.

[24] Nabarro, F. R. N., The Proceedings of the Physical Society, Vol. 59, 1947, pp 256-272.

[25] Cheung, K., "Atomistic Study of Dislocation Nucleation at a Crack Tip," Ph.D. Thesis, Massachusetts Institute of Technology, Cambridge, Massachusetts, 1990.

[26] Sun, Y., Rice, J.R., and Truskinovsky, L., High-Temperature Ordered Intermetallic Alloys, edited by Johnson, L. A., Pope, D. T. and Stiegler, J. O., Proceeding of Materials Research Society, Vol. 213, Materials Research Society, Pittsburgh, 1991, pp 243-248.

[27] Kaxiras, E., and Duesbery, M.S., "Free Energies of Generalized Stacking Faults and Implications for the Ductile-Brittle Transition", Submitted, 1993.

[28] Sun, Y., Beltz, G. E. and Rice, J.R., Materials Science and Engineering, A, in press 1993.

[29] Rice, J.R., Journal of Applied Mechanics, Vol. 35, 1968, pp 379-386.

[30] Cheung, K., Yip, S., and Argon, A. S., Journal of Applied Physics, Vol. 69, 1991, pp 2088-2096.

[31] Ferrante, J. and Smith, J.R., Physical Review, Vol. B 31, 1985, pp 3427-3434.

Figure Captions

Fig.1 The fracture surfaces of the Σ9 [110]/(2$\bar{2}$1) Cu bicrystals. a), Cracking in the [1$\bar{1}$4] direction and b), cracking in the [$\bar{1}$14] direction. The arrow indicates the cracking direction.

Fig.2. Side view of a Cu/sapphire specimen after 4-point bending test showing decohesion in the $[\bar{1}14]_{Cu}$ direction and blunting in the $[1\bar{1}4]_{Cu}$ direction. The attached photo shows slip traces in Cu near the crack-tip region of the $[1\bar{1}4]_{Cu}$ direction.

Fig.3. The IGSCC propensity vs. the tilt angle for symmetrical [010]-tilt bicrystals for cracking in the opposite directions. (by courtesy of Vehoff et.*al.* [11].)

Fig.4. The fracture surfaces of the Σ5[100]/(021) bicrystals after corrosion fatigue. a), Cracking in the positive direction, fatigue striations are shown, and b), in the negative direction, cleavage.

Fig.5. The fracture surfaces of the Σ5[100]/(021) bicrystals after SCC plus corrosion fatigue. Cracking in the positive, a), and negative, b), directions.

Fig.6. The critical mode I G_{disl} vs.θ in Cu bicrystals. The opposite directions in the Σ9 [110]/(2$\bar{2}$1) bicrystals tested are indicated.

Fig.7. The critical G_{disl} vs. θ for Cu/sapphire interfaces loaded in pure bend. The opposite directions tested are indicated.

Fig.8. The applied energy release rate vs. the amount of slip at the crack tip for the two angles of interest. Effects of tension-shear coupling are shown.

Fig.9. G_{disl} vs. ψ' for Cu/sapphire bimaterials. The numbers attached are the inclination angles θ of the potentially active slip planes.

Fig.10. The mode I G_{disl} vs. θ in Fe bicrystals. G_{disl} for the Σ5[100]/(021) bicrystals cracking in the opposite directions are marked.

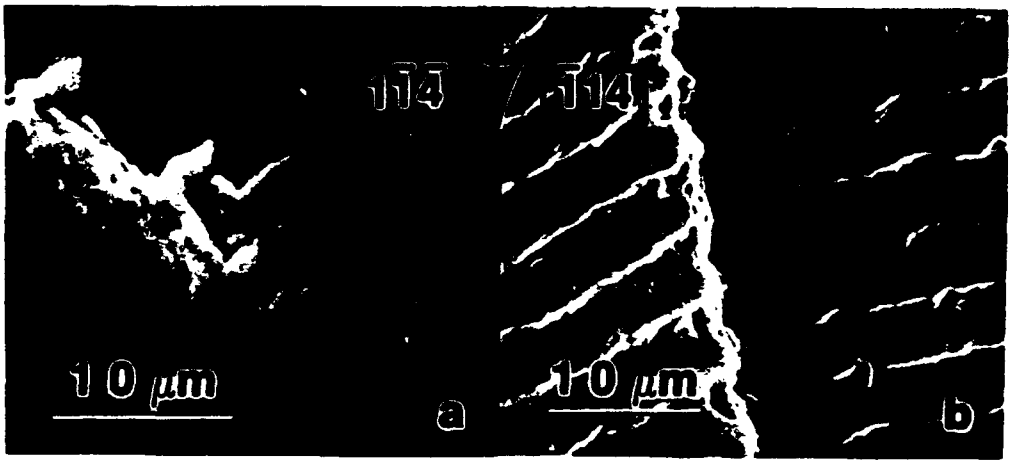

Fig.1 The fracture surfaces of the Σ9 [110]/($2\bar{2}\bar{1}$) Cu bicrystals. a), Cracking in the [$\bar{1}\bar{1}4$] direction and b), cracking in the [$\bar{1}14$] direction. The arrow indicates the cracking direction.

Fig.2. Side view of a Cu/sapphire specimen after 4-point bending test showing decohesion in the $[\bar{1}14]_{Cu}$ direction and blunting in the $[1\bar{1}4]_{Cu}$ direction. The attached photo shows slip traces in Cu near the crack-tip region of the $[1\bar{1}4]_{Cu}$ direction.

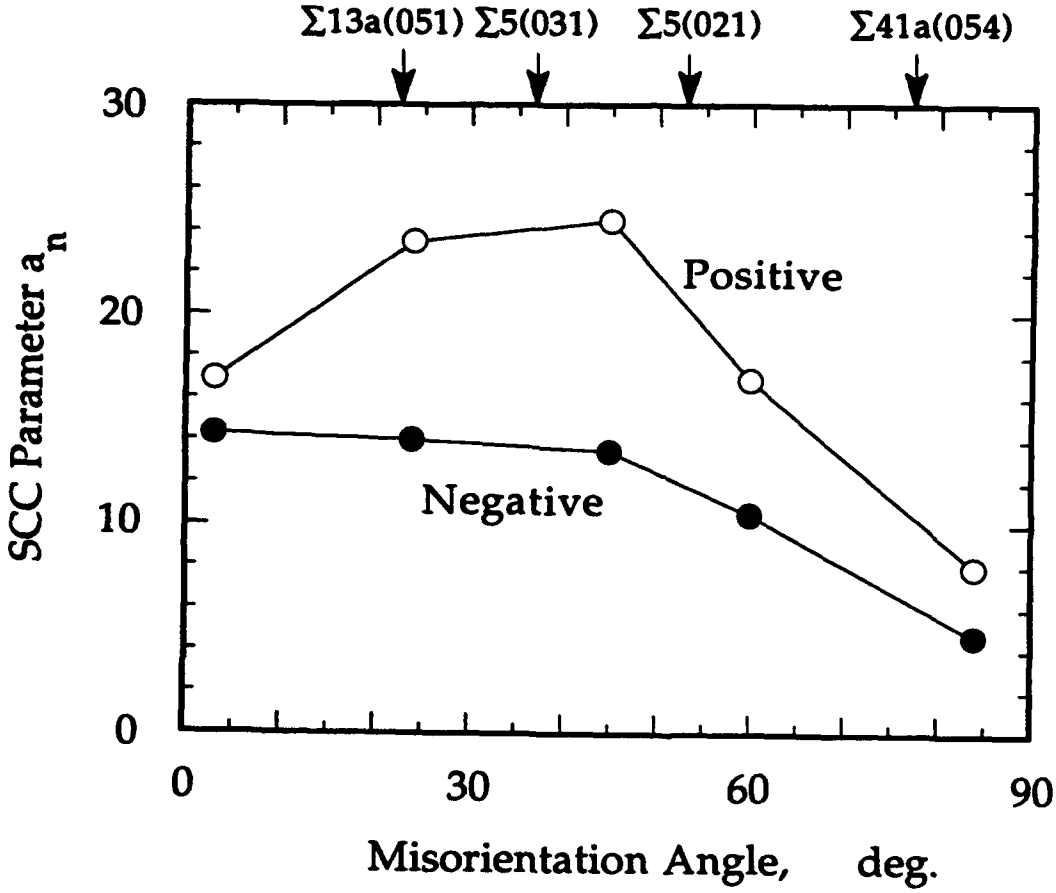

Fig.3. The IGSCC propensity vs. the tilt angle for symmetrical [010]-tilt bicrystals for cracking in the opposite directions. (by courtesy of Vehoff *et.al.* [11].)

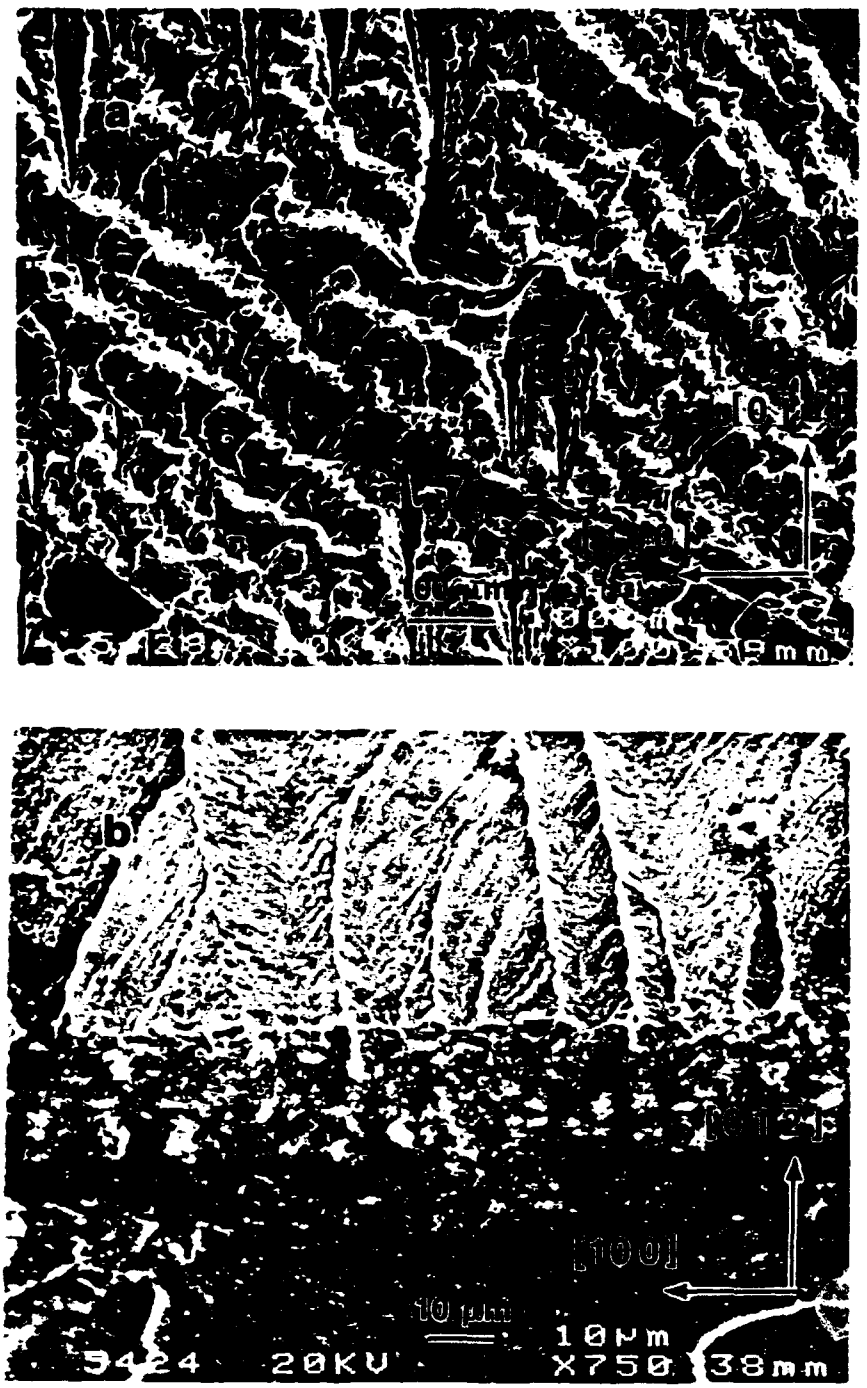

Fig.4. The fracture surfaces of the Σ5[100]/(021) bicrystals after corrosion fatigue. a), Cracking in the positive direction, fatigue striations are shown, and b), in the negative direction, cleavage.

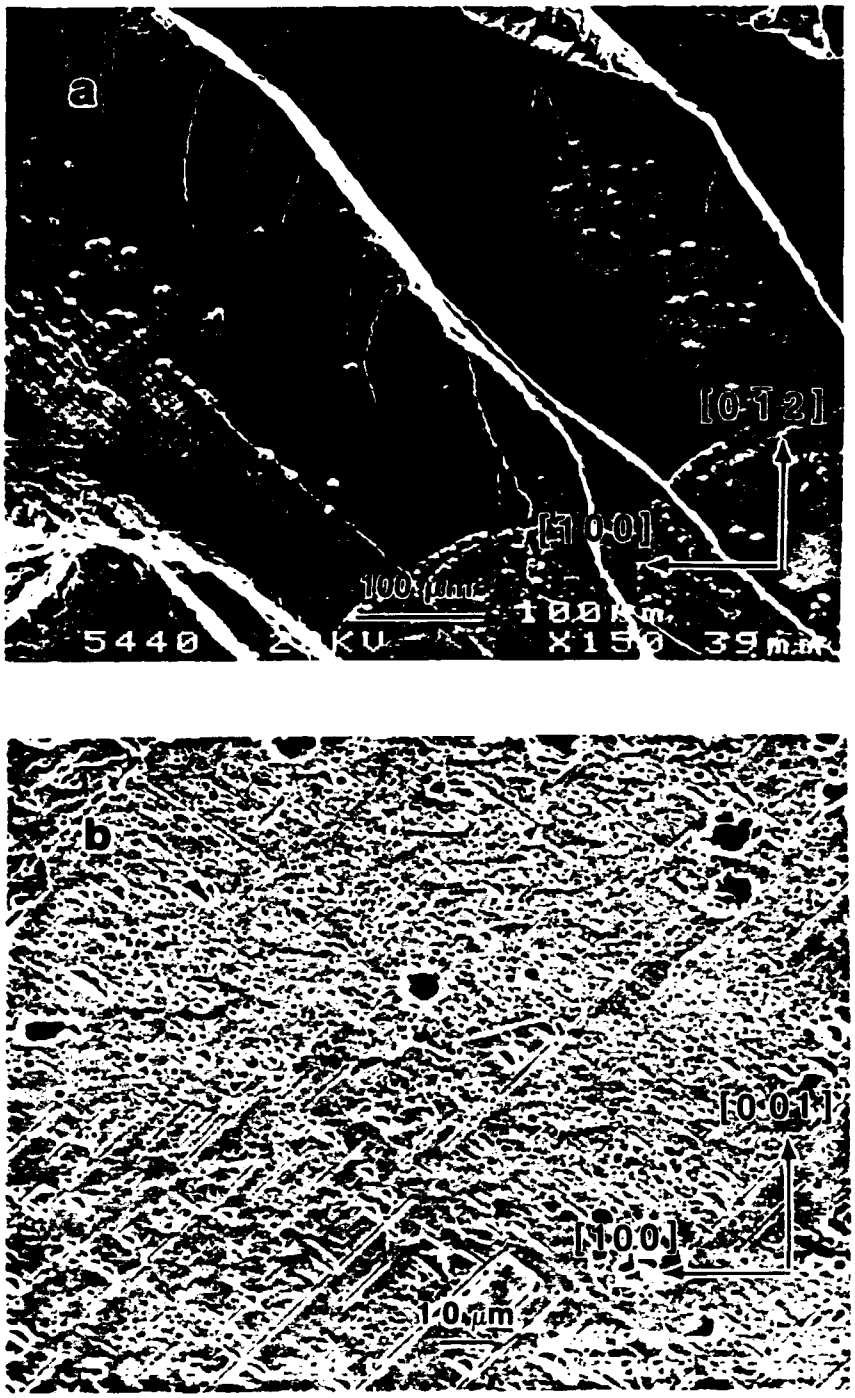

Fig.5. The fracture surfaces of the Σ5[100]/(021) bicrystals after SCC plus corrosion fatigue. Cracking in the positive, a), and negative, b), directions.

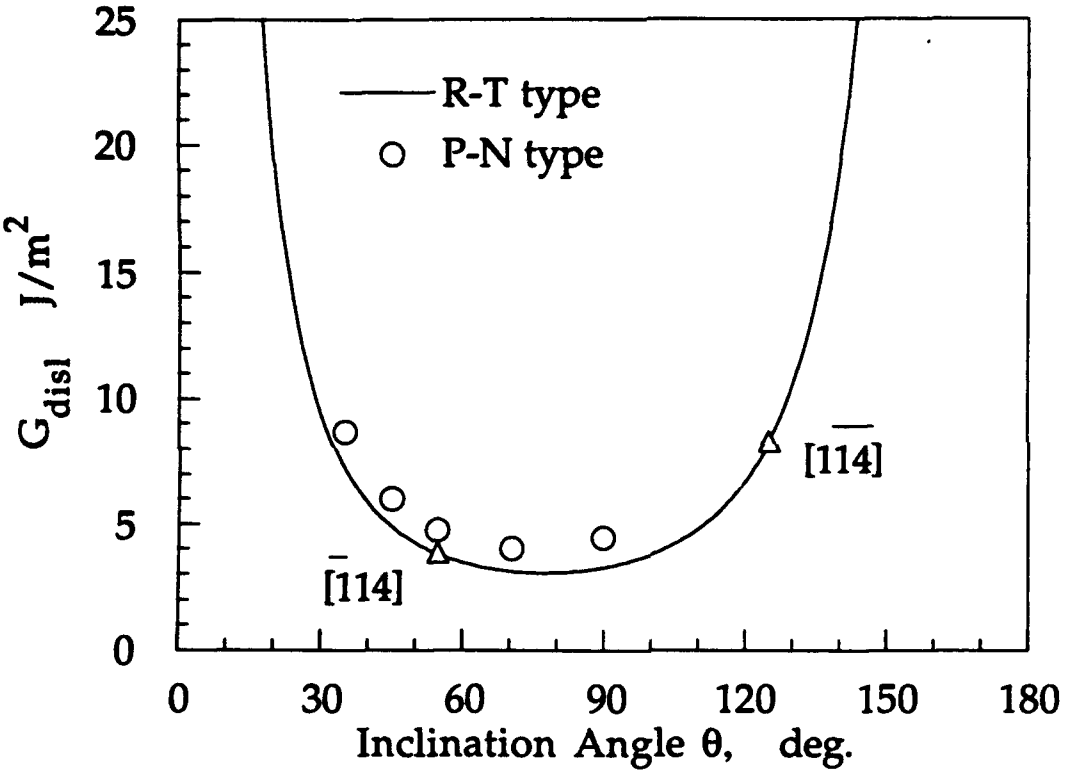

Fig.6. The critical mode I G_{disl} vs.θ in Cu bicrystals. The opposite directions in the Σ9 [110]/(2$\bar{2}$1) bicrystals tested are indicated.

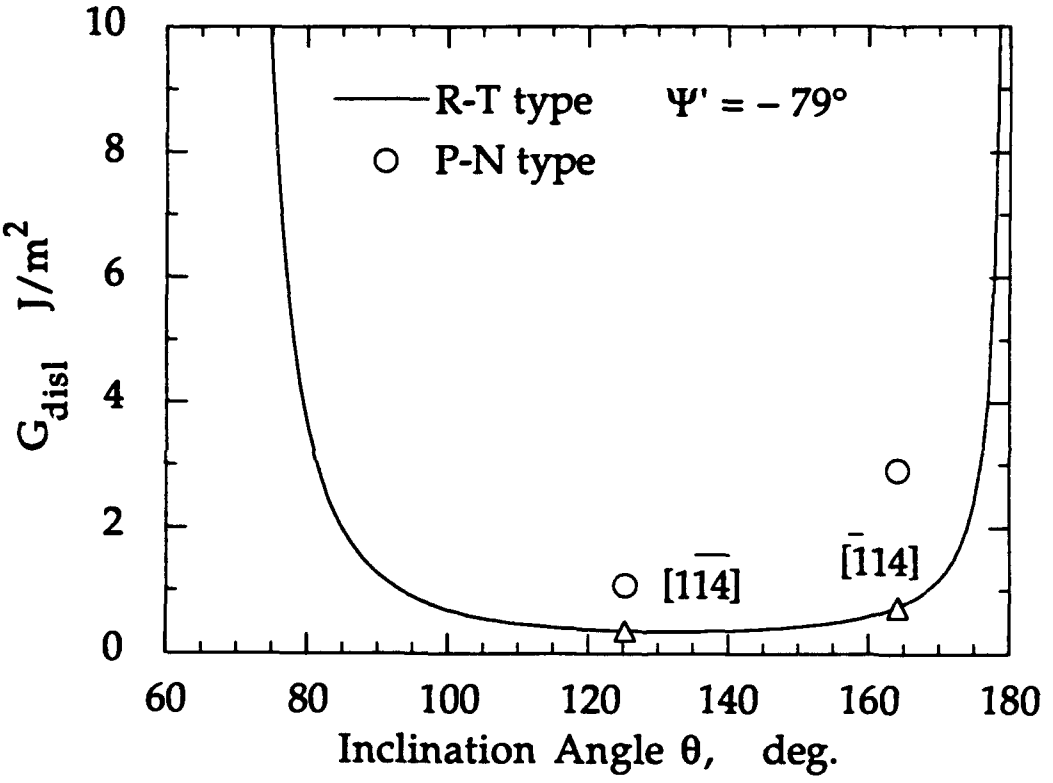

Fig.7. The critical G_{disl} vs. θ for Cu/sapphire interfaces loaded in pure bend. The opposite directions tested are indicated.

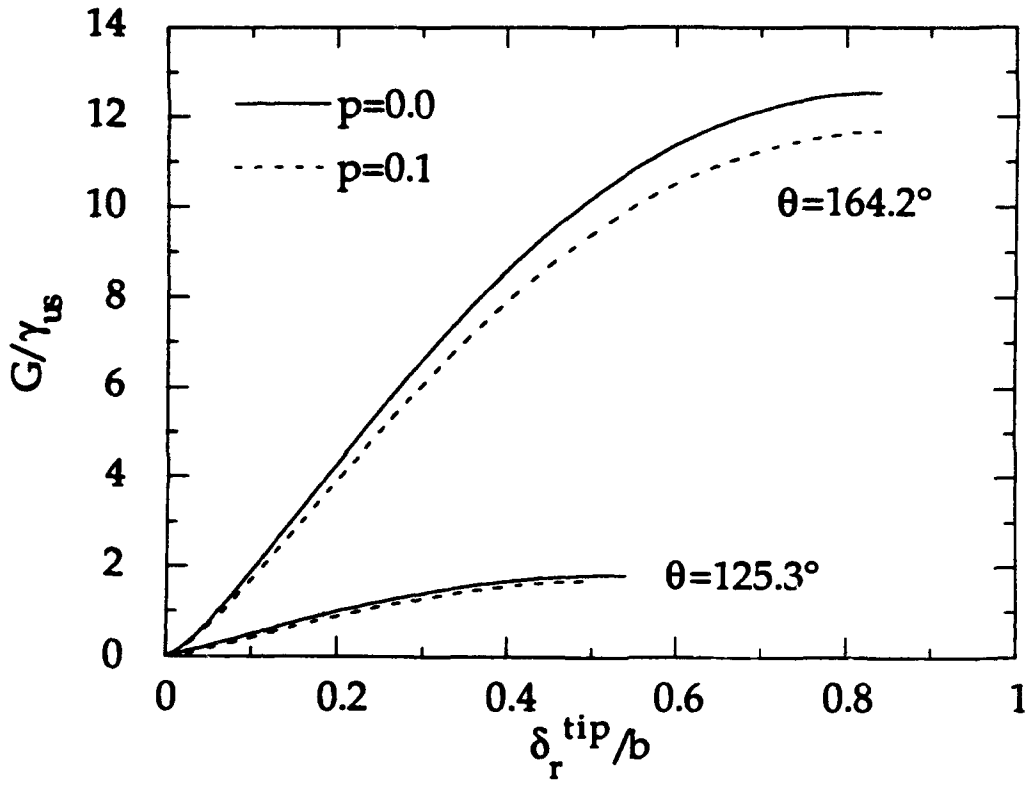

Fig.8. The applied energy release rate vs. the amount of slip at the crack tip for the two angles of interest. Effects of tension-shear coupling are shown.

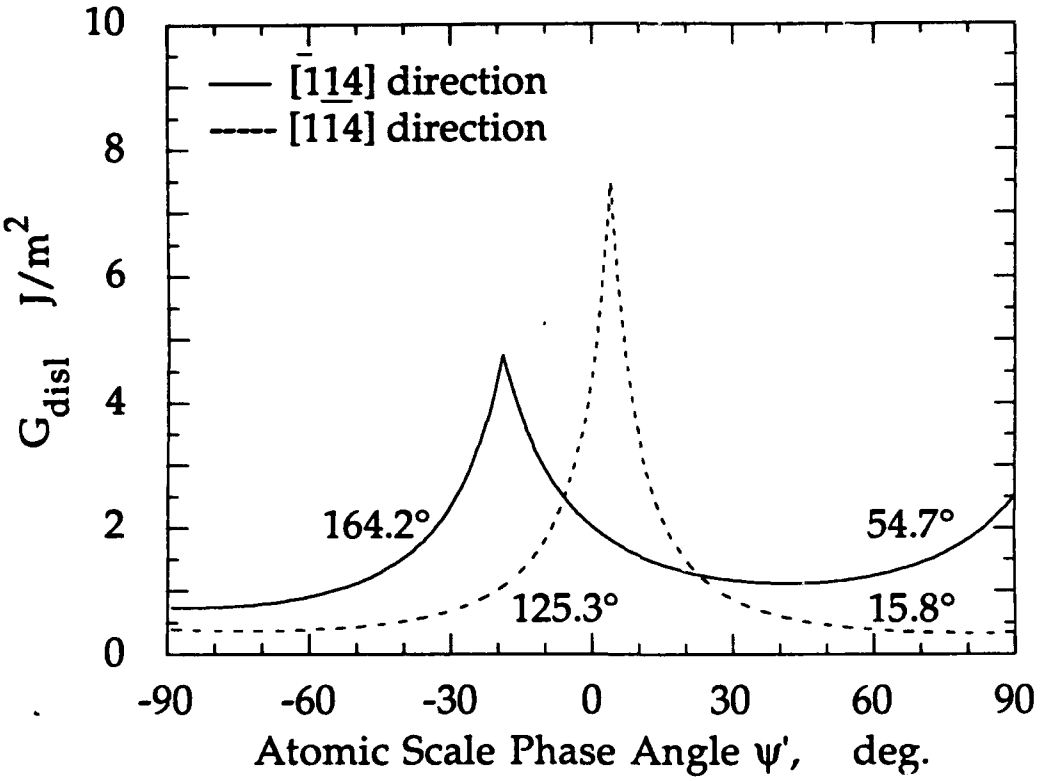

Fig.9. G_{disl} vs. ψ' for Cu/sapphire bimaterials. The numbers attached are the inclination angles θ of the potentially active slip planes.

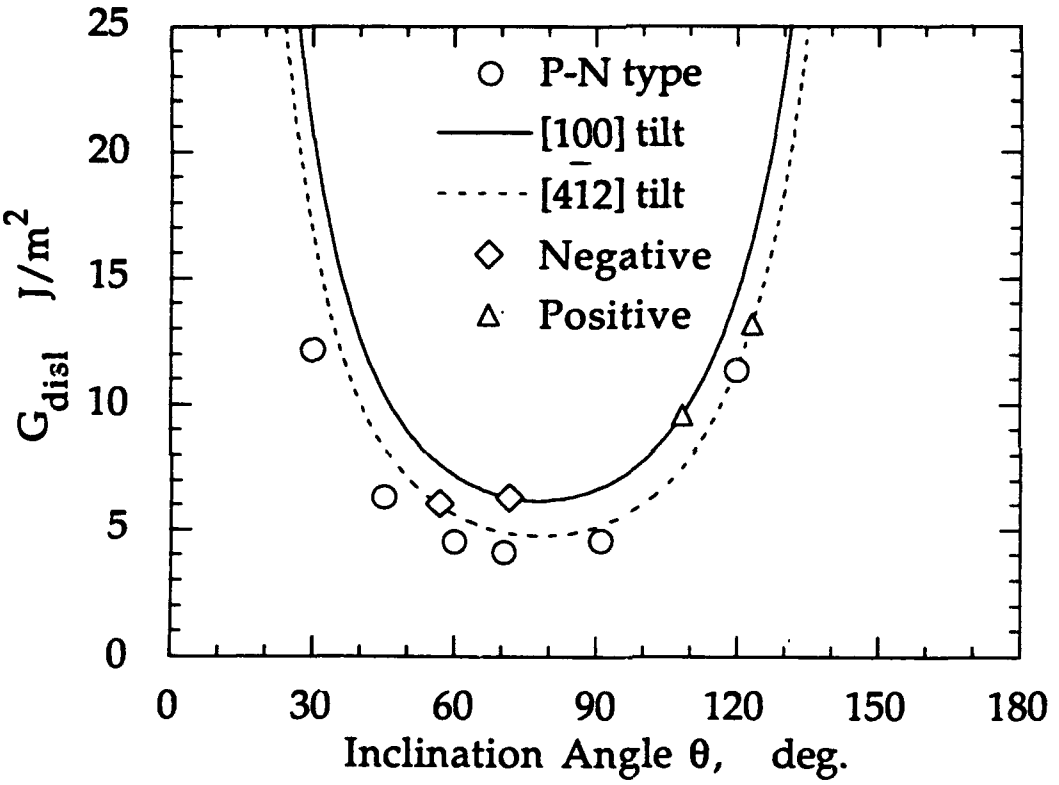

Fig.10. The mode I G_{disl} vs. θ in Fe bicrystals. G_{disl} for the Σ5[100]/(021) bicrystals cracking in the opposite directions are marked.

Fundamentals of Metal-Matrix Composites, eds. S. Suresh, A. Mortensen and A. Needleman, Butterworth-Heinemann (1993)

Chapter 12

Models for Metal/Ceramic Interface Fracture

ZHIGANG SUO
C. FONG SHIH

Metal-matrix composites are excellent candidate materials for advanced engineering systems. However, they have one major shortcoming that has limited their widespread use—their tendency to fracture easily. In many systems, the low ductility or brittleness of these composites is caused by microfailure processes that invariably begin at the interfaces. Thus, the mechanical behavior and the overall performance of metal-matrix composites are not limited by bulk properties or bulk phases, but by interface properties and toughness. Theories on interface fracture are reviewed in this chapter. With few exceptions, attention is limited to continuum mechanics considerations. Readers are referred to Rice et al. (1989, 1990, 1992) and references therein for atomistic and thermodynamic aspects of this subject. This article is concerned with recent advances within the confines of small-scale inelasticity and loading conditions, such that a major portion of the crack faces remain open. We review works regarding relatively brittle interfaces where the inelastic zone is small compared to the overall component. Large-scale bridging is reviewed by Bao and Suo (1992). Large scale contact has been treated by Hutchinson and Jensen (1990) within the context of fiber pullout against frictional sliding. The focus of this article is on theories. For a broader coverage of topics, the reader is referred to published proceedings of symposia on interfacial fracture. These include those edited by Suresh and Needleman (1989), Rühle et al. (1990), and Ashby et al. (1992). Experimental aspects of interface fracture and fatigue are reviewed by Evans et al. (1990), Kim (1991), and Cannon et al. (1992). Several aspects of fatigue are also discussed in a recent article (Woeltjen et al. 1992).

The mechanics of interface fracture has its root in the earlier works of Griffith (1921) and Irwin (1960) on the general theory of fracture, of Williams (1959) on the elastic stress distribution around an interface crack, of England (1965), Erdogan (1965), and Rice and Sih (1965) on explicit solutions for interface cracks, and of many practicing engineers on ingenious methods to measure adhesive strength of bonds. However, the subject did not take off until the 1980s. Advanced composites for high temperature engines, and layered materials for microelectronic and optical devices, have been the main technical driving force for new theoretic developments. Rapid advancement in high-resolution microscopes, high-speed computers, and the general theory of fracture have all provided tools for solving these challenging technical problems.

The classical fracture mechanics, as advanced by Irwin (1960), Rice (1968), and Hutchinson (1979), and as summarized in the textbook by Kanninen and Popelar (1985), is largely phenomenological. It enables us to predict, without a detailed description of the crack tip processes, crack growth in a structure by utilizing the observed crack growth behavior in a fracture specimen. This approach relies on the existence of stress intensity factor and on fracture resistance measured by mechanical testing. The advantage and the deficiency of this black-box approach both originate from the same fact: this approach requires little, nor does it generate much, knowledge of the physical process of fracture.

Mechanism-based fracture mechanics attempts to link the fracture resistance to the microstructural variables, providing guidelines for processing better and newer materials. This approach is as old, if not as fully developed, as the phenomenological approach. Indeed, in his original paper, Griffith prescribed a phenomenological fracture criterion as well as a physical mechanism of fracture resistance: rearranging atoms in a bulk into surfaces requires energy. It was eminently clear to Irwin that any form of heat dissipation that accompanies fracture, such as plastic flow in metals, contributes to fracture resistance. But just how atomic separation and irreversible atomic movements are interconnected remains an open question even today. Partial theories, each valid for a particular mechanism at a particular length scale, have been devised, largely in the earlier works by Cottrell (1963) and Rice and Johnson (1970) on hole growth, by Ritchie et al. (1973) on cleavage of alloys, and by Aveston et al. (1971) on fiber reinforced components. An example of the success of the mechanism-based approach is the thorough understanding of advanced ceramics toughened by ductile particles, or transforming particles, or strong fibers that has been achieved (Evans 1990). As a by-product of the mechanism-based approach, short cracks, small components, and nagging questions in the framework of classical fracture mechanics can be addressed with a unified, conceptually simple viewpoint (Stump and Budiansky 1989; Bao and Suo 1992). The dual approach, phenomenological and mechanism-based, is kept in mind throughout this review article.

The chapter is organized as follows. Section 12.1 reviews the energy consideration for a traction-free interface crack under small-scale inelasticity conditions, leading to the concepts of debond driving force, $\mathcal{G}$, and debond resistance, Γ. Supplemented by elasticity solutions of $\mathcal{G}$ for given components and loading conditions and experimentally measured Γ for given materials, this energy consideration is sufficient for most engineering applications. Section 12.2 reviews Williams' solution for an interface crack between two elastic half spaces. The near-tip stress field lends itself to a precise definition of mode mixity; the near-tip opening sets the condition for small-scale contact. Calibration of fracture specimen is also discussed. Crack-tip plasticity is reviewed in Section 12.3. The relevant mode mixity is the ratio of shear over tension on the interface immediately outside of the plastic zone. The plastic zone size is shown to depend on the mode mixity, as is the opening of the blunted crack tip. An analysis of a metal foil sandwiched between two ceramic plates is included, demonstrating the effect of constrained plastic flow on the fracture resistance. Section 12.4 reviews results on growing cracks and the concepts leading to a fundamental understanding of fracture resistance. Included are crack growth in elastic-plastic materials, crack bridging with or without background plasticity, and cleavage in the presence of plastic flow.

12.1 Energy Balance

The following energy arguments are essentially the same as those of Griffith (1921) and Irwin (1960). Cracks often run when a test-piece is still predominantly elastic, inelastic deformation being localized in thin layers beneath the crack surfaces. Taking advantage of this fact, one can partition the total energy supplied by the applied work into (1) elastic energy stored in the test-piece and (2) the heat dissipated by plastic flow and residual energy stored in the thin layers. From (1) comes a definition of debond driving force, $\mathcal{G}$, and from (2) comes debond resistance, Γ. Obviously, this partition becomes meaningless when the inelastic deformation spreads over a large part of the test-piece, either because the test-piece is small, or because the material is very ductile. These have been reviewed elsewhere (Stump and Budiansky 1989; Bao and Suo 1992).

12.1.1 Debond Driving Force

Consider an interface crack extending over an area A (Figure 12.1). Material near the crack front undergoes inelastic deformation; the interface is usually ill defined, containing misfit dislocations, an interdiffusion zone, or reaction compounds. However, these zones are typically small compared to the overall dimension of the test-piece, so that the crack front can be treated as a mathematical line, and the interface a mathematical plane. In computing the elastic energy stored in the test-piece, the two solids are taken to be (possibly nonlinearly) elastic. That is, each solid can be described by a strain energy density function $w(\epsilon_{11}, \epsilon_{12}, ...)$, such that stresses σ_{ij} are derived from

$$dw = \sigma_{ij} d\epsilon_{ij} \tag{12.1}$$

Coupled with equilibrium and compatibility equations, these considerations define an elasticity problem. In particular, stress and strain are computed everywhere in the test-piece, down to the crack front and the interface; likewise the energy density w is computed everywhere. The elastic energy stored in the test-piece is an integral extended over the entire test-piece, such that

$$U = \int_V w dV \tag{12.2}$$

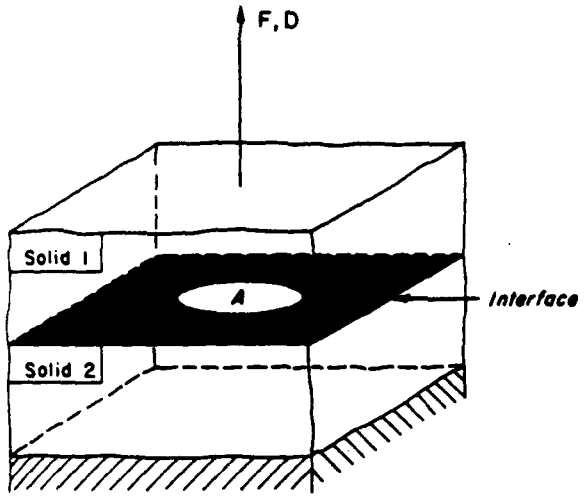

Figure 12.1. A partially debonded interface is subjected to applied load.

The test-piece in Figure 12.1 is loaded by displacement D, with work-conjugating force F. The elastic energy U depends on applied displacement and the crack size, thus,

$$U = U(D,A) \tag{12.3}$$

Note that U also depends on the geometry of the test-piece and the elastic moduli, but they remain constant during testing.

Upon loading, U varies as

$$dU = FdD - \mathcal{G}dA \tag{12.4}$$

With crack size held fixed ($dA = 0$), the above equation simply states that the energy increment equals the work applied. Because all the other quantities are defined, Equation 12.4 defines the quantity $\mathcal{G}$ when $dA \neq 0$. Just as F is the driving force for D, $\mathcal{G}$ is the driving force for crack size A. Explicitly, $\mathcal{G}$ is the decrease of elastic energy associated with a unit increment of crack area:

$$\mathcal{G} = -\frac{\partial U(D,A)}{\partial A} \tag{12.5}$$

Note that $\mathcal{G}$ has dimension energy/area.

The above concepts can be explained graphically. Figure 12.2(a) shows a load-displacement curve of the test-piece measured with fixed crack size ($dA = 0$). The curve should be straight for linear elastic materials. From Equation 12.4, U is the area under the load-displacement curve. Figure 12.2(b) shows two such load-displacement curves, measured in two independent tests with slightly different crack sizes, A and $A + dA$. The test-piece with the larger crack is more compliant; the shaded area is the energy decrease, dU, associated with dA. In early days, this graphical interpretation was employed to experimentally determine $\mathcal{G}$ (Rivlin and Thomas 1953).

Standard thermodynamics manipulations apply to the present discussions. For load-controlled tests, for example, it is more convenient to work with the potential energy

$$\Pi = U - FD \tag{12.6}$$

which is indicated in Figure 12.2(a). The independent variables are now F and A. Upon loading, Equation 12.4 becomes

$$d\Pi = -DdF - \mathcal{G}dA \tag{12.7}$$

Therefore, an alternative definition of $\mathcal{G}$ is

$$\mathcal{G} = -\frac{\partial \Pi(F,A)}{\partial A} \tag{12.8}$$

The definitions (12.5) and (12.8) are of course equivalent.

For an interface along the x_1-axis, and with displacement and traction continuous across the interface, Rice's J-integral (1968)

$$J = \int (wn_1 - n_i\sigma_{ij}u_{j,1})\, ds \tag{12.9}$$

vanishes over contours not enclosing any singularity. For a traction-free crack on the interface, $\mathcal{G}$ equals the J-integral over any path that begins at a point on the

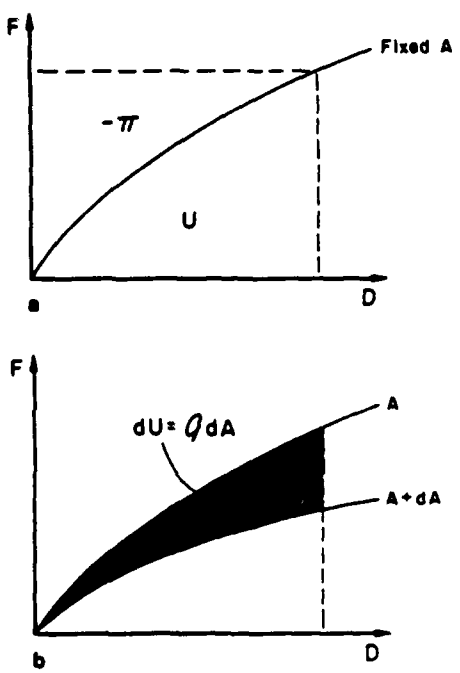

Figure 12.2. Graphic interpretation of (a) U and π and (b) $\mathcal{G}$.

lower crack face, and ends at another point on the upper crack face. This provides a tool for calculating $\mathcal{G}$ in finite element analysis (Moran and Shih 1987).

In general, $\mathcal{G}$ can be computed with an elasticity analysis of a given test-piece. Several illustrations requiring only elementary mechanics are given. Solutions to a wide range of geometries can be found in Hutchinson and Suo (1992) and the references therein.

Consider a fiber being pulled out of a matrix (Figure 12. 3). The energy stored in the fiber can be estimated by regarding the fiber as a tensile bar, clamped at the debond front. The pullout displacement is $D = L\sigma/E$, so that $U = (\sigma^2/2E)(\pi R^2 L)$. The potential energy is

$$\Pi(\sigma,L) = -\frac{\sigma^2}{2E}\pi R^2 L. \qquad (12.10)$$

Because the debond area is $A = 2\pi RL$, carrying out the differentiation in Equation 12.8 gives

$$\mathcal{G} = R\sigma^2/4E \qquad (12.11)$$

The estimate, which ignores the compliance of the fiber-matrix junction, is accurate when the debond length is large compared to the fiber diameter. Observe that $\mathcal{G}$ does not depend on the debond length L. Once debond starts, it will run to the other end of the fiber without any increase in load.

Thin-film cracking of many patterns has inspired a new problem area (Evans et al. 1988; Hutchinson and Suo 1992). Figure 12.4 illustrates a circular interface crack emanating from the edge of a hole in a thin film, driven by a residual tensile stress in the film. The stress in the debonded film is partially relieved, leading to a reduction in the elastic strain energy. The debonded film may be treated as a ring in plane stress, clamped at the debond front. The energy release rate is found to be

$$\mathcal{G} = \frac{2hE\epsilon_0^2}{1-\nu^2}\left[1 + \frac{1-\nu}{1+\nu}\left(\frac{a}{a_0}\right)^2\right]^{-2} \qquad (12.12)$$

where ϵ_0 is the mismatch strain between the film and the substrate caused by thermal or epitaxial mismatch,

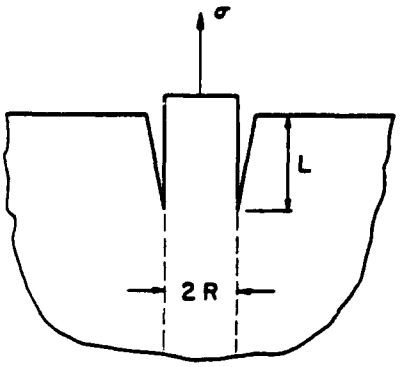

Figure 12.3. A fiber is being pulled out from a matrix.

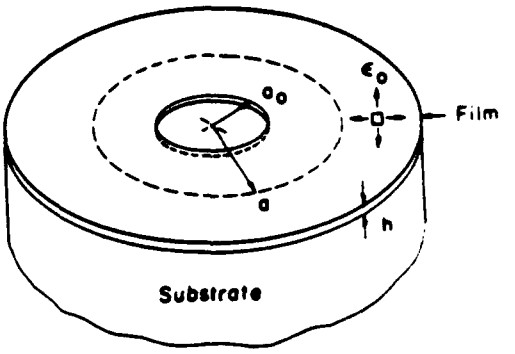

Figure 12.4. Thin-film decohesion emanating from a circular hole.

a_0 is the hole radius, a is the debond radius, and E and ν are the elastic constants of the film (Farris and Bauer 1988). Observe that $\mathcal{G}$ decreases rapidly as a increases, so that the debond is stable. Also note that $\mathcal{G}$ scales linearly with film thickness h: the thinner the film, the smaller the decohesion area. Debond can be practically suppressed if the film is sufficiently thin.

12.1.2 Debond Resistance

The essential idea of Griffith and Irwin is illustrated in Figure 12.5. Inelastic processes, such as atomic separation, twinning, phase transformation, and dislocation motion, require sufficiently high stress to activate, so they are confined to a region close to the crack tip where the stress is intensified. As the crack front extends, thin layers beneath the crack surface are left in the wake in which the atoms have undergone irreversible movements. The processes near the tip are complex and the quantification requires detailed knowledge of deformation mechanisms. Nonetheless, an effectively uniform deformation state along the x_1-axis is attained in the wake. Consider two cylinders of unit cross-sectional area normal to the interface, one far ahead of the crack front (A), and the other far behind (B). Let Γ be the energy spent to transform cylinder A to cylinder B. Obviously Γ depends on the deformation history that cylinder B underwent, including surface energy, heat dissipation, and elastic energy trapped in the wake.

The total energy variation, elastic as well as inelastic, is given by

$$F dD - \mathcal{G} dA + \Gamma dA \qquad (12.13)$$

When D is held fixed, no work is externally applied to the test-piece and the total energy remains unchanged, so that

$$\mathcal{G} = \Gamma \qquad (12.14)$$

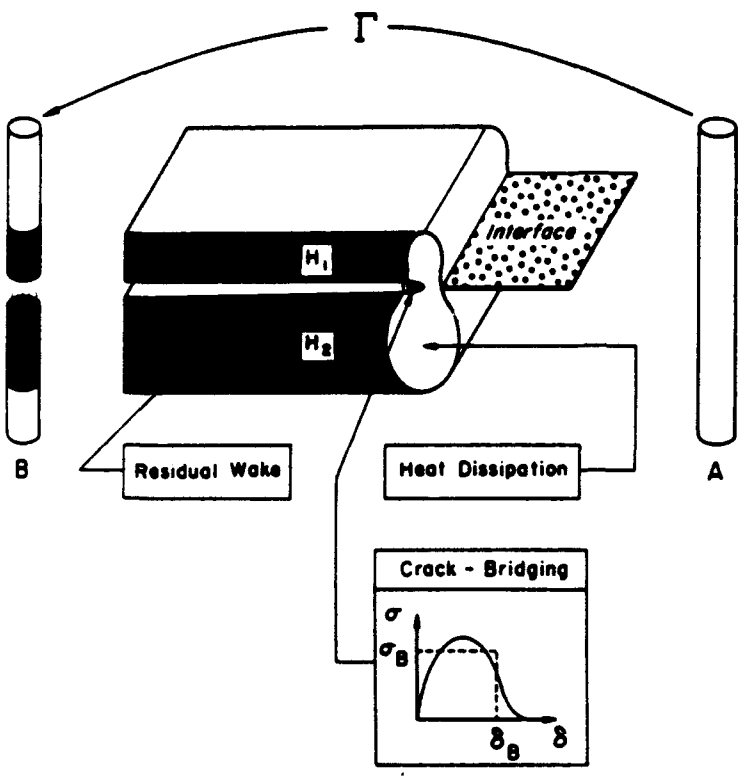

Figure 12.5. Inelastic processes accompanying debond.

The driving force $\mathcal{G}$ depends on the test-piece and can be evaluated by an elastic stress analysis. Fracture resistance Γ depends on the inelastic mechanisms. Equation 12.14 provides a connection between the macroscopic loading condition of a test-piece and the microscopic inelastic process associated with debonding.

Debond resistance can be measured phenomenologically. For example, this can be carried out using the fiber pullout experiment shown in Figure 12.3. The stress required to drive debond is measured, which can be translated to Γ using Equation 12.11 and noting Equation 12.14. This approach is purely phenomenological—no detailed knowledge of physical processes is required, nor is such knowledge generated. Nevertheless, the key quantity, debond resistance Γ, is measured and this can be used in device design. Debond resistance has been measured for a range of bimaterials for applications to thin films and fiber/matrix composites (Evans et al. 1990; Cannon et al. 1992).

In principle, test pieces of any geometry can be used to measure debond resistance. Several convenient geometries are sketched in Figure 12.6. It has been observed experimentally that debond resistance depends on the geometry of the test-piece. Specifically, debond resistance depends on the ratio of the sliding to normal loading parameterized by ψ:

$$\Gamma = \Gamma(\psi) \qquad (12.15)$$

Mode mixity ψ will be elaborated upon later. The trend of the curve is shown in Figure 12.6. The double cantilever beam is predominantly opening mode ($\psi \approx 0°$) and the measured debond resistance is low. The fiber pullout is shear dominant ($\psi \approx 70°$), giving a high debond resistance. The other two, four-point bend and microindentation, produce nearly equal amounts of opening and shear ($\psi \approx 45°$), representative of the conditions in thin-film delamination and fiber/matrix debonding. Microindentation is particularly convenient for small samples (Davis et al. 1991). Other geometries have also been used to measure debond resistance (Argon et al. 1989; Kim 1991; Liechti and Chai 1992; O'Dowd et al. 1992a; Thouless 1990; Wang and Suo 1990).

The dependence of Γ on loading phase can be understood on the basis of inelastic mechanisms. For example, the fiber pullout experiment is dominated by shearing while friction adds to the debond resistance. This mechanism has been examined quantitatively by Hutchinson and Evans (1989). In metal/ceramic interfaces, shear-dominated loading produce larger plastic zones which increase debond resistance (O'Dowd et al. 1992b).

12.2 Williams' Singularity

This section collects mathematical details that refine the concept of mode mixity. The two solids are linearly

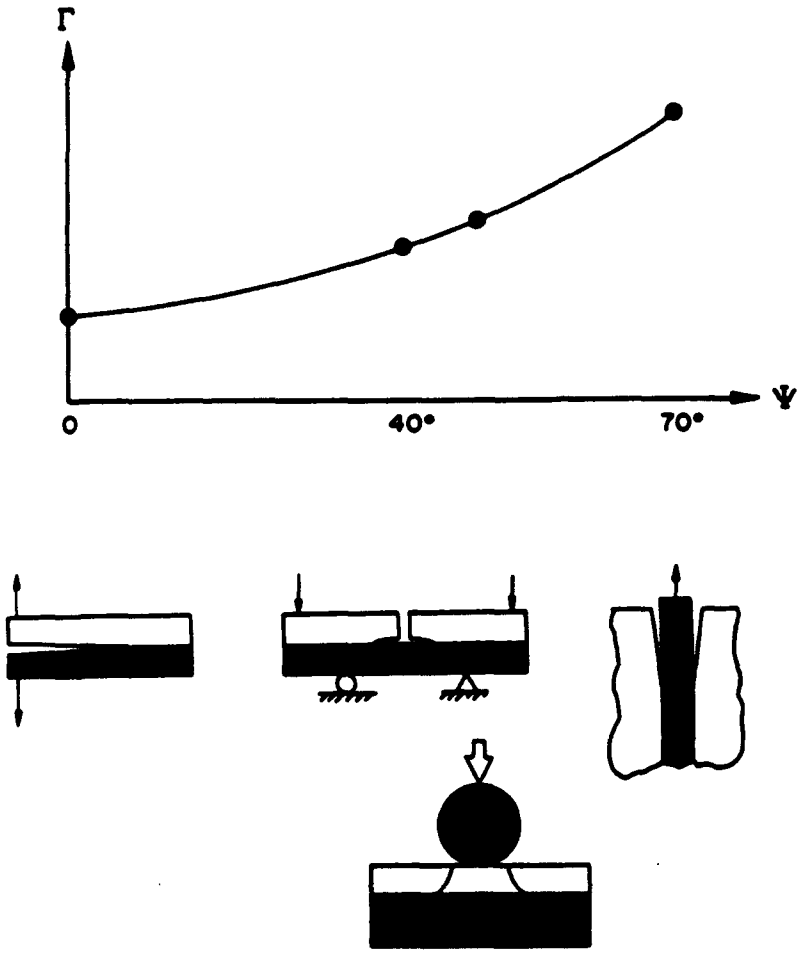

Figure 12.6. Convenient geometries to measure debond resistance.

elastic and isotropic; corresponding results for anisotropic elasticity have been reviewed elsewhere (Suo 1990). The inelastic region is taken to be small compared to all other relevant dimensions of the crack geometry, so that the crack front is a mathematical line, the interface is a mathematical plane, and the crack is semi-infinite. The crack faces are traction-free. This eigenvalue problem was solved by Williams (1959). The essential features of the solution, stress oscillation and crack face contact, are described below. The following interpretation is largely due to Rice (1988).

12.2.1 Slow Oscillation in Stress Field

The tractions at a distance r ahead of the crack tip, on the interface, are found to be

$$\sigma_{yy} + i\sigma_{yx} = \frac{Kr^{i\varepsilon}}{\sqrt{2\pi r}} \qquad (12.16)$$

In the above, x and y are Cartesian coordinates centered at the tip and $i = \sqrt{-1}$. The bimaterial constant ε is defined by

$$\varepsilon = \frac{1}{2\pi} \ln\left[\frac{(3-4\nu_1)/\mu_1 + 1/\mu_2}{(3-4\nu_2)/\mu_2 + 1/\mu_1}\right] \qquad (12.17)$$

Here ν is Poisson's ratio, μ the shear modulus, and subscripts 1 and 2 refer to material 1 and 2, respectively; the constant ε is bounded, $|\varepsilon| < (1/2\pi)\ln 3 = 0.175$.

The complex-valued stress intensity factor, K, cannot be determined by the eigenvalue problem, but can be determined by solving the full boundary-value problem for a given test-piece. The magnitude of K scales with the applied stress, and the phase angle of K represents the relative amount of shear to tension. It can be seen from (12.16) that K has the dimensions

$$K = [\text{stress}]\,[\text{length}]^{1/2 - i\varepsilon} \qquad (12.18)$$

Let $\hat{L}$ be an *arbitrary* length, and define $\hat{\psi}$ by

$$K = |K|\hat{L}^{-i\varepsilon}\exp(i\hat{\psi}) \qquad (12.19)$$

The magnitude, $|K|$, has the dimension stress × length$^{1/2}$, which is independent of the choice of $\hat{L}$, because $|\hat{L}^{i\varepsilon}| = 1$. Indeed, $|K|$ is related to $\mathcal{G}$ (Malyshev and Salganik 1965) by

$$\mathcal{G} = \frac{1}{4}\left(\frac{1-\nu_1}{\mu_1} + \frac{1-\nu_2}{\mu_2}\right)\frac{|K|^2}{\cosh^2 \pi\varepsilon} \quad (12.20)$$

Consequently, $|K|$ and $\mathcal{G}$ are equivalent quantities characterizing the magnitude of the applied load.

Next examine the significance of $\hat{\psi}$. Combining Equations 12.16 and 12.19 yields

$$\sigma_{yy} + i\sigma_{yx} = \frac{|K|}{\sqrt{2\pi r}} \exp i[\hat{\psi} + \varepsilon \ln(r/\hat{L})] \quad (12.21)$$

The identity, $(r/\hat{L})^{i\varepsilon} \equiv \exp[i\varepsilon \ln(r/\hat{L})]$, is used in the above. From Equation 12.21, the ratio of shear stress to tensile stress at a distance r ahead of the crack tip is given by

$$\sigma_{xy}/\sigma_{yy} = \tan[\hat{\psi} + \varepsilon \ln(r/\hat{L})] \quad (12.22)$$

Observe that the traction ratio varies with position r, and that $\tan \hat{\psi}$ equals the ratio of the shear stress to the tensile stress at $r = \hat{L}$. This feature of interface cracks, caused by elastic mismatch, does not exist in mixed mode fracture in homogeneous materials. The result in Equation 12.22 is commonly referred to as the oscillatory singularity, and ε is referred to as the oscillation index. Contrary to a popular misconception, this oscillation is *not* rapid, because ε is small and because a logarithm is a slowly varying function. Thus, in specifying mode mixity, $\hat{L}$ need not be precisely defined, so long as it is broadly representative of the length scale of interest.

Up to this point, $\hat{L}$ has not been given any physical identity. Because Williams' elastic solution describes the stress state outside of the inelastic zone, it is sensible to specify $\hat{L}$ to be on the order of the inelastic zone size. For example, in discussing dislocation emission from an atomistically sharp crack tip, a natural choice of $\hat{L}$ is atomic spacing, so that $\hat{\psi}$ describes the stress state over several atomic spacing (Rice et al. 1990). For a metal/ceramic interface, where dislocation motion prevails over distances many times of the lattice constants, $\hat{L}$ should be chosen as the plastic zone size. Given two choices L and $\hat{L}$, the corresponding loading phases, ψ and $\hat{\psi}$, shift by

$$\psi - \hat{\psi} = \varepsilon \ln(L/\hat{L}) \quad (12.23)$$

Debond resistance Γ should depend on stress state surrounding the inelastic zone, which in turn is characterized by the local phase angle $\hat{\psi}$. Consequently, Equation 12.15 can be rewritten in a more rigorous form.

$$\Gamma = \Gamma(\hat{\psi}) \quad (12.24)$$

Because the size of the inelastic zone depends on fracture mechanisms ranging from nanometers to centimeters, it is meaningless to employ a single $\hat{L}$ for all bimaterials. For interfaces with debond resistance sensitive to mode mixity, the value of $\hat{\psi}$, together with $\hat{L}$, must be reported together with the value of Γ. Moreover, a common $\hat{L}$ must be used in the definition of $\hat{\psi}$ when comparing toughness values at different mode mixities.

12.2.2 Small-Scale Contact

In a homogeneous material, crack faces come into contact under compression. By contrast, interface crack faces may come into contact regardless of loading condition. The size of the contact zone depends on the mode mixity. In composites, the fiber and the matrix may remain in contact because of the residual compression or asperities, sliding against friction during pullout. This provides an example of large-scale contact (Hutchinson and Jensen 1990). In many other technical problems, such as thin-film decohesion, contact zone is small compared to the overall dimension. This section provides a criterion for small-scale contact.

Williams elastic solution shows that the displacement jump at a distance r behind the crack tip is

$$\delta_y + i\delta_x = \left(\frac{1-\nu_1}{\mu_1} + \frac{1-\nu_2}{\mu_2}\right) \cdot \frac{Kr^{i\varepsilon}}{(1+2i\varepsilon)\cosh \pi\varepsilon}\sqrt{\frac{2r}{\pi}} \quad (12.25)$$

From the above, the crack opening is

$$\delta_y = \delta \cos[\hat{\psi} + \varepsilon \ln(\hat{L}/r) - \tan^{-1}(2\varepsilon)] \quad (12.26)$$

where $\delta = (\delta_x^2 + \delta_y^2)^{1/2}$ is the magnitude of the displacement jump. If $\hat{L}$ is interpreted as the process zone size, and if the crack is required to remain open, i.e., $\delta_y > 0$, within $\hat{L} < r < 100\hat{L}$, the mode mixity must be confined within

$$\begin{aligned} -\pi/2 + 2\varepsilon < \hat{\psi} < \pi/2 + 2.6\varepsilon \quad &\text{for } \varepsilon > 0 \\ -\pi/2 - 2.6\varepsilon < \hat{\psi} < \pi/2 + 2\varepsilon \quad &\text{for } \varepsilon < 0 \end{aligned} \quad (12.27)$$

The number 100 is arbitrary, but the condition in Equation 12.27 is not sensitive to this number. When $\varepsilon = 0$, the above condition simply states that contact will not occur under tension, which is known for homogeneous materials.

12.2.3 Specimen Calibrations

For a given test piece, the complex stress intensity factor K can be solved by an elastic stress analysis. It has the generic form

$$K = YT\sqrt{L}L^{-i\varepsilon}\exp(i\psi) \qquad (12.28)$$

where T is a representative stress magnitude, and L a characteristic crack dimension. Y and ψ are dimensionless real numbers that depend on elastic constants, geometric parameters, and loading. Note that ψ is by definition the phase of $KL^{i\varepsilon}$. Solutions have been compiled by Hutchinson and Suo (1992).

As an example, consider a Griffith crack of length L on the interface between two materials (Figure 12.7). The complex stress intensity factor is

$$K = (1 + 2i\varepsilon)\sqrt{\pi L/2}L^{-i\varepsilon}T\exp(i\omega) \qquad (12.29)$$

where ω is the remote loading angle. Driving force $\mathcal{G}$ is obtained by substituting Equation 12.29 in Equation 12.20; the loading angle consistent with Equation 12.28 is $\psi = \omega + \tan^{-1}(2\varepsilon)$. The mode mixity at $r = \hat{L}$ is given by

$$\hat{\psi} = \omega + \tan^{-1}(2\varepsilon) + \varepsilon\ln(\hat{L}/L). \qquad (12.30)$$

For a numerical illustration, consider an alumina/glass interface ($\varepsilon = -0.05$). The crack size $L = 1$ mm, and the process zone size is of the order $\hat{L} = 1$ nm. Under remote tension, $\omega = 0°$, one finds $\hat{\psi} = 34°$, that is, a large shear component exists near the crack tip. Now change the crack size to $L = 1$ cm, and everything else being the same, the new phase angle becomes $\hat{\psi} = 40°$.

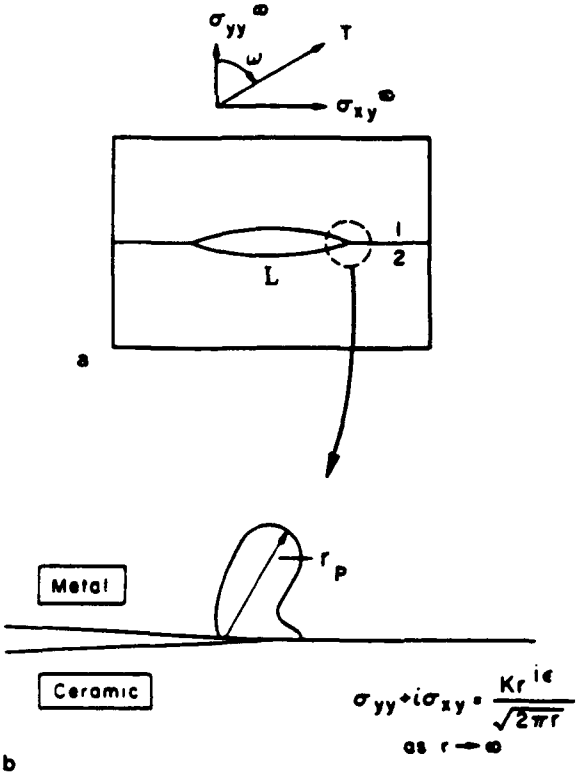

Figure 12.7. (a) A finite interface crack subjected to a remote tension T at angle ω; the plastic zone size is assumed to be small compared to the crack size. (b) A small-scaled yielding problem is posed.

12.3 Crack Tip Plasticity

Plastic flow around the tip of an interface crack has been analyzed by Shih and Asaro (1988), Shih et al. (1991), and Zywicz and Parks (1989, 1992). Plasticity aspects of interface cracks are reviewed by Shih (1991). Consider a stationary interface crack between two materials, at least one of which is plastically deformable (Figure 12.7). Small-scale yielding conditions prevail—that is, the plastic zone size r_p is much smaller than the characteristic specimen dimension (e.g., crack size L for a finite crack in an infinite body). Stress distribution over distances $r \gg r_p$ is approximately determined by elasticity, as if near-tip plasticity were nonexistent. In particular, the stress field in the annulus, $r_p \ll r \ll L$, is given by Williams' singular solution discussed in Section 12.2. The boundary value problem thus consists of two semi-infinite materials bonded over $x_1 > 0$, but unbonded over $x_1 < 0$; Williams' stress distribution is applied as boundary conditions as $r \to \infty$, with a complex stress intensity factor as follows:

$$K = |K|L^{-i\varepsilon}\exp(i\psi) \qquad (12.31)$$

Here L is the crack size, and ψ the load angle in the elasticity problem of finite crack. The elastic-plastic response is characterized by J_2 flow theory.

12.3.1 Plastic Zone Size

The problem contains two length scales, L and $(|K|/\sigma_Y)^2$, σ_Y being the lower yield stress of the two materials. Elementary considerations suggest that r_p scales with $(|K|/\sigma_Y)^2$, providing a natural length to define mode mixity. Define a dimensionless number by

$$\xi = \psi + \varepsilon\ln\left(\frac{|K|^2}{\sigma_Y^2 L}\right) \qquad (12.32)$$

According to the interpretation in Section 12.2.1, $\tan\xi$ broadly represents the traction ratio σ_{xy}/σ_{yy} near $r = (|K|/\sigma_Y)^2$, or just outside of the plastic zone.

The plastic zone size is given by

$$r_p = \mathfrak{R}(|K|/\sigma_Y)^2 \qquad (12.33)$$

The dimensionless factor $\mathfrak{R}$ depends weakly on material constants, but is sensitive to mode mixity, ranging from

0.15 to about 0.65 as $|\xi|$ increases from 0 to $\pi/2$. Furthermore, the shape of the plastic zone depends on the sign of ξ, which may lead to different debond resistance for loading with opposite shear directions. The above results are rigorously correct for deformation plasticity; numerical calculations have shown that they are quite accurate for flow theory.

12.3.2 Stress Distribution Around a Blunted Crack Tip

Next consider the stress distribution *within* the plastic zone. The region of interest is bounded by the plastic zone size r_p, and the crack tip opening displacement δ_t. The latter is given by

$$\delta_t = \mathfrak{D} J/\sigma_Y \qquad (12.34)$$

The prefactor, $\mathfrak{D}$, ranges from 0.5 to 0.7 for $|\xi| \le \pi/6$ when the metal has low strain hardening ($N \le 0.1$). The two lengths, r_p and δ_t, differ by a factor comparable to the yield strain.

The traction ratio, σ_{xy}/σ_{yy}, ahead of the blunted crack tip, within $\delta_t < r < r_p$, is shown in Figure 12.8. Note that $\tan \xi \approx \sigma_{xy}/\sigma_{yy}$ near $r = (|K|/\sigma_Y)^2$. For the opening mode $\xi \approx 0$, the traction ratio remains small over the range of distances shown. Under mixed mode loading $\xi \neq 0$, moderate variation in the traction ratio is observed. The trends displayed in Figure 12.8 are representative of metal/ceramic interfaces. Figure 12.9 shows the distribution of the hoop stress ahead of the crack tip. Focus on the curve for $\xi = 0$. The blunted crack tip relieves the constraint, leading to a low stress

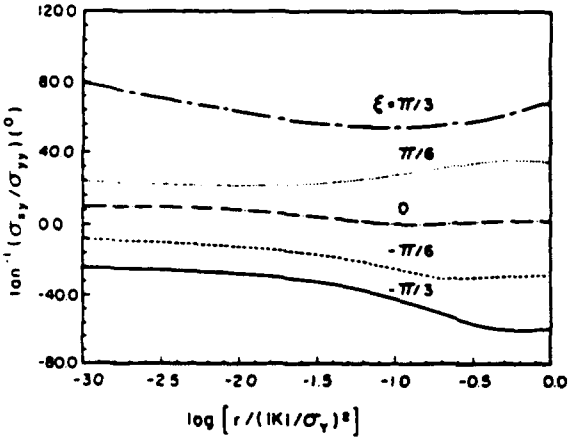

Figure 12.8. The ratio of shear over tension ahead of the crack tip, on the interface, in the range $\delta_t \le r \le r_p$. Metal/ceramic bimaterial; metal properties are $N = 0.1$, $\varepsilon_Y = 0.003$, and $\nu = 0.3$.

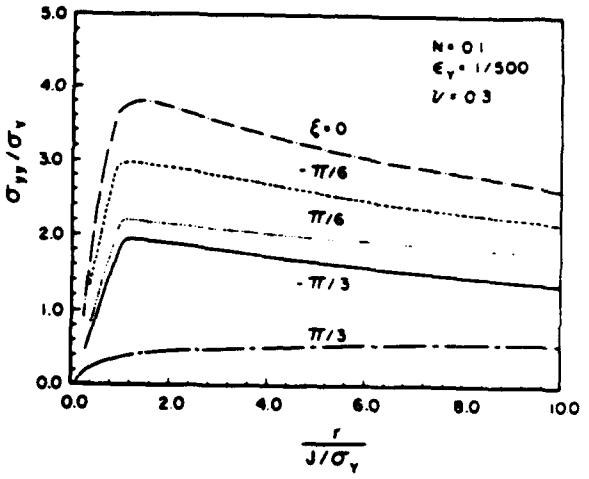

Figure 12.9. Tensile stress ahead of the crack tip, on the interface. Note that $\delta_t \sim J/\sigma_Y$. Metal/ceramic bimaterial; metal properties are $N = 0.1$, $\varepsilon_Y = 0.003$, and $\nu = 0.3$.

within $r < J/\sigma_Y$. The hoop stress reaches a maximum at distance $r \approx J/\sigma_Y$. The stiffer substrate provide additional constraint to plastic flow so that the stress for $\xi = 0$ is about 10% higher than the level for the corresponding homogeneous material (Shih et al. 1991). The constraint is partially relieved when the loading contains a large shear component.

In recent experiments with niobium diffusion bonded to alumina, O'Dowd et al. (1992b) found that debond resistance varies significantly with mode mixity; for example, $\Gamma(40°)/\Gamma(0°) \approx 10$. An attempt was made to correlate mixed mode debond resistance on the basis of a cleavage stress at a characteristic distance (for example, distance between triple point junctions in Al_2O_3), as an extension of the early work of Ritchie et al. (1973) on mode I fracture in mild steels.

The evolution of cyclic near-tip fields ahead of a stationary interface crack has been investigated by Woeltjen et al. (1992). Under monotonic loading to peak tensile load an essentially mode I near-tip field is observed over the major portion of the plastic zone, similar to the result in Figure 12.8 for $\xi = 0$. However, a mixed-mode field is generated near the tip upon removal of the tensile load. The development of strong shear tractions ahead of the interface crack tip has important implications for fatigue fracture mechanisms and fatigue life.

12.3.3 Constrained Plasticity

Reimanis et al. (1991) have carried out fracture experiments with gold foils that were diffusion bonded between sapphire plates. The foil thickness, h, is much smaller than the overall dimension of the specimen. The

plastic zone is comparable to (or even larger than) h, but the total inelastic zone size is small compared to specimen dimensions. Therefore, the remote load can be prescribed by a stress intensity factor. Upon loading, partial debond develops at a distance several times the foil thickness ahead of the crack tip. These micro-debonds do not connect with the crack tip. With furthur loading, new debonds nucleate at a even larger distance ahead of the crack tip, as shown in Figure 12.11(d). The intact metal ligaments bridge the crack, leading to a rapidly rising resistance curve (R—curve). Here we focus on the initiation of the micro-debond, the precursor to bridging.

The above phenomenon is an extreme form of large-scale yielding (relative to the foil thickness h), in which the metal foil is highly constrained by the sapphire plates. A finite element analysis by Varias et al. (1991, 1992) reveals that the hydrostatic stress in the metal foil increases steadily as the applied load increases; this is in contrast to the stress distribution ahead of an interface crack between two substrates that cannot elevate above three to four times the yield stress. The behavior of the mean stress in the metal foil is shown in Figure 12.10. Near the tip ($r/h \ll 1$), the stress distribution is not affected by the constraint of the foil thickness, so the mean stress is about three times the yield stress, similar to the distribution in Figure 12. 9. At a distance several times the foil thickness, the mean stress reaches the maximum, which increases with applied load; the location of the maxima shifts ahead as the load increases. These elevated stress maxima are responsible for micro-debonds.

12.4 Growing Cracks and Debond Resistance

Debonding rearranges the atoms that form the interface into two free surfaces, consuming the Griffith energy

$$\Gamma_G = \gamma_1 + \gamma_2 - \gamma_{int} \qquad (12.35)$$

Here γ_1 and γ_2 are the surface energies of material 1 and 2, respectively, and γ_{int} is the interface energy. The Griffith energy is small, since only a few layers of atoms participate in irreversible movements. To increase debond resistance, more atoms must be brought into the inelastic process, through mechanisms activated by stress lower than that required for atomic separation. For example, $\Gamma_G < 10$ J/m^2 for Al_2O_3, but even single crystal Al_2O_3 has fracture resistance exceeding 30 J/m^2. Some heat-dissipating, atomic-scale snapping processes might exist, involving atoms off the crack plane (K.-S. Kim, private communication). The fracture resistance of polycrystalline Al_2O_3 is further increased by grain-scale dissipating mechanisms such as pullout against friction (Vekinis et al. 1990).

Studies on crack growth resistance in metals were initiated by McClintock and Irwin (1965). They used small-scale yielding solutions for growing cracks in mode III, together with a growth criterion based on the attainment of a critical strain at a characteristic distance ahead of the tip. Later developments along this line were given by Drugan et al. (1982), and have been extended by Drugan (1991) and Ponte Castañeda and Mataga (1992) to cracks growing along bimaterial

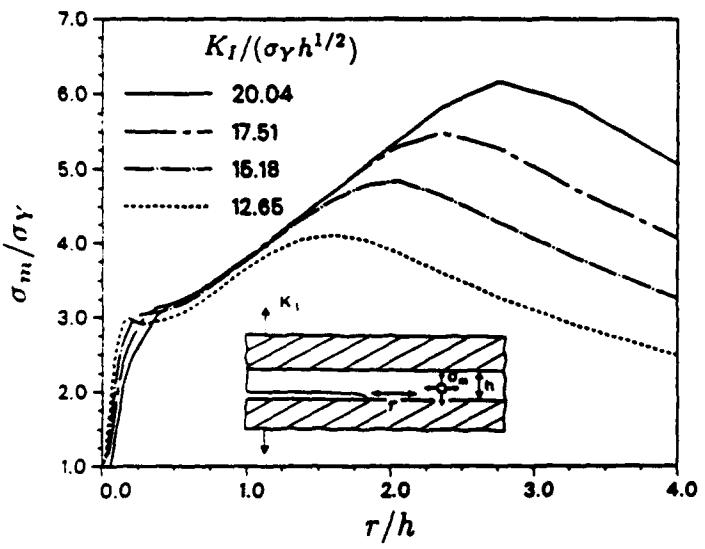

Figure 12.10. Inset: a metal foil bonded between two ceramic substrates, subjected to a remote Mode I stress intensity factor. The mean stress distribution ahead of the crack tip is plotted for several loading levels.

interfaces. Mechanism-based models to relate debond resistance to micromechanisms have been developed recently, and provide a focus for the subsequent presentation. We will limit our attention to predominantly opening mode of fracture.

12.4.1 Crack-Bridging

A solid will fall apart unless something holds it together. A far reaching, unifying idea, sufficiently rigorous for our purpose, is to represent "binding" by a relation between attractive stress, σ, and separation, δ. Such a relation is sketched in Figure 12.5, and is written as

$$\sigma/\sigma_B = \chi(\delta/\delta_B) \tag{12.36}$$

The dimensionless function χ describes the shape of the relation and the scale is set by σ_B and δ_B. The energy required to separate unit area of surfaces so bridged is

$$\Gamma_B = \sigma_B\delta_B\int_0^\infty \chi(\kappa)d\kappa \tag{12.37}$$

The dimensionless integral is of order unity. In practice, the shape function χ is difficult to determine precisely, but the quantities σ_B and δ_B are readily related to microstructural variables (Evans 1990). One can therefore estimate fracture resistance by

$$\Gamma_B \approx \sigma_B\delta_B \tag{12.38}$$

Sketched in Figure 12.11 are several bridging mechanisms, and Table 12.1 lists the representative values of σ_B, δ_B and Γ_B for these mechanisms. Atomic bond has high strength but small debond separation, resulting in a small fracture resistance. Ductile, crack-bridging ligaments give rise to a substantially higher fracture resistance; these ligaments are believed to operate in polycrystalline steels at lower shelf (Hoagland et al. 1972), and in a ceramic matrix containing metallic particles. In the latter, δ_B scales with the diameter of the particles. It remains unclear for polycrystalline steels whether δ_B is set by grain size or some other microstructural lengths. Holes can nucleate in ductile alloys around hard inclusions, or on metal/ceramic interface around pores or

Table 12.1. Illustrative Properties for Bridging Mechanisms

	$\sigma_B(N/m^2)$	$\delta_B(m)$	$\Gamma_B \approx \sigma_B\delta_B(J/m^2)$
Atomic bond	10^{10}	10^{-10}	1
Ductile ligament	10^8	10^{-5}	10^3
Hole growth	10^9	10^{-4}	10^5
Metal foil	10^7	10^{-5}	10^2

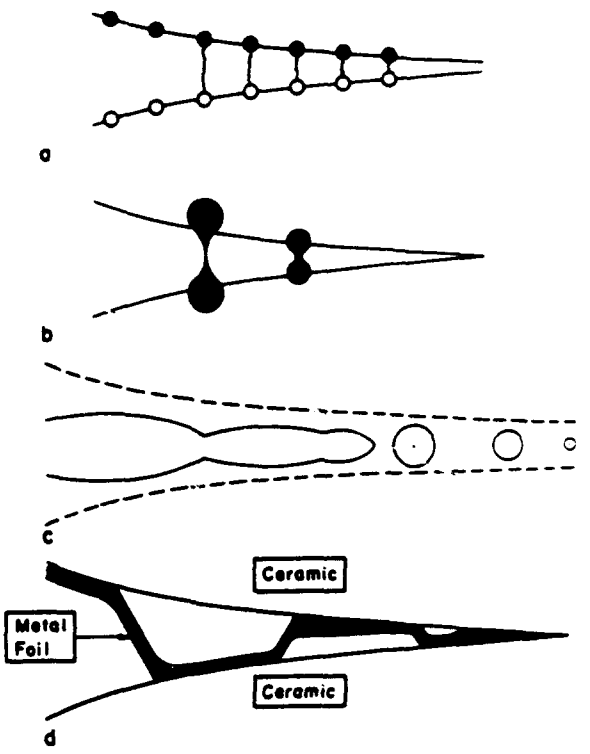

Figure 12.11. Crack-bridging mechanisms: (a) atomic adhesion, (b) ductile ligaments, (c) hole growth, and (d) alternating debonding.

triple-point junctions. Hole growth usually dissipates large amounts of energy. Thin metallic foils sandwiched between two ceramic substrates may debond along alternating interfaces, either because of periodic weak spots fabricated during bonding (Oh et al. 1988), or because of constrained plastic flow (Reimanis et al. 1991; Varias et al. 1991, 1992). More detailed review on crack-bridging concepts can be found elsewhere (Bao and Suo 1992; Suo et al. 1993).

12.4.2 Crack-Bridging and Background Plasticity

It is assumed in the previous section that inelastic deformation can be fully represented by a bridging law while the background material is elastic. In practice, several inelastic mechanisms can operate simultaneously. An interesting example involves a ceramic matrix containing both ductile and transforming particles. The ductile particles form bridges, while the transforming particles contribute to background dissipation. Bridging increases the height of the wake, transforming more particles and thereby dissipating more energy; transformation shields the bridging zone. Thus, the synergism (Amazigo and Budiansky 1988).

Consider the deformation history that a material at distance y off the interface experiences as the crack tip passes by. The energy density variation for the entire process is

$$W(y) = \int_0^{\varepsilon_{ij}} \sigma_{ij} d\varepsilon_{ij} \qquad (12.39)$$

The integral is carried over the entire history, including the heat dissipation when the particle is in the active plastic zone, and the residual stress energy when the particle is in the wake. Let H_1 and H_2 be the depths of the inelastic layers in the two materials. The total energy expended in the background for the steady-state crack to move unit distance is

$$\Gamma_P = \int_{-H_2}^{H_1} W(y) dy \qquad (12.40)$$

The total fracture resistance, which includes Griffith energy, bridging energy, and stress work in the background, is given by

$$\Gamma = \Gamma_G + \Gamma_B + \Gamma_P \qquad (12.41)$$

Because Γ_P and Γ_B are typically much larger than Γ_G, it is sometimes assumed that Γ_G is an irrelevant parameter for fracture involving substantial plasticity. However, several authors have pointed out that if cleavage is the basic fracture mechanism, Γ_P or Γ_B must, in some way, depend on Γ_G — that is, the small quantity Γ_G serves as a "valve" for large dissipation Γ_B and Γ_P (Jokl et al. 1980). For example, in transformation-toughened ceramics, the matrix toughness sets the extent of the transformation zone and thereby Γ_P (McMeeking and Evans 1982; Budiansky et al. 1983).

A more familiar example is ductile fracture of alloys, where the near-tip mechanism of hole growth and coalescence serves as the valve for larger-scale plastic dissipation. This process has been analyzed by Needleman (1987, 1990), Varias et al. (1990), and Tvergaard and Hutchinson (1992). Consider a precut remotely loaded by a monotonically increasing $\mathcal{G}$. When $\mathcal{G} < \Gamma_B$, the bridging develops ahead of the crack tip, as does the plastic zone, while the crack remains stationary. The crack begins to grow or, rather, the bridges start to break when $\mathcal{G} = \Gamma_B$. In this sense, background plasticity does *not* provide any shielding prior to crack growth. This can be readily understood by the J-integral, and by the fact that plastic flow is proportional prior to crack growth. A reference length is defined by

$$R_B = \frac{1}{3\pi} \frac{\Gamma_B}{\sigma_Y \varepsilon_Y} \qquad (12.42)$$

This reference length scales with the extent of the plastic zone size when $\mathcal{G} = \Gamma_B$.

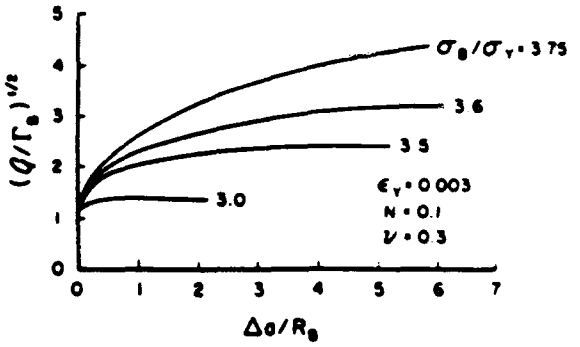

Figure 12.12. Fracture resistance curve resulting from background plasticity shielding. *(From Tvergaard and Hutchinson 1992.)*

As the crack grows, the bridging zone translates in the material: old bridges are broken in the wake, and new bridges are formed in the front. The background material also experiences elastic unloading and possibly reverse plastic loading. The complicated deformation shields the crack. The shielding ratio, $\mathcal{G}/\Gamma_B$, increases with the crack increment Δa, as shown in Fig 12.12. It is evident that the steady-state is established when the crack growth is greater than several times R_B. The steady-state fracture resistance, Γ_{SS}, depends on σ_B/σ_Y. The trend can be better seen in Figure 12.13. For a nonhardening material ($N = 0$), no contribution is derived from the background plasticity if $\sigma_B/\sigma_Y < 2$; conversely, the crack is "lock up," or has infinite fracture resistance when $\sigma_B/\sigma_Y \geq 3$. Similar trends are observed for strain-hardening materials.

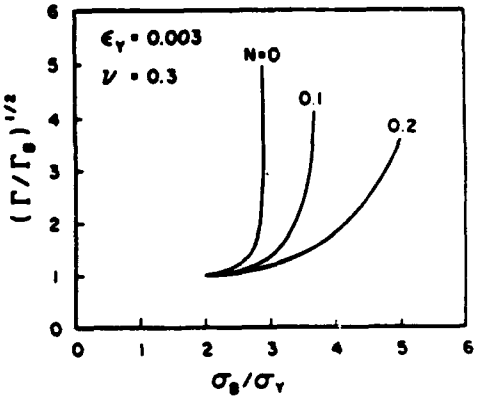

Figure 12.13. Steady-state shielding ratio as a function of bridging strength relative to yield strength. *(From Tvergaard and Hutchinson 1992.)*

12.4.3 *Brittle Debonding in the Presence of Plastic Flow*

It is known that a sharp, cleaving crack can propagate, slowly or dynamically, surrounded by substantial dislocation motion. For example, a sharp crack can grow slowly by cleavage along a gold/sapphire interface even though the gold deforms plastically; the measured fracture energy is much larger than Γ_G (Reimanis et al. 1991). Similar behavior is observed in copper/glass (Oh et al. 1987), copper/sapphire (Beltz and Wang 1992), niobium/alumina (O'Dowd et al. 1992b), and copper bicrystals contaminated by bismuth (Wang and Anderson 1991). This phenomenon cannot be explained by the models discussed in the previous sections. Atomic cohesive strength, σ_B, is known to be orders of magnitude higher than macroscopic yield strength, σ_Y. When σ_B/σ_Y exceeds about 4, crack-bridging models within the framework of continuum plasticity predict that the crack blunts, limiting the near-tip stress to several times σ_Y (Figure 12.9). Consequently, cleavage cannot proceed from the crack tip. Instead, one has to appeal to other fracture mechanisms, such as hole growth (Rice and Johnson 1970) and cleavage from a remote defect (Ritchie et al. 1973), both leading to rough fracture surfaces not observed in experiments cited in the previous paragraph.

Figure 12.14 conveys the essentials of a theory proposed by Suo et al. (1993). The fundamental process for plastic flow is discrete, consisting of at least two length scales: the Burgers vector $b \sim 10^{-10}$ m, and dislocation spacing $D \sim 10^{-6}$ m. On one scale, atoms exhibit individuality ultimately governed by quantum mechanics. On the other scale, dislocations interact through continuum elasticity. Continuum plasticity applies when stress variation over a multiple of D is small compared to the macroscopic yield strength. The discreteness becomes important for events occurring between lengths b and D.

The theory is based on a single premise: the crack front does not emit dislocations. This happens, for example, for cleavable materials such as steel and silicon below the ductile-brittle transition temperature, or contaminated grain boundaries, or interfaces subjected to environmental degradation, or interfaces with a few atomic layers of brittle reaction compounds. As illustrated in Figure 12.14, so long as dislocation spacing D is much larger than the lattice constant, the probability for a pre-existing dislocation to blunt a major portion of the crack front should be extremely small. Consequently, a crack that does not emit dislocation will remain nanoscopically sharp, advancing by atomic decohesion. Within the cell, essentially free of dislocations that surrounds the crack front, the crystal is linearly

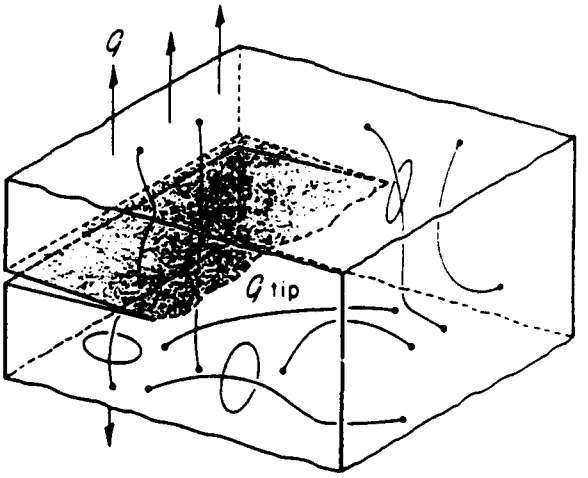

Figure 12.14. A decohesion front in a network of pre-existing dislocations. The diameter of the decohesion core is about 1 nm; the average dislocation spacing is more than 100 nm.

elastic down to a nanometer. Near the crack tip, nonlinearity arises from partial atomic separation and nanoscopic shear bands. The size of the elastic cell, represented by D, is several orders of magnitude larger than the nonlinear zone size. Consequently, information regarding the nanoscopic nonlinearity is transmitted—to an observer outside the elastic cell—through a single quantity: the Griffith energy Γ_G. The elastic cell provides a medium through which the stress decays rapidly, matching the high atomic debond stress on one side, and the low macroscopic yield stress on the other. For example, with $b = 10^{-10}$m and $D = 10^{-6}$m, the stress decays approximately by a factor $\sqrt{D/b} = 100$ over a distance of 1 μm. The dislocation motion at the characteristic distance D away from the crack tip dissipates plastic energy, Γ_P, which is typically much larger than Γ_G. In summary, atoms around a crack front can be divided into three regions: nanoscopic decohesion zone, microscopic elastic cell, and macroscopic dislocation dissipative background.

The elastic cell is a nanomechanics concept with imprecise, if any, continuum description. The concept can be approximately understood in terms of spatially varying yield strengths. Sketched in Figure 12.15 is yield strength varying with the distance from a representative atom at the crack tip. The theoretical shear strength is approached near the crack tip; the strength decays to the macroscopic yield strength in the background. The shape of the decay function has not been investigated; dislocation cell models may provide some

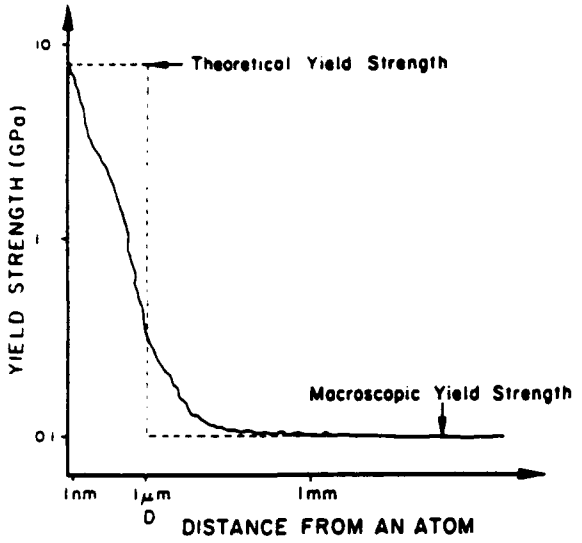

Figure 12.15. Yield strength as a function of the distance from an atom at the center of an elastic cell.

insight (Lubarda et al. 1993; Kubin et al. 1992). Nevertheless, the decay function *must* have a characteristic length comparable to the dislocation spacing D.

Consider a cleavable, rate-independent material with Griffith energy Γ_G, yield strength σ_Y and yield strain $\epsilon_Y = \sigma_Y/E$, E being Young's Modulus. The crack tip energy release rate, $\mathcal{G}_{tip}$, is shielded by background dislocation motion from the remotely applied energy release rate, $\mathcal{G}$. Dimensional analysis dictates that

$$\mathcal{G}/\mathcal{G}_{tip} = g(D\epsilon_Y\sigma_Y/\mathcal{G}_{tip}) \qquad (12.43)$$

The shielding ratio g also depends on crack increment and material constants such as ϵ_Y, Poisson's ratio ν and in particular, the shape of the decay function in Figure 12.15. For properties representative of metals (e.g. $D \sim 1\ \mu m$, $\epsilon_Y \sim 10^{-3}$, $\sigma_Y \sim 10^8\ N/m^2$, $\Gamma_G \sim 1\ J/m^2$), the parameter $D\ \epsilon_Y\sigma_Y/\Gamma_G$ ranges from 10^{-2} to 10. The parameter can be understood in several ways; e.g., all else being fixed, an increase in elastic cell size D reduces the total energy dissipation. Under steady-state growth, $\mathcal{G}_{tip} = \Gamma_G$ and $\mathcal{G}$ equals the measured fracture energy Γ. The plastic dissipation Γ_P is given by $\Gamma = \Gamma_P + \Gamma_G$.

In the present theory, it is assumed that no low strength, long range bridges, such as tearing caused by cleavage plane reorientation between neighboring grains, operate in the crack wake. These bridges are responsible for the large "cleavage energy" reported for polycrystalline steels. When operating, the bridges may serve as a bigger valve than atomic decohesion. If this is the case, a bridging law may be used in the present model. Indeed, when $\sigma_B/\sigma_Y < 4$, the present model should reduce to a regular bridging model without an elastic cell.

Further simplifications are needed to make quantitative predictions (Figure 12.16). The decohesion zone is small compared to D so that the square root singular elasticity solution prevails in $b \ll r \ll D$. Detailed atomistic description of decohesion is unnecessary except for a prescription of a cleavage energy Γ_G. The shape of the elastic cell is unimportant because the plastic zone height is typically much larger than D; we use a strip to represent the elastic cell. A disc translating with the crack tip can be another convenient choice, but the difference is expected to be minor in so far as $\mathcal{G}/\mathcal{G}_{tip}$ is concerned. The background dislocation motion is represented by continuum plasticity. A refinement, if needed, may include individual dislocations or a dislocation network in the transition region between the elastic cell and the continuum plastic flow.

The crack starts to grow when $\mathcal{G} \geq \Gamma_G$; more load is required to maintain the growth, leading to a resistance curve. The plastic zone also increases as the crack grows, attaining a steady-state height H. The energy release rate reaches a steady-state value Γ_{SS}. The model geometry is analyzed in the steady-state using finite elements. Figure 12.17 shows that the shielding ratio increases rapidly as D or σ_Y decrease. The influence of strain hardening exponent, N, can also be seen. For nonhardening metals, the plastic dissipation completely shields the crack tip at a finite $D\ \epsilon_Y\sigma_Y/\mathcal{G}_{tip}$. In practice, D may be used as a fitting parameter to correlate experimental data. For example, a metal with $\sigma_Y = 10^8\ N/m^2$, $\epsilon_Y = 3.3 \times 10^{-3}$ and $\Gamma_G = 2\ J/m^2$ gives $\Gamma_G/\sigma_Y\epsilon_Y = 6\ \mu m$. If the measured fracture energy $\Gamma_{SS} = 20\ J/m^2$, one finds from Figure 12.17 that $D \approx 0.1\ \mu m$.

In an experiment with a single crystal of copper diffusion bonded to a sapphire disc (Beltz and Wang

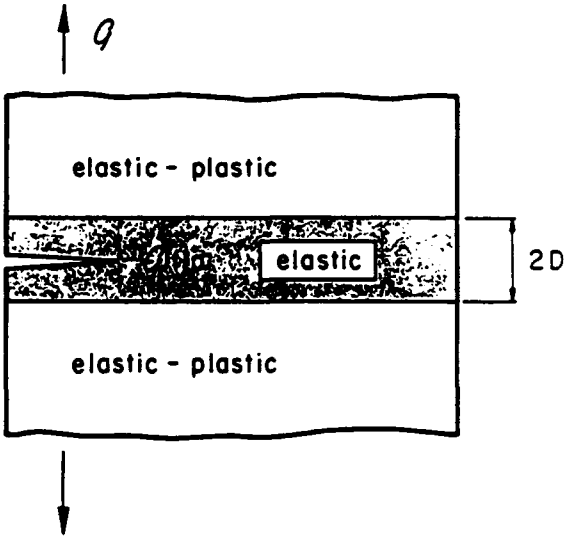

Figure 12.16. A model system with a step-function decay in yield strength.

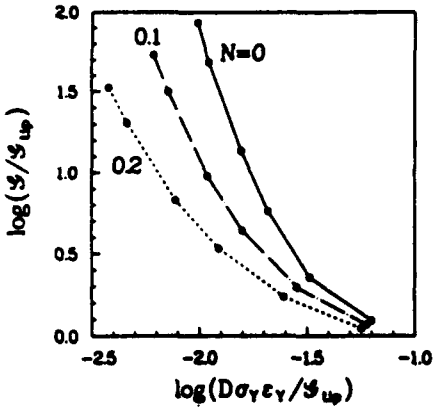

Figure 12.17. A fracture resistance curve: the fracture energy increases as the crack grows. Computed shielding ratio as a function of various parameters: N—hardening exponent, D—elastic cell size.

1992), interface debonding was driven in two crystallographic directions at slightly different energy release rates. The phenomenon was interpreted according to the Rice-Thomson model (1974): dislocations emit from the crack tip in one direction but not from the other. An alternative interpretation appears to be possible on the basis of the present theory: both crack tips do not emit dislocations and the different debond energies result from the different extent of background dislocation motion. Indeed, the micrographs show much denser slip lines in one case than they do in the other. Experiments at higher magnifications are needed to ascertain which of the two interpretations is appropriate for the copper/sapphire system. Calculations within the framework of the present theory, taking into account single crystal plasticity, are in progress to facilitate a direct comparison with such experiments.

Obviously, the competition between atomic decohesion and dislocation emission (Rice et al., 1992) cannot be addressed by the present theory. Instead, the consequences of the premise that dislocations do not emit from the crack front can be explored. Included in Suo et al. (1993) are slow cleavage cracking, stress-assisted corrosion, fast-running crack, fatigue cracking, constraint effects, and mixed mode fracture along metal/ceramic interfaces.

Acknowledgements

The work of Z.S. was supported by an NSF Young Investigator Award, by DARPA/URI Contract N00014-86-K-0753, and by a Visiting Associate Professor appointment at Brown University funded by NRC/ONR Grant N00014-90-J1380. The work of C.F.S. was supported by NRC/ONR Grant N00014-90-J13800, and by the Materials Research Group funded by NSF through Grant DMR-9002994.

References

Amazigo, J.C., and B. Budiansky. 1988. *J. Mech. Phys. Solids.* 36:581–595.

Aveston, J., Cooper, G.A., and A. Kelly. 1971. *In:* The Properties of Fiber Composites. Conference Proceedings, National Physical Laboratory (Guildford UK). 15–24, Teddington, UK: IPC Science and Technology Press, Ltd.

Argon, A.S., Gupta, V., Landis, H.S., and J.A. Cornie. 1989. *J. Mater. Sci.* 24:1406–1412.

Ashby, M.F., Rühle, M. (eds.). 1992. Proceedings of International Symposium on Metal/Ceramic Interfaces. To be published in *Acta Metall. Mater.*

Bao, G., and Z. Suo. 1992. *Appl. Mech. Rev.* In Press.

Beltz, G.E., and J.-S. Wang. 1992. *Acta Metall. Mater.* 40:1675–1683.

Budiansky, B., Hutchinson, J.W., and J.C. Lambropoulos. 1983. *Int. J. Solids Struct.* 19:337–355.

Cannon, R.M., Dalgleish, B.J., Dauskardt, R.H. et al. 1992. *In:* Fatigue of Advanced Materials (R.O. Ritchie, R.H. Dauskardt, and B.N. Cox, eds.) Edgbaston, UK: MCEP Publishing Ltd.,

Cao, H.C., and Evans, A.G. 1989. *Mech. Mater.* 7:295–305.

Cottrell, A.H. 1963. *In:* Tewksbury Symposium on Fracture. 1–27, Melbourne: University of Melbourne.

Davis, J.B., Cao, H.C., Bao, G., and A.G. Evans. 1991. *Acta Metall. Mater.* 39:1019–1024.

Drugan, W.J. 1991. *J. Appl. Mech.* 58:111–119.

Drugan, W.J., Rice, J.R., and T.-L. Sham. 1982. *J. Mech. Phys. Solids.* 30:447–473.

England, A.H., 1965. *J. Appl. Mech.* 32:400–402.

Erdogan, F. 1965. *J. Appl. Mech.* 32:403–410.

Evans, A.G. 1990. *J. Am. Ceram. Soc.* 73:187–206.

Evans, A.G., Drory, M.D., and M.S. Hu. 1988. *J. Mater. Res.* 3:1043–1049.

Evans, A. G., and J.W. Hutchinson. 1989. *Acta Metall. Mater.* 37:909–916.

Evans, A.G., Rühle, M., Dalgleish, B.J., and P.G. Charalambides. 1990. *Mater. Sci. Eng.* A126:53–64.

Farris, R.J., and C.L. Bauer. 1988. *J. Adhesion.* 26:293–300.

Griffith, A.A. 1921. *Phil. Trans. Roy. Soc. Lond.* A221:163–197.

Hoagland, R.G., Rosenfield, A.R., and G.T. Hahn. 1972. *Metall. Trans.* 3:123–136.

Hutchinson, J.W. 1979. Nonlinear Fracture Mechanics. Department of Solid Mechanics, Technical University of Denmark.

Hutchinson, J.W., and H.M. Jensen. 1990. *Mech. Mater.* 9:139–163.

Hutchinson, J.W., and Z. Suo. 1992. *Adv. Appl. Mech.* 29:63–191.

Irwin, G.R. 1960. *In:* Structural Mechanics. (J.N. Goodier and N.J. Hoff, eds.), 557–591, Oxford: Pergamon Press.

Jokl, M.L., Vitek, V., and C.J. McMahon, Jr. 1980. *Acta Metall.* 28:1479–1488.

Kanninen, M.F., and C.H. Popelar. 1985. Advanced Fracture Mechanics. Oxford: Oxford University Press.

Kim, K.-S. 1991. *Mat Res Soc Symp Proc.* 203:3–14.

Kubin, L.P., Canova, G., Condat, M. et al. 1992. *In:* Nonlinear Phenomena in Materials Science II (G. Martin and L. P. Kubin, eds.). In press.

Liechti, K.M., and Y.-S. Chai. 1992. *J. Appl. Mech.* 59:295–304.

Lubarda, V.A., Blume J.A., and A. Needleman. 1992. *Acta Metall. Mater.* 41:625–642.

Malyshev, B.M., and R.L. Salganik. 1965. *Int. J. Fract. Mech.* 5:114–128.

McClintock, F.A., and G.R. Irwin. 1965. ASTM-STP 381, 84–113, Philadelphia: ASTM.

McMeeking, R.M., and A.G. Evans. 1982. *J. Am. Ceram. Soc.* 65:242–246.

Moran, B., and C.F. Shih. 1987. *Eng. Fract. Mech.* 27:615–642.

Needleman, A. 1987. *J. Appl. Mech.* 54:525–531.

Needleman, A. 1990. *J. Mech. Phys. Solids.* 38:289–324.

O'Dowd, N.P., Shih, C.F., and M.G. Stout. 1992a. *Int. J. Solids Struct.* 29:571–589.

O'Dowd, N.P., Stout M.G., and C.F. Shih. 1992b. *Phil. Mag.* 66A:1037–1064.

Oh, T.S., Cannon, R.M., and R.O. Ritchie. 1987. *J. Am. Ceram. Soc.* 70:C352–C355.

Oh, T.S., Cannon, R.M., and R.O. Ritchie. 1988. *Acta Metall.* 36:2083–2093.

Ponte Castañeda, P., and P.A. Mataga. 1992. Submitted for publication.

Reimanis, I.E., Dalgleish, B.J., and A.G. Evans. 1991. *Acta Metall. Mater.* 39:3133–3141.

Rice, J.R. 1968. *J. Appl. Mech.* 35:379–386.

Rice, J.R. 1988. *J. Appl. Mech.* 55:98–103.

Rice, J.R., Beltz, G.E., and Y. Sun. 1992. *In:* Topics in Fracture and Fatigue. (A.S. Argon, ed.), 1–58, Berlin: Springer-Verlag.

Rice J.R., and M.A. Johnson. 1970. *In:* Inelastic Behavior of Solids. (M.F. Kanninen, W.F. Adler, A.R. Rosenfield, and R.I. Jaffee, eds.), 641–672, New York: McGraw-Hill.

Rice, J.R., and G.C. Sih. 1965. *J. Appl. Mech.* 32:418–423.

Rice, J.R., Suo, Z., and J.S. Wang. 1990. *In:* Metal-Ceramic Interfaces, Acta-Scripta Metallurgica Proceedings Series (M. Rühle, A.G. Evans, M.F. Ashby, and J.P. Hirth, eds.), Vol. 4, 269–294, Oxford: Pergamon Press.

Rice, J.R., and R.M. Thomson. 1974. *Phil. Mag.* 29:73–97.

Rice, J.R., and J.S. Wang. 1989. *Mater. Sci. Eng.* A107:23–40.

Ritchie, R.O., Knott, J.F., and J.R. Rice. 1973. *J. Mech. Phys. Solids.* 21:395–410.

Rivlin, R.S., and A.G. Thomas. 1953. *J. Polym. Sci.* 10:291–318.

Rühle, M., Evans, A.G., Ashby, M.F., and J.P. Hirth (eds.) 1990. Metal-Ceramic Interfaces, Acta-Scripta Metallurgica Proceedings Series, Vol. 4. Oxford: Pergamon Press.

Shih, C.F. 1991. *Mater. Sci. Eng.* A143:77–90.

Shih, C.F., and R.J. Asaro. 1988. *J. Appl. Mech.* 55:299–316.

Shih, C.F., Asaro, R.J., and N.P. O'Dowd. 1991. *J. Appl. Mech.* 58:450–463.

Stump, D.M., and B. Budiansky. 1989. *Acta Metall. Mater.* 37:3297–3304.

Suo, Z. 1990. *Proc. R. Soc. Lond.* A427:331–358.

Suo, Z., Shih, C.F., and A.G. Varias. 1993. A Theory for Cleavage Cracking in the Presence of Plastic Flow. *Acta Metall. Mater.* 41:1551–1557.

Suresh, S., and A. Needleman, eds. 1989. Interfacial Phenomena in Composites: Processing, Characterization and Mechanical Properties. London: Elsevier Applied Science.

Thouless, M.D. 1990. *Acta Metall.* 38:1135–1140.

Tvergaard, V., and J.W. Hutchinson. 1992. *J. Mech. Phys. Solids.* 40:1377–1397.

Varias, A.G., O'Dowd, N.P., Asaro, R.J., and C.F. Shih. 1990. *Mater. Sci. Eng.* A126:65–93.

Varias, A.G., Suo, Z., and C.F. Shih. 1991. *J. Mech. Phys. Solids.* 39:963–986.

Varias, A.G., Suo, Z., and C.F. Shih. 1992. *J. Mech. Phys. Solids.* 40:485–509.

Vekinis, G., Ashby, M.F., and P.W.R. Beaumont. 1990. *Acta Metall. Mater.* 38:1151–1162.

Wang, J.S., and P.M. Anderson. 1991. *Acta Metall. Mater.* 39:779–792.

Wang, J.S., and Suo, Z. 1990. *Acta. Metall. Mater.* 38:1279–1290.

Williams, M.L. 1959. *Bull. Seismol. Soc. Am.* 49:199–204.

Woeltjen, C., Shih, C.F., and S. Suresh. 1993. "Near-Tip Fields for Fatigue Cracks along Metal–Metal and Metal–Ceramic Interfaces." *Acta Metall. Mater.* 41:2317–2335.

Zywicz, E., and D.M. Parks. 1989. *J. Appl. Mech.* 56:577–584.

Zywicz, E., and D.M. Parks. 1992. *J. Mech. Phys. Solids.* 40:511–536.

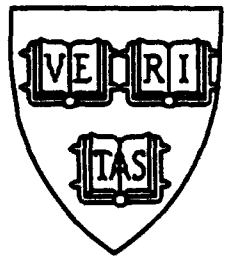

MECH - 213

The Activation Energy for Dislocation Nucleation from a Crack Tip

James R. Rice[1] and Glenn E. Beltz[2]

[1] Division of Applied Sciences and
Department of Earth and Planetary Sciences
Harvard University, Cambridge, *Massachusetts* 02138

[2] Department of Mechanical and Environmental Engineering
University of California, Santa Barbara, CA 93106
(*Affilation to January 1994*: Max-Planck-Institut für Metallforschung,
Institute für Werkstoffwissenschaft, D-70714 Stuttgart, Germany)

May 1993

Published, *Journal of the Mechanics and Physics of Solids*, **Vol. 42**, pp. 333-360, Feb. 1994

THE ACTIVATION ENERGY FOR DISLOCATION NUCLEATION AT A CRACK

James R. Rice[1] and Glenn E. Beltz[2]

[1]Division of Applied Sciences and Department of Earth and Planetary Sciences,
Harvard University, Cambridge, MA 02138

[2]Department of Mechanical and Environmental Engineering,
University of California, Santa Barbara, CA 93106
(*affiliation to January 1994:* Max-Planck-Institut für Metallforschung,
Institut für Werkstoffwissenschaft, D-70174 Stuttgart, Germany)

May 1993

Abstract--The activation energy for dislocation nucleation from a stressed crack tip is calculated within the Peierls framework, in which a periodic shear stress versus displacement relation is assumed to hold on a slip plane emanating from the crack tip. Previous results have revealed that the critical G (energy release rate corresponding to the "screened" crack tip stress field) for dislocation nucleation scales with γ_{us} (the unstable stacking energy), in an analysis which neglects any coupling between tension and shear along the slip plane. That analysis represents instantaneous nucleation and takes thermal effects into account only via the weak temperature dependence of the elastic constants. In this work, the energy required to thermally activate a stable, incipient dislocation into its unstable "saddle-point" configuration is directly calculated for loads less than that critical value. We do so only with the simplest case, for which the slip plane is a prolongation of the crack plane. A first calculation reported is two-dimensional in nature, and hence reveals an activation energy per unit length. A more realistic scheme for thermal activation involves the emission of a dislocation loop, an inherently three-dimensional phenomenon. Asymptotic calculations of the activation energy for loads close to the critical load are performed in 2D and in 3D. It is found that the 3D activation energy generally corresponds to the 2D activation energy per unit length multiplied by about 5 - 10 Burgers vectors (but by as many as 17 very near to the critical loading). Implications for the emission of dislocations in copper, α-iron, and silicon at elevated temperature are discussed. The effects of thermal activation are very significant in lowering the load for emission. Also, the appropriate activation energy to correspond to molecular dynamics simulations of crack tips is discussed. Such simulations, as typically carried out with only a few atomic planes in a periodic repeat direction parallel to the crack tip, are shown to greatly exaggerate the (already large) effects of temperature on dislocation nucleation.

1. INTRODUCTION

We build on recent advances in the modeling of dislocation nucleation at a crack tip based the Peierls-Nabarro concept (Rice, 1992; Beltz and Rice, 1991, 1992; Rice *et al.*, 1992; Beltz, 1992; Sun *et al.*, 1993; Sun, 1993). These have provided a consistent description of the genesis of a dislocation, free of core cut-off parameters of earlier approaches, and have predicted a critical load for emission in various materials. The analyses presented thus far, however, have neglected thermal effects, except perhaps through the weak temperature dependence of the elastic constants which enter the analysis. They thus correspond to instantaneous emission without aid of thermal fluctuations. The purpose of this paper is to extend the Peierls model to calculate the activation energy associated with the nucleation of a dislocation, thereby gaining insights on the effects of elevated temperatures. The basic premise is that, assuming a crack is loaded *below* the critical load for instantaneous emission of a dislocation, a dislocation could nevertheless be emitted if thermal activation supplies enough energy to overcome the predicted activation energy barrier. Realistically, this is a very localized process, involving the unstable emission of a dislocation loop, and hence the problem is inherently three-dimensional. Initially, a 2D activation energy (per unit length off dislocation line) for dislocation nucleation within the Peierls framework is calculated directly and then via an asymptotic analysis (good for loadings near the critical loading for emission). Next the asymptotic analysis is extended to the 3D situation, so as to approximately calculate the activation energy and shape of the activated slip configuration.

Rice and Thomson (1974) regarded the ductile versus brittle behaviour of materials as a competition between dislocation emission at an atomistically sharp crack and cleavage decohesion. In their work, the activation energy was calculated for a crack which had been subjected to the Griffith load for cleavage (i.e., when G, the "applied" energy release rate attained the value $2\gamma_s$, the ideal work of fracture, defined as twice the surface energy). A disadvantage is that their analysis considered a pre-existing, fully-formed dislocation on a slip plane intersecting the crack tip and hence relied on the uncertain core-cutoff parameter r_o from elastic dislocation theory (see Figure 1a); that and other ad-hoc energy cut-offs, especially at the near-atomic length scales involved, provided what are now regarded as very questionable estimates of the activation energy (Argon, 1987). With this limitation in mind, various crystals were classified as ductile or brittle based on the outcome of this calculation. In general, dislocations in fcc metals were found to become unstable when the fully formed dislocation was within one core radius of the crack tip, and since the elastic forces considered in this calculation are ill–defined on the length scales considered,

it was argued that dislocations were spontaneously emitted in these materials. The bcc metals, as well as the covalent and ionic crystals considered were found to have positive activation energies with an activated dislocation loop that was sensibly large. Examples include iron, with an activation energy of 2.2 electron volts (which is small enough for thermal activation to be important, as will be discussed later), and silicon, with an activation energy of 111 electron volts (which is prohibitively high for thermal activation to occur at room temperature), but which is much higher than what is found here.

Through extensions by Mason (1979), Anderson (1986), and Anderson and Rice (1986), the Rice-Thomson model evolved to a state where the competition between dislocation emission and cleavage was evaluated not in terms of an activation energy but rather via the separate calculation of G_{crit}, the energy release rate associated with the emission of a single dislocation and G_{cleave}, the Griffith cleavage energy. The former depends not just on the geometry of the slip system relative to the fracture plane, but also on the ratios of stress intensity factors (modes I, II, and III) to one another. If $G_{crit} < G_{cleave}$, then it is assumed that a dislocation would be spontaneously emitted before decohesion and vice versa. The calculation of the activation energy for dislocation emission has been additionally considered within the Rice-Thomson framework by Li (1981, 1986) who calculated the activation energy as a function of the applied energy release rate, rather than evaluating it at the Griffith cleavage level. Li's result, valid for a mode II load and a slip plane coplanar with the crack plane, gives the the activation energy (per unit dislocation length) to emit an edge dislocation and can be written as

$$\frac{(1-\nu)\,\Delta U_{act}}{\mu b^2} = \frac{-1}{4\pi} \ln\left(\frac{G}{G_{crit}}\right), \tag{1}$$

where μ and ν are the shear modulus and Poisson's ratio, respectively. This result will be seen to overestimate the more exact 2D results calculated here.

Calculations of the activation energy for dislocation emission in silicon have been of interest recently because this material undergoes a relatively sharp ductile-to-brittle transition at a temperature dependent on loading rate, e.g., at approximately 562° C at a strain rate of 1.3×10^{-6} s^{-1} (see experimental work by Samuels and Roberts (1989), Chiao and Clarke (1989), Warren (1989), Michot and George (1986), and references therein). Dislocation motion below the transition is not observed, and the transition temperature increases with strain rate: increasing the strain rate by a factor of 20 increases the transition temperature by about 100 C°. As mentioned before, however, the Rice-Thomson estimate of the activation energy at the fracture stress for Si was 111 electron volts, making thermally activated dislocation nucleation at the transition

temperature impossible. Haasen (1983) has estimated the activation energy in Si at the Griffith load to be as low as 0.5 eV, taking into account the fact that the stacking fault energy in Si is relatively low and hence nucleation of a partial dislocation with Burgers vector $\mathbf{b} = (a/6)[112]$ is favored. Additionally, I.-H. Lin and R. Thomson (private communication, 1992) have carried out a calculation of the activation energy for a rectangular partial dislocation loop in Si and obtain values between 0.5 and 1.0 eV, making thermal activation possible; the difference between these numbers and the one calculated by Rice and Thomson is attributable to the fact that a partial dislocation is considered, and a much different saddle-point configuration was assumed (rectangular versus circular). The aforementioned numbers seem too low to account for the ductile to brittle transition in silicon, especially in light of recent atomic calculations by Duesbery *et al.* (1991) and Kaxiras and Duesbery (1993), which reveal anomalously large values of the unstable stacking energy γ_{us} (= 1.91 J/m^2 for relaxed shear, commonly referred to as $\gamma_{us}^{(r)}$, on the so-called "glide-set" and 1.67 J/m^2 on the "shuffle" set), the parameter which controls dislocation nucleation within the Peierls framework (Rice, 1992) and which will be discussed in further detail below. It has become increasingly evident in recent years that it may be lattice friction against motion of dislocations, not the nucleation event itself, which controls the ductile-to-brittle transition of silicon (Michot and George, 1986; Brede and Haasen, 1988; Chiao and Clarke, 1989; Warren, 1989; Hirsch *et al.*, 1989; Hirsch and Roberts, 1991; Hsia and Argon, 1993). However, the issue remains incompletely resolved. Further discussion of the instantaneous nucleation of dislocations in silicon may be found in recent work by Sun et al. (1993) based on parameters for Peierls modeling of Si from Kaxiras and Duesbery (1993) and Huang *et al.* (1991); additionally, the detailed application of the ideas presented in this paper to the understanding of thermal activation in the brittle-to-ductile transition in silicon is the subject of a follow-up paper (Beltz and Rice, 1993).

The most serious drawback to the Rice-Thomson model is that is treats a fully-formed dislocation on a slip plane intersecting the crack tip, as depicted schematically in Figure 1a The activation energy analysis proceeds by considering a given set of applied loads and then finding stable and unstable configurations which satisfy equations of equilibrium, in terms of r (the radius of the pre-existing loop). As pointed out by Argon (1987), and more recently Schöck (1991), a dislocation is likely to emerge from a crack tip as a Peierls-like shear distribution of atoms across the slip plane, and hence the Burgers shear displacement of the loop, as well as the radius of the loop, should be considered as the activation parameters. A simple argument given by Argon shows that the consequences for the activation energy should be appreciable: the primary scaling factor for the energy analysis (as will become apparent later in this work) is μb^3 (μ is the shear modulus and b is the magnitude of the Burgers vector); hence, if the incipient dislocation

configuration involves slip of less than a full atomic spacing, then the activation energy should be strongly reduced due to the power of *3* (the same argument applies as well to the Haasen (1983) analysis of partial dislocations in silicon). Schöck (1991) has treated the nucleation from a crack tip within the Peierls framework in an approximate fashion for a straight dislocation and a dislocation loop has been similarly treated by Schöck and Püschl (1991). The activation energy analysis in this paper follows procedures within the Peierls framework set out by Rice (1992), and further developed by Beltz and Rice (1991, 1992), Rice et al. (1992), Beltz (1992), Sun et al. (1993), and Sun (1993), in which exact 2D solutions for incipient shear distributions at a crack tip are determined.

2. THE PEIERLS-NABARRO FRAMEWORK FOR NUCLEATION

To review the Peierls, or Peierls-Nabarro, model for dislocation nucleation, suppose that one of the possible slip planes in a crystal intersects a crack tip. Here we assume that the material is an isotropic elastic solid, that the emergent dislocation is of edge character releative to the crack tip, and that there is negligible effect of tensile stress on the shear response along slip planes (analyses that remove all these simplifications are given in the works cited above). If the solid is loaded, an incipient dislocation may begin to form on a slip plane (see Figure 1b); under increasing load the dislocation may become emitted if the load reaches a critical value. Alternatively, cleavage decohesion could occur causing the crack to propagate; this scenario is not addressed in this paper but it is important when evaluating the ductile versus brittle behaviour of materials. The shear stress τ on the potentially active slip plane is taken to be a periodic function of δ ($\equiv \delta_r = \delta_x$ for the mode II case to be discussed), the shear displacement discontinuity across the plane. Once $\tau = \tau(\delta)$ is known, the shear displacement profiles $\delta = \delta(x)$ (x is the distance from the crack tip) as a function of the applied stress intensity factors can be determined via the solution of an integral equation to be introduced below. In the simplest case, when the slip plane is taken to be coplanar with the crack plane, Rice (1992) showed that an incipient edge dislocation becomes unstable when G, the "applied" Griffith energy release rate associated with the mode II component of loading, given by $G = (1-\nu)(K_{II})^2/2\mu$, attains the value of the unstable stacking energy, corresponding to the first maximum undergone by the energy per unit area of the slip plane, $\Phi = \Phi(\delta) = \int \tau(\delta)d\delta$. Emission criteria for the case when the slip plane is inclined at some angle θ may be extracted from the same type of integral equation solution, assuming that a suitable function $\tau(\delta)$ is known, chosen to at least approximately include the effects of tension normal to the slip plane (Rice *et al.*, 1992; Beltz and Rice, 1992; Sun *et al.*, 1993).

The shear stress τ on a slip plane is typically expressed as a function of Δ, the relative atomic displacement undergone by atoms on opposite sides of the cut, which differs from δ due to an elastic shear strain τ/μ acting over a distance h normal to the cut, where h is the interplanar spacing. The simplest modeling assumes that the function $\tau(\delta)$ is given parametrically by the relations (Rice, 1992)

$$\tau = (\pi\gamma_{us}/b)\sin(2\pi\Delta/b), \tag{2}$$

with

$$\delta = \Delta - (b/2\pi)\sin(2\pi\Delta/b). \tag{3}$$

An extensive literature exists (see Rice *et al.* (1992), Sun et al. (1993), and references therein) concerning more realistic forms for τ versus δ, most of which include a coupling effect due to tensile stresses normal to the slip plane. Equation (2) is commonly associated with the Frenkel model, in which the initial slope of τ versus Δ is identified with the shear modulus, giving

$$\gamma_{us} = \mu b^2/2\pi^2 h, \tag{4}$$

thus within the model γ_{us} is fully determined by μ, b, and h.

Results from atomic calculations (Rice *et al.*, 1992; Sun *et al.*, 1993) suggest that Equation (4) overestimates the unstable stacking energy for a wide range of materials, or underestimates it, in the case of silicon. In this analysis it is convenient to note that until now the parameter h appears *only* in Equation (4); hence it may be regarded not as the true interplanar spacing but rather as a fitting parameter which allows μ and γ_{us} to be independently specified for a given material. To be more specific, if h is literally interpreted as the interplanar spacing, $h/b = \sqrt{2}$ for a Shockley partial in the fcc lattice, $\sqrt{2}/4$ for a Shockley "glide" partial in the diamond cubic lattice, and $\sqrt{2/3}$ for a full dislocation (<111> type slip direction) in the bcc lattice, thus the Frenkel model rigorously states that for the three lattices, γ_{us} should be $0.036\mu b$, $0.143\mu b$, and $0.062\mu b$, respectively. If, however, it is known that γ_{us} differs from the Frenkel prediction, for example in the glide planes of silicon, where the atomic calculation referenced earlier gives $\gamma_{us}^{(r)} = 0.142\mu b$, an "effective" value of h/b, determined from Equation (4), would then be $1/(0.142)2\pi^2 \approx 0.357$ (versus the actual value of 0.354). It is interesting to note that the Frenkel theory overestimates $\gamma_{us}^{(r)}$ in silicon by only about 1%.

The energy per unit area quantities $\Psi(\Delta)$ and $\Phi(\delta)$ are defined such that $\tau d\Delta = d\Psi$ and $\tau d\delta = d\Phi$. Combining with Equation (3) reveals that $\Phi(\delta) = \Psi(\Delta) - h\tau^2(\Delta)/2\mu$, and integrating the same equation gives

$$\Psi = \gamma_{us} \sin^2(\pi\Delta/b), \tag{5a}$$

$$\Phi = \gamma_{us} \sin^4(\pi\Delta/b). \tag{5b}$$

The latter is expressed in terms of δ by Equation (3). Figure 2 shows plots of $\Phi(\delta)$ as well as $\tau(\delta)$. Assuming that the slip plane is coplanar with the crack plane and there is mode II loading, Rice (1992) showed that the slip at the crack tip, δ_{tip} [= $\delta(x)$ at x = 0] is given by

$$G = \Phi(\delta_{tip}) \equiv \int_0^{\delta_{tip}} \tau d\delta, \tag{6}$$

in any solution which renders stationary the energy functional U, the total potential energy of a slipped configuration per unit distance along the crack front. When δ_{tip} lies along the branch of the curve labelled A in Figure 2, the instability state is one of locally minimum energy and corresponds to a stable configuration of an incipient edge dislocation. When G reaches γ_{us}, an instability occurs, and the dislocation is emitted. Note that for a given G less than G_{crit} ($G_{crit} = \gamma_{us}$ in this simplified case of coincident crack and slip plane under mode II loading), additional solutions exist. Points A', A'', etc. correspond to stable incipient dislocations after one, two, etc. dislocations have been emitted from the crack tip. When δ_{tip} lies along the portion labelled C, the stationary state represents a *saddle-point* configuration -- the slip distribution corresponding to C is unstable due to the fact that the equilibrating load decreases as the distribution expands outward. For a given applied energy release rate $G < G_{crit}$ ($= \gamma_{us}$) the activation energy is defined as

$$\Delta U_{act} = U[\delta_{sad}(x)] - U[\delta_{min}(x)], \tag{7}$$

where $\delta_{sad}(x)$ denotes the solution for $\delta(x)$ having $\delta(0)$ [= δ_{tip}] on branch C and $\delta_{min}(x)$ is the solution on branch A. As mentioned earlier, the saddle configuration is first analyzed by constraining the field to be two-dimensional, so that ΔU_{act} is an energy per unit length.

3. DIRECT CALCULATION OF THE 2D ACTIVATION ENERGY PER UNIT LENGTH ΔU_{act}

The functional U giving energy of a 2D field per unit length along a crack front may be written for a linear elastic solid under a mode II load as (Rice, 1992)

$$U[\delta(x)] = U_0 + \int_0^\infty \Phi\,[\delta(x)]\,dx + \frac{1}{2}\int_0^\infty s[\delta(x)]\,\delta(x)\,dx - \int_0^\infty \frac{K_{II}}{\sqrt{2\pi x}}\,\delta(x)\,dx, \tag{8}$$

with

$$s[\delta(x)] = \frac{\mu}{2\pi(1-\nu)} \int_0^\infty \sqrt{\frac{\xi}{x}} \frac{d\delta(\xi)/d\xi}{x-\xi} d\xi . \qquad (9)$$

The first term in Equation (8), U_o, denotes the energy of the unslipped solid, i.e., the energy of the loaded solid when $\delta(x)$ is constrained to zero. The second term is the energy gained on the slip plane when $\delta(x)$ develops, and the remainder of the terms account for the energy change of the material outside the slip plane and of the loading system due to the introduction of $\delta(x)$. The functional $s[\delta(x)]$ gives the amount by which the shear stress τ decreases upon introduction of the slip, with its "kernel" function $[\mu / 2\pi(1-\nu)]\sqrt{\xi/x} / (x-\xi)$ identified as the shear stress at distance x due to a unit edge dislocation located at position ξ [see, e.g., Thomson (1986) or Beltz (1992)]. Rendering Equation (8) stationary with respect to $\delta(x)$ yields the integral equation

$$\tau[\delta(x)] \equiv \Phi'[\delta(x)] = \frac{K_{II}}{\sqrt{2\pi x}} - s[\delta(x)] , \qquad (10)$$

which corresponds to enforcing stress equilibrium along the slip plane. Stable, or minimum energy, solutions $\delta_{min}(x)$ of Equation (10) have been determined numerically by Beltz and Rice (1991, 1992) and Beltz (1992) in connection with the dislocation emission problem (i.e, in the range where G and δ_{tip} lie on branch A of the energy curve in Figure 2). Solutions are shown as solid lines for $\gamma_{us} = \mu b / 2\pi^2$ and $\nu = 0.3$ in Figure 3a at various load levels up to instability. In order to determine the saddle-point solutions, a *second* solution of Equation (10) must be determined for each level of applied load. These solutions are found via the method used to determine the stable solutions, except that initial guesses of $\delta(x)$ are used that are *greater* than the solution corresponding to $G = G_{crit}$, and which have a δ_{tip} given by the larger solution of Equation (6). These solutions are shown as dashed lines in Figure 3a for the same values of G as were used to determine the stable solutions, shown as solid lines. For more general conditions than assumed here (e.g., slip plane inclined with respect to crack plane, screw and edge components of emergent dislocation, tension-shear coupling, and mixed-mode loading, all as dealt with in references cited above) G_{crit} should be interpreted as the maximum G for which a stable solution can be determined. Thus, while $G_{crit} = \gamma_{us}$ in the specific case analyzed here we shall generally phrase reults in terms of the ratio G/G_{crit}, supposing them to be at least approximately valid in those more general situations.

Inserting Equation (8) into Equation (7) and simplifying with the help of Equation (10) gives the following expression for the 2D activation energy, which can be simply evaluated numerically for a given pair $\delta_{min}(x)$, and $\delta_{sad}(x)$:

$$\Delta U_{act}^{2D} = \int_0^\infty \left\{ \hat{\Phi}[\delta_{sad}(x)] - \hat{\Phi}[\delta_{min}(x)] \right\} dx - \frac{1}{2} K_{II} \int_0^\infty \frac{\delta_{sad}(x) - \delta_{min}(x)}{\sqrt{2\pi x}} dx, \qquad (11)$$

where $\hat{\Phi}(\delta) \equiv \Phi(\delta) - \delta\Phi'(\delta)/2$. Evaluation of Equation (11) is carried out for $\gamma_{us} = \mu b / 2\pi^2$ and $\nu = 0.3$. As will be discussed later, the calculation is extremely insensitive to these values, however. In Figure 4, the results are plotted as a function of applied load as a solid line. Table 1 shows the results for specific G values. The first column gives ΔU_{act}^{2D} (an energy per unit dislocation length). The entry in each of the remaining columns gives an estimate of the 3D activation energy ΔE obtained by writing $\Delta E = 7.5\ b\ \Delta U_{act}^{2D}$ (i.e., assuming an activated dislocation length of 7.5b), for a Shockley partial dislocation in copper, a full dislocation in iron, and a partial dislocation in silicon. The ΔE estimated are listed in units of kT as evaluated at room temperature; implications for thermally activated nucleation are discussed later in this paper.

4. ASYMPTOTIC CALCULATION OF THE 2D ACTIVATION ENERGY

In order to more simply evaluate the 2D activation energy near critical loading, and to provide a basis for the 3D analysis to come, we present here an asymptotic calculation of the activation energy per unit length, good for small deviations of the applied load from the critical load for emission. The method proceeds via a perturbation analysis of the shear distribution. It is useful to regard a given shear profile, satisfying Equation (10), as being a function of x *and* of δ_{tip}, i.e., $\delta = \delta(x; \delta_{tip})$. Note that a pair of δ_{tip} values corresponds to a given G (less than G_{crit}) by Equation (6), and Figure 2, so one $\delta(x; \delta_{tip})$ is $\delta_{min}(x)$ and the other is $\delta_{sad}(x)$. Suppose $\delta = f(x)$ is the shear profile at instability ($G = G_{crit}$); in the case of a mode II shear crack with the Frenkel form, $f(x) = \delta(x; b/2)$, which corresponds to the last solid line in Figure 3a. If the applied energy release rate G is slightly less than G_{crit}, the shear distribution may be written as

$$\delta(x) = f(x) + \varepsilon g(x), \qquad (12)$$

where $\varepsilon = \delta_{tip} - b/2$ characterizes the extent of the perturbation and $g(x)$ is defined by

$$g(x) \equiv \left[\frac{\partial \delta(x; \delta_{tip})}{\partial \delta_{tip}} \right]_{\delta_{tip} = b/2} \qquad (13)$$

Note that ε has units of length and $g(x)$ is dimensionless. A relation satisfied by the function $g(x)$ may be determined by differentiating Equation (10) with respect to δ_{tip} and evaluating for

The incipient profile $\{\delta_\alpha(s)\}$ is, as before, modeled here as a continuous distribution of an individual dislocation at location s of an infinitesimal Burgers vector $\left[-\frac{d\delta_\alpha(s)}{ds}\,ds\right]$, which in turn will exert stresses $\sigma_{\theta\alpha}(r) = g_{\alpha\beta}(r, s; \theta)\left[-\frac{d\delta_\beta(s)}{ds}\,ds\right]$ on a point r along the slip plane via the linear elastic medium. Therefore, the Green's functions $g_{\alpha\beta}(r, s; \theta)$ so defined can be obtained by solutions of a line dislocation with the crack tip in the anisotropic linear elastic medium. Some details are presented in the Appendix. The force balance at a point r along the slip plane gives the equations of equilibrium:

$$\sigma_{\theta\alpha}[\delta(r)] = \sigma^0_{\theta\alpha}(r) + \int_0^\infty g_{\alpha\beta}(r, s, \theta)\left[-\frac{d\delta_\beta(s)}{ds}\,ds\right], \tag{34}$$

where, $\{\alpha, \beta = (r, \theta, z)$, but also denoted as $(1, 2, 3)\}$, the same as the convention used in previous section, and $\sigma^0_{\theta\alpha}(r)$, the unrelaxed stress from the crack loading K_α, are given as $\sigma^0_{\theta\alpha}(r) = F_{\alpha\beta}(\theta)\, K_\beta / \sqrt{2\pi r}$, as before. The summations over repeated indices are also used here.

The term $\sigma_{\theta\alpha}[\delta_\gamma(r)]$ is the lattice restoring shear and tension stresses against the displacement discontinuities across the slip plane at point r, with which a potential $\Phi[\delta_\alpha(r)]$ is associated, such that

$$\sigma_{\theta\alpha}[\delta(r)] = \frac{\partial\Phi[\delta(r)]}{\partial\delta_\alpha(r)}, \tag{35}$$

Equations (34) and (35) constitute a complete set of equations, which can be solved jointly.

We inquire about properties of the Green's functions $g_{\alpha\beta}(r, s; \theta)$. It can be shown that

$$g_{\alpha\beta}(r, s; \theta) = \frac{1}{4\pi}\sqrt{\frac{s}{r}}\,\frac{[\Lambda^{(\theta)-1}_{\alpha\beta} + h_{\alpha\beta}(r/s, \theta)]}{r - s}, \tag{36}$$

where the following properties of the function $h_{\alpha\beta}(t, \theta)$ are of interest: First,

$$h_{\alpha\beta}(1, \theta) = 0. \tag{37}$$

in order to have proper stress fields in the linear elastic medium near the dislocation point s. Furthermore, the Rice-Thomson image force theorem for a dislocation line at a crack tip implies that

$$\partial h_{\alpha\beta}(t = 1, \theta)/\partial t \text{ is antisymmetrical for indices } \alpha \text{ and } \beta, \text{ i.e.,} \tag{38}$$

$$\partial h_{rr}(t = 1, \theta)/\partial t = 0,$$
$$\partial h_{\theta\theta}(t = 1, \theta)/\partial t = 0,$$
$$\partial h_{zz}(t = 1, \theta)/\partial t = 0,$$
$$\partial h_{r\theta}(t = 1, \theta)/\partial t + \partial h_{\theta r}(t = 1, \theta)/\partial t = 0,$$
$$\partial h_{rz}(t = 1, \theta)/\partial t + \partial h_{zr}(t = 1, \theta)/\partial t = 0,$$
$$\partial h_{\theta z}(t = 1, \theta)/\partial t + \partial h_{\theta z}(t = 1, \theta)/\partial t = 0.$$

These two conditions by Eq. (37) and (38) are trivially satisfied for $\theta = 0$, that is, $h_{\alpha\beta}(r/s, 0) = 0$. Proof of the two theorems about the stress functions $g_{\alpha\beta}(r, s; \theta)$ is presented in the Appendix.

We also apply the constrained slip path approximation here. Let the slip be constrained to be along the direction s (the same as b) that makes an angle ϕ with the r axis in the slip plane, $\delta_\alpha(r) = [\delta_s(r)\cos\phi, \delta_\theta(r), \delta_s(r)\sin\phi]$ and the stress $\tau = \sigma_{\theta r}\cos\phi + \sigma_{\theta z}\sin\phi$ and $\sigma = \sigma_{\theta\theta}$. As before, we seek the condition under which the profile becomes unstable, after which a dislocation line of a finite edge component emerges and moves away from the crack tip until being stopped by the lattice resistance, the Peierls stress σ_p, or by interactions with distant dislocations, etc. We

obtain the following equations,

$$\tau[\delta_s(r), \delta_\theta(r)] = \frac{K_\tau^{eff}}{\sqrt{2\pi r}} - \int_0^\infty \bar{g}_{11}(r,s;\theta,\phi)\frac{d\delta_s(s)}{ds}ds - \int_0^\infty \bar{g}_{12}(r,s;\theta,\phi)\frac{d\delta_\theta(s)}{ds}ds, \tag{39}$$

$$\sigma[\delta_s(r), \delta_\theta(r)] = \frac{K_\sigma^{eff}}{\sqrt{2\pi r}} - \int_0^\infty \bar{g}_{21}(r,s;\theta,\phi)\frac{d\delta_s(s)}{ds}ds - \int_0^\infty \bar{g}_{22}(r,s;\theta,\phi)\frac{d\delta_\theta(s)}{ds}ds, \tag{40}$$

where $K_\tau^{eff} = \sqrt{2\pi r}\,[\cos\phi\,\sigma_{\theta r}^0(r,\theta) + \sin\phi\,\sigma_{\theta z}^0(r,\theta)] = s_\alpha(\phi)\,F_{\alpha\beta}(\theta)\,K_\beta$, and $K_\sigma^{eff} = \sqrt{2\pi r}\,\sigma_{\theta\theta}^0(r,\theta) = F_{2\beta}(\theta)\,K_\beta$. These are defined for the singular stresses $\sigma_{\theta r}^0$, $\sigma_{\theta z}^0$ and $\sigma_{\theta\theta}^0$ at the crack tip under external loading before the emergence of the incipient profile. The $\bar{g}_{11}$, $\bar{g}_{12}$, $\bar{g}_{21}$ and $\bar{g}_{22}$ are the stress functions of a straight dislocation at a crack tip: $\bar{g}_{11}(r, s; \theta) = s_\alpha(\phi)\,g_{\alpha\beta}(r, s; \theta)\,s_\beta(\phi)$, $\bar{g}_{12}(r, s; \theta) = s_\alpha(\phi)\,g_{\alpha 2}(r, s; \theta)$, $\bar{g}_{21}(r, s; \theta) = g_{2\alpha}(r, s; \theta)\,s_\alpha(\phi)$ and $\bar{g}_{22}(r, s; \theta) = g_{22}(r, s; \theta)$. All of these terms and functions can be obtained from the singular field of a loaded crack tip and solution of a dislocation near a crack tip using the anisotropic elasticity formulation; see e.g., Atkinson (1966), Asaro (1975), and Suo (1989).

The terms $\tau[\delta_s(r), \delta_\theta(r)]$ and $\sigma[\delta_s(r), \delta_\theta(r)]$ are lattice restoring shear and tension stresses against the displacement discontinuities across the slip plane; a potential $\Phi[\delta_s(r), \delta_\theta(r)]$ is assumed to exist, such that

$$\tau[\delta_s(r), \delta_\theta(r)] = \frac{\partial\Phi[\delta_s(r), \delta_\theta(r)]}{\partial\delta_s(r)}, \tag{41}$$

$$\sigma[\delta_s(r), \delta_\theta(r)] = \frac{\partial\Phi[\delta_s(r), \delta_\theta(r)]}{\partial\delta_\theta(r)}. \tag{42}$$

Modeling of the constitutive law $\Phi[\delta_s(r), \delta_\theta(r)]$ from embedded atom method results for Ni, Al, and Ni_3Al and Fe, from sources noted above, and from density functional studies of Si by Kaxiras and Duesbery (1993), Duesbery et al. (1990) and Huang et al. (1991) and Huang (1992) has been provided in Sun, Beltz and Rice (1993) and Rice, Beltz and Sun (1992), and Sun (1993). The same potential from such atomic models is used here. The analytical representations of the stresses and the potentials can be found in Beltz and Rice (1991), Rice, Beltz and Sun (1992) and Sun, Beltz and Rice (1993). Equations (39), (40), (41), and (42) constitute a complete set of equations, which can be solved jointly to determine the critical loading and corresponding incipient configuration, see references cited in the previous sentence. The solutions are obtainable by numerical methods, by use of Newton-Raphson method and Chebyshev polynomials of the second kind [for reference see, e.g., Erdogan (1975) and Erdogan and Gupta (1972)].

2. The shear-only model

In the shear-only model, where only the slip displacements and shear stress are considered, there exists a simpler set of equations,

$$\tau[\delta_s(r)] = \frac{K_\tau^{eff}}{\sqrt{2\pi r}} - \int_0^\infty \bar{g}_{11}(r,s;\theta,\phi)\frac{d\delta_s(s)}{ds}ds. \tag{43}$$

Equation (43) is accompanied by a sinusoidal law

$$\tau(\Delta_s) = (\pi \gamma_{us} / b) \sin (2\pi\Delta_s / b) , \quad (44)$$

where Δ_s is the relative atomic sliding displacement between the two adjacent slipping atomic layers, which is related to δ_s, the displacement discontinuity across the slip plane by

$$\delta_s = \Delta_s - (b / 2\pi) \sin (2\pi\Delta_s / b) . \quad (45)$$

V EXACT RESULTS AND CONCLUSIONS

1. The significance of anisotropic elasticity

While the conceptual framework is established by the isotropic elasticity formulation [Rice, 1992; Rice, Beltz and Sun, 1992; Sun, Beltz and Rice, 1993], the importance of the anisotropic formulation is illustrated as follows.

The anisotropic effect is surveyed initially in three parts. It appears in the angular dependence of the singular shear stress $\sigma^0_{\theta r}$ (r, θ) near a crack tip under pure tensile loading, i.e., $F_{12}(\theta)$ in previous notation. In isotropic elasticity, $F_{12}(\theta) = \cos^2 (\theta/2) \sin (\theta/2)$, corresponding to the dashed curves in Fig. 4, 5, 6 and 7 for reference. Let us choose a crack growing in [010], with crack front along [100] and crack planes on (001) planes, labeled Crack A. Figures 4 and 5 show the comparison and contrast of anisotropy with isotropy. We see that the anisotropy results have significantly different shapes from the isotropic ones, more so in bcc than fcc. Also, Figs. 6 and 7 show results for EAM Fe crack orientations, Crack B, with $[\bar{1}10]$-[001]-[111], and Crack C [011]-$[0\bar{1}1]$-[100], where the first vector is the crack direction, the second is the crack plane normal and the third is the crack front.

Figure 8 shows that the function $\bar{g}_{11}(r, s, \theta)$ b, which contributes to the expression for $\sigma_{\theta r}$ (r), and is the key function in the shear-only model, in the anisotropic EAM Fe, in Crack A; the slip plane is tilted so that $\theta = 45^\circ$. The figure shows the Cauchy singularity (1/x) as implied by Eq. (36). It is seen that a similar shape of the function results for anisotropy and isotropy formulations, though their numerical values are not identical, as anticipated.

Finally, the critical loading G_d as determined in the shear-only model is shown in Fig. 9 as a function of inclination angle θ of the slip plane, in anisotropic and isotropic formulations for EAM Fe in Crack A under pure mode I loading and of pure edge character. The anisotropic effect is numerically significant; it differs from the curve obtained in isotropic elasticity, which can overestimate or underestimate the anisotropic results, depending on θ.

2. A survey of anisotropic effects on critical loadings

Consider the case such that the slip is in a plane coplanar with crack planes, and has only edge components. The critical loading G_d for dislocation emission is equal to γ_{us} in the shear-only model, as aforementioned. The tension effect on dislocation emission in Model A, using anisotropic elasticity with EAM Fe, is analyzed by varying the amount of tensile loading with respect to shear loading, $\psi = \arctan (K_{II}/K_I)$. Fig. 10 shows the results. The critical $G_d(\psi)$ in the isotropic formulation, taken from Fig. 3.2(b) of Sun, Beltz and Rice (1993), accompanies those in the anisotropic formulation. It shows that by the proper treatment of anisotropic effects, the two formulations render almost the same results in the tension-shear coupling model. That seems more general than the following case: It was shown in Section III, in the case of orthotropic crack and coplanar crack and slip planes, both formulations would predict the same G value for edge dislocation emission in the shear-only model. As in Sun, Beltz and Rice (1993) with the isotropic elasticity, the combined tension-shear model is fitted by the modified shear-only model, which

uses the tension reduced $\gamma_{us}(\psi)$, namely,

$$G_d(\psi) = \gamma_{us}(\psi) / \sin^2 \psi. \tag{46}$$

where $\gamma_{us}(\psi) = \gamma_{us}^{(r)} - \alpha\,[\gamma_{us}^{(u)} - \gamma_{us}^{(r)}]\,(\pi/2 - \psi)$ for tension reduction. The modified shear-only model gives a good description. The same α coefficient applies to both anisotropic and isotropic results. For EAM Fe, α is 0.841.

For further illustration of anisotropic effects, imagine a tilted slip plane making an inclination angle θ with the crack plane. The crack is loaded in pure mode I. We present results for crack orientations A, B and C in bcc EAM-Fe. Here the angle θ ranges from 40° to 120° and angle ϕ = 0°. Of course, these (θ, ϕ) angles may not be the actual inclination and screw/edge mixing angles for a slip system in the crack orientation model A, B and C; we merely intend to show the dependence of the critical loading G_d upon anisotropic medium effects. The critical loading as a function of inclination angle θ, expressed as G_d as determined in the combined tension-shear model (labeled σ–τ), shear-only model (labeled τ) and effective shear intensity factor model in the anisotropic elasticity formulation for model A is shown in Fig. 11, Crack B in Fig. 12 and C in Fig. 13. The effective stress approximation gives a good description of the general shape, although it overestimates the loading by about 20%, compared to the numerical results of the shear-only model. The combined tension and shear model further reduces the loading by 10 to 15%.

3. The recipe for a rough estimate

From the above discussions, we have a procedure for calibrating the effective stress intensity factor method on the basis of exact numerical solutions to account for tension-shear coupling. Let the critical stress intensity factor K_d as estimated from the effective method, be multiplied by a factor η so as to equal the shear-only K_d. The η factor ranges from 0.86 to 0.95. The tension-shear coupling is handled by the tension reduced $\gamma_{us}(\psi)$ value, which was treated in Sun, Beltz and Rice (1993), though in isotropic formulations. We showed that this tension-reduced unstable stacking energy is valid for EAM Ni, Al, Fe and Ni_3Al, but less well for DFT/LDA Si. We expect that it will work equally well in the anisotropic formulation.

We can summarize individually for each common crack orientation and the easiest slip system (i.e., θ, ϕ angles) that are listed in Table 1. The critical loading for dislocation emission under mode I loading is summarized in Table 2, as determined by the three methods. The critical condition under pure mode I loading, was determined via the numerical procedure, in the shear-only model and the effective model. By comparing the two solutions for the same situation, we can obtain the η coefficient for each orientation, and slip system (i.e., θ, ϕ angles). Here we assume that the coefficient η is unique for each set of θ and ϕ angles, which approximately holds true for every material. The tension-shear coupling would, as we expect, reduce the loading at the critical condition, the results are also presented in Table 2. As for the tension-shear coupling, we use the ideas presented in Sun, Beltz and Rice (1993) developed from the isotropic elasticity formulation. The tension reduced γ_{us} according to the phase angle ψ is

$$\gamma_{us}(\psi) = \gamma_{us}^{(r)} - \alpha\,[\gamma_{us}^{(u)} - \gamma_{us}^{(r)}]\,(\pi/2 - \psi)\,, \tag{47}$$

where the phase angle is for the effective shear versus tensile stress intensity

$$\psi = \arctan\,(K_\tau / K_\sigma)\,. \tag{48}$$

The coefficient α is from Sun, Beltz and Rice (1993) for tension-shear coupling. It is different for each EAM material and slip system. In particular, α has the values 1.323, 1.145, 0.969 and 0.841 for the Ni, Al, Ni_3Al and Fe as modeled by EAM, respectively. For DFT/LDA Si, the α for the glide set, is determined to be 7.249. For the shuffle set, it is interesting to note that p is negative.

The α for the shuffle set is determined to be –2.234; note that the α coefficient is negative since p is. As for EAM Fe, on the twinning slip system (1/2) [111] ($\bar{2}11$), we simply take it as obtained for the usual slip system 1/2) [111] ($0\bar{1}1$), i.e., 0.841. Such estimates give good results, within a few percent for G under pure mode I.

We accordingly give the procedure for a rudimentary estimate of the critical loading for dislocation emission from a crack tip:

(A) Find the effective stress intensity factor for r-θ-z coordinates via a tensor transformation, so as to find the K_τ and K_σ under general loading (K_I, K_{II}, K_{III}), and then the phase angle ψ.

(B) Find the tension reduced γ_{us} (ψ) according to Eq. (47).

(C) Apply the calibrated equation for the critical condition, use the appropriate η coefficient.

$$K_\tau = \eta \sqrt{\gamma_{us}\, p(\theta,\phi)} \cdot \tag{49}$$

This procedure gives an estimated error within the range ± 7% in G_d when applied to typical cases.

As can be seen in Table 2, the parameter η is of about the same value in different materials for each crack orientation and (θ, ϕ) angle. For example, regarding emission of the first Shockley partial in Crack D (54.7°, 60°), the η is about 0.954; in Crack E (54.7°, 60°), 0.968 for II-Ni, III-Ni, Al, Ni_3Al and Si (glide set).

4. Conclusion and summary

The meaning of the critical loading for dislocation emission from a crack tip given in Table 2 can be elucidated by comparing with available atomistic simulations of loaded crack tips of EAM Fe [Cheung et al., 1990] and EAM Al [Hoagland et al., 1990]. It is also useful to compare to the Griffith cleavage for crack extension when $G_c = 2\gamma_s$, so as to predict the intrinsic ductile versus brittle response.

The critical loading for each crack orientation and material listed in Table 2 is compared with those based on the isotropic formulations in Table 4 of Sun, Beltz and Rice (1993).

For Crack A in EAM Fe, for which the usual slip system consists of $\theta = 45°$ and $\phi = 35.3°$, the anisotropic G is 2.4 times the isotropic one in the shear-only model; in the combined tension-shear model, even the instability is different in that the anisotropic model gives crack branching while the isotropic mode gives dislocation emission. The two G's are similar, though. For crack B, the combined tension-shear G's for dislocation emission in the anisotropic formulation are 40 % less than the isotropic equivalent; For Crack C, the anisotropic G is 2.4 times the isotropic G. Therefore, the anisotropic formulation is essential for α-Fe.

For fcc materials, the G's in the two formulations are about 10% to 25% different, including both the shear-only and tension-shear coupled model. To illustrate that the anisotropic formulation can matter even for the smaller differences, we present detailed results for Ni_3Al in two crack orientations under mode I loading.

The mechanics problem of dislocation nucleation at a crack tip based on Peierls concept is set up in the anisotropic formulation with $C_{11} = 2.516 \times 10^{11}$ Pa, $C_{12} = 1.370 \times 10^{11}$ Pa and $C_{44} = 1.262 \times 10^{11}$ Pa, which are the fitted elastic moduli via the EAM functions. The corresponding problem in the isotropic formulation is set up with the Voigt averaged elastic moduli of the three elastic constants, $\mu = (C_{11} - C_{12} + 3\,C_{44}) / 5 = 0.9864 \times 10^{11}$ Pa, $\lambda = (C_{11} + 4\,C_{12} - 2\,C_{44}) / 5 = 1.094 \times 10^{11}$ Pa, and the corresponding Poisson ratio ν is 0.263. The results of the two types of formulation will be compared.

On the other hand, for crack extension under pure mode I, the critical loading can be determined by the Griffith condition, i.e., $G_c = \gamma_{s1} + \gamma_{s2}$, for cleaving the perfect crystal plane,

where γ_{s1} and γ_{s2} are the surface energies of the two cleaved surfaces; expressed in terms of the crack extension force, the cleavage condition is the same for both anisotropic and isotropic elasticity.

We treat two crack orientations, D and E, in Ni_3Al. For crack tip orientation D with (001) crack plane, growing along $[\bar{1}10]$, with a [110] front, the slip plane is $(1\bar{1}1)$, and therefore the inclination angle $\theta = 54.7°$. The first Shockley partial that is emitted would correspond to $\phi = 60°$. In the shear-only model, the solution of the critical condition in the anisotropic formulation and with the sinusoidal law gives the $G_d / \gamma_{us} = 28.43$. Using the isotropic formulation, the shear-only model gives $G_d / \gamma_{us} = 22.79$. Here, the isotropic approximation gives a 19.9 % discrepancy. G_c for crack orientation D equals 3.51 J/m^2, while G_d is, using the relaxed value of 0.315 J/m^2 for γ_{us}, equal to 8.96 J/m^2 under the anisotropic treatment. Because G_d is much larger than G_c, the (001) cracks are brittle. The isotropic treatment gives G_d equal to 7.18 J/m^2, and thus predicts that the (001) cracks are brittle.

In the tension-shear coupled model, the critical condition for dislocation emission from Crack D in the anisotropic formulation is that $G_d = 5.59$ J/m^2 with the tension-shear coupled law for the first Shockley partial slip as determined in Sun, Beltz and Rice (1993) for Ni_3Al. Hence, Crack D is predicted to be brittle for emission of the first Shockley partial. In the isotropic formulation, G_d = 5.77 J/m^2, which is greater than G_c . Hence, the isotropic formulation gives a 3.2 % discrepancy from the anisotropic, and also predicts that {001} cracks growing along <110> are in a brittle crack orientation. The G_d values cited are close enough to G_c that thermal activation would be an important factor, allowing nucleation when $G_d \approx G_c$.

Crack tip orientation E, with a $(\bar{1}10)$ crack plane, growing along [001], with a [110] front, is associated with the slip plane is $(1\bar{1}1)$ slip plane and so the inclination angle θ is 35.3°. The first Shockley partial that is emitted would correspond to $\phi = 0°$ here. In the shear-only model, anisotropic formulation, the solution of the critical condition gives the $G_d / \gamma_{us} = 10.39$, so G_d is 3.27 J/m^2. For crack E to extend, G_c is 3.65 J/m^2. Because G_d is lower than G_c, the {110} cracks growing along <001> are ductile. However, using the isotropic formulation, G_d / γ_{us} = 12.21, which means that G_d is 3.85 J/m^2 and is greater than G_c for cleavage. Here, the isotropic formulation not only gives a 17.5 % discrepancy to the anisotropic but also predicts that Crack E is brittle, which is contrary to the anisotropic prediction.

To differentiate the similar critical loading conditions for dislocation emission and cleavage in this case, the results as treated in the tension-shear coupled model are also presented. In the anisotropic formulation, $G_d = 2.60$ J/m^2 with the tension-shear coupled law for the first Shockley partial slip; hence, Crack E is predicted to be ductile for emission of the first Shockley partial. The isotropic formulation gives $G_d = 3.025$ J/m^2, which is less than G_c . Here, the isotropic formulation gives a 16.3 % discrepancy, and also predicts that {110} cracks growing along <001> are ductile.

As we might expect to be the general trend, the bcc structure is more anisotropic than the fcc structure (including Ni, Al, Ni_3Al and Si). The difference in the critical G for bcc materials between isotropic and anisotropic formulations is larger than in fcc materials. Such differences should correlate with the anisotropic factors of these materials, $2\,C_{44} / (C_{11} - C_{12})$, which are 7.00 for Fe, 3.24, 3.01 and 2.20 for Ni, Al and Ni_3Al, and, 1.56 for Si (the smallest).

In the tension-shear model, the two formulations may present different instability modes of either dislocation nucleation or crack branching, as described above for α-Fe and Ni_3Al. The

anisotropic G's may be less or greater than the isotropic correspondents. For EAM α-Fe, the anisotropic formulation results are 2.4 times the isotropic ones in Crack C, similarly in the effective approximation model, the shear-only and tension-shear coupled model; in Crack A, the anisotropic formulation values are again 2.4 times the isotropic ones in the effective approximate model and shear-only model. But in Crack B, the anisotropic formulation results are 40 % less than the isotropic ones, similarly in the effective approximation model, the shear-only and tension-shear coupled model and tension-shear coupled model. In the fcc lattices, Ni, Al and Ni_3Al, we conclude that the two formulations give results with a difference in the range of 10 to 25%. For DFT-LDA Si, both the glide and shuffle slip systems, the two formulations are very similar; the difference in the critical G is less than 14%. In the tension-shear coupled model, the two formulations give the same instability for dislocation emission or crack branching, and the difference is less than 4%. We may conclude that for Si, the isotropic formulation is a good approximation. It would consequently support the use of isotropic formulation in the analysis of activation energy for dislocation emission in Si by Rice and Beltz (1994) and Beltz and Rice (1994).

VI THE CASE WHEN IN-PLANE AND ANTI-PLANE ELASTICITY IS COUPLED

So far, we assumed that the z axis along the crack front is perpendicular to a mirror plane for the lattice, so that the in-plane field quantities are decoupled from the anti-plane ones. If this were not true, the assumption is only good as an approximation. For the exact method of treatment for the coupled case, see Stroh (1958), Asaro and Barnett (1972) and Suo (1989).

ACKNOWLEDGEMENT

We would like to thank Prof. James R. Rice for suggesting this research topic, and encouraging us throughout this work, and critically reading the manuscript. The studies reported here have been supported by the Office of Naval Research, Mechanics Division (grants N00014-90-J-1379 and N00014-92-J-1960). We also thank Douglas Galpin for proofreading the manuscript. Additional support came from a University Research Initiative (subcontract POAVB38639-0 from the University of California, Santa Barbara, based on ONR/DARPA contract N00014-86-K-0753). Some of the computations were carried out using CRAY Y-MP and C90 computers under NSF support at the Pittsburgh Supercomputing Center. GEB also acknowledges support of a postdoctoral appointment with Solid Mechanics group at Brown University, as well as a fellowship from the Alexander von Humboldt Foundation (carried out at the Max-Planck-Institut für Metallforschung, Institut für Werkstoffwissenschaft, Stuttgart), during the conducting stages of this work.

REFERENCE

Asaro, R. J. (1975), "An image force theorem for a dislocation near a crack in an anisotropic elastic medium," J. Phys. F: Metal Phys., **5**, 2249-2255.

Atkinson, C. (1966) "The interaction between a dislocation and a crack," Int. J. Fracture Mech., **2**, 567-575.

Barnett, D. M. and R. J. Asaro (1972), "The fracture mechanics of slit-like cracks in anisotropic media," J. Mech. Phys. Solids, **20**, 353-366.

Barnett, D. M. and J. Lothe (1974), "An image force theorem for dislocations in anisotropic bicrystals," J. Phys. F: Metal Phys., 4, 1618-1635.

Beltz, G. E. (1992), "The mechanics of dislocation nucleation at a crack tip," Ph.D. thesis, Div. of Applied Sciences, Harvard University, Cambridge, MA, USA.

Beltz, G. E., and J. R. Rice (1991), "Dislocation nucleation versus cleavage decohesion at crack tips," in *Modeling the Deformation of Crystalline Solids*, ed. T. C. Lowe, A. D. Rollett, P. S. Follansbee, and G. S. Daehn, TMS, 457-480.

Beltz, G. E. and J. R. Rice (1994), "The activation energy for dislocation nucleation in silicon," to appear in Theory and Simulation of Time-Dependent Processes in Materials, edited by M. I. Baskes, A. Needleman, and S. Pantelides, M.R.S. (1994).

Bilby, B. A. and J. D. Eshelby (1968), "Dislocations and the theory of fracture," in Fracture: A*n Advanced Treatise*, ed. H. Liebowitz, **1**, 99-182, New York, Academic Press.

Cheung, K. S. (1990), "Atomistic study of dislocation nucleation at a crack tip," Ph.D. Thesis, Dept. of Nuclear Engineering, MIT, Cambridge, MA, USA.

Cheung, K. S., A. S. Argon and S. Yip (1991), "Activation analysis of dislocation nucleation from a crack tip in α-Fe," J. Appl. Phys., **69**(4), 2088-2096.

Cheung, K. S. and S. Yip (1990), "Brittle-ductile transition in intrinsic fracture behavior of crystals," Phys. Rev. Lett., **65** (22), 2804-2807.

Daw, M. S. and M. I. Baskes (1984), "Embedded Atom Method: derivation and application to impurities, surfaces, and other defects in metals," Phys. Rev. B, **29**(12), 6443-6453.

Duesbery, M. S., Michel, D. J., Kaxiras, E. and Joos, B. (1990) "Molecular dynamics studies of defects in Si," in *Defects in Materials*, ed. by P. D. Bristowe, J. E. Epperson, J. E. Griffith and Z. Liliental-Weber, MRS Symp. Proc. **209**, 125-130.

Erdogan, F. and G. D. Gupta (1972), "On the numerical solution of singular integral equations," Quart. Appl. Math., **29**, 525-534.

Erdogan, F. (1975), "Complex function technique," in *Continuum Physics*, ed. by A. C. Eringen, Academic Press, 523-603.

Foiles, S. M., M. I. Baskes, and M. S. Daw (1986), "Embedded-atom-method functions for the fcc metals Cu, Ag, Au, Ni, Pd, Pt, and their alloys," Phys. Rev. B., 33, 7983-7991.

Foiles, S. M. and M. S. Daw (1987), "Application of the embedded atom method to Ni_3Al," J. Mater. Res., **2** (1), 5-15.

Harrison, R. J., F. Spaepen, A. F. Voter, and A. F. Chen (1990), "Structure of grain boundaries in iron," in *Innovations in Ultrahigh- Strength Steel Technology*, ed. G. B. Olson, M. Azrin

and E. S. Wright, Plenum Press, 651-675.

Hirth, J. P. and J. Lothe (1982), *Theory of Dislocations*, 2nd Edition, McGraw Hill, New York.

Hoagland, R. G., M. S. Daw, S. M. Foiles and M. I. Baskes (1990), "An atomic model of crack tip deformation in aluminum using an embedded atom potential," J. Mater. Res., **5**, 313-324.

Huang,Y. M., J. C. H. Spence, O. T. Sankey and G. B. Adams (1991), "The influence of internal surfaces on the (2×1) shuffle and glide cleavage reconstructions for Si (111)," Surface Science, **256**, 344-353.

Huang, Y. M. (1992), Private communication.

Kaxiras, E. and M. S. Duesbery (1993), "Free energies of generalized stacking faults in Si and implications for the brittle-ductile transition," Phys. Rev. Lett. **70** (24), 3752-3755.

Nabarro, F. R. N. (1947), "Dislocations in a simple cubic lattice," Proc. Phys. Soc., **59**, 256–272.

Peierls, R. E. (1940), "The size of a dislocation," Proc. Phys. Soc, **52**, 34-37.

Rice, J. R. (1968a), "A path independent integral and the approximate analysis of strain concentration by notches and cracks," J. Appl. Mech., **35**, 379-386.

Rice, J. R. (1968b), "Mathematical analysis in the mechanics of fracture," Ch. 3 of *Fracture: An Advanced Treatise (vol. 2, Mathematical Fundamentals)*, ed. H. Liebowitz, Academic Press, NY, 191-311.

Rice, J. R., (1985), "Conserved integrals and energetic forces," in *Fundamentals of Deformation and Fracture (Eshelby Memorial Symposium)*, Ed. B. A. Bilby, K. J. Miller and J. R. Willis, Cambridge University Press, pp. 1-56.

Rice, J. R. (1992), "Dislocation nucleation from a crack tip: an analysis based on the Peierls concept," J. Mech. Phys. Solids, **40**, 239 - 271.

Rice, J. R. (1992b), private communication.

Rice, J. R. and G. E. Beltz (1994), "The Activation Energy for Dislocation Nucleation at a Crack," in press, J. Mech. Phys. Solids **42**, No. 2.

Rice, J. R., G. E. Beltz, andY. Sun (1992), "Peierls framework for dislocation nucleation from a crack tip," in *Topics in Fracture and Fatigue*, ed. A. S. Argon, Springer-Verlag, 1-58.

Rice, J. R., and R. Thomson (1974), "Ductile vs. brittle behavior of crystals," Phil. Mag., **29**, 73-97.

Schöck, G. (1991), "Dislocation emission from crack tips," Phil. Mag., **A63**, 111-120.

Stroh, A. N. (1958), "Dislocations and cracks in anisotropic elasticity," Phil. Mag., **3**, 625-646.

Sun, Y. (1993), "Atomistic aspects of dislocation/crack tip interaction," Ph.D. thesis, Div. of Applied Sciences, Harvard University, Cambridge, MA, USA.

Sun, Y., G. E. Beltz and J. R. Rice (1993), "Estimates from atomic models of tension-shear coupling in dislocation nucleation from a crack tip," Mater. Sci. and Eng. **A 170**, pp. 67-85.

Suo, Z. (1989), "Singularities interacting with interfaces and cracks,", Int. J. Solids and Struct., **25**(10), pp. 1133-1142.

Suo, Z. (1990), "Singularities, interfaces and cracks in dissimilar anisotropic media," Proc. R. Soc. Lond. **A 427**, pp. 331-358.

APPENDIX
DISLOCATION AND CRACK TIP INTERACTIONS IN AN ANISOTROPIC ELASTIC MEDIUM

As mentioned in Chapter Four, we need the function $F_{\alpha\beta}(r, s, \theta)$ and $g_{\alpha\beta}(r, s, \theta)$ for the crack problem. The stress distribution around the tip in an anisotropic medium without a dislocation and with one has been solved, originally by Stroh (1958), Atkinson (1966), Barnett and Asaro (1972), Asaro (1975) and summarized by Suo (1989) using the stress function method. Here, we prove two elegant theorems about the function $g_{\alpha\beta}(r, s, \theta)$. The scenario is illustrated in Fig. 14. Suppose a dislocation of Burgers vector b_β is located at (s, θ) in polar coordinate system from the crack tip. The local polar coordinate system at the dislocation core is (ρ, ω).

Near the dislocation, the stress $\sigma_{ij}(\rho, \omega)$ behaves like $1/\rho$. From Rice (1985), we deduce that,

$$h_k(\phi)\, \sigma_{ki}(\rho, \omega) = \frac{1}{4\pi} \frac{\Lambda_{ij}^{-1} b_j}{\rho}, \ \rho \text{ is small}, \tag{50}$$

where $h_\gamma(\omega)$ is the unit vector in the direction of increasing ω. Note that the right hand side of Eq. (50) is independent of ω, which results from the equation of stress equilibrium. The indices i and j are those of tensors. Therefore, we can transform from (x, y, z) denoted as Latin letters coordinate system to (r, θ, z) as in Greek indices α and β by tensor transformation, by a rotation of angle θ around the z axis. We obtain that, taking ϕ equal to θ,

$$\sigma_{\theta\alpha}(\rho, \theta) = \frac{1}{4\pi} \frac{\Lambda_{\alpha\beta}^{(\theta)-1} b_\beta}{\rho}, \ \rho \text{ is small}, \tag{51}$$

From the Aktinson (1966) solution and Suo (1989) treatment of a dislocation interacting with a crack tip in an anisotropic medium, we can show that when the dislocation lies in front of the crack tip and in the crack plane, i.e., $\theta = 0$, the stress $\sigma_{2i}(r)$ ahead of the crack tip and in the plane is,

$$\sigma_{2i}(r) = \frac{1}{4\pi} \sqrt{\frac{s}{r}} \frac{\Lambda_{ij}^{-1} b_j}{r - s}. \tag{52}$$

From Eq. (52) we can deduce that the stress intensity factors induced by the dislocation are

$$K_i = -\frac{1}{2\sqrt{2\pi s}} \Lambda_{ij}^{-1} b_j, \tag{53}$$

where, i = 1, 2, and 3 for mode II, I and III, which was given by Rice (1985). We also observe that Eq. (52) satisfies Eq. (51).

For a dislocation lying in the inclined slip plane as shown in Fig. 14, we write the generalization of (52) as,

$$\sigma_{\theta\alpha}(r, \theta) \equiv g_{\alpha\beta}(r, s; \theta)\, b_\beta = \frac{1}{4\pi} \sqrt{\frac{s}{r}} \frac{[\Lambda_{\alpha\beta}^{(\theta)-1} + h_{\alpha\beta}(r/s, \theta)]\, b_\beta}{r - s}, \tag{54}$$

In order to satisfy Eq. (51) when $\rho = r - s$ is small, we demand that,

$$h_{\alpha\beta}(t = 1, \theta) = 0, \text{ for } r = s, \tag{55}$$

in order to have proper stress fields in the linear elastic medium near the dislocation point s. Furthermore, the Rice-Thomson image force theorem (1974), which was generalized by Asaro (1975) to anisotropic elasticity, and further generalized by Rice (1985) to the sector-wise different anisotropic elasticities at a crack tip, for a dislocation line at a crack tip implies that

$$\partial h_{\alpha\beta}(t = 1, \theta) / \partial t \text{ is antisymmetrical for indices } \alpha \text{ and } \beta. \qquad (56)$$

Eq. (56) is proven next. We point out that Eq. (55) and (56) are generalizations from isotropic results deduced by Rice (private communication, 1992).

From Rice (1985), the attraction force received by the dislocation should be

$$f_r = -\frac{b_i \ \Lambda_{ij}^{-1} \ b_j}{8 \pi s} = -\frac{b_\alpha \ \Lambda_{\alpha\beta}^{(\theta)-1} \ b_\beta}{8 \pi s} \ . \qquad (57)$$

We can obtain the image force f_r by the following procedure. Consider the stress field of Eq. (54) and decompose it into the field of a dislocation in an uncracked crystal, plus another term which is bounded at the dislocation. That other term, evaluated at r = s and multiplied by b_α , gives the Peach-Koehler force, which must be consistent with Eq. (57). Thus we establish that

$$b_\alpha \, \partial h_{\alpha\beta} \, (t = 1, \theta) / \partial t \, b_\beta = 0 \, , \qquad (58)$$

which is equivalent to Eq. (56). We have omitted the details.

Table 1. The crack and slip systems.

lattice	crack model	x_1-x_2-x_3, crack coord.	slip system
bcc	A	[010]-[001]-[100]	(1/2) [11$\bar{1}$] (011)
bcc	B	[$\bar{1}$10]-[001]-[110]	(1/2) [11$\bar{1}$] ($\bar{1}$10)
bcc	C	[011]-[0$\bar{1}$1]-[100]	(1/2) [11$\bar{1}$] (011)
fcc	D	[$\bar{1}$10]-[001]-[110]	(1/6) [121] (1$\bar{1}$1)
fcc	E	[001]-[$\bar{1}$10]-[110]	(1/6) [$\bar{1}$12] ($\bar{1}$1$\bar{1}$)
fcc	F	[111]-[1$\bar{1}$0]-[11$\bar{2}$]	(1/6) [2$\bar{1}\bar{1}$] (11$\bar{1}$)
fcc	G	[1$\bar{1}$2]-[$\bar{1}$11]-[110]	(1/6) [$\bar{1}$12] ($\bar{1}$1$\bar{1}$)

Table 2. Critical loading $G_d / \gamma_{us}^{(r)}$ for dislocation emission from an anisotropic crack under mode I loading.

mat.	crack orient.	(θ, ϕ in °)	eff	τ	$\sigma-\tau$	η recipe
Fe	A	(–45, 35.3)	29.96	27.40	10.58(C)	0.9577
Fe	B	(–90, 54.7)	11.85	9.144	8.106	0.8785
Fe	C	(–90, 35.3)	23.80	19.48	17.75	0.9058
Ni	D	(54.7, 60)	32.02	29.06	22.09	0.9528
Ni	E	(35.3, 0)	10.48	9.92	8.103	0.9720
Al	D	(54.7, 60)	28.40	25.72	19.85	0.9518
Al	E	(35.3, 0)	11.54	10.89	8.705	0.9716
Al	F†	(90, 30)	10.71	8.315	7.664	0.8813
Ni_3Al	D	(54.7, 60)	30.27	28.43	17.91(C)	0.9557
Ni_3Al	E	(35.3, 0)	11.05	10.40	8.342	0.9698
Si, glide	D	(54.7, 60)	29.13	26.70	2.959(C)	0.9574
Si, glide	E	(35.3, 0)	11.66	10.89	2.041(C)	0.9665
Si, glide	F†	(90, 30)	10.27	7.879	5.784	0.8758
Si, glide	G†	(70.5, 0)	6.521	5.253	3.226	0.8975
Si, glide	G†	(70.5, 60)	20.56	17.97	4.729(C)	0.9348
Si, shuffle	D	(54.7, 30)	11.26	9.560	2.642(C)	0.9213
Si, shuffle	E	(35.3, 30)	14.54	13.69	1.979(C)	0.9702

Si, shuffle	**F†**	(90, 0)	8.243	6.166	6.345	0.8649
Si, shuffle	**G†**	(70.5, 30)	8.082	6.669	3.882(C)	0.9084

---

†: the in-plane elasticity is taken to be decoupled from the anti-plane elasticity to simplify the treatment, which is only approximate.
(C): the instability may correspond to decohesion along the inclined slip plane rather than dislocation emission.

Figure Captions

Fig. 1 A semi-infinite crack tip is shear loaded by K_{II}, while an incipient shear zone of edge character on the coplanar plane with the crack relieves the singular shear stress field. J-integrals are evaluated along the far and slit paths.

Fig. 2 The periodic relation of shear stress (solid curve) and its associated potential (dashed curve) versus the slip displacement within the Peierls concept. Each is scaled by its maximum; the displacement by b.

Fig. 3 An incipient dislocation, represented by a distribution of sliding and opening displacements, develops along a tilted slip plane at angle θ with respect to the crack plane, in response to the mixed loading K_{II} and K_I.

Fig. 4 The angular distribution of the singular shear stress $\sigma_{\theta r}(r, \theta)\sqrt{2\pi r} / K_I = F_{12}(\theta)$ near Crack tip A under mode I loading in EAM Fe, anisotropic versus isotropic formulations.

Fig. 5 The angular distribution of the singular shear stress $\sigma_{\theta r}(r, \theta)\sqrt{2\pi r} / K_I = F_{12}(\theta)$ near Crack tip A under mode I loading in EAM Al, anisotropic versus isotropic formulations.

Fig. 6 The angular distribution of the singular shear stress $\sigma_{\theta r}(r, \theta)\sqrt{2\pi r} / K_I = F_{12}(\theta)$ near Crack tip B under mode I loading in EAM Fe, anisotropic versus isotropic formulations.

Fig. 7 The angular distribution of the singular shear stress $\sigma_{\theta r}(r, \theta)\sqrt{2\pi r} / K_I = F_{12}(\theta)$ near Crack tip C under mode I loading in EAM Fe, anisotropic versus isotropic formulations.

Fig. 8 The distribution of the stress $\sigma_{\theta r}(r, \theta) = g_{11}(r, s, \theta)\, b$ produced by an edge dislocation of Burgers vector b located at s = 5 b on a 45° tilted slip plane in Crack tip A, anisotropic versus isotropic formulations.

Fig. 9 The critical load G_d as a function of inclination angle θ for dislocation emission from Crack A in EAM Fe under mode I loading as determined in the shear-only model, anisotropic versus isotropic formulations.

Fig. 10 The critical load G_d as a function of the phase angle ψ of loading for edge dislocation emission from Crack A in EAM Fe on a coplanar slip plane, as determined in the tension-shear coupled model, anisotropic versus isotropic formulations. Fitting by the isotropic shear-only model with the tension reduced unstable stacking energy $\gamma_{us}(\psi)$ is also shown is.

Fig. 11 The critical loading G_d as a function of the inclination angle θ for edge dislocation emission from Crack A in EAM Fe under mode I loading, as determined in the effective approximation, shear-only and tension-shear coupled model (scaled by $\gamma_{us}^{(u)}$), anisotropic formulations.

Fig. 12 The critical loading G_d as a function of the inclination angle θ for edge dislocation

emission from Crack B in EAM Fe under mode I loading, as determined in the effective approximation, shear-only and tension-shear coupled model (scaled by $\gamma_{us}^{(u)}$), anisotropic formulations.

Fig. 13 The critical loading G_d as a function of the inclination angle θ for edge dislocation emission from Crack C in EAM Fe under mode I loading, as determined in the effective approximation, shear-only and tension-shear coupled model (scaled by $\gamma_{us}^{(u)}$), anisotropic formulations.

Fig. 14 A dislocation interacting with crack tip in an anisotropic medium.

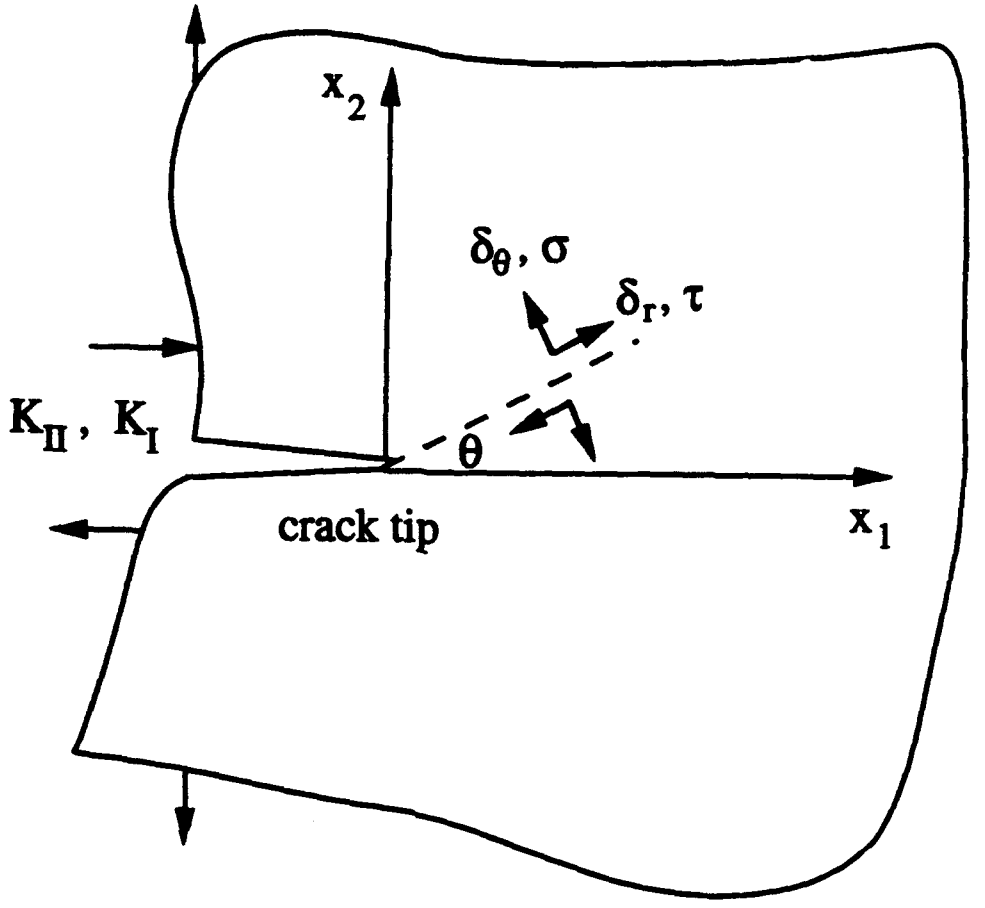

Fig. 1

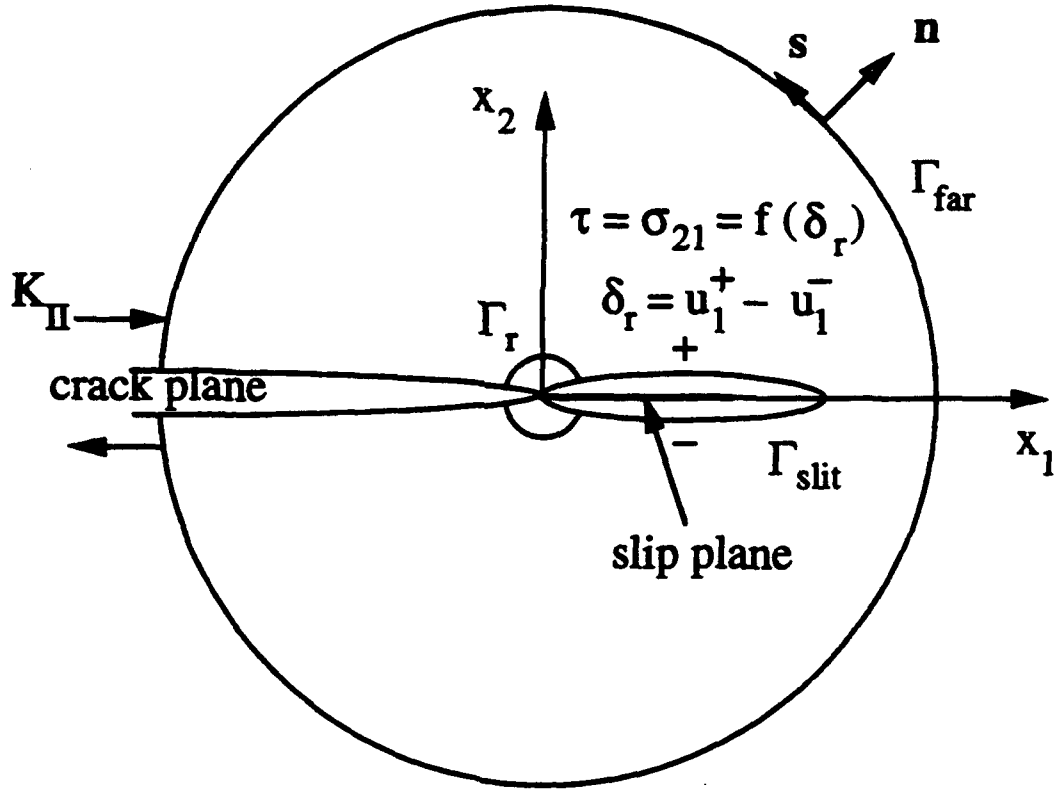
s
n
x_2
Γ_{far}
$\tau = \sigma_{21} = f(\delta_r)$
$\delta_r = u_1^+ - u_1^-$
K_{II}
Γ_r
+
crack plane
−
Γ_{slit}
x_1
slip plane

Fig. 2

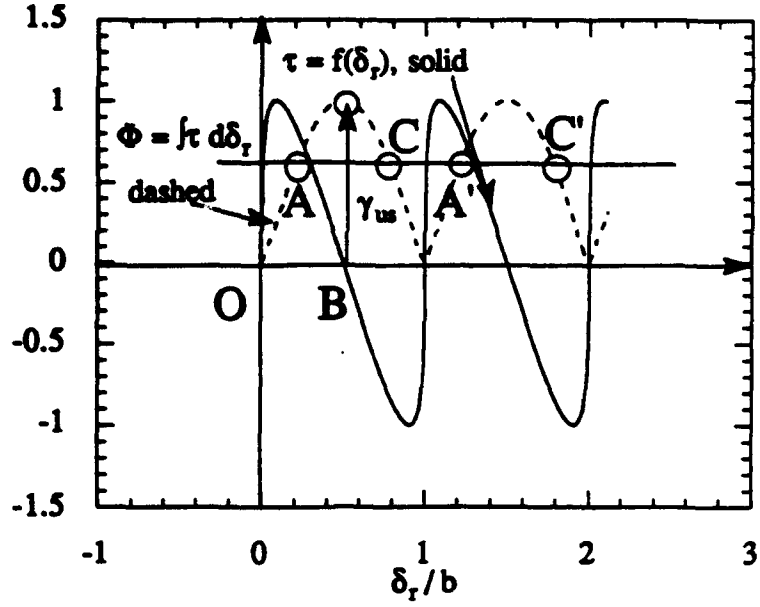
1.5
1
0.5
0
-0.5
-1
-1.5
-1
0
1
2
3
δ_r/b
$\tau = f(\delta_r)$, solid
$\Phi = \int \tau \, d\delta_r$
dashed
A
B
C
C'
A'
O
γ_{us}

Figure 3

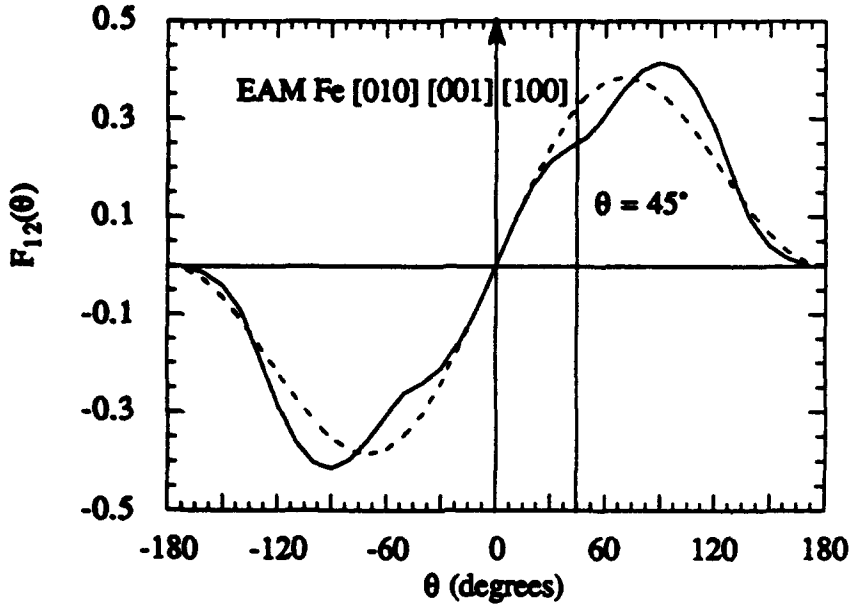

Figure 4

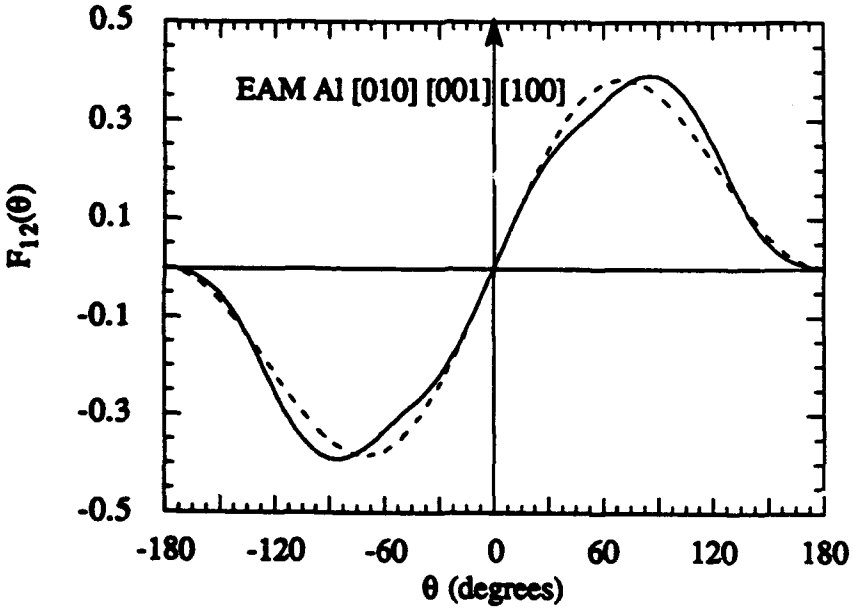

Figure 5

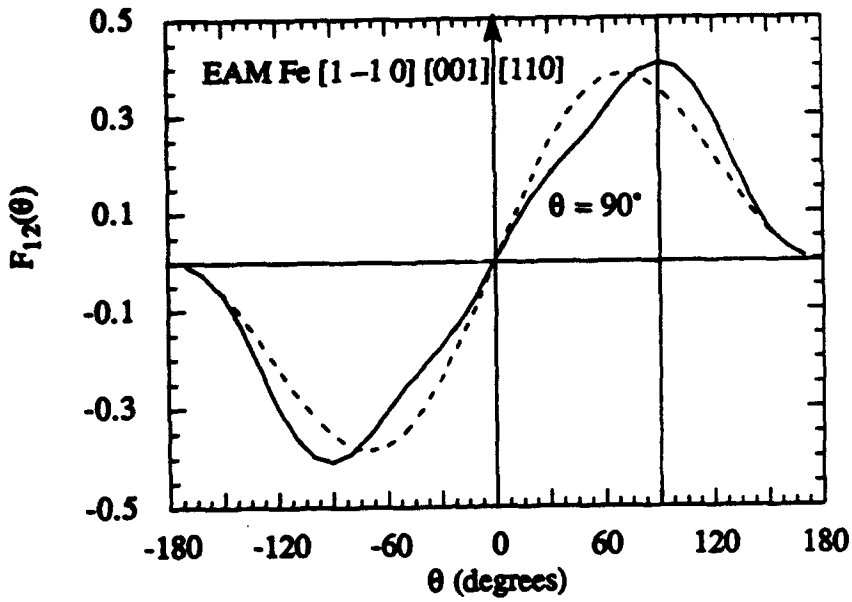

Figure 6

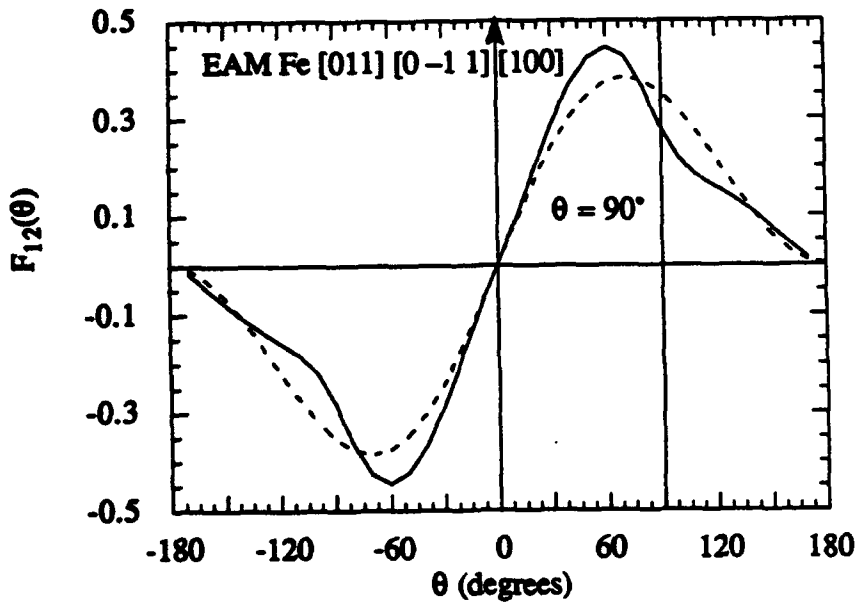

Figure 7

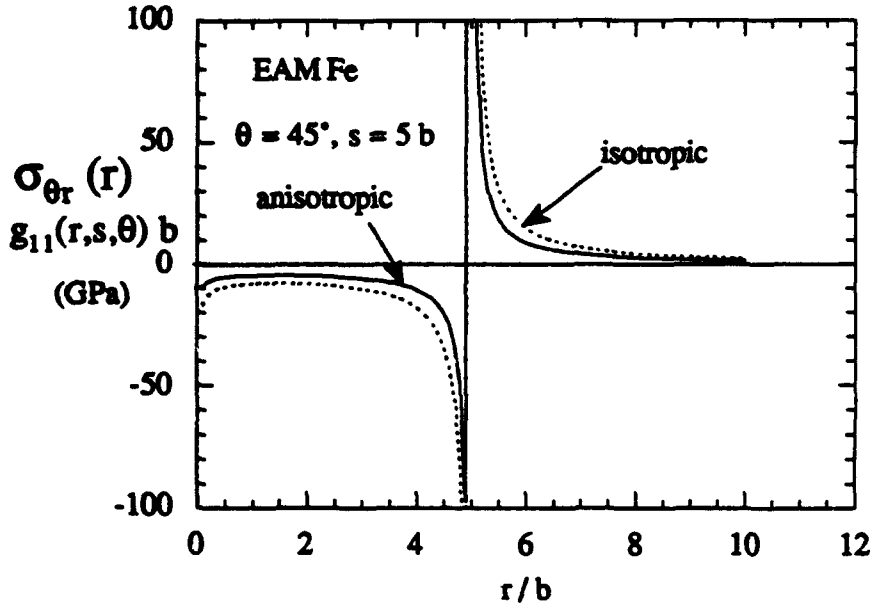

Figure 8

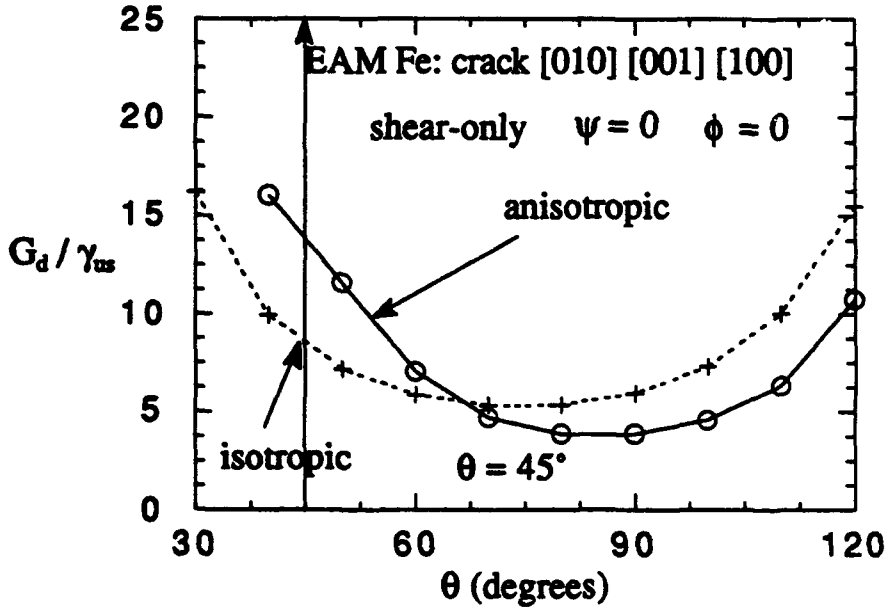

Figure 9

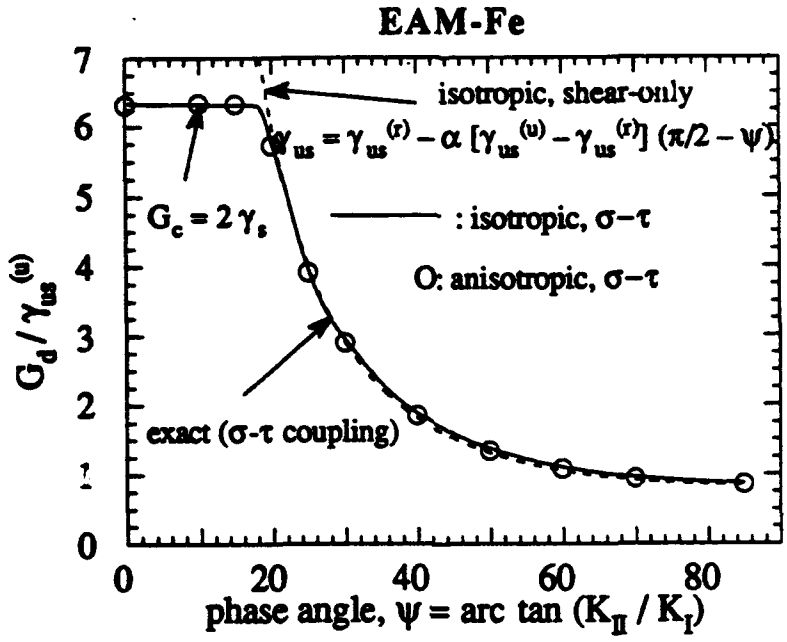

Figure 10

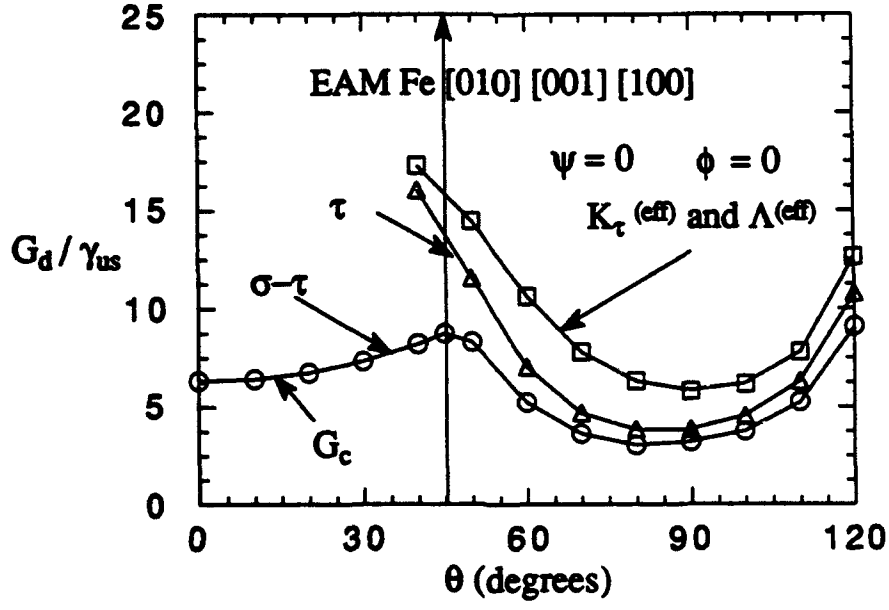

Figure 11

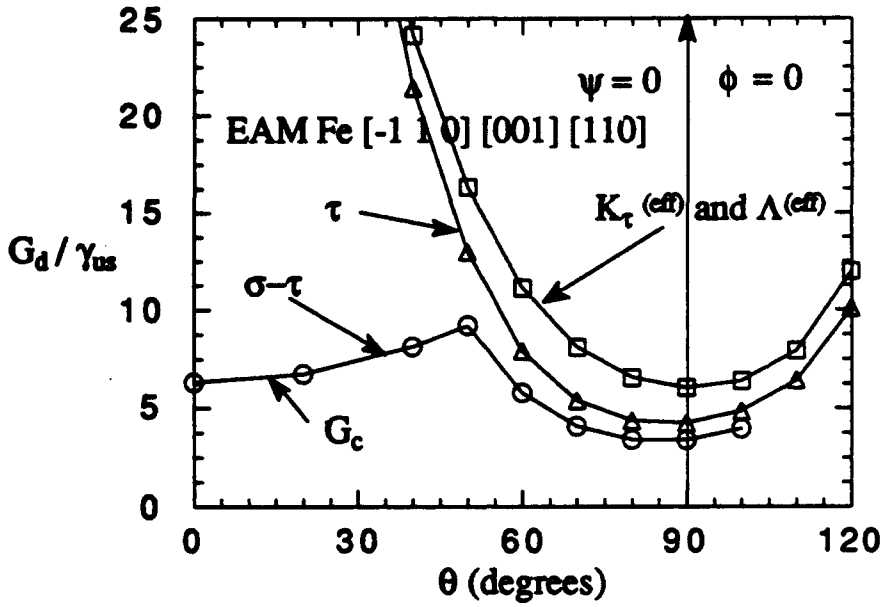

Figure 12

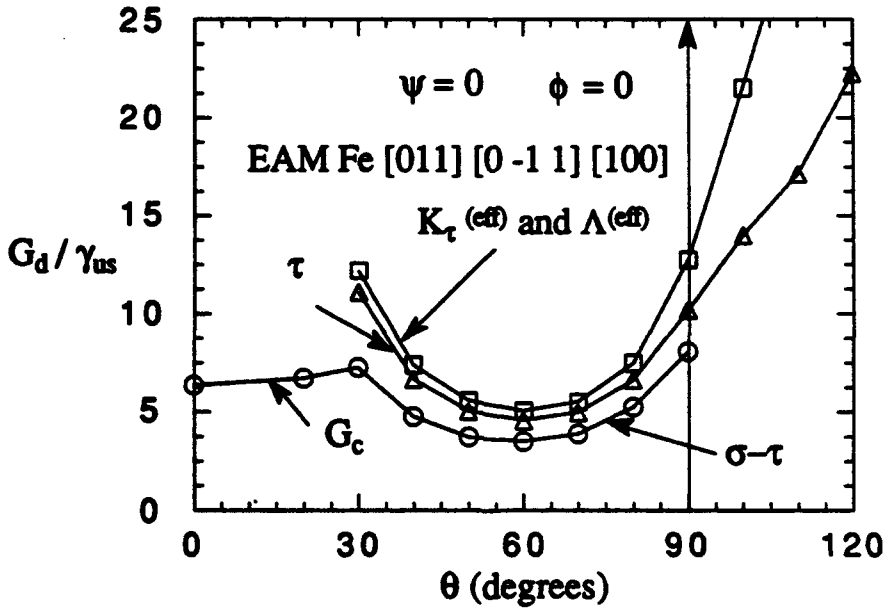

Figure 13

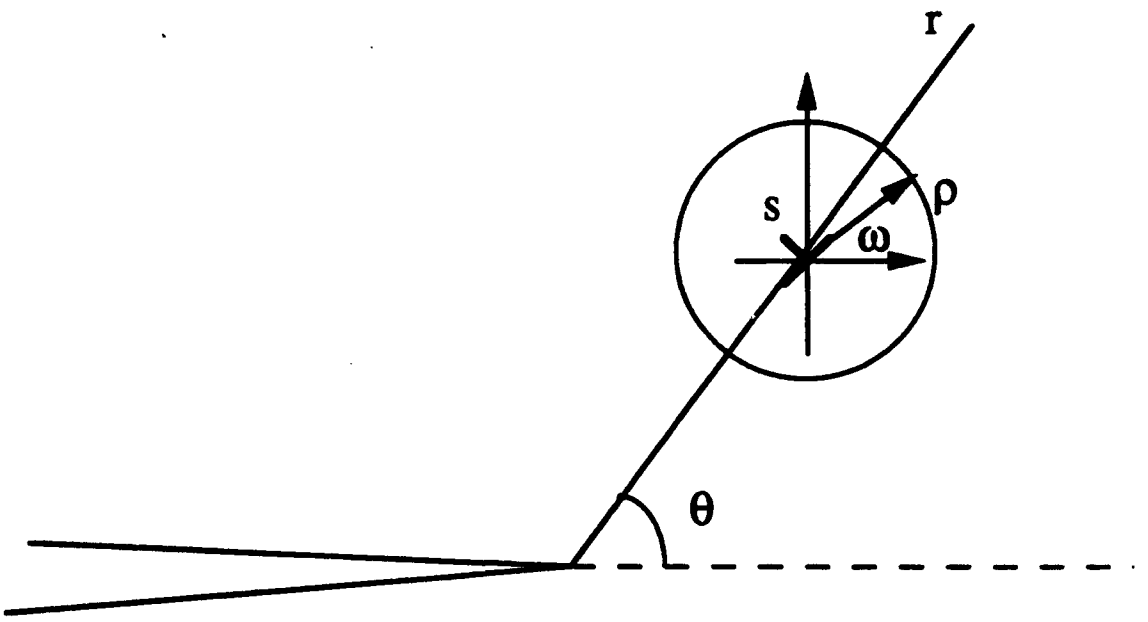

Fig. 14 A dislocation interacting with a crack tip in an anisotrpic medium.